Improvement and interpretation of the tropospheric ozone columns retrieved based on SCIAMACHY Limb-Nadir Matching approach

Dissertation zur Erlangung des Grades *Doktor der Naturwissenschaften* (*Dr.rer.nat.*)

von

Jia Jia

Institut für Umweltphysik

Fachbereich Physik und Elektrotechnik

Universität Bremen

Mai 2016

1. Gutachter:	Priv.-Doz. Annette Ladstaetter-Weissenmayer
2. Gutachter:	Prof. Christian von Savigny
Betreuer:	Priv.-Doz. Annette Ladstaetter-Weissenmayer
Dissertation eingereicht am:	25. Mai 2016
Datum des Kolloquiums:	30. Juni 2016

怕什么真理无穷，进一寸有一寸的欢喜

--------- 胡适（1891—1962）

To the years in Bremen

Abstract

Tropospheric ozone, one of the most important green-house gases and one of the most essential components of photochemical smog, has been monitored from space by different retrieval techniques since the late 1980s. Satellite measurements are well suitable to investigate sources and transport mechanisms of tropospheric ozone, as well as its atmospheric chemistry on regional and global scales. Nevertheless, the retrieval of tropospheric ozone columns (TOCs) from satellite data constitutes a big challenge since approximately 90% of the total ozone amount is located in the stratosphere, and only the remaining 10% is located in the troposphere.

The Limb-Nadir Matching technique is one of the methods that has been widely used to retrieve TOCs from space borne measurements. In previous studies, this approach has been applied to measurements from the SCIAMACHY instrument, which alternates limb and nadir geometry. An accurate tropopause height, retrieved from the ECMWF database, was used to subtract the stratospheric ozone column from the total ozone column.

In this thesis, a three-step approach is shown that was developed to improve the current Limb-Nadir Matching TOC retrieval technique, and resulted in the new database version 1.2. Several improvements in the V1.2 TOC data have been achieved. The obtained amount of TOC V1.2 data has increased by a factor of two in comparison to the original dataset. Furthermore, the data quality has improved in many aspects. First of all, the V1.2 TOC data set reduces the negative (>10 DU) and positive (~10 DU) biases over tropics and high latitudes, respectively. The reduction is achieved by use of the improved limb ozone data set V3.0, which was tested and validated against the previous version V2.9 in this thesis. The TOC values were also optimized over the midlatitudes by decreasing its positive biases. The yearly averaged V1.2 TOC data set agrees well with ozonesonde measurements within 5 DU globally. More details on the TOC distribution were successfully captured because of the improved accuracy of the data. The clear observation of the spring TOC maxima (~42 DU) over the Arabian Sea (AS) during the pre-monsoon is one of the benefits of using the V1.2 TOC product.

In the present thesis, the potential sources of the AS spring ozone pool are investigated by use of multiple data sets (e.g., SCIAMACHY Limb-Nadir-Matching TOC, OMI/MLS TOC, TES

TOC, MACC reanalysis data, MOZART-4 model and HYSPLIT model). 3/4 of the enhanced ozone concentrations are attributed to the 0-8 km height range. The main source of the ozone enhancement is considered to be caused by long range transport of pollutants from India (~ 50% contributions to the lowest 4 km, ~ 20% contributions to the 4-8 km height range), the Middle East, Africa and Europe (~30% in total). In addition, the vertical pollution accumulation in the lower troposphere, especially at 4-8 km, was found to be important for the AS spring ozone pool. Local photochemistry, on the other hand, plays a negligible role in producing ozone at the 4-8 km height range. In the 0-4 km height range, ozone is quickly removed by wet-deposition. The AS spring TOC maxima are influenced by the dynamical variations caused by the sea surface temperature (SST) anomaly during the El Niño period in 2005 and 2010 with a ~5 DU decrease.

The Limb-Nadir Matching retrieval improvement scheme developed in this thesis leads to a much more accurate TOC product measured by SCIAMACHY and a better understanding of tropospheric ozone distributions.

List of Publications

Parts of this thesis (including text passages, figures, and tables) have been previously presented in various research articles, conference talks, and conference posters.

Peer-reviewed publications

Jia, J., Rozanov, A., Ladstätter-Weißenmayer, A., and Burrows, J. P.: Global validation of SCIAMACHY limb ozone data (versions 2.9 and 3.0, IUP Bremen) using ozonesonde measurements, Atmos. Meas. Tech., 8, 3369-3383, doi:10.5194/amt-8-3369-2015, 2015.

Jia, J., Ladstätter-Weißenmayer, A., Rozanov, A., and Burrows, J. P.: Towards a Better Tropospheric Ozone Data Product from SCIAMACHY: Improvements in High Latitude Stratospheric Ozone, Towards an Interdisciplinary Approach in Earth System Science, SpringerBriefs in Earth System Sciences, doi: 10.1007/978-3-319-13865-7, 2015.

Jia, J., Ladstätter-Weißenmayer, A., Hou, X., Rozanov, A., and Burrows, J. P.: Tropospheric ozone maxima observed over the Arabian Sea during the pre-monsoon, Manuscript in preparation for publication in Atmos. Chem. Phys.

Proceedings

Jia, J., Ladstätter-Weißenmayer, A., Rozanov, A., Ebojie, F., and Burrows, J. P.: Improvement of the SCIAMACHY Limb-Nadir-Matching method in retrieving tropospheric ozone columns, Manuscript in preparation for publication.

Conference contributions

Posters

Jia, J., Rozanov, A., Ladstätter-Weißenmayer, A., Burrows , J.P., Sonde validation of improved SCIAMACHY ozone limb data on global scale: V2.9 to V3.5, Living Planet Symposium 2016, *Prague, Czech Republic, 9-13 May 2016*

Jia, J., Ladstätter-Weißenmayer, A., Hou, X., Rozanov, A., Burrows, J.P., Tropospheric ozone pool over Arabian sea during pre-monsoon, *EGU General Assembly, Vienna, Austria, April 2016*

Jia, J., Rozanov, A., Ladstätter-Weißenmayer, A., Burrows, J.P., Sonde validation of improved SCIAMACHY ozone limb data on global scale, *8th atmospheric limb workshop, Gothenburg, Sweden, 15-17 September 2015*

Jia, J., Ladstätter-Weißenmayer, A., Rozanov, A., Burrows, J.P., The tropospheric ozone variation over Arabian sea: the importance of SCIAMACHY Limb-Nadir Matching tropospheric data improvement, *Panda summer school, Bremen, Germany, 23-29 August 2015*

Jia, J., Ladstätter-Weißenmayer, A., Ebojie, F., Rozanov, A., Burrows, J.P., The tropospheric ozone variation over Arabian sea during pre-monsoon, *EGU General Assembly, Vienna, Austria, April 2015*

Jia, J., Rozanov, A., Ladstätter-Weißenmayer, A., Ebojie, F., Burrows, J.P., Towards a better tropospheric ozone product from SCIAMACHY: improvements in Limb-Nadir Matching method, *ESSReS retreat, Bremenhaven, Germany, November 2014*

Jia, J., Ladstätter-Weißenmayer, A., Ebojie, F. , Rozanov, A., Burrows, J.P., Tropospheric ozone retrieval by using SCIAMACHY Limb-Nadir-Matching method, *EGU General Assembly, Vienna, Austria, April 2014*

Jia, J., Ladstätter-Weißenmayer, A., Rozanov, A., Ebojie, F., Burrows, J.P., Validation of improved SCIAMACHY ozone limb data". *7th Atmospheric Limb Conference , Bremen, Germany, June 2013*

Jia, J., Ladstätter-Weißenmayer, A., Rozanov, A., Ebojie, F., Burrows, J.P., Analysis and improvement of SCIAMACHY limb data for tropospheric ozone retrieval, *EGU General Assembly, Vienna, Austria, April 2013*

Jia, J., Ladstätter-Weißenmayer, A., Rozanov, A., Ebojie, F., Burrows, J.P., Improvement of SCIAMACHY Limb-Nadir Matching Tropospheric O3 Retrieval : Preliminary results, *1st ESSReS retreat, Bremen, Germany, November 2012*

Talks

Jia, J., et al., Enhanced tropospheric ozone over Arabian sea during pre-monsoon: the importance of SCIAMACHY Limb-Nadir Matching tropospheric data improvement, IUP Seminar Talk, Bremen, Germany, December 11, 2015

Jia, J., et al., An improved tropospheric ozone database retrieved from SCIAMACHY Limb-Nadir-Matching method, EGU General Assembly, Vienna, Austria, April 2015

Jia, J., et al., Towards a better tropospheric ozone product from SCIAMACHY Limb-Nadir-Matching method, DPG, Heidelberg, Germany, March 2015

Jia, J., et al., Validation of SCIAMACHY O_3 LIMB measurement, ESSReS retreat, Bremenhaven, Germany, November 8, 2013

Jia, J., et al., Analysis and improvement of SCIAMACHY data about tropospheric ozone, IUP Seminar Talk, Bremen, Germany, December 21, 2012

Acknowledgements

This work couldn't have been possibly done without the support I received during the time of my PhD studies at IUP, University of Bremen. I am deeply grateful for the opportunity to be a PhD student here at IUP. Therefore, I want to thank my mentors, colleagues, friends, family, and the institutions for their help and support. Thank you!

In the first place, I want to thank my supervisor, Priv.-Doz. Annette Ladstätter-Weißenmayer, who has been guiding me and taking care of me since our first meeting in Qingdao, China. I deeply appreciate your mentoring, tolerance, and respect that you gave me. Thank you for encouraging me to express my own opinions freely, regarding both work and private topics. I am very thankful to your patience and support in my growth from 'a kid' to 'an adult' in science. Thank you for your trust!

My deep gratitude goes to Prof. John P. Burrows for giving me the opportunity to carry out my PhD research in his group. I am thankful for your encouragement, motivation, and support. Thank you for all the time and patience you had for me despite your busy schedule.

Dr. Alexei Rozanov has provided me insightful advices in and out of my study field. Thanks to you and your help, I didn't get lost in the second year of my PhD and was able to continue further. I have a deep respect for your professional knowledge about limb ozone retrieval and validation, and I'm thankful for sharing it with me. I will always appreciate the opportunities that you have created for me, by sharing my research to other, more senior scientists, in the last years.

I would like to thank Prof. Christian von Savigny, who has always provided generous help whenever I contacted him. Thank you very much for agreeing and taking time to be the second reviewer of this thesis.

I am deeply grateful for being included in the DOAS group. My many thanks go to the group leader Dr. Andreas Richter, who has always been rational and calm in his discussions with me. He has given me plenty of support whenever I was confused, and I could learn so much from him. I am also very thankful to the all DOAS group members, who have provided me with the most relaxed and friendly atmosphere to enjoy work, meetings, lunches, and many other activities. Thank you all! Special thanks go to (in alphabetical order) Leonardo Alva-

rado, Anne Blechschmidt, Andreas Hilboll, Andreas Meier, Anja Schönhardt, Stefan Schreier, Folkard Wittrock.

My thanks go to Felix Ebojie, Nabiz Rahpoe, and Stefan Bötel for the useful discussions and meetings regarding tropospheric ozone retrieval.

I also thank the limb group for allowing me to occasionally join their group meetings. I have appreciated the discussions very much, and the knowledge, that I have gained there, had helped me a lot in my research.

I am deeply grateful for being a member of the Earth System Science Research School (ESSReS), an initiative of the Helmholtz Association of German research centre (HGF) at the Alfred Wegener Institute for Polar and Marine Research. My special thanks go to Klaus Grosfeld, Stefanie Klebe, Ludvig Loewemark, and Helge Meggers for putting their efforts in coordinating and supporting the program. ESSReS has broadened my scientific view and elevated my research abilities by providing numerous lectures, excursions, and soft skill trainings. I am very grateful for having a chance to meet all other ESSReS members and becoming good friends with them. Special thanks go to some of my ESSReS colleagues (in alphabetical order): Leonardo Alvarado, Hella van Asperen, Matthias Buschmann, Lars Beierlein, Dimitar Misev, Yoshihiro Nakayama, Jelmer Oosthoek, Stefan Schreier, and Aleksandra Wolanin, who were always there for me to discuss and support me in my research, to cheer me up when I was most troubled and helpless, and to push me forward during writing this thesis.

I am especially grateful to (in alphabetical order) Hella van Asperen, Anna Blechschmidt, Andreas Hilboll, Alexei Rozanov, Niall Ryan, and Anja Schönhardt in reading parts of my thesis draft. Thank you all!

I am also thankful to the former and current colleagues at IUP. Special thanks go to (in alphabetical order) Faiza Azam, Lena Brinkhoff, Martin Budde, Kai-Uwe Eichmann, Claus Gebhardt, Thomas Krings, Elpida Leventidou, Luca Lelli, Patricia Liebing, Junshen Lu, Linlu Mei, Christian Melsheimer, Vladyslav Nenakhov, Stefan Noël, Anna Serdyuchenko, Mark Weber, Katja Weigel, Jongmin Yoon.

Many thanks to Petra Horn, Geraldine Schmiechen, Stephanie Drath, Anja Gatzka, and Birgit Teuchert for their administrative support.

I also thank Heiko Schellhorn and Heiko Schröter for the technical support.

I want to thank the Chinese Scholar Council (CSC) for funding my research in the first four years of my PhD studies. My thanks also go to the University of Bremen, ESSReS, and Post-graduate International Physics Programme (PIP) for providing funding in the latest stage of my PhD, and financially supporting my travels to conferences, workshops and meetings.

My special thanks go to the supervisor of my master thesis, Prof. Dong Wu, who encouraged me to purchase the opportunity to continue my studies abroad.

I am very grateful to my family and close friends in China, who have loved me and trusted me all along my 'journey'. 谢谢你们无条件的爱，信任和支持！

Last but not least, I want to thank René Tammen for his unconditional support, love and patience during the stressful time of writing this thesis.

Contents

1 Introduction

Earth's ecosystem change has been driven by humans, especially since the industrial revolution in Europe, i.e. since the late 18th century. While the world population increased from ~1 billion in 1800 to ~7.4 billion in 2016, mankind has developed new and powerful ways of influencing the environment. Within two centuries mankind has exhausted the fossil fuels that were generated over several hundred million years. Fossil fuel combustion leads to enormous emissions of trace gases to the Earth's atmosphere. These trace gases include carbon dioxide (CO_2) and methane (CH_4), which cause more than 2 Wm^{-2} increases in radiate forcing (RF) and lead to global warming, and nitrogen oxides (NO_x = NO + NO_2), carbon monoxide (CO), sulfur dioxide (SO_2), and volatile organic compounds (VOCs), leading to acid rain and photochemical smog. The global effects of human activities have become so clearly noticeable a new term, the 'Anthropocene', has been proposed and expressed to denote the current epoch (Crutzen and Stoermer, 2002).

Tropospheric ozone is not a directly emitted trace gas but rather a secondary product. Most tropospheric ozone is produced in situ by photochemical reactions of its precursors (NO_x, CO, CH_4 and VOCs) in the presence of sunlight, while some tropospheric ozone naturally originates in the stratosphere. Tropospheric ozone impacts on mankind in many aspects: (1) It is one of the most important components of photochemical smog. High surface ozone values are detrimental to human health by causing respiratory illnesses, and can also lead to losses in agricultural crops (see Van Dingenen et al., 2009; Mills et al., 2015 and references therein). (2) Tropospheric ozone is one of the most important green-house gases. With an average lifetime of ~23 days (Stevenson et al., 2006; Young et al., 2013), tropospheric ozone can influence the Earth's atmosphere on a global scale by long range transport. (3) It plays a central role in the chemistry of the troposphere, on account of the fact that it is the primary tropospheric source of the hydroxyl (OH) radical, which determines the lifetime and thus directly influences the concentrations of trace gases affected by oxidation.

The 'escape' of trace gases emitted from fossil fuel and biomass combustion give rise to photochemical ozone in the troposphere. The tropospheric ozone burden has increased by ~30% from pre-industrial times to the present day (IPCC, 2007; Young et al., 2013). According to the newest 'State of the Climate' reported in 2014, the global tropospheric ozone burden is

observed to continuously and significantly increase with a linear rate of 1.9 ± 0.8 Tg yr^{-1} in the last decade using satellite based data (Cooper and Ziemke, 2014). The positive trend is also seen in the in situ measurements of surface ozone (Fig. 1.1, Cooper et al., 2014). The rise of the tropospheric ozone burden has led to an RF growth of +0.35 ± 0.15W m^{-2} based on model simulations (IPCC, 2013). Nowadays, ozone-related mortality is estimated to make up ~5-20% of the mortality related to air pollution (see Monks et al., 2015 and references therein).

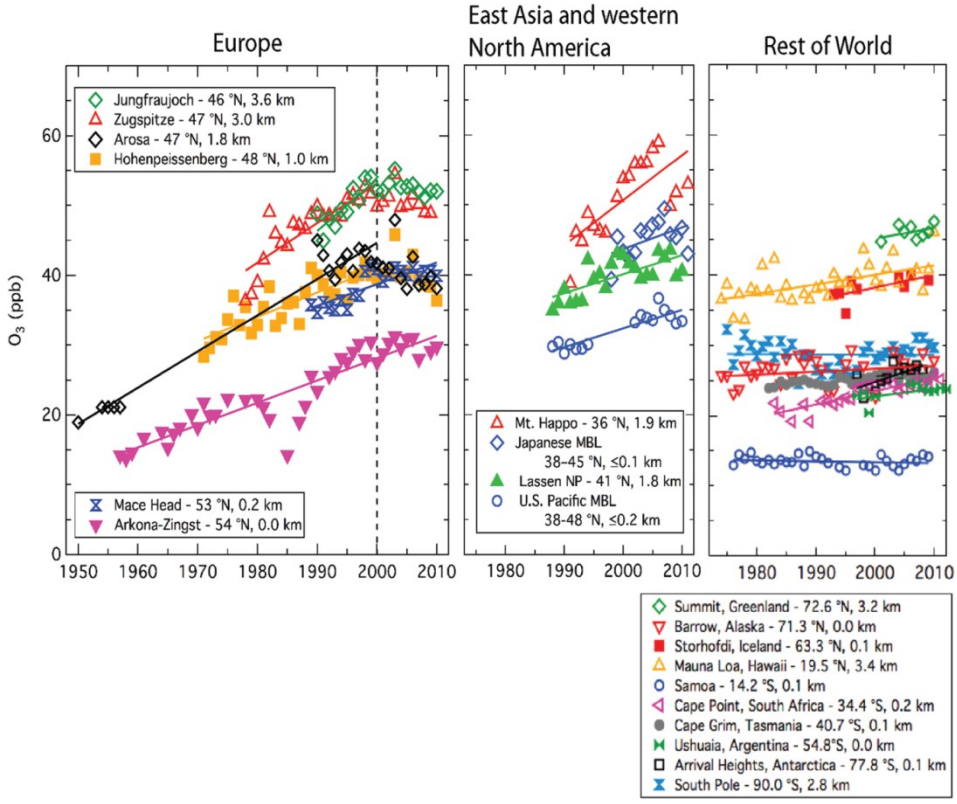

Figure 1.1 Surface ozone time series at several rural sites around the world (Fig. 1 in Cooper et al., 2014).

Satellite based retrievals of tropospheric ozone have been developed for around three decades and the observations have revealed more details about the spatial distribution compared to in situ measurements. The tropospheric ozone residual (TOR) method was the very first retrieval method applied to determine global tropospheric ozone columns (TOCs, Fishman et

al., 1990). In this method, tropospheric ozone is retrieved by subtracting the stratospheric ozone columns retrieved from limb measurements, from the collocated total ozone columns acquired from nadir measurements, by utilizing tropopause height data. Due to the fact that 90% of ozone is situated in the stratosphere, TOCs retrieved by this method are extremely sensitive to the errors of its three inputs. The Limb-Nadir Matching method is a TOR method that is developed for tropospheric trace gas retrievals using the SCIAMACHY (SCanning Imaging Absorption spectroMeter for Atmospheric CHartographY, Burrows et al., 1995; Bovensmann et al., 1999) and any other instrument with both nadir and limb measurements. There are two immediate advantages of the Limb-Nadir Matching retrieval. First, the trace gas total columns derived from nadir measurements and the stratospheric columns from the limb profiles have spatial and temporal coherence, and second, the two quantities are measured by the same instrument. SCIAMACHY Limb-Nadir Matching has been proven feasible (Ebojie et al., 2014). Nevertheless, several issues were identified in the retrieval which cause TOC results to fail in catching well-known distribution patterns and to overestimate ozone concentrations over mid-/high latitudes in the Northern Hemisphere. The improvements of the retrieval and measurement techniques are prerequisites for achieving better data quality and to assessing the consistency between satellite records required for synergistic exploitation.

One aim of the present thesis is to improve the retrieval of TOCs from SCIAMACHY using the Limb-Nadir Matching method. A considerable lack of data is found in the 7-year data analysis of the previous TOC product. This issue will be solved by improving the limb data screening process. Severe overestimation at the northern high latitudes will be corrected by improving the stratospheric column accuracy using the optimized limb ozone profile retrieval. The collocated tropopause height (TPH) will be obtained in a more sophisticated way in order to decrease the TPH induced errors. Both the retrieved limb ozone profiles and the resulting TOCs will be validated using balloon-borne ozonesonde measurements. A second aim of the present thesis is to investigate the global distribution of tropospheric ozone. Knowledge of the global distribution is necessary as a basis to increase our understanding of chemical influences and of the coupling between tropospheric ozone and the climate system. Following the data improvement, the tropospheric ozone pool over the Arabian Sea (AS) in boreal spring will be investigated and interpreted with the help of multiple data sets and models. The potential sources and the inter-annual variability of the high TOCs will be discussed.

This thesis is structured as follows: In Chapter 2, the scientific background of the Earth's atmosphere, atmospheric chemistry and the role of ozone, and the fundamentals of and instruments used for satellite measurements of tropospheric ozone are presented. The current state of tropospheric ozone research, including the measurement techniques and global distribution, is presented in Chapter 3. Chapter 4 introduces the main data used in this study. Chapter 5 forms the main part of the thesis and describes the various improvements of the Limb-Nadir Matching approach for tropospheric ozone retrieval. The enhancement of the tropospheric ozone concentrations over the AS during the pre-monsoon season is reported in Chapter 6. Finally, Chapter 7 summarizes the conclusions of the thesis and gives an outlook on proposed future work in the field of tropospheric ozone.

2 Scientific background

2.1 The Earth's atmosphere

The Earth's atmosphere is a thin layer of gas which uniformly covers the whole Earth, and is retained by Earth's gravity (Jacobson et al., 2000, p. 132). Today's atmosphere comprises a variety of constituents, including the main constituents – nitrogen (N_2), oxygen (O_2), argon (Ar), water (H_2O gas, liquid and solid), together with numerous trace gases – e.g., ozone (O_3), methane (CH_4), and oxides of nitrogen (N_2O, NO_x etc) (see Tab. 2.1).

Table 2.1: Major gaseous constituents of the Earth's atmosphere (up to 105 km) in fractional concentrations in volume, with respect to dry air (from Wallace and Hobbs, 2006, p. 8).

Constituent	**Molecular weight**	**Fractional concentration by volume**
Nitrogen (N_2)	28.013	78.08%
Oxygen (O_2)	32.000	20.95 %
Argon (Ar)	39.95	0.93 %
Water vapor (H_2O)	18.02	0-5 %
Carbon dioxide (CO_2)	44.01	>400 ppm
Neon (Ne)	20.18	18 ppm
Helium (He)	4.00	5 ppm
Methane (CH_4)	16.04	1.75 ppm
Krypton (Kr)	83.80	1 ppm
Hydrogen (H_2)	2.02	0.5 ppm
Nitrous oxide (N_2O)	56.03	0.3 ppm
Ozone (O_3)	48.00	Up to 10 ppm

Based on the vertical variation of the temperature profiles with altitude, the atmosphere is commonly divided into five layers: the troposphere, the stratosphere, the mesosphere, the thermosphere and the exosphere (Fig. 2.1). In the troposphere, the lowest atmospheric layer, the temperature decreases with increasing altitude, as a result of the adiabatic expansion of

rising air. The temperature pattern in the stratosphere is different. In this layer, the absorption of solar radiation by a rapidly increased O_2 density towards lower altitudes results in the presence of O atoms, $O(^3P)$. These atoms react with O_2 and form the ozone layer (Burrows et al., 2011). The ozone layer is very important because it protects the biosphere from being damaged by absorbing the harmful solar UltraViolet (UV) radiation (UV-b and UV-c). The presence of the ozone layer in the stratosphere leads to the stratosphere heating with higher altitude and causes a temperature maximum at ~50 km. In the thermosphere, the temperature profile also has a positive gradient due to the absorption of solar UV radiation in association with the dissociation of the diatomic nitrogen and oxygen molecules (Wallace and Hobbs, 2006, p. 11). The presence of these two temperature inversions defines the five atmospheric layers and the layer-pauses in between, namely the tropopause, the stratopause and the mesopause (Fig. 2.1).

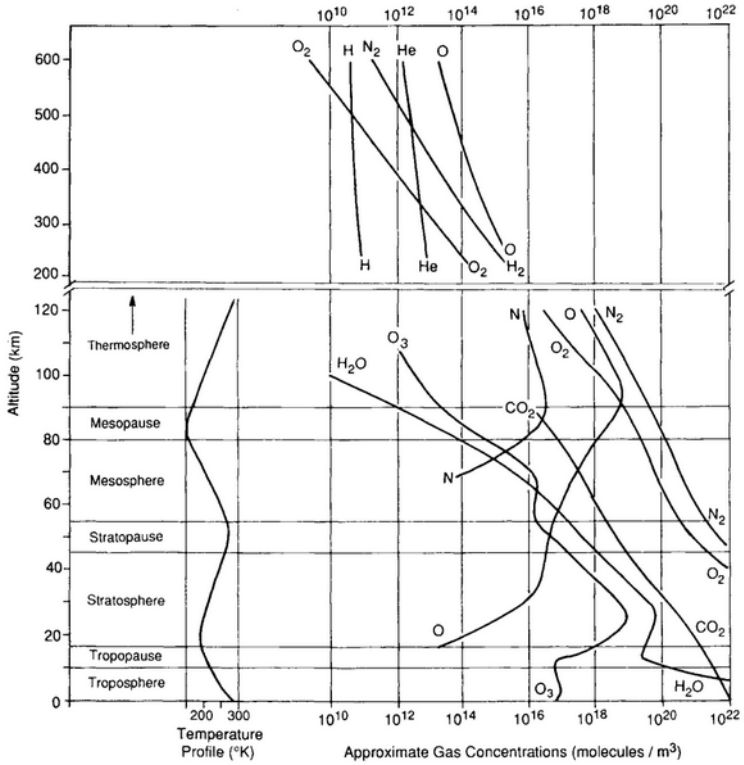

Figure 2.1. Atmospheric vertical structure including its temperature composition. In the figure, conventional names of atmospheric layers or regions are given (from Jacobson et al., 2000, p. 133).

The density of the atmosphere decreases with height in the same manner as the atmospheric pressure. Around 90% of the atmosphere's mass is distributed below 16 km, while 50% is below 5.6 km (Lutgens and Edward, 1995). The troposphere, which name means 'well mixed layer' in Latin, provides our weather and has a direct impact on life on Earth. Furthermore, it is also the lower layer and, together with the stratosphere, is the layer which is the most easily influenced by human activity. One well-known example of human influence on the atmosphere is the 'ozone hole' – the stratospheric ozone depletion caused by the tropospheric release of chlorofluorocarbon, CFC, which, in the end, caused ozone to become a subject of public interest.

2.2 Atmospheric chemistry and the role of ozone

2.2.1 Stratospheric ozone

The stratosphere contains about 90% of the ozone in the Earth's atmosphere. As briefly mentioned in Sect. 2.1, the stratospheric ozone is formed by the photolysis of O_2. The photolysis of O_2 yields two O atoms:

$$O_2 + hv(\lambda < 240nm) \rightarrow O + O\,. \qquad (R1)$$

wherein O atoms are in the ground-level triplet state O(^{3}P). These highly reactive atoms combine rapidly with O_2 to form ozone:

$$O + O_2 + M \rightarrow O_3 + M\,. \qquad (R2)$$

The ozone molecules are further photolyzed by the following reactions:

$$O_3 + hv\left(\lambda < 320nm\right) \rightarrow O_2 + O\left(^1D\right). \qquad (R3)$$

$$O\left(^1D\right) + M \rightarrow O + M\,. \qquad (R4)$$

From reaction 4, the O atoms can recombine with O_2 to regenerate ozone. The net generation of stratospheric ozone can be described as:

$3O_2 + h\nu \rightarrow 2O_3$.

The ozone production depends approximately on the square of the O_2 concentration (Chapman, 1930).

For ozone loss, the O atom undergoes another reaction:

$O_3 + O \rightarrow 2O_2$. (R5)

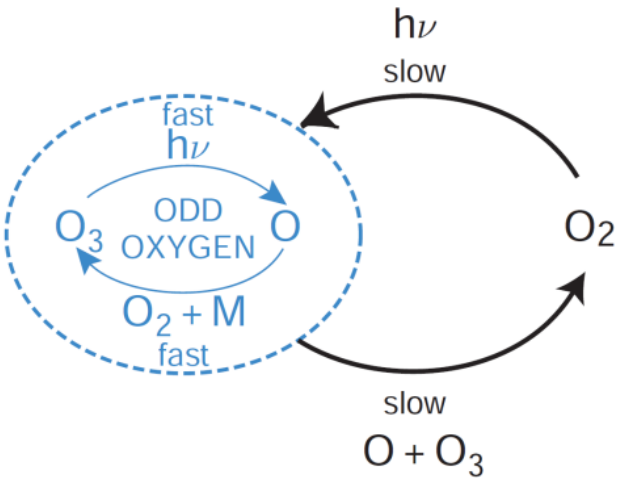

Figure 2.2. Schematic of the Chapman reactions (Wallace and Hobbs, 2006, p. 188).

The reactions (R1)-(R5) are called the Chapman reactions (Fig. 2.2).

Catalytic cycles involving the NO_x, HO_x, ClO_x and BrO_x families deplete ozone in the stratosphere. The representative generic reaction can be presented as:

$X + O_3 \rightarrow XO + O_2$. (R6)

$XO + O \rightarrow X + O_2$. (R7)

Net: $O + O_3 \rightarrow 2O_2$.

where X equals H, OH, NO, Cl, Br etc.

For instance, in the case of ozone loss with rising CFCs inserted from the troposphere, the CFC molecules are transported to the stratosphere, where they photolyze to release Cl atoms. For example, CFC-12 photolyzes as:

$$CF_2Cl_2 + h\nu \rightarrow CF_2Cl + Cl\,. \qquad (R8)$$

The Cl atoms then trigger a catalytic cycle involving the ClO_x family (Cl and ClO) as showed in (R6)-(R7).

The occurrence of the 'Antarctic ozone hole' improved our understanding of ozone loss by showing new catalytic cycles involving self-reactions in conditions of high ClO concentrations, which are further explained with the existence of PSCs (Polar Stratospheric Clouds). The new catalytic cycles are:

(1), the ClO + ClO cycle

$$ClO + ClO + M \rightarrow ClOOCl + M\,. \qquad (R9)$$

$$ClOOCl + h\nu \rightarrow ClOO + Cl\,. \qquad (R10)$$

$$ClOO + M \rightarrow O_2 + Cl + M\,. \qquad (R11)$$

$$Cl + O_3 \rightarrow ClO + O_2\,. \qquad (R12)$$

which are responsible for ~ 70% of the polar ozone destruction,

and (2), the ClO + BrO cycle

$$Cl + O_3 \rightarrow ClO + O_2\,. \qquad (R13)$$

$$Br + O_3 \rightarrow BrO + O_2\,. \qquad (R14)$$

$$BrO + ClO \rightarrow Br + Cl + O_2\,. \qquad (R15)$$

Both cycles have the net reaction: $2O_3 \rightarrow 3O_2$. Further details on these cycles can be found in e.g., Jacob (1999).

The existence of the stratospheric ozone layer affects both the stratosphere as well as the troposphere and its human activities. The crucial function of stratospheric ozone is to prevent harmful solar UV radiation from penetrating to the Earth's surface, as already mentioned in Sect. 2.1. By absorbing the radiation it acts as a net heating mechanism in the stratosphere. This is balanced by the net infrared cooling of CO_2 and H_2O (Ramanathan and Dickinson,

1979). Stratospheric ozone also causes a net heating of the troposphere-surface system. This heating comes from downward infrared emission by stratospheric ozone, plus the enhanced emission from stratospheric CO_2 and H_2O owing to the higher stratospheric temperatures (Dessler, 2000, p. 3). Besides this, stratospheric ozone influences the tropospheric ozone by stratosphere-troposphere exchange (STE, Holton et al., 1995). A reduction of stratospheric ozone would lead to enhanced UV radiation at the Earth's surface and in the troposphere. The generation of tropospheric ozone would then increase via photochemistry, as would the rate of skin cancer.

2.2.2 Tropospheric ozone

Initially, it was suggested that the primary source of tropospheric ozone is transport from the stratosphere (STE). Research on the Los Angeles smog helped to establish the conclusion that ozone is also photochemically produced in the troposphere. In the present day, the photochemistry in the troposphere is known to be the dominant source of tropospheric ozone, exceeding the flux from the stratosphere by factors of 7-15. 30% of this photochemically produced ozone is attributable to human activity (Cooper et al., 2014). Ozone is a secondary photochemical product. The photochemical precursors of the tropospheric ozone are NO_x, CO, CH_4 and VOCs emitted from fossil fuel combustion, biomass burning, industrial emissions, agriculture etc. The chemical process is briefly as follows.

At wavelengths <430 nm, NO_2 is photolyzed:

$$NO_2 + h\nu(<430nm) \rightarrow NO + O\,. \qquad (R16)$$

whereby O atoms are quickly combined with O_2 to produce ozone as shown in (R2). The produced ozone is removed by:

$$O_3 + NO \rightarrow NO_2 + O_2\,. \qquad (R17)$$

The combination of (R2), (R16) and (R17) constitutes a null cycle that neither creates nor destroys ozone. Meanwhile, the ozone molecules are photolyzed and yield high-energy $O(^1D)$ (R3), which reacts with water vapor to form two hydroxyl radicals:

$$O\left(^1D\right) + H_2O \rightarrow 2OH\,. \qquad (R18)$$

OH is rapidly transformed to HO_2 or RO_2:

$$OH + CO \rightarrow H + CO_2 . \quad \text{(R19a)}$$

$$H + O_2 + M \rightarrow HO_2 + M . \quad \text{(R19b)}$$

or

$$OH + RH \rightarrow R + H_2O . \quad \text{(R19c)}$$

$$R + O_2 + M \rightarrow RO_2 + M . \quad \text{(R19d)}$$

where R is from an alkane, e.g. CH_3, CH_3O, C_2H_5O. In the absence of NO_x, the reactions

$$HO_2 + HO_2 \rightarrow H_2O_2 + O_2 . \quad \text{(R20a)}$$

$$HO_2 + RO_2 \rightarrow ROOH + O_2 . \quad \text{(R20b)}$$

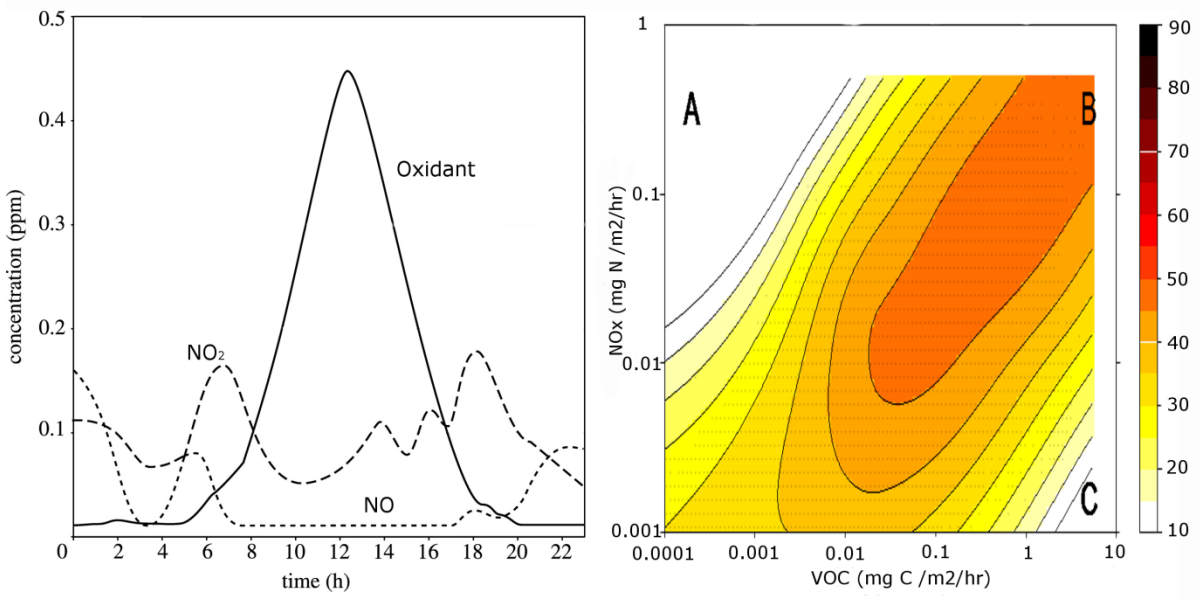

Figure 2.3. Left panel: Variations of nitrogen and oxidant (mainly ozone) in air concentration during a smoggy day in Southern California (adjusted from Finlayson-Pitts and Pitts, 1977). Right panel: Ozone mixing ratios (ppb) as a function of VOC and NO_x emissions as computed using the UKCA model (http://www.ukca.ac.uk) of atmospheric chemistry (Archibald et al., 2011). Three main regions are identified. Top left corner (A): region of NO_x saturation and ozone titration. Bottom right corner (C): region of VOC saturation and ozone destruction. Diagonal elements (A–C, B–C): efficient conversion of NO–NO_2 and hence ozone production increasing with increasing VOC and NOx emissions (Monks et al., 2015).

take place. H_2O_2 and ROOH are removed quickly from the troposphere by wet-deposition. In the presence of NO_x, which is the case for polluted air, ozone is formed by

$$HO_2 + NO \rightarrow NO_2 + OH\,. \qquad \text{(R21a)}$$

$$RO_2 + NO \rightarrow NO_2 + RO\,. \qquad \text{(R21b)}$$

together with reactions (R16), (R2), and (R19), in which chain reactions NO is converted to NO_2. The interrelations among NO, NO_2, VOC and ozone concentrations during an air-pollution episode are shown in Fig. 2.3.

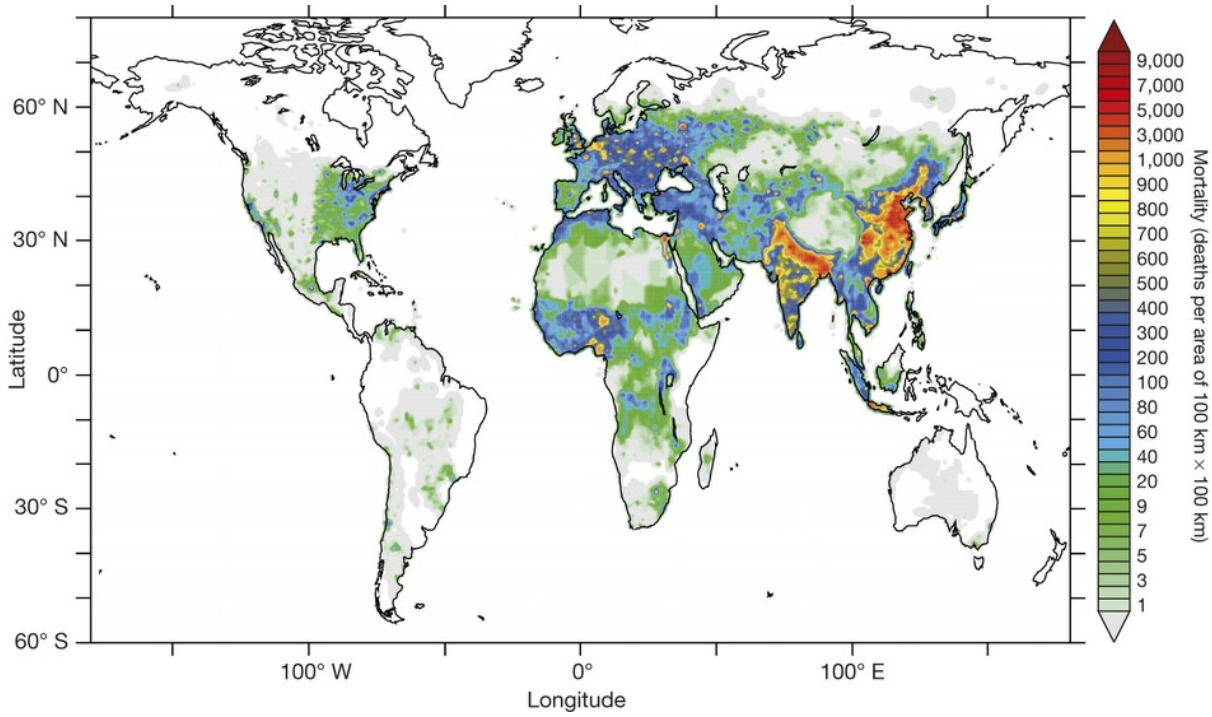

Figure 2.4. Mortality linked to outdoor air pollution ($PM_{2.5}$ and O_3) in 2010. In the white areas, annual mean $PM_{2.5}$ and O_3 are below the concentration–response thresholds where no excess mortality is expected (from Fig.1 in Lelieveld et al., 2015).

Tropospheric ozone has 'good' and 'bad' effects on the environment.

On one hand, it plays a central role in the chemistry of the troposphere. It is the primary tropospheric source of the OH radical which determines the lifetime and thus the concentrations

of trace gases affected by oxidation (R3, 18 and 19). Tropospheric ozone is also the third most important greenhouse gas. Due to ozone changes, an estimated globally averaged RF increased +0.40 ± 0.20 W m^{-2}, comparing to ~+0.48 W m^{-2} from CH_4, +1.66 W m^{-2} from CO_2 and little to no direct effect for ozone precursors, e.g., CO, NO_x and non-methane VOCs (NMVOCs, IPCC, 2013). Already in the late 1970s, it was reported that a uniform percentage decrease of ozone in the troposphere has around the same net radiative cooling effect on the surface-troposphere system as the same percentage decrease of ozone in the stratosphere due to the similar infrared (IR) opacity (Ramanathan and Dickinson, 1979; Fishman et al., 1979).

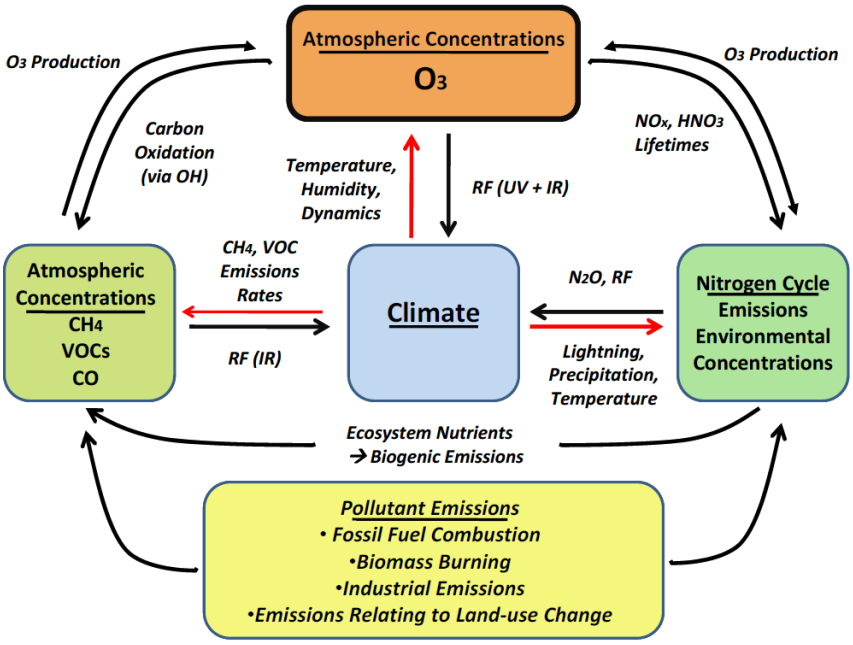

Figure 2.5. The interactions of tropospheric ozone in the Earth's system (from Fig. 1-1 in EPA, 2009).

On the other hand, ozone at the surface is an air pollutant. As an extremely powerful oxidizing agent, ozone can damage rubber, plastics and can harm humans and plants even at low concentrations (~several tens of ppbv) (Wallace, 2006, p. 165). WHO (World Health Organization) has stated that "the daily mortality rises by 0.3% and that for heart diseases by 0.4%

per 10 μg/m^3 increase in ozone exposure". Enhanced ozone has also been linked to the chronic obstructive pulmonary disease (COPD) and lung cancer (Lelieveld et al., 2015; Uysal and Schapira, 2003). Figure 2.4 shows the mortality linked to outdoor air pollution ($PM_{2.5}$ and O_3) in 2010, in which 223 000 deaths are from lung cancer, as stated by International Agency for Research on Cancer (IARC). The potential of ozone to damage vegetation has been known for more than 40 years, including visible leaf injury, growth and yield reductions (e.g. Fuhrer et al., 1997; Mills et al., 2016 and references therein). The yield losses for the four major agricultural crops (wheat, rice, maize and soybeans) induced by ozone in 2000 were estimated to cost an economic loss in the range $14-$26 billion as reported by Van Dingenen et al. (2009).

While ozone has a relatively short lifetime in the boundary layer (typically hours as a combined result of the losses to the surface by dry deposition and oxidative reactions), it has a lifetime in the order of several weeks when lifted up to the free troposphere (Young et al., 2013). Both the atmosphere's vertical mixing and the horizontal mixing in a hemisphere take ~1-2 weeks. Therefore ozone is long-range transported and mixed and can be influenced by climate variability (Fig. 2.5) before its deposition. None of these processes can be well understood without precise measurements of the tropospheric ozone distribution, which can be obtained by satellite measurements. In the following, the mechanisms behind atmospheric concentration measurements by use of satellites will be described.

2.3 Satellite measurements of tropospheric ozone: fundamentals

2.3.1 Electromagnetic radiation and molecular energy states

Satellite measurements rely on the fundamentals of interaction between electromagnetic radiation and matter.

Electromagnetic radiation

Electromagnetic radiation is described classically as electromagnetic waves that propagate at the speed of light through a vacuum in the form of synchronized oscillations of electric and magnetic fields, according to which the frequency ν is linked with the wavelength λ by

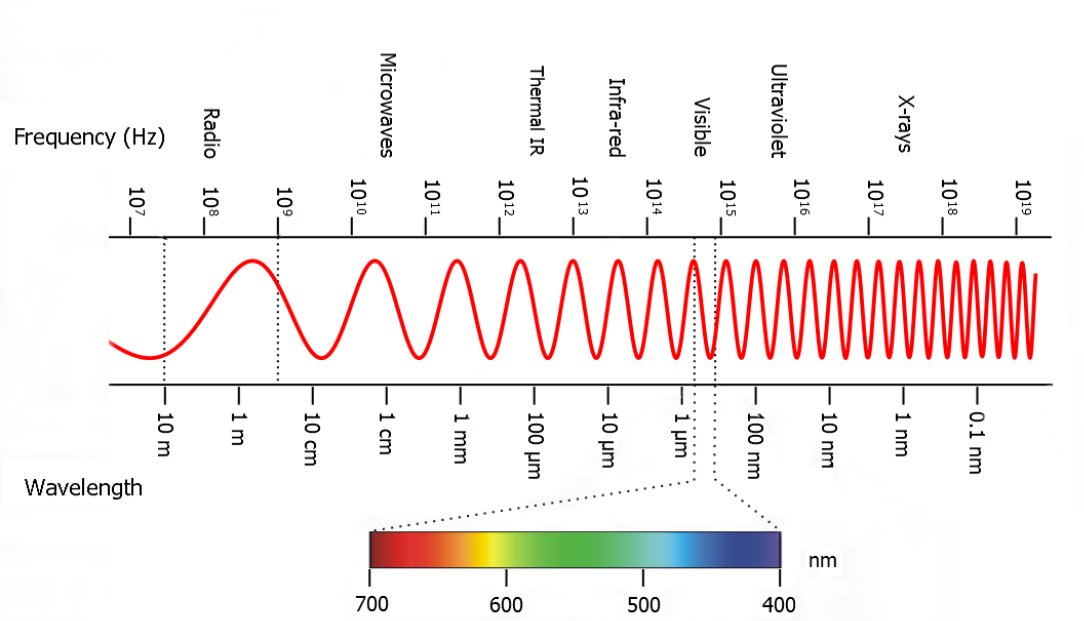

Figure 2.6. Sketch of the electromagnetic spectrum.

$$c = v \times \lambda \,. \tag{2-1}$$

where c is the speed of light for vacuum (2.998 x 10^8 m/s). Based on different wavelength or frequency, the electromagnetic radiation can be divided into different regions, e.g., Ultra-Violet (UV), Visible (Vis), Infrared (IR), microwaves (MW), etc. Figure 2.6 illustrates the corresponding wavelength/frequency with radiation types.

In quantum mechanics, electromagnetic radiation is also described as a stream of particles. These particles are called photons. The energy E of the photons depends on the frequency of the radiation v:

$$E = h\nu \,. \tag{2-2}$$

wherein h is Planck's constant (6.626 x 10^{-34} Js).

Molecular energy states

A molecule is defined as an electrically neutral group of two or more atoms held together by chemical bonds. A molecule is considered as a multi-particle system in quantum mechanics and thus has discrete energy states. The molecular energy states consist of three parts: the rotation of the entire molecule – rotational energy states; the vibration of the atoms – vibrational energy states; and the changed configuration of the electrons – electronic energy states.

Quantum mechanically, the rotational energy levels are calculated as

$$E_j = B \cdot J(J+1). \tag{2-3}$$

wherein B is the rotational constant of the particular molecule and rotation mode (rotation axis), and J is the rotational quantum number. The energy difference ΔE_j between two adjacent states is then given as

$$\Delta E_j = E_{j+1} - E_j = 2B(J+1). \tag{2-4}$$

Thus a rotational band consists of a series of equally spaced lines.

The vibration of atoms can be understood as harmonic oscillations. The energy levels are given by

$$E_v = (v+1/2) \cdot h\omega_0. \tag{2-5}$$

wherein v is the vibrational quantum number (vibration level), and $1/2h\omega_0$ is the zero-point energy of the molecular oscillator. Thus, the energies are proportional to the vibrational quantum number v. During the vibrational excitation, the molecules are likely to be rotationally excited at ambient temperatures. As a result, each vibrational state splits into a series of rotational-vibrational (ro-vibrational) states. The electronic energy states are caused by the changed configuration of the electrons. The molecular bond length and strength change with the electronic configuration. Therefore, each electronic state has its own set of vibrational and rotational states. Figure 2.7 shows the ro-vibrational energy levels of two electronic states of a molecule, which gives an example of the electronic transition. The electronic transition occurs vertically as governed by the *Frank-Condon principle*, which can be briefly explained as the unchanged nuclei position during the electron reconfiguration.

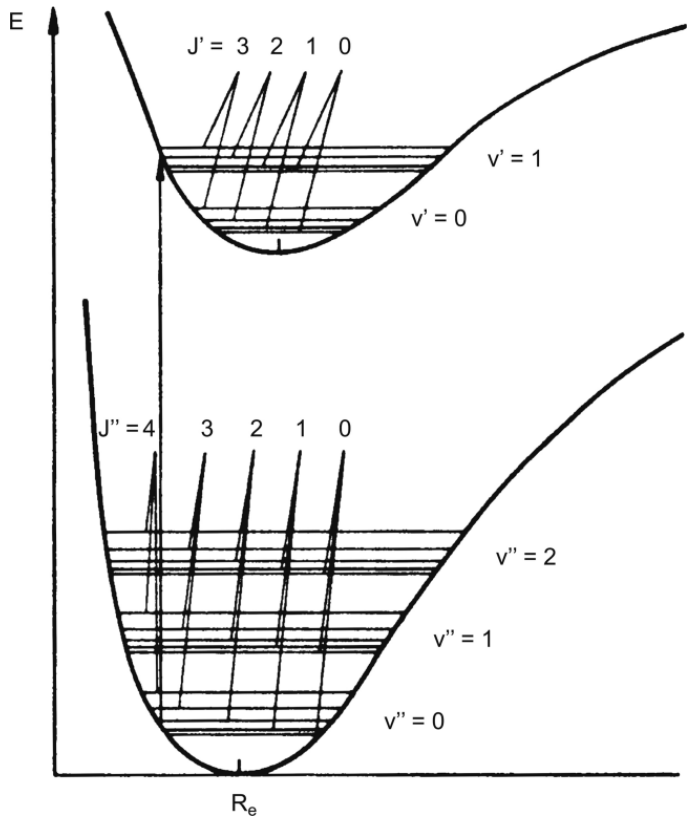

Figure 2.7. Sketch of ro-vibrational energy levels of two electronic states of a (diatomic) molecule. Electronic energies are given as a function of the distance between the nuclei of the atoms within the molecule. They are minimal at a certain distance *R*e, which is usually different in the different electronic states due to the changed configuration. The equidistant, horizontal groups of lines denote the lowest rotational levels of the vibrational states (ground state: $v = 0, 1, 2$, excited state: $v' = 0, 1$). Note that the energy separation of the rotational states (marked as J'' and J' in the sketch) is exaggerated in comparison to the vibrational energies. (Platt and Stutz, 2008, p. 82)

2.3.2 Interaction of molecules with radiation

Electromagnetic radiation passing through a gaseous mixture may either be scattered or absorbed.

Scattering of radiation

According to the existence of energy state changes in the molecules, the scattering can be distinguished as elastic scattering and inelastic scattering.

- When the scattered molecule/particle is unaffected but only the photon's direction is changed, it is called elastic scattering. Depending on the ratio of the particle size (circumference) and the photon's wavelength, $\alpha = \pi \cdot D_p / \lambda$, the elastic scattering includes Rayleigh scattering ($\alpha \ll$, corresponding to the gas molecules in the air), Mie scattering ($\alpha \approx 1$, corresponding to the aerosols, particles and clouds), and geometric scattering ($\alpha \gg$, corresponding to the rain drops or ice crystals). For Rayleigh scattering, the scattering depends on the wavelength of the light ($I \propto \frac{1}{\lambda^4}$). This type of scattering causes the Earth's sky to have different colors: the blue sky can be explained by the larger scattering of shorter wavelengths (blue), and the red sunsets are caused by the loss of all blue scattered light due to longer light path through atmosphere. Mie scattering is not so strongly wavelength dependent as Rayleigh scattering, and produces the almost white glare around the sun when a lot of particulate materials are present in the air. It is also the reason for the white light from mist, fog and the white clouds. Compared to Rayleigh scattering, Mie scattering has a strong dominance of the forward direction in the scattered light. Due to the corresponding matter size, the geometric scattering is not considered in clear-sky conditions.
- Raman scattering is an example of inelastic scattering. It is a weak interaction of radiation with matter between scattering and absorption. While the photons are scattered by the molecules, an internal transition between energy states (vibration or rotation or both) could happen. The scattered photon thus has a different energy from the exciting photon. Although Raman scattering is weak, it can be used to determine the molecular concentrations (Burrows et al., 2011).

Absorption of radiation

A photon can be absorbed by a molecule when the energy of the photon equals the energy difference between two energy states of the molecule. Therefore, for a certain molecule con-

figuration, only a set of specific wavelengths can be absorbed by the molecule. Thus the absorption of the radiation can provide information that can be used to identify gas species

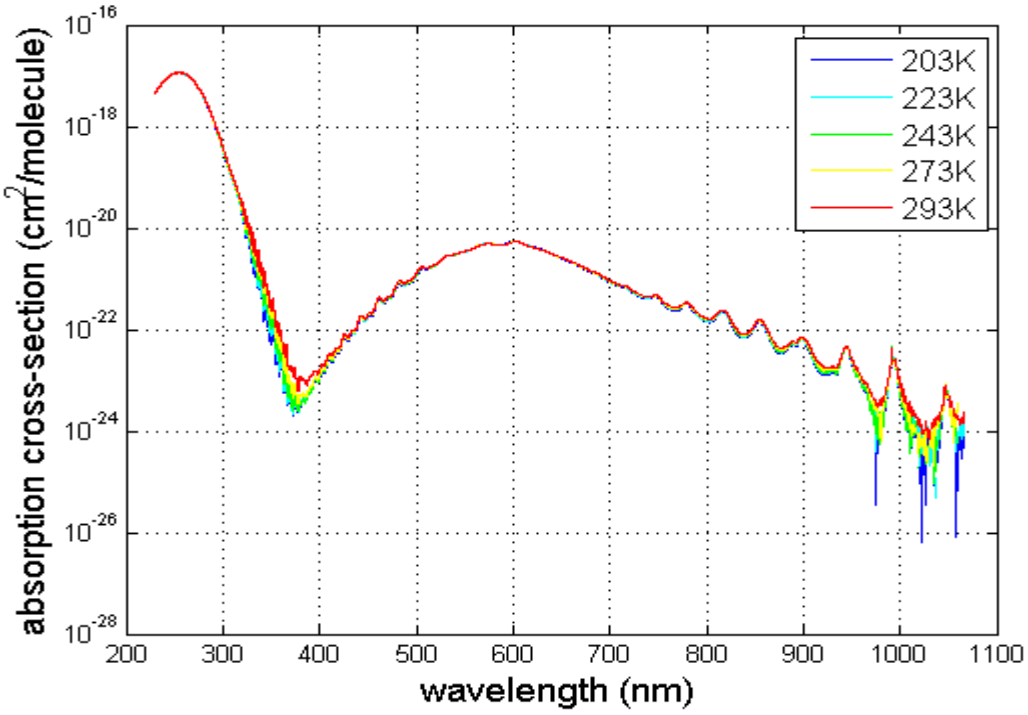

Figure 2.8. High spectral resolution ozone absorption cross section in the vacuum wavelength 230 - 1066 nm using the SCIAMACHY spectrometer (Gorshelev et al., 2014).

and determine gas concentration. The absorption cross section $\sigma_a(\lambda)$ describes the absorption by a molecule at wavelength λ. It can be treated as the effective area of the molecule for removing a photon's energy from radiation and can be measured in the laboratory. Figure 2.8 gives an example of the ozone absorption cross section over different wavelengths. The absorption cross section changes with molecule configuration and thus can be influenced by temperature and pressure (not shown) (Bohren and Clothiaux, 2006, p. 61). Quantitatively the absorption of radiation is known as the *Beer-Lambert law*:

$$I(\lambda) = I_0(\lambda) \cdot \exp\left(-\sigma_a(\lambda) \cdot c \cdot L\right). \qquad (2\text{-}6)$$

wherein $I_0(\lambda)$ is the initial intensity emitted by a radiation source, $I(\lambda)$ is the radiation intensity after passing through a certain thickness (L) of the medium, $\sigma_a(\lambda)$ denotes the absorption cross section, and c represents the concentration of the measured species.

Absorption bands – a range of wavelengths, frequencies or energies in the electromagnetic spectrum – are characteristic of a particular transition from its initial to final energy state. Ozone absorption bands are: Hartley bands (200-300 nm), Huggins bands (320-360 nm), Chappuis bands (375-650 nm) and Wulf bands (> 700 nm in IR range).

Emission of radiation

When a molecule transforms from a higher energy state to a lower energy state, photons are emitted. The energy of the emitted photon can be determined by quantifying the energy difference between the two states. For a black body, the photon energy (or spectral) is distributed by the Planck distribution (or Planck function):

$$P_e(\lambda) = \frac{h\omega^3}{4\pi^2 c^2} \cdot \frac{1}{\exp(h\omega / k_B T) - 1}. \qquad (2\text{-}7)$$

wherein c is the speed of light, h is the Planck constant, k_B is the Boltzmann constant and ω is the transformation from circular frequency to wavelength ($\omega = \frac{2\pi}{\lambda} \cdot c$). This equation describes the spectral intensity of a "blackbody" as a function of temperature (absolute temperature) and wavelength (Bohren and Clothiaux, 2006, p. 6).

Thermal emission from air molecules or aerosol particles in the atmosphere takes place at infrared wavelengths. Thermal emission can be neglected in the visible part of the electromagnetic spectrum. Thus, the observed spectral signatures in the visible can be directly related to absorption spectra of atmospheric constituents (Burrows et al., 2011).

2.3.3 The solar spectrum

The main source of the earth-received radiation is solar electromagnetic radiation, which is emitted from the superheated gas on the Sun's surface. Solar electromagnetic radiation shows wavelength-dependen emission, absorption and scattering processes. Figure 2.9 illustrates the

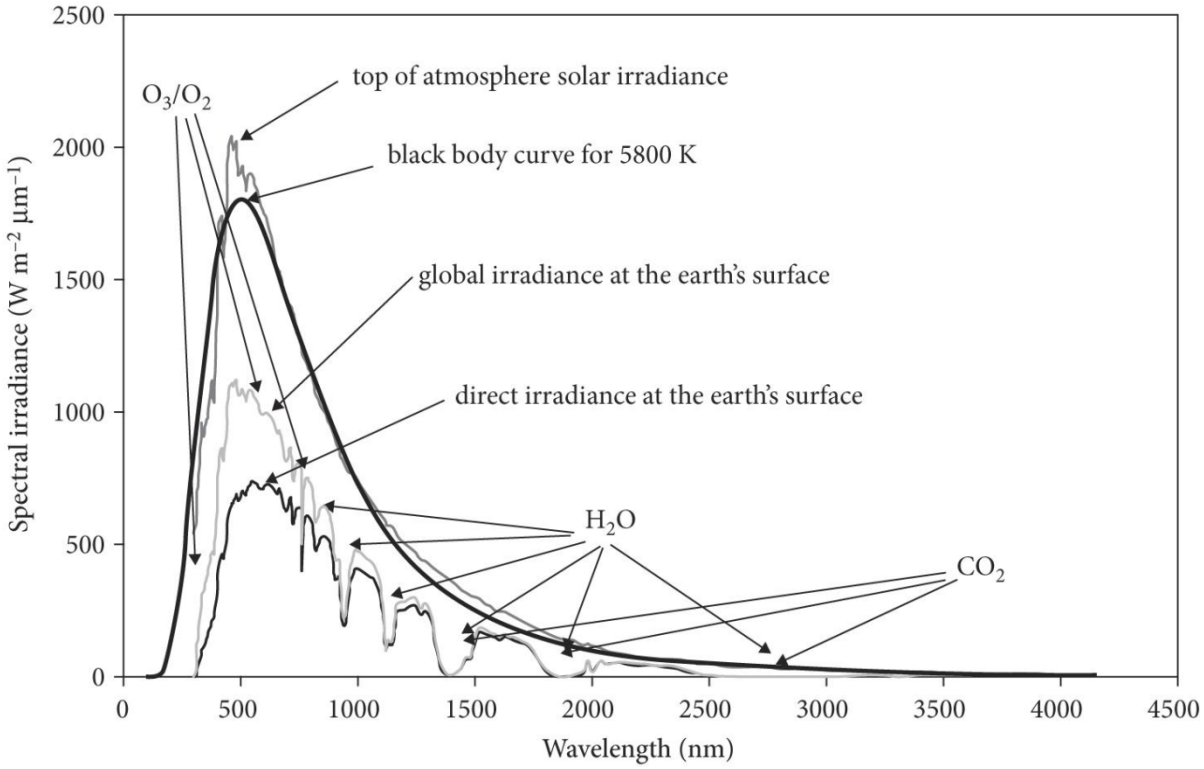

Figure 2.9. The solar radiation spectrum in terms of energy per unit wavelength at the top of the atmosphere and at the surface (Jones and Vaughan, 2010, p. 17).

solar irradiance curve. The irradiance is the radiated energy received per unit area per time. This radiation transfer related quantity is expressed in units of W m^{-2} (Platt and Stutz, 2008).

The solar irradiance spectrum at the top of the atmosphere approximately follows the energy distribution of a blackbody at temperature 5800 K as determined by Eq. 2.7 (Liou, 2002). It contains a set of dark lines, which are the so-called *Fraunhofer lines*. The Fraunhofer lines are typical absorption lines that are caused by chemical elements in the solar atmosphere. The differences between the irradiation at the top of the atmosphere and at sea level illustrate the attenuation of the solar radiation in the Earth's atmosphere. The main contributions to the attenuation are caused by Rayleigh scattering in the Vis wavelength range, and absorption by molecules (e.g. ozone, water vapor and carbon dioxide) in the UV and IR range.

2.3.4 Atmospheric radiative transfer

The radiance passing through the Earth's atmosphere can be attenuated by scattering and absorption. The combination of absorption and scattering is presented often as extinction. An important tool to simulate changes in the solar radiation due to atmospheric extinction is a radiative transfer model (RTM), also referred to as *Forward Model* (Gottwald and Bovensmann, 2012). These models can simulate the radiances, as they would be measured by a sensor, at given atmospheric conditions with the use of the *Beer-Lambert Law*. For a single species the law is given as:

$$dI_\lambda = -[\varepsilon_a(\lambda) + \varepsilon_s(\lambda)] \cdot I_\lambda \cdot ds = -[\sigma_a(\lambda) + \sigma_s(\lambda)] \cdot n \cdot I_\lambda \cdot ds \,. \qquad (2\text{-}8)$$

wherein dI_λ is the change in intensity, which is defined as the flux of energy in a given direction per second per unit wavelength range per unit solid angle per unit area perpendicular to the given direction (Liou, 2002); $\varepsilon_a(\lambda)$ and $\varepsilon_s(\lambda)$ are absorption and scattering coefficients; $\sigma_a(\lambda)$ and $\sigma_s(\lambda)$ are the corresponding cross sections of the molecule; *n* is the number density of absorbers/scatterers; and *ds* is the travel distance. Integration is then performed along the direct solar beam from the surface to the top of the atmosphere.

Several terms are involved in the radiative transfer:

- Albedo (ω): to be more precise, the single-scattering albedo, determines the possibility of a photon to be absorbed or scattered while interacting with a volume element. An albedo value of 1 illustrates a 100% scattering.
- Phase function ($p(\gamma)$): the term $p(\gamma) \cdot \frac{d\Omega}{2\pi}$ denotes the probability that the radiation is scattered within a solid angle $d\Omega$ with a direction and form an angle γ.
- Ring effect: a filling in (broadening and reduction of depth) of solar Fraunhofer lines in scattered sunlight (Chance and Spurr, 1997). It is caused by the very little (around 4% in total scattering, this number is obtained from Gottwald and Bovensmann, 2012) Rotational Raman Scattering (RRS).

The usual input parameters that are used for the computation of a radiative transfer are the solar spectral input, the extinction optical depth (the sum of the layer optical depths due to molecular absorption, Mie and Rayleigh scattering), the single-scattering albedo, and the

phase function of scattered radiation (Ricchiazzi et al., 1998). Further information about radiative transfer can be found in Liou (2002).

The radiative transfer model SCIATRAN (Rozanov et al., 2014) is used at the Institute for Environmental Physics in University of Bremen (IUP). A radiative transfer model like SCIATRAN does not only provide simulations of the radiation, but is also capable of calculating additional parameters, e.g.,

- Air mass factors: a measure for the photon path in the atmosphere.
- Weighting function: describes how sensitive radiance changes are to modifications in the parameters. (Gottwald and Bovensmann, 2012)

2.4 Satellite measurements of tropospheric ozone: instruments

Instruments which measure ozone can be divided in three categories: UV-Vis backscattering spectrometer, microwave spectrometer, and IR spectrometer. Here the main spectrometers related to the research presented in this thesis are briefly introduced. Table 2.2 gives a summary of each instrument's related characteristics.

Table 2.2: Summary of the characteristics of the selected satellite instruments which are used to measure atmospheric ozone.

Instrument	Equator crossing	Global Coverage	Availability period	Pixel size [km^2]
GOME	10:30 LT	3 days	1995/10–2003/06	40 × 320
SCIAMACHY	10:00 LT	6 days	2002/08–2012/04	30 × 60
GOME-2	9:30 LT	~1 day	2007/01–	40 × 80
OMI	13:45 LT	1 day	2004/10–	13 × 24
MLS	13:45 LT	1 day	2004/07*–	5 × 500 × 3
TES	13:38 LT	16 days	2004/10–	5.3 × 8.5
IASI	9:30 LT	< 1 day	2006/10–	12(diameter)

* only consider MLS on board Aura

2.4.1 GOME

The Global Ozone Monitoring Experiment (GOME) on board the Second European Remote Sensing Satellite ERS-2 was launched in April 1995. The satellite is operated in a near-polar sun-synchronous orbit with an equator overpass time of 10:30 on descending node and has a global coverage within 3 days (Burrows et al., 1999). GOME is a small-scale version of SCIAMACHY (Sect. 2.4.2) and is used for global monitoring of ozone and other trace gases. It is a multi-channel spectrometer with four channels covering the wavelength range from 240 nm to 790 nm, with a moderate spectral resolution of 0.2 – 0.3 nm. GOME is a nadir-viewing mode instrument with a spatial resolution of 320 km × 40 km (across/along track). The spatial resolution was increased to 80 km x 40 km after June 1997 with a narrow-swath mode, wherefore the instrument's scan angle was reduced from ±31.0° to ±8.7° (Beirle, et al., 2004).

2.4.2 SCIAMAMCHY

The SCanning Imaging Absorption spectroMeter for Atmospheric CHartographY (SCIAMACHY) instrument operated from August 2002 to April 2012 on board the European satellite Envisat (Burrows et al., 1995; Bovensmann et al., 1999). Envisat operated in a sun-synchronous, near-polar orbit with a local equatorial overpass time at around 10:00 at the descending node. SCIAMACHY was a passive spectrometer designed to measure radiances in eight spectral channels covering a wide range from 214 nm to 2384 nm with a moderate spectral resolution of 0.21 nm to 1.56 nm including 8 channels. SCIAMACHY performed observations in three viewing modes: nadir, limb and solar/lunar occultation.

In nadir geometry, the instrument's Line of Sight (LOS) was pointed directly under the instrument, with a 4 s across track scan, followed by a 1 s back scan. The across track swath is 960 km. The size of the individual ground pixels is dependent on the selected integration time. The resolution varied from 26 km × 30 km (along-track × across-track) up to 32 km × 930 km for wide swath settings (Gottwald and Bovensmann, 2011). The typical spatial resolution was about 30 km × 60 km.

In limb-viewing geometry, SCIAMACHY observed the atmosphere with the line of sight pointed tangentially to the Earth’s surface, with a field of view of 110 km horizontally and

2.6 km vertically at the tangent point. A limb measurement sequence started from 3 km below the horizon (0 km after October 2010) and continued with a vertical scan up to around 93 km. At each tangent height, SCIAMACHY performed a horizontal scan with a total swath of about 960 km. The horizontal scan is typically read out into four measurements with different azimuth angles (only one measurement in channel 1). The tangent height step between the subsequent horizontal scans is around 3.3 km. The spatial resolution is typically 960 km × 400 km in channel 1 and 240 km × 400 km (across/along track) in all other channels (Gottwald and Bovensmann, 2011). The relative azimuth angle between the instrument and the sun changes in the course of the orbit. In the high northern latitudes, the instrument measurement field of view faces the solar light with a small relative azimuth angle while in the southern latitudes the sunlight comes from behind the instrument field of view and the relative azimuth angle is large (See Fig. 4.3 and Fig. 4.4 in Ernst, 2013).

In occultation mode, the instrument directly measured the radiation of the sun or the moon using the same geometry as in the limb mode. The solar occultation measurements are performed during the sunrise with the latitude range of 65° – 90° N. Lunar occultation are measured during moonrise at the latitude bin of 30° – 90° S.

The ozone profile retrieval algorithm employed in this study uses limb measurements in the Hartley and Chappuis absorption bands in SCIAMACHY special channels 1 (214-314 nm), 3 (392-605 nm) and 4 (598-790 nm), while the total ozone columns are retrieved using measurements in the Huggins bands in channel 2 (326.6-334.5 nm).

2.4.3 GOME-2

After the big successes of the GOME spectrometer, the second-generation sensor – GOME-2 – was launched aboard ESA's MetOp (Meteorological Operational) satellite series (MetOp-A and MetOp-B) in October 2006 and September 2012, respectively, with a local equator crossing time of 9:30. Just like the GOME spectrometer, the GOME-2 is also a UV-Vis spectrometer with four bands covering the 240 – 790 nm spectral range with a spectral resolution of 0.24 – 0.53 nm (Callies et al., 2000). With a swath width of 1920 km, GOME-2 measurements can reach a global coverage within one day. The instrument has nadir-viewing, and the spatial resolution is typically 640 km × 40 km in band 1a and 80 km × 40 km (across/along track) in all other channels. The bands 1 (240 – 315 nm) and 2 (310 – 403 nm)

are used for ozone retrieval. In July 2013, operations of the GOME-2 instrument on board MetOp-A were switched to a 'narrow swath' mode, enabling a swath width of 960 km, yielding a horizontal resolution of 40 km × 40 km (Hilboll, 2013). The MetOp satellite series A, B and C have projected mission lifetime of six years, respectively, which makes GOME-2 the first of a series of three identical instruments that will provide more than 15 years of space-borne UV-Vis observations of the atmosphere. The MetOp-C is planned to be launched in October 2018.

2.4.4 OMI

The Ozone Monitoring Instrument (OMI) is a UV-Vis nadir viewing spectrometer onboard the Earth Observing System (EOS) Aura mission together with MLS (Sect. 2.4.5) and TES (Sect. 2.4.6). OMI was launched into a polar sun-synchronous orbit in July 2004. It was designed to continue NASA's Total Ozone Mapping Spectrometer (TOMS) record for total ozone and other atmospheric parameters related to ozone chemistry and climate. OMI was launched in July 2004 with a local passing time of 13:45 (ascending node), detecting back-scattered solar radiation over the 270 - 500 nm wavelength range with a spectral resolution of 0.42 – 0.63 nm (Levelt *et al.*, 2006). It has a very high spatial resolution (13 km × 24 km at nadir) and a daily global coverage by using a two-dimensional CCD (Charge Coupled Device) detector. The nadir pointing telescope of OMI has a very large field of view of 114°. The spatial resolution becomes coarser (till 13 km × ~150 km) towards the edges of the large swath (~ 2600 km). After January 2009, the ground coverage of OMI was significantly decreased due to 'row anomaly' of the instrument (Hilboll, 2013). OMI has a designed lifetime of 5 years. The Aura spacecraft is operating under good condition and is expected to operate until at least 2022, and likely beyond.

2.4.5 MLS

The Microwave Limb Sounder (MLS) is a thermal-emission microwave limb sounder onboard the EOS Aura. It has a local passing time of 13:45 at ascending node. The aim of the instrument is to improve the understanding of stratospheric ozone chemistry, the interaction of composition and climate, and the pollution in the upper troposphere (Waters et al., 2006). MLS contains heterodyne radiometers operating at ambient temperature in five spectral re-

gions: 118 (R1), 190 (R2), 240 (R3), 640 (R4) GHz, and 2.5 (R5) THz. The 240 GHz radiometer R3 was included to cover the strong ozone lines in the region where upper absorption by water vapor is small enough to allow measurements of upper tropospheric ozone (Waters et al., 2006). The MLS field of view detects in the forward direction and the limb scanning in the upward direction. Vertical profiles of 14 target atmospheric trace gases are retrieved from the MLS observations with a 165 km horizontal spacing at altitudes between 8 and 90 km. The spatial resolution of MLS is 500 km × 500 km (along-track × across-track). The tangent height step between the subsequent horizontal scans is around 3.2 km depending on the parameter under observation (Waters et al., 2006). The design life of MLS is five years with an operational goal of six years.

2.4.6 TES

The Tropospheric Emission Spectrometer (TES) on the EOS Aura mission is an infrared Fourier transform spectrometer (Beer et al, 2001; Beer, 2006). It primarily aims at mapping the global three-dimensional distribution of tropospheric ozone and its precursors, and was originally designed to permit both nadir and limb views. TES covers the globe in 16 days in the cross-track mode with a local passing time of 13:38 at ascending node. The spectrometer probes the Earth's atmosphere in the thermal infrared spectral range between 650 and 3050 cm^{-1} at a spectral resolution of 0.1 cm^{-1} in the nadir viewing mode and 0.025 cm^{-1} in the limb viewing mode. The limb observations were eliminated after launching (Beer, 2006). TES ozone is retrieved from the 9.6 um ozone absorption band using the 995 – 1070 cm^{-1} spectral range. In cloud-free conditions, the nadir vertical profiles have around four degrees of freedom (DOF) for signal, approximately two of which are in the troposphere, giving an estimated vertical resolution of about 6 km with a footprint of 5.3 km × 8.5 km, covering an altitude range of 0-33 km (see Beer et al., 2001; Nassar et al., 2008 and the references therein). TES has a projected mission lifetime of 5 years.

2.4.7 IASI

The Infrared Atmospheric Sounding Interferometer (IASI) is another Fourier transform spectrometer on orbit. IASI was launched onboard the MetOp platforms in October 2006 (IASI-A)

and September 2012 (IASI-B) together with GOME-2. IASI covers the spectral range of 645 - 2760 cm^{-1} in nadir mode, measuring the spectrum emitted by the Earth's atmosphere with a spectral resolution of 0.3-0.5 cm^{-1}. The IASI footprint is a matrix of 2 × 2 pixels, each with 12 km diameter at nadir (Clerbaux et al., 2009). IASI monitors the atmospheric composition two times per day (the satellite's ground track is at about 9:30 a.m. and 9:30 p.m. local time). Ozone vertical profiles are retrieved in near real time using a dedicated radiative transfer and retrieval software for the IASI ozone product, the Fast Optimal Retrievals on Layers for IASI (FORLI-O_3) (Hurtmans et al., 2012; Safieddine, et al., 2015). The vertical profiles have around 3-4 degrees of freedom (indicative value, details can be found in e.g. Boynard et al., 2009). The IASI series will provide 15 years of global scale observations.

2.4.8 Instruments for stratospheric ozone measurement

Retrieving stratospheric ozone profiles with a high accuracy is not only important for stratospheric ozone studies, but also a requirement for the establishment of an essential long-term climate variable data record. To achieve this goal, ground-based, balloon-borne, airborne and satellite instruments have been used to monitor ozone abundances in the atmosphere during the last decades. For satellite instruments, different observation techniques including solar/stellar occultation measurements (e.g., SAGE – Stratospheric Aerosol and Gas Experiment (McCormick et al., 1989); HALOE – Halogen Occultation Experiment (Russell et al., 1994); ACE – Atmospheric Chemistry Experiment (McElroy et al., 2007); GOMOS – Global Ozone Monitoring by Occultation of Stars (Bertaux et al., 2010)), limb scatter/emission measurements (e.g., MLS; MIPAS – Michelson Interferometer for Passive Atmospheric Sounding (Fischer et al., 2008); OSIRIS – Optical Spectrograph and InfraRed Imager System (Llewellyn et al, 2004)) and nadir measurements (e.g., GOME/GOME2, OMI, IASI) have been used in the last three decades (see, e.g., Sofieva et al., 2013; Hassler et al., 2014, and references therein). The passive imaging spectrometer used in this study, SCIAMACHY, provided vertical distributions of atmospheric trace gases by use of the limb-scattering measurement technique (Burrows et al., 1995; Bovensmann et al., 1999). Figure 2.10 shows an overview of some ozone profile records.

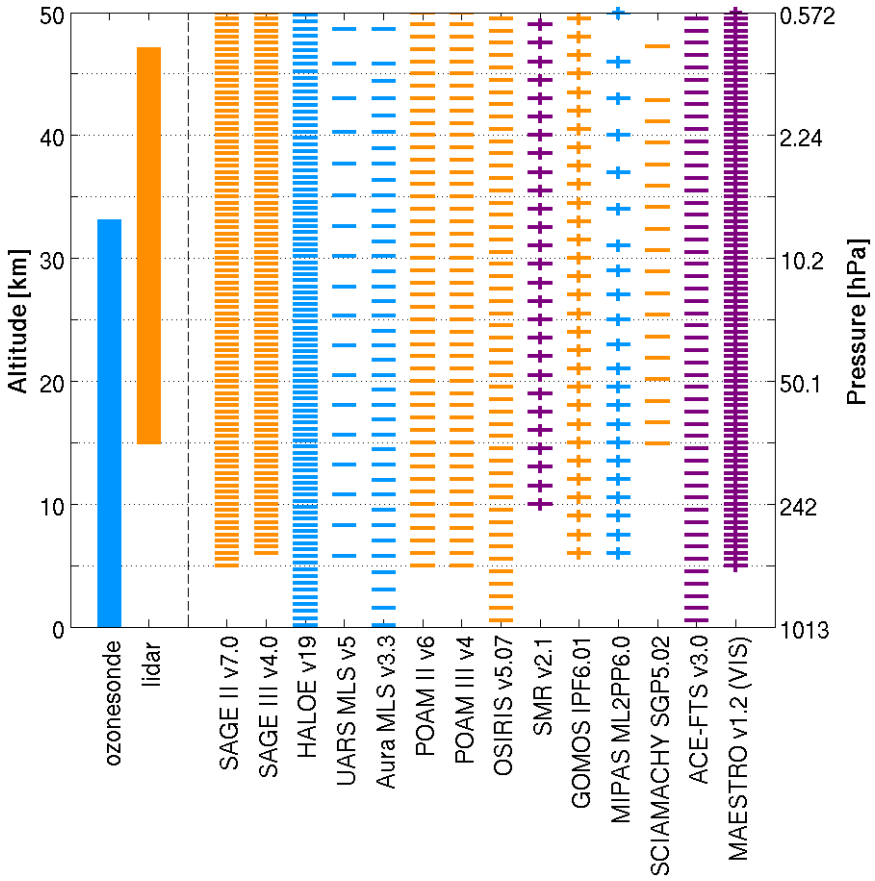

Figure 2.10. Overview of the native representation of the ozone profile records. The different vertical distances represent the vertical resolution of each ozone profile data set. The total vertical range defines the measurement altitude range. Colours differentiate different ozone products, including altitude versus O_3 number density (orange), altitude versus ozone volume mixing ration (VMR, purple) and pressure versus ozone VMR (blue). Vertical grids that are profile-dependent are marked with small vertical bars (Fig. 1 in Hubert et al., 2015).

3 State of the art of tropospheric ozone

Satellite-based monitoring of tropospheric ozone is of critical importance in order to gain knowledge on processes and phenomena affecting air quality and the greenhouse effect (Sellitto et al., 2011). Tropospheric ozone was one of the first chemical species (other than water) which was derived from satellite-based total ozone column observations based on UV radiances measured by the TOMS instrument, combined with stratospheric measurements by SAGE and SBUV (Solar Backscatter Ultraviolet) to determine the tropospheric residuals (Fishman et al., 1990; 1996). Due to the fact that the satellites detect the atmosphere from up to down, which makes the measurements less sensitive to the lower altitude, and due to the fact that almost 90% of the atmospheric ozone is distributed in the stratosphere, current tropospheric ozone monitoring is with low accuracy and is therefore a topic of urgent investigation. In this chapter, the state-of-the-art of the current tropospheric ozone retrieval approaches and the data interpretations will be presented.

3.1 Measurement techniques

The measurement techniques which exist within the field of tropospheric ozone retrieval are normally grouped as three major techniques by means of different basic retrieval ideas: the Optimal Estimation of ozone profiles from nadir (OE), the convective cloud differential method (CCD) and the tropospheric ozone residual (TOR) method. In this thesis the measurement approaches are re-systemized in two categories: (1) the direct retrieval, including OE (Sect. 3.1.1.1) and NN (Neural Network algorithm, Sect. 3.1.1.2), and (2) the indirect retrieval, including the CCD (Sect. 3.1.2.1), RSM (Reference Sector Method, Sect. 3.1.2.2), and TOR (Sect. 3.1.2.3).

3.1.1 Direct retrieval

The tropospheric ozone columns can be measured directly by means of satellite retrieval of the vertical distribution of ozone by nadir measurements. Depending on the wavelength range

used, the ozone profiles can be retrieved from the backscattered UV-Vis radiation (e.g., from GOME, SCIAMACHY, OMI, and GOME-2). Measurements of thermal radiation (e.g., from TES and IASI) can also be used for the quantification of the ozone profiles by measuring the pressure-broadening-dominated emission lines. Depending on whether the inverse relationship between the radiance spectra and the ozone profiles is obtained by use of optimal estimation (OE) or by use of a training model, the direct retrieval of ozone can be classified as OE approach and Neural Network Ozone Retrieval System (NNORSY). Figure 3.1 shows the comparison of the OE and the NNORSY retrieval approaches.

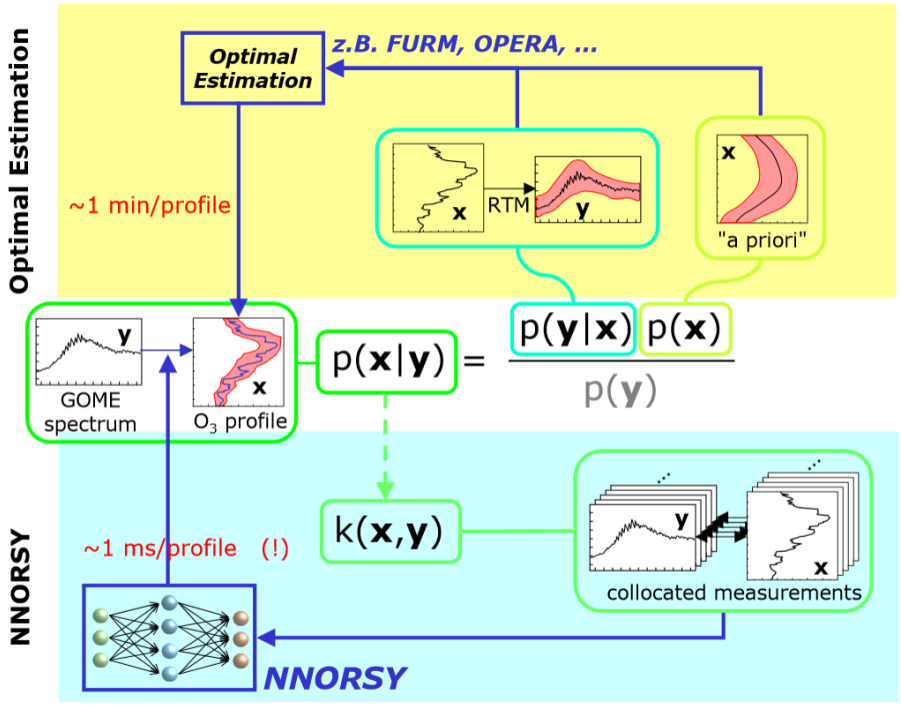

Figure 3.1. Schematic comparison of the direct retrieval approaches: OE and NNORSY (Kaifel et al., 2006).

3.1.1.1 OE

Traditionally, the ozone profiles are derived from the well-known OE approach (Rodgers, 2000). A typical process of OE based retrieval is for instance the GOME ozone profile retrieval. For this retrieval, first a forward RTM is used, which is essential for the calculation of

radiances and weighting functions that are needed for the vertical ozone retrieval from GOME spectra. The ozone cross sections measured in the laboratory (such as shown in Fig. 2.8) are used in this step. Secondly, the inverse method, e.g. the Full Retrieval Method (FURM, Hoogen et al., 1999), or the Ozone ProfilE Retrieval Algorithm (OPERA, van Peet et al., 2014), is used to derive ozone profiles. These inverse methods are based on the OE approach. To solve the inverse problem, additional independent information (so called 'a priori') is needed. The a priori is the typical atmospheric ozone distribution derived from models, and from various in situ and remote sensing techniques. In the case of GOME, the TOMS V8 climatology model is used as a priori and as a priori variance (McPeters et al., 2007). The OE approach has been applied to GOME, SCIAMACHY, OMI, GOME-2, TES and IASI measurements (e.g., Hoogen et al., 1999; Liu et al., 2010; Miles et al., 2015; Bowman et al., 2006; Boynard et al., 2009 and the references therein). Validation results show that the mean deviation between sondes and satellite instruments are often within accuracy requirements by the climate users (20% in the troposphere, 15% in the stratosphere).

The OE ozone profile retrieval has a moderate to low vertical resolution (6-10 km), which is limited by the equation of the radiative transfer (Rodgers, 2000). Furthermore, in the UV-Vis wavelength ranges, the measurements have low signal to noise ratio in the lower altitudes, while in the thermal IR wavelength ranges, the measurement is only sensitive to the regions where the temperature difference between the atmosphere and the Earth's surface is high. The sensitivity of the measured radiance spectra to ozone variations in the lower troposphere is weak (often less than 0.5 DOF). To enable measurements of the spatial distribution of ozone plumes in the lowermost troposphere, the OE is developed to multispectral synergism of the UV-Vis and thermal IR wavelength ranges, e.g., joint OMI with TES (Fu et al., 2013), and GOME-2 with IASI (Guesta et al., 2013). It is reported that the DOFs for multispectral retrievals increases by 0.1 (40% in relative terms) for the lowermost troposphere (0-3 km) (Guesta et al., 2013).

3.1.1.2 NNORSY

The NN algorithm is another alternative analysis method to retrieve the tropospheric ozone column, and was developed in order to improve the accuracy of the retrieval results in the lower troposphere. NN is a mathematical model extracting the underlying relationship between input and output quantities, using a learning and a testing stage (Sellitto et al., 2011)

instead of using RTM and OE. The input quantities – spectral data and other parameters (e.g., space-time information, observation geometry and temperature profiles) – are collocated with the existing ozone profile measurements from ozonesondes or other satellite measurements. The two sets of collocated measurements are given to the NN to train the model. In contradiction to the classical retrievals schemes based on OE, the use of a priori profiles and forward model is not needed for this method. Therefore once trained, the NN is able to operate in real time with 10^3-10^5 times faster than classical OE retrieval techniques (Müller et al., 2003). Consequently, high performance computers are not required. NN is expected to be less sensitive to systematic errors, clouds and aerosols (Sellitto et al., 2011) induced from the forward models. In the last decades, NN has been used for ozone profile retrievals for the data obtained by GOME, SCIAMACHY, GOME-2 and OMI (see, e.g., Müller et al., 2003, Stellitto et al., 2008, 2011, 2012). The accuracy of the data from NN is at the same level as the one from OE. A detailed description of the NN technique can be found in e.g., Bishop (1995).

3.1.2 Indirect retrieval

Indirect retrievals of tropospheric ozone exploit the fact that 90% of ozone in the total ozone column is located in the stratosphere. While it is hard to be directly derived from satellite observations, the tropospheric ozone information can be inferred by subtracting stratospheric ozone from the total ozone columns. According to the different approaches in obtaining the stratospheric ozone, the indirect retrieval mainly consists CCD, RSM and TOR.

3.1.2.1 CCD

The Convective Cloud Differential (CCD) method utilizes two facts: (1), high reflectivity cloud cases are often associated with strong convection and cloud tops near the tropopause (Ziemke et al., 1998 and references therein) and (2), the characteristics of zonal symmetry of tropical stratospheric ozone columns are well known. Ziemke et al. (1998) calculated the total ozone column with a low reflectivity ($R<0.2$). The stratospheric ozone columns are derived for every 5° latitude band and averaged from 120°E to 120°W using the lowest values of the above-cloud column amounts (above the tops of very high clouds with high reflectivity($R>0.9$)). These stratospheric ozone columns are then assumed to be independent of longitude in a given latitude bin. The region which is used to calculate stratospheric ozone col-

umns is chosen by subtracting two temporal standard deviations from monthly mean cloud top pressures, to be able to locate where convective clouds are most often associated with the cloud tops near the tropopause. The CCD method was later modified by Valks et al. (2003, 2014) and Leventidou et al. (2016) by using Cloud Fraction (CF) of 0.1 and 0.8 instead of using the reflectivity (Fig. 3.2). This modification provides more precise information on aerosol loading and high-reflectivity caused by bright surfaces (for instance, desert). Furthermore, CF is retrieved by using the Polarization Measurement Devices (PMDs). PMD spectral ranges (Vis) can provide a better spatial resolution compared to the UV wavelength ranges used for reflectivity retrieval. The CCD method has been applied to TOMS, OMI, GOME, SCIAMACHY and GOME-2 data (Ziemke et al., 1998; Ziemke and Chandra, 2012; Valks et al., 2003, 2014; Leventidou et al., 2016).

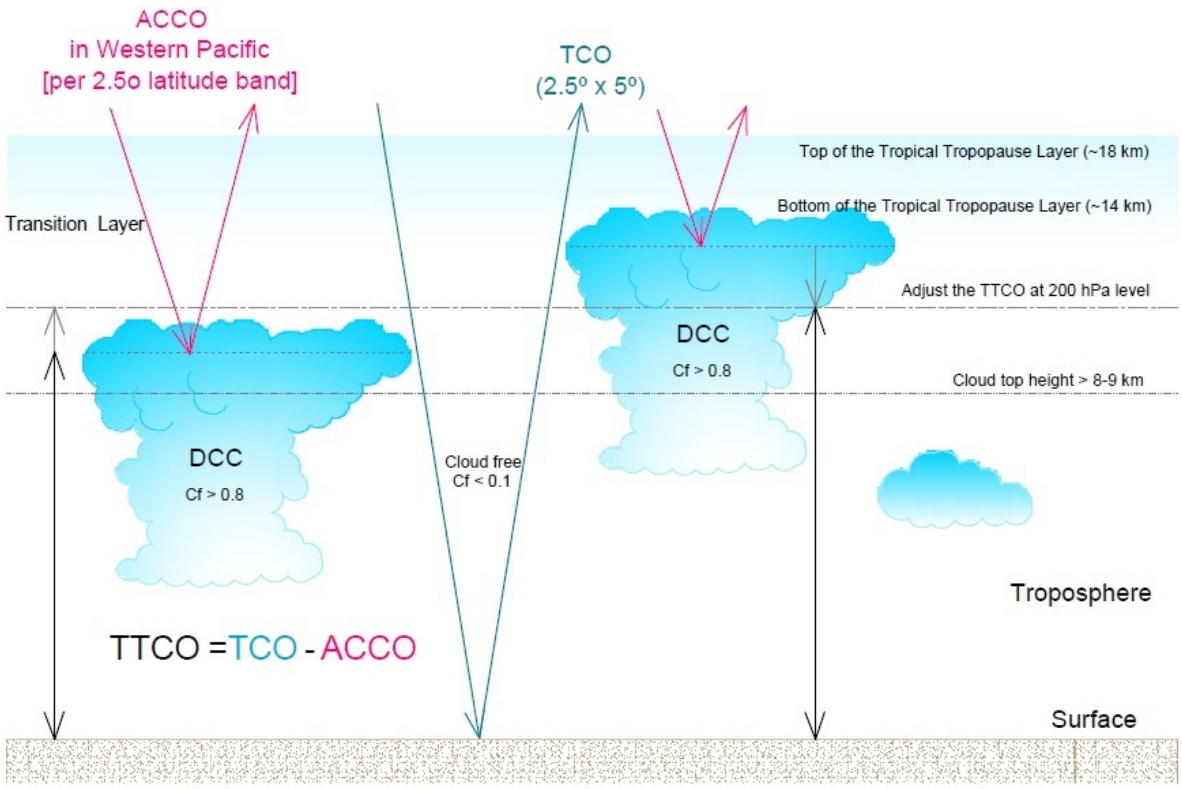

Figure 3.2. Schematic description of the CCD technique. DCC are the deep convective clouds, Cf is the cloud fraction, ACCO is the above cloud column of ozone, TCO is the total column of ozone and TTCO is the tropical tropospheric column of ozone (Leventidou et al., 2016).

The Cloud Slicing (CS) method is an extension of the CCD method. It was developed to yield tropospheric ozone profile information (the upper tropospheric ozone columns) with the combination of the collocated measurements of above-cloud ozone columns and cloud-top pressure (details can be found in Zimke et al., 2001). The drawbacks of the CCD and the CS method are that their suitability is limited in regions with deep convective clouds (narrow region in the tropics). Furthermore, both methods cannot be applied to individual satellite pixels.

3.1.2.2 RSM

The Reference Sector Method (RSM, also referred to as Tropospheric Excess Method – TEM) is, partly similar to the CCD method, also build on the assumption of the total stratospheric ozone column's longitudinal homogeneity in the tropics. The averaged total columns measured on the same day and at the same latitude over a relatively clean air region (e.g., the Pacific region 180–190° E was used for GOME data in Ladstätter-Weißenmayer et al. (2005)) can be used as an approximation of the stratospheric column (so-called reference sector) for the region of interest. To yield TOCs, the derived reference sectors are subtracted from the corresponding nadir measurements for individual satellite pixels at equal latitude. The regions wherein the RSM method can be used are still limited to the tropics, as is also the case for the CCD method. Besides, due to the long life time of ozone and the high stratospheric ozone concentration near the tropopause, the relatively clean regions are easily contaminated by transport processes in comparison to other trace gases, e.g., NO_2 (Sierk et al., 2006). For instance, Folkins et al. (1999) have shown that the upper troposphere over Samoa (14°S, 171°W) between 14 and 17 km includes air with a considerable stratospheric signature. Samoa is thus defined as 'beyond strictly tropical air' (Thompson and Hudson, 1999). Using the 'beyond strictly tropical air' as reference sector can yield unphysical values at other longitudes in the same latitude bins. Figure 3.3 illustrates the TOCs retrieved by the RSM method using the reference region 180-210° E. The total ozone column at 10-30° N at the reference sector can no longer be used to represent the clean tropospheric ozone background. A usage of these total columns as reference sector leads to the use of RSM unsuccessful in this latitude band.

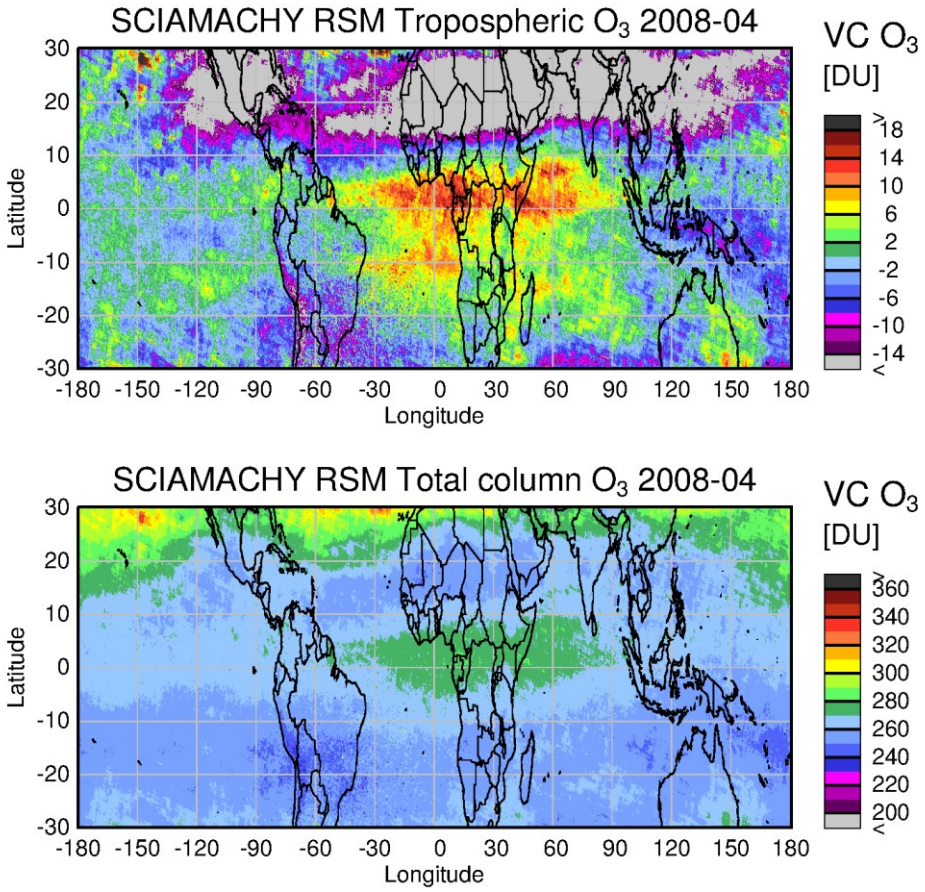

Figure. 3.3. Ozone columns derived from SCIAMACHY data by using the RSM method in April 2008. The top panel shows the TOCs. The bottom panel shows the total ozone columns used in RSM retrieval.

3.1.2.3 TOR

The tropospheric ozone residual (**TOR**) method was the very first retrieval method applied to gain global TOCs. The difference between the so-called TOR method and the other indirect tropospheric ozone retrieval approaches is the use of limb measurements. The CCD and RSM methods both only use nadir data, and are limited to the tropics. The TOR method combines the total ozone columns acquired from nadir measurements with the collocated stratospheric ozone columns retrieved from the limb measurements, by using the tropopause height data. The method was first reported by Fishman et al. (1990), using TOMS/SAGE for nadir and limb ozone data. The standard tropopause height information was derived from National Center Environmental Prediction (NCEP). The OMI/MLS TOC retrieval is the current inheritor

of the TOMS/SAGE TOR approach with the advantage that the MLS measurements are made ~7 min before OMI views at the same location during the daytime tracks (Ziemke et al., 2011). For these two-sensor-TOR cases, one must deal with measurements from two different sensors considering issues related to non-homogeneous data sets. The adjustment for inter-calibration differences of OMI and MLS instruments is performed by using the CCD method. Both OMI-CCD and MLS measurements of the stratospheric ozone are averaged over the Pacific (120° W-120° E) for the comparison (Ziemke et al., 2006). The MLS data is adjusted according to the observed differences. The advantage of using TOR is that it doesn't require any further assumptions, such as zonal homogeneity of stratospheric ozone. However, the horizontal resolution can be degraded by the use of limb measurements. To compensate this drawback, MLS is interpolated in two steps: first a moving 2-D Gaussian window along orbit is performed to fill in intermittent gaps along-track, which is followed by linear interpolation along longitude. In the end OMI/MLS is able to provide daily-based global TOCs (Ziemke et al., 2006; 2011).

The Limb-Nadir Matching (**LNM**) method is a specialized TOR method performed for instrument like SCIAMACHY, which has both limb and nadir measurements. Therefore, inter-instrument calibration is not necessary, which avoids the calibration error introduced during the adjustment. It is worth to point out that, because of the alternately monitoring under nadir and limb mode, the limb ozone profile samplings by using SCIAMACHY is much more sparse than the ones by using MLS measurement. The limb data interpolation induced in the OMI/MLS retrieval should not be implemented in the SCIAMACHY Limb-Nadir Matching method because of the large uncertainty of the limb ozone data in the bigger measuring gaps along-track. The Limb-Nadir Matching retrieval method is the focus of this thesis and will be discussed in detail in Chapter 5.

Besides the use of limb measurements to derive stratospheric ozone columns, ozonesonde climatology can be combined with the satellite cloud-free nadir total ozone columns to separate stratospheric ozone columns. This residual method has been used successfully to retrieve the tropical tropospheric ozone columns (**TTO**) by using TOMS derived total ozone with climatology of 1991-1992 ozonesonde data (Kim et al., 1996, Hudson and Thompson, 1998). This so-called modified residual (**MR**) method is based on the assumption of the existence of total stratospheric ozone column's longitudinal homogeneity in the tropics as well, and is therefore only used in the strict tropics ($\pm$10° latitude band).

3.2 Tropospheric ozone distribution

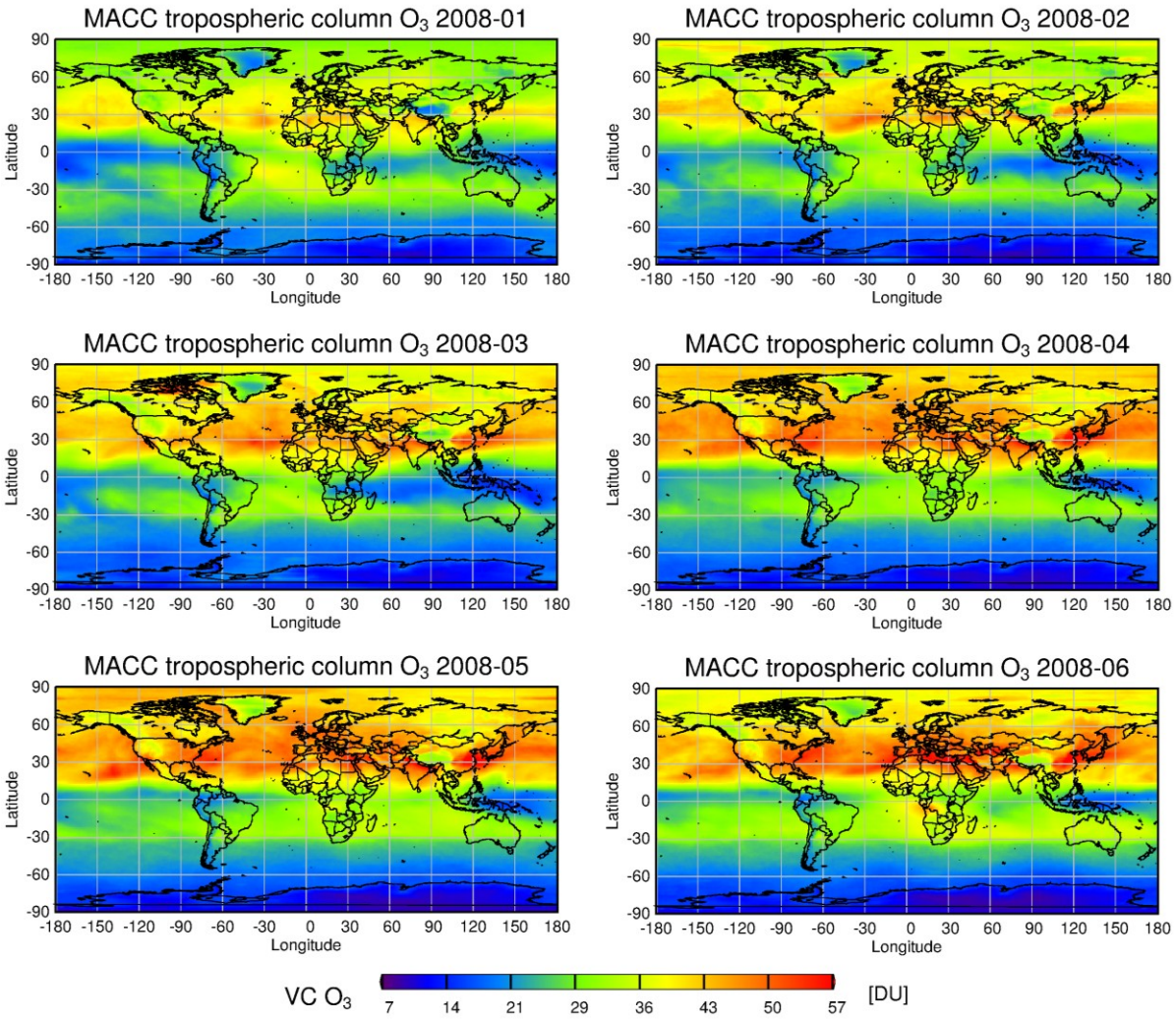

Figure 3.4. Global distribution of the monthly TOCs using MACC reanalysis data (Sect. 4.5).

The spatial and seasonal distribution of tropospheric ozone (see Fig. 3.4) can be driven by variations in precursor emissions, by systematic seasonal changes in meteorological conditions, or by seasonal changes of photochemical oxidation and removal processes.

Figure 3.5 illustrates the percentage of contributing factors (anthropogenic, biomass burning and biogenic sources) of three major tropospheric ozone precursors: NO_x, CO and VOCs in

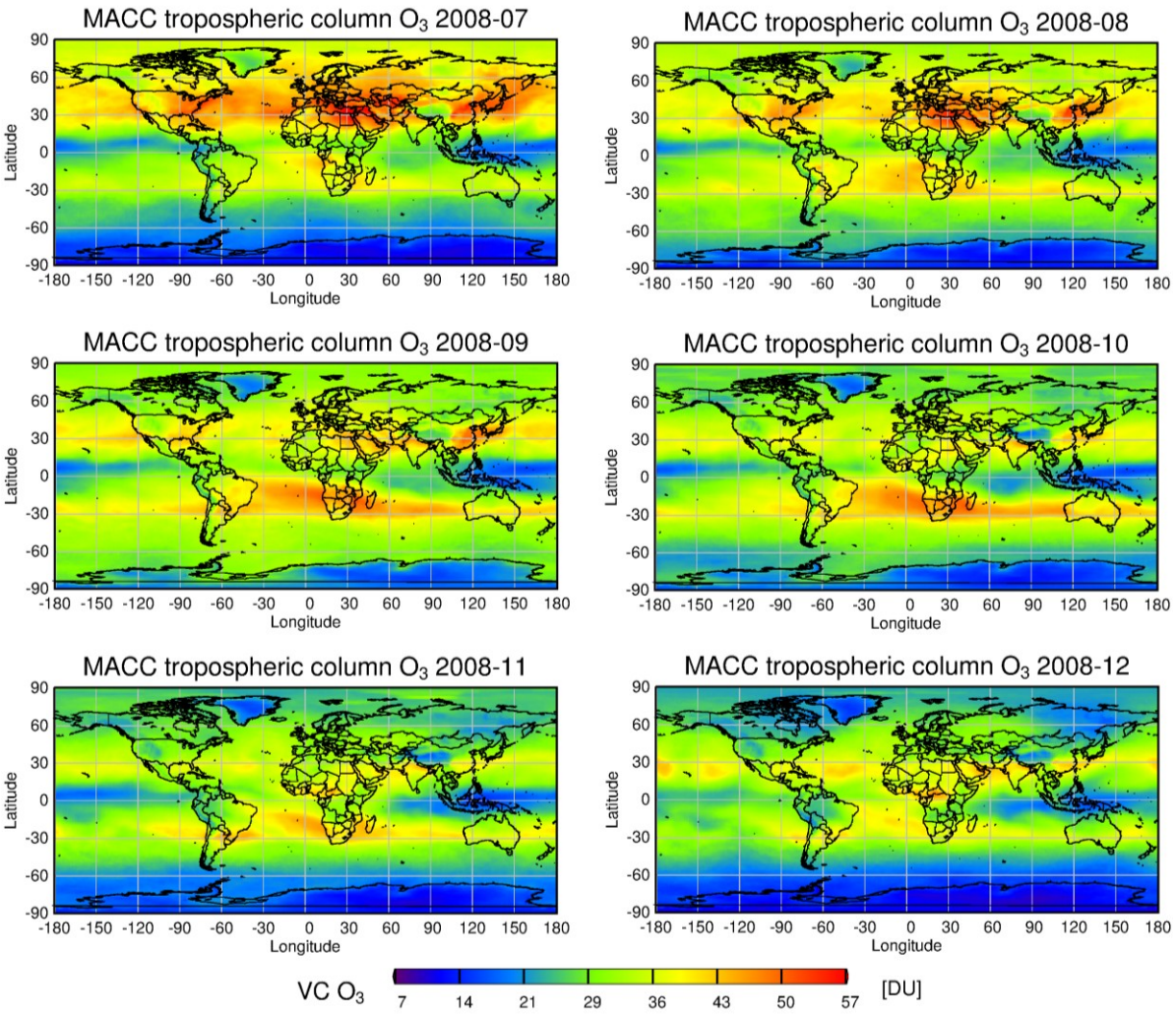

Figure 3.4. Continue.

response to the global emission budget. As **anthropogenic emissions** being the major source of the precursors, the TOC distribution shows an ***asymmetrical hemispheric pattern***, with most ozone located in the Northern Hemisphere, especially over China, the West coast of US, Europe and the Middle East, where most megacities are (see the tropospheric NO_2 volumes in Fig. 3.6). The TOC maxima are occurring in spring (March-May) and in summer (June-August), when the solar radiation is strongest and therefore the photochemical reactions most

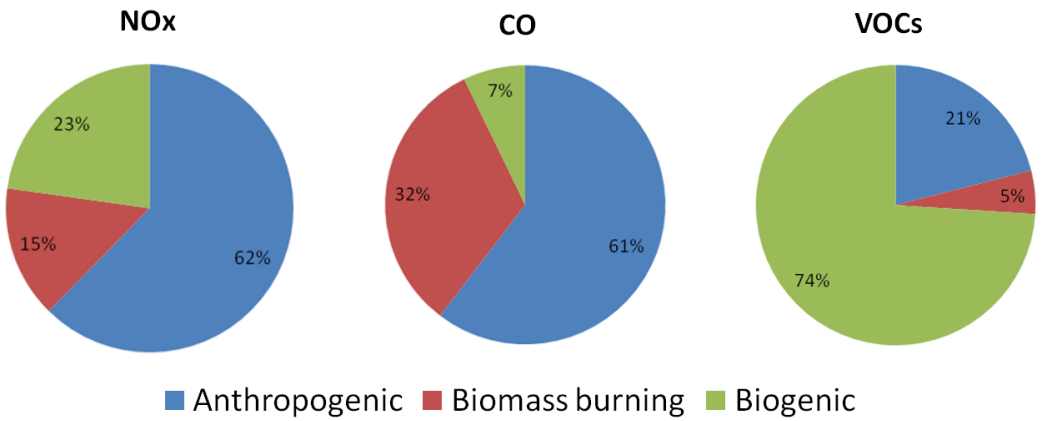

Figure 3.5. Global emission factors for ozone precursors emitted from different sources. The values are taken from Jaeglé et al. (2005), Guenther et al. (1995) and IPCC (2001 p. 256-260) for NO_x, VOCs and CO, respectively. Here the anthropogenic emissions include emissions from transport vehicles, combustion of fossil fuels, industrial activities (e.g., power generation), agriculture etc. The biogenic sources consist of lightning, volcanoes, emissions from oceans and vegetation, etc. Note that the budgets are given by using a range of values from modelling thus have a large uncertainty, e.g., the 74% of biogenic contribution to emit VOCs are calculated with VOCs budget of 377-1150 TgC/yr.

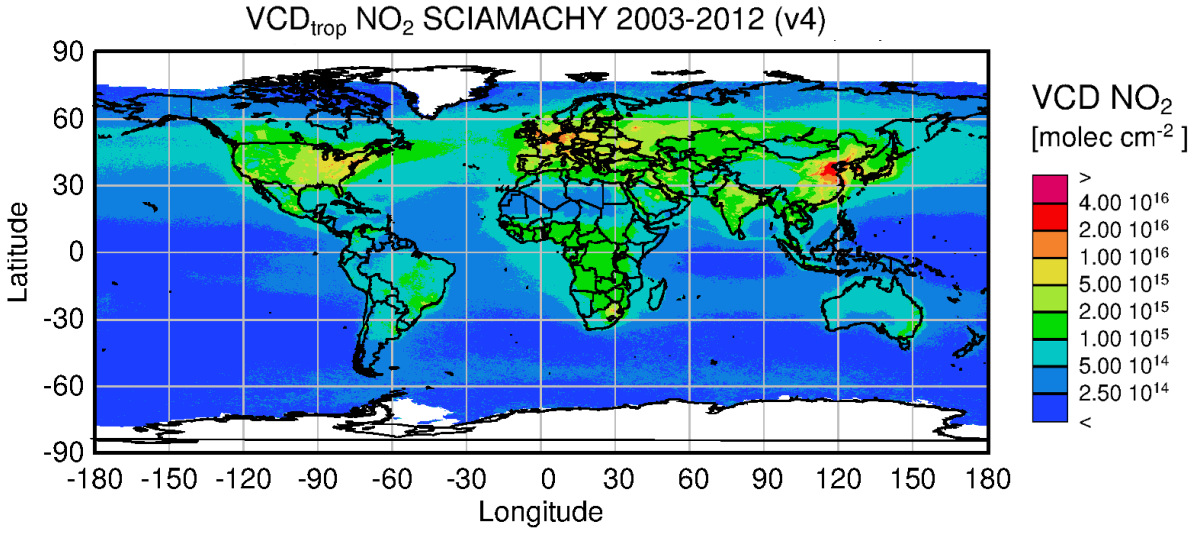

Figure 3.6. Averaged tropospheric NO_2 volumes retrieved using SCIAMACHY Limb-Nadir Matching (Hilboll et al., 2014) during 2003-2012.

efficient. In the mid-latitudes of the Northern Hemisphere, the general circulation is dominated by westerly winds that flow from Asia across the North Pacific Ocean to North America, from North America across the North Atlantic Ocean to Europe, and from Europe into Asia. Tropospheric ozone is **intercontinentally transported** along these transport pathways and therefore circles the globe (see e.g. Jaffe et al., 1999; Parrish et al., 2012; Stohl and Eckhardt, 2004; HTAP, 2010 and the references therein).

Table 3.1: Global and regional estimates of ozone production from wildfires (adjusted from Jaffe and Wigder, 2012).

Fire/time period	**Ozone production**	**References**
Southern Hemisphere (Africa and South America)/during the dry season	17 Tg $month^{-1}$	Mauzerall et al., 1998
Alaska and Canada/summer 2004	11-15 Tg	Pfister et al., 2006
Boreal Northern Hemisphere	13 Tg yr^{-1}	Jaffe and Wigder, 2012
Temperate Northern Hemisphere	3 Tg yr^{-1}	Jaffe and Wigder, 2012
Northern Hemisphere Tropical and Equatorial Region (10°S-30 °N)	103 Tg yr^{-1}	Jaffe and Wigder, 2012
Southern Hemisphere south of 10°S	54 Tg yr^{-1}	Jaffe and Wigder, 2012
Global total	174 Tg yr^{-1}	Jaffe and Wigder, 2012

Biomass burning is the second largest source of CO after fossil fuel combustion. Burnings emit substantial amounts of ozone precursors, e.g., NMVOCs, CO, CH_4 and NO_x, thus make a significant contribution to tropospheric ozone concentrations both regionally and globally (Crutzen et al., 1979). Table 3.1 shows the regional and global estimates of ozone production from biomass burnings based on several studies, in which wildfires/biomass burning are reported to produce approximately 170 Tg of ozone per year. This is 3.5% of all global tropospheric ozone production (Jaffe and Wigder, 2012). The ***tropospheric ozone biomass burning plume in the Southern Hemisphere*** in austral spring (to be more precisely, the zonal ozone belt that transported over the Southern Atlantic, the coast of South Africa, along Indian Ocean and towards Australia, hereafter biomass burning plume) is well identified as a result of the combination of, e.g., widespread biomass burning in southern Africa and South Amer-

ica, lightning and continuous downward flows (e.g., Fishman et al., 1986, 1991; Pickering et al, 1996; Thompson et al., 1996, 2001; Lelieveld and Dentener, 2000; Staudt et al., 2002; Sinha et al., 2004). In the Northern Hemisphere, the boreal fires contribute more than half to the global ozone production from biomass burning (see Jaffe and wigder, 2012 and the references therein). Figure 3.7 shows the seasonal distribution of the fire activities.

Biomass burning impacts on ozone production via two pathways: it emits precursors of ozone directly, and it influences ozone photochemistry through emission of particles like aerosols. Parrington et al. (2013) studied the ozone production rate within biomass burning plumes. They showed that ozone formation increases with plume age as calculated by non-methane hydro carbons (NMHC) ratios, wherein aerosols are very likely to drive ozone production efficiency by influencing the photolysis rate of NO_2 to form ozone.

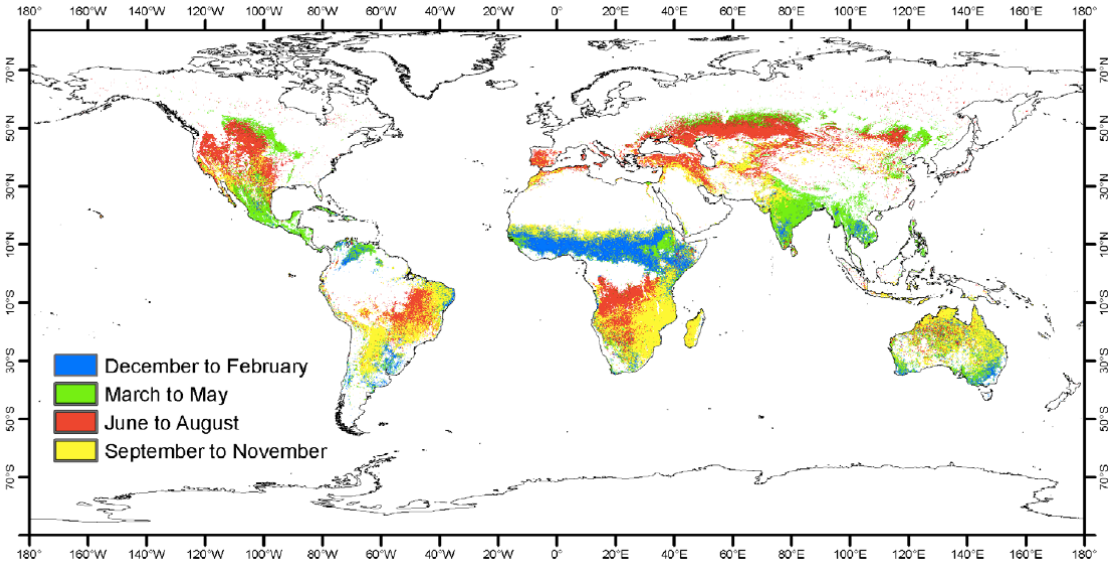

Figure 3.7 Seasonal cycle of the global fire activity obtained from accumulated spatial-temporal distribution of the globally burnt surface products for the period 1982-1999 (Carmona-Moreno et al., 2005).

Climate change and climate phenomena can influence the tropospheric ozone distribution by influencing the frequency and the intensity of biomass burnings, the strength of the tropi-

cal convection and the horizontal propagation. Gillett et al. (2004) has shown that global warming had an impact on the frequency of the area burned for Canadian forests. ENSO (El Niño–Southern Oscillation) is identified to influence ozone production as well by changing emissions and dynamics. During El Niño periods, emissions from burnings can be up to two times larger than during other time (Akagi et al., 2011). Chandra et al. (1998) reported that 50% of the TOC enhancements during the Indonesian fire episode in 1997 were due to El Niño related transport changes, while 50% came from the enhanced fire emissions. The ***wave-one pattern*** in equatorial tropospheric ozone is a persistent feature caused by the Walker circulation, with higher ozone values over the southern Atlantic tropics and lower values over the Pacific (e.g., Thompson and Hudson, 1999; Chandra et al., 2003). This longitudinal structure was first reported as a pattern of the total column ozone (Shiotani, 1992). Observed amplitudes of the tropical wave-one in total ozone using 11-year TOMS data are largest (smallest) during September-November (March-May). Later on, by analysis of ozonesondes and stratospheric ozone derived from SAGE and MLS, the stratospheric ozone amount in the tropics was found to have exceedingly small zonal variability of only a few DU on all time scales including daily measurements (Shiotani and Hasebe, 1994; Ziemke et al., 1996; 2010). This discovery, which was made in the mid-1990s, proved that the wave-one pattern is existing in the troposphere.

Stratospheric-Tropospheric-Exchange (STE) is another factor that greatly impacts the global tropospheric ozone distribution (Tab. 3.2). STE induces stratospheric ozone into the troposphere. It can result in increasing of the tropospheric ozone concentrations. It is responsible for the observed ***Mediterranean ozone pool*** in boreal summer (Zanis et al., 2014) and is also thought to play a role in the observed higher ozone amounts in summer over Tibetan Plateau (e.g., Lal et al., 2014).

Numerous other factors can also influence the tropospheric ozone distribution, e.g., biogenic emission, which increases ozone at regional European scale and plays an important role of ozone distribution in Southeast China (Tagaris et al., 2014). These factors will not be discussed further in this dissertation. To sum up, the knowledge about tropospheric ozone distribution has grown dramatically since the late 1980s, along with the development of more in situ measurements, satellite observations and data retrieval techniques. Increasing amounts of measurements and improving accuracies of the retrieval will benefit us by providing us more insight in tropospheric ozone. For instance, the 'Atlantic ozone paradox', which refers to the

persistence of higher TOCs over the South Atlantic in comparison to the northern tropical Atlantic, as observed by ozonesondes and satellite measurements, is not valid anymore owing to the insight provided by additional in situ observations 6 years after its discovery (Thompson et al., 2000; Sauvage et al., 2006). In the following chapters, I will focus on the optimization of existing tropospheric ozone retrieval techniques based on SCIAMACHY Limb-Nadir Matching method. Furthermore, with the benefit of the improved TOC database, an ozone distribution pattern over the AS, which has hardly been studied before, will be investigated.

Table 3.2: Global budget of tropospheric ozone (Tg yr^{-1}) for the present-day atmosphere (adapted from IPCC, 2007).

Model	STE	Chemical production	Chemical loss	Dry Deposition	Burden	Lifetime (days)	Reference
TM3	570	3310	3170	710	350	33	Lelieveld and Dentener, 2000
GEOS-Chem	470	4900	4300	1070	320	22	Bey et al., 2001
MOZART-2	340	5260	4750	860	360	23	Horowitz et al., 2003
STOCHEM	395	4980	4420	950	273	19	Stevenson et al., 2004
25 models	520±200	5060±570	4560±720	1010±220	340±40	22±2	Stevenson et al., 2006

4 Data sets used for this study

In this chapter, the main data sets which were used for this study, such as the satellite data sets (SCIAMACHY nadir and limb ozone data), the tropopause height data retrieved from European Centre for Medium-Range Weather Forecasts (ECMWF) database, the balloon based measurement (ozonesonde data), the Monitoring Atmospheric Composition and Climate (MACC) reanalysis data and the HYbrid Single-Particle Lagrangian Integrated Trajectory (HYSPLIT) model, will be presented.

4.1 SCIAMACHY nadir ozone data

The SCIAMACHY V6 total ozone product provides total ozone column data, which is expressed in Dobson Unit (DU) for each measurement. It is retrieved by using the Weighting Function Differential Optical Absorption Spectroscopy (WFDOAS) algorithm (Coldewey-Egbers et al., 2005) applied to the UV spectral range (fitting window of 326.6-334.5 nm) in SCIAMACHY channel 2. The product also contains the cloud parameters 'cloud fraction' and 'cloud top height'. The 'cloud fraction' represents the percentage of the cloud coverage for each single nadir pixel. The value of the 'cloud top height' represents the altitude of the upper side of the highest cloud. Both these parameters are default products determined by using the SACURA algorithm (SemiAnalytical CLoUd Retrieval Algorithm, Rozanov and Kokhanovsky, 2004). Since the part of the ozone columns which are positioned below the clouds cannot be detected by the UV channels from the satellite, a ghost vertical column (GVC) is estimated from the climatological vertical ozone profiles and these GVC values are added to the vertical columns retrieved from the spectral fit.

4.2 SCIAMACHY limb ozone data *

The IUP Bremen level 2 SCIAMACHY limb ozone product provides ozone data expressed as number densities (molecules per cubic centimeter) and as VMRs (parts per million by volume (ppmv)) vs. the altitude for each measurement. The ECMWF operational pressure and temperature data are used to calculate the air density, which is needed for converting the number

* This subsection has been previously published as part of Jia et al. (2015).

densities into mixing ratios. The product also provides the corresponding a priori ozone profiles as well as error estimates in both number density and volume mixing ratio representations. The cloud information in the limb data is retrieved by using the SCODA (SCIAMACHY Cloud Detection Algorithm) database (Eichmann et al., 2011) and is provided as 'cloud flag' in the data. Note that the cloud information in nadir and limb data are derived by different algorithms. During this study, the SCIAMACHY limb ozone retrieval has been modified from V2.9 via V3.0 to V3.5 to achieve a more accurate ozone profile database (details are described in Sect. 3.5). In the V3.0 and V3.5 data products, the vertical resolution is added. The vertical resolution S_i is calculated from the spread of the averaging kernels (G. E. Backus and F. E. Gilbert, 1970) as:

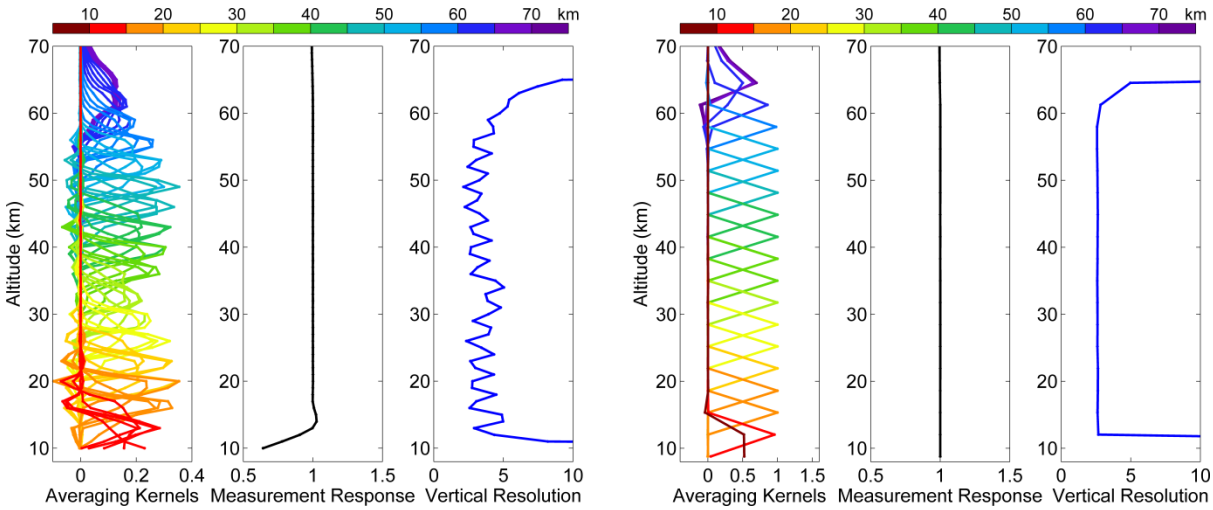

Figure 4.1. Averaging kernels, measurement response and vertical resolution from SCIAMACHY V2.9 (left panel) and V3.0 (right panel). Note that the x axis range is different between the two panels. The example is calculated for orbit 21223; measured at 17:36 UTC on 22 March 2006; solar zenith angle of 74.95; at 75.44°N and 93.58°W.

$$S_i = 12 \cdot \sum_j A_{ij}^2 \cdot \left(Z_j - Z_i\right)^2 \cdot \Delta Z_j \Big/ \left(\sum_j A_{ij} \cdot \Delta Z_j\right)^2 . \qquad (4\text{-}1)$$

where i represents the elevation step, Z is the altitude, and A_{ij} refers to the corresponding

element of the averaging kernel matrix. To perform the integration, the averaging kernels need to be resampled to a finer grid. In this study 20 sub-layers are used. Although the vertical resolution is not included in the V2.9 data products, for the purpose of the data selection of this study, I calculated it in the same way as is done for the V3.0 data product (see Sect. 3.6.3). Examples of the averaging kernels, measurement response and vertical resolution originating from the V2.9 and V3.0 are given in Fig. 4.1. As the retrieval is carried out at the measurement tangent heights, the averaging kernels for V3.0 reach a value of 1.0 at the maxima between 12 and 60 km. For V2.9 the value is around 0.3, which is due to the retrieval at a finer grid (1km) compared to the measurement grid (~3 km). Measurement response is calculated by summing the elements of the corresponding averaging kernel. It describes how much information comes from the measurement. The values of Measurement response in Fig. 4.1 indicate that

1. The retrieved profile is completely independent from the a priori information within the whole altitude range for V3.0 and above 12 km for V2.9.
2. Below 12 km, V2.9 may contain less information from the measurement and is more strongly affected by the a priori information compared to V3.0 (note that V3.0 uses measurement down to 8 km, while V2.9 stops at 12 km).

From the averaging kernels the following can be observed: at altitudes above 65 km, profile information comes from the 60 - 70 km altitude range for both data sets. Information from below 12 km partially originates from the upper layers for both versions (V2.9 and V3.0).

The retrieval algorithms of limb V2.9 and V3.0 are presented in Sect. 5.5.1 and 5.5.2.

4.3 ECMWF tropopause height

Knowledge of the tropopause height is required to extract accurate stratospheric ozone columns from the limb profile data. In the Limb-Nadir Matching method, thermal and dynamical criteria are executed and retrieved by means of meteorological model data from ECMWF ERA-Interim reanalysis (Dee et al., 2011), following an approach similar to the one discussed in Hoinka (1998). The thermal definition (also called WMO definition) was provided in 1957. It defines the tropopause as the point where the temperature lapse rate is larger than -2 K/km for at least 2 km. The dynamic tropopause height is defined with a threshold value of 3.5

PVU (1PVU = 10^{-6} $km^2s^{-1}kg^{-1}$) in potential vorticity. In the tropopause height retrieval, the thermal criterion is applied for tropical regions (±20°), while the dynamical criterion is used at latitude regions higher than 30°. The two regimes were combined and weighted with the distance from the regime boundaries in the transition regions (±20°- ±30°). Further description of the retrieval is given in Ebojie (2014).

The retrieved ECMWF TPH data has a resolution of 1.5° x 1.5°. Each grid contains four values per day, corresponding to the four analysis times (00, 06, 12 and 18 UTC).

4.4 Ozonesonde data

The ozonesonde is a lightweight, balloon-borne instrument that is mated to a conventional meteorological radiosonde. The most common heart of the ozonesonde is an electrochemical concentration cell (ECC) that senses ozone as it reacts with a dilute solution of potassium iodide to produce a weak electrical current proportional to the ozone concentration of the sampled air (R22 - 23, Komhyr, 1969).

$$2KI + O_3 + H_2O \rightarrow I_2 + O_2 + 2KOH\,. \qquad \text{(R22)}$$

$$I_2 + 2e^- \rightarrow 2I^-\,. \qquad \text{(R23)}$$

The balloon carrying the instrument package ascends through the atmosphere and will ascend to altitudes of about 35 km before it bursts. The radiosonde measures air temperature (degree Celsius), pressure (hPa), and relative humidity (%), and transmits all of the ozone and weather data back to a ground receiving station during the 2 hour weather balloon ascent with a very fine resolution (mostly within 10 meter). In the ozonesonde measurement, the ozone value is expressed as partial pressure. The ozone concentrations expressed in number density can be obtained by conversion following the ideal gas law:

$$ND = P_{O_3} \cdot N_a / R / (T + 273.15)\,, \qquad \text{(4-2)}$$

where N_a is the Avogadro constant, R is the ideal, or universal, gas constant which equals to 8.314 $J \cdot K^{-1} \cdot mol^{-1}$, and T is the temperature in degree Celsius. Considering the expensive costs of a measurement, usually there is only one measurement per day and 1-5 measurements per month (except during intensive campaigns).

The ozonesonde data from the WOUDC (World Ozone and Ultraviolet Radiation Data Centre) stations are used for satellite ozone data validation. 61 ozonesonde stations were used in this work, wherein 14 stations are located in the tropics, 31 stations in the northern midlatitudes, 6 stations in the northern high latitudes, 6 stations in the southern midlatitudes and 4 stations in the southern high latitudes (see Tab. 4.1).

4.5 MACC reanalysis data

MACC is a research project with the aim to establish core global and regional atmospheric environmental services for the European GMES (Global Monitoring for Environment and Security) initiative (Inness et al., 2013). MACC combines a wealth of atmospheric composition data with a state-of-the-art numerical model and data assimilation system to produce a reanalysis of the atmospheric composition. The ozone retrievals assimilated in the MACC reanalysis are listed in Tab. 4.2.

MACC reanalysis data of ozone, CO and specific humidity used in this study are available in 6-h time intervals (00, 06, 12 and 18UTC) and were provided in monthly files with the unit of kg/kg under the website http://apps.ecmwf.int/datasets/data/macc-reanalysis/levtype=ml/. The horizontal resolution of the model is 1.125° × 1.125°. Variables were provided as 3D fields in pressure hybrid vertical coordinates. The vertical coordinate system is given by 60 hybrid sigma-pressure levels, with a model top at 0.1 hPa. Barometric formula was used to derive altitude. With the 2D surface pressure data P_s, the upper and lower pressure for each layer *i* can be calculated by:

$$P_{upper}(i) = 1000 \cdot a(i) + P_s / 100 \cdot b(i) . \quad (4\text{-}3)$$

$$P_{lower}(i) = 1000 \cdot a(i+1) + P_s / 100 \cdot b(i+1) . \quad (4\text{-}4)$$

where *a* and *b* can be obtained from the MACC webpage. Ozone profiles in Dobson Unit can be derived for each layer at each grid cell by:

$$O_3(i) = P_{col}(i) \cdot O_{3\_org}(i) / 2.687 \times 10^{16} . \quad (4\text{-}5)$$

where the partial pressure can be calculated by

$$P_{col}(i) = N_a \cdot (P_{lower}(i) - P_{lower}(i)) / M_{o_3} / G . \quad (4\text{-}6)$$

in which N_a is the Avogadro constant, $M_{o_3} = 0.048\ kg/mol$ is the molar mass of ozone, and G is the gravitational acceleration. By using the same tropopause height as SCIAMACHY Limb-Nadir Matching, TOCs derived from MACC reanalysis are obtained.

4.6 HYSPLIT model

HYbrid Single-Particle Lagrangian Integrated Trajectory (HYSPLIT) is a system for the computation of simple air parcel trajectories from the National Oceanic and Atmospheric Administration (NOAA). It is based on the Global Data Assimilation System (GDAS) meteorological databases. In order to investigate the forward and backward trajectory of the air mass, the web-based version of the HYSPLIT model (Stein et al., 2015) is used for this study. The webpage is as follows: http://ready.arl.noaa.gov/hypub-bin/trajtype.pl?runtype=archive.

Table 4.1: WOUDC and SHADOZ (Southern Hemisphere ADditional OZonesondes) stations used in the validation.

Station Name	Height (m)	Country	Latitude	Longitude
NH high latitude				
Alert	66	CAN	82.5°N	62.3°W
Eureka	10	CAN	80.0°N	85.9°W
Lerwick	80	GBR	60.1°N	1.2°W
Ny-Aalesund	11	NOR	78.9°N	11.9°E
Resolute	46	CAN	74.7°N	94.9W
Sodankyla	179	FIN	67.4°N	26.6°E
NH midlatitude				
Ankara	890	TUR	39.9°N	32.8°E
Barajas	631	ESP	40.4°N	3.5°W
BrattsLake	580	CAN	50.2°N	104.7°W
Churchill	30	CAN	58.7°N	94.1°W
DeBilt	4	NLD	52.1°N	5.1°E
Egbert	251	CAN	44.2°N	79.7°W
Hohenpeissenberg	976	DEU	47.8°N	11°E
Holtville[a]	-19	USA	32.8°N	115.3°W
HongKong	66	HKG	22.3°N	114.1°E
Houston	19	USA	29.7°N	95.4°W
Huntsville	196	USA	34.7°N	86.6°W
Isfahan	1550	IRN	32.5°N	51.7°E
Kelowna	456	CAN	49.9°N	119.4°W
Legionowo	96	POL	52.4°N	20.9°E
Naha	28	JPN	26.2°N	127:6°E
Narragansett	21	USA	41.4°N	71.4°W
Payerne	491	CHE	46.5°N	6.5°E
Praha	304	CZE	50.0°N	14.4°E
Richland[a]	123	USA	46.2°N	119.1°W
SableIsland	4	CAN	43.9°N	60.0°W
Sapporo	26	JPN	43.0°N	141.3°E
Stonyplain	766	CAN	53.5°N	114.1°W
TableMountain	2285	USA	34.4°N	117.7°W
TrinidadHead	20	USA	40.8°N	124.1°W
Tsukuba	31	JPN	36.0°N	140.1°E
Uccle	100	BEL	50.8°N	4.3°E
ValentiaObservatory	14	IRL	51.9°N	10.2°W
Valparaiso[a]	240	USA	41.5°N	87°W
WallopsIsland	13	USA	37.9°N	75.4°W
Walsingham	200	CAN	42.6°N	80.6°W
Yarmouth	9	CAN	43.8°N	66.1°W
Tropics				
Alajuela [b]	899	CRI	9.9°N	84.2°W
AscensionIsland [b]	79	SHN	7.9°S	14.4°W
Barbados[a] [b]	32	BRB	13.1°N	59.4°W

Heredia [b]	1176	CRI	10°N	84.1°W
Hilo [b]	2994	USA	19.4°N	155.0°W
Malindi [b]	-6	KEN	3.0°S	40.2°E
Maxaranguape (Natal) [b]	14	BRA	5.5°S	35.2°W
Nairobi [b]	1795	KEN	1.2°S	36.8°E
Paramaribo [b]	7	SUR	5.8°N	55.2°W
Samoa [b]	77	ASM	14.2°S	170.5°W
SanCristobal [b]	8	ECU	0.9°S	89.6°W
SepangAirport [b]	17	MYS	2.7°N	101.7°E
Tecamec [b]	2272	MEX	19.3°N	99.1°W
Watukosek (Java) [b]	50	IDN	7.5°S	112.6°E
SH midlatitude				
Broadmeadows	109	AUS	37.7°S	144.9°E
Irene [b]	1524	ZAF	25.9°S	28.2°E
LaReunionIsland [b]	24	REU	21.0°S	55.4°E
Lauder	370	NZL	45.0°S	169.6°E
MacquarieIsland	7	AUS	54.5°S	158.9°E
Ushuaia	17	ARG	54.8°S	68.3°W
Antarctic				
Davis	18	ATA	68.5°S	77.9°E
Marambio	198	ATA	64.2°S	56.6°W
Neumayer	38	ATA	70.6°S	8.2°W
Syowa	22	JPN	69.0°S	39.5°E

[a] stations with less than 30 ozonesonde profiles; [b] stations originally from SHADOZ

Table 4.2: Satellite retrievals of ozone that were actively assimilated in the MACC reanalysis.

Sensor	**Satellite**	**Provider**	**Version**	**Type**
GOME	ERS-2	RAL	-	Profiles
MIPAS	ENVISAT	ESA	-	Profiles
MLS	AURA	NASA	V02	Profiles
OMI	AURA	NASA	V003	Total columns
SBUV/2	NOAA-16	NOAA	V8	Partial columns
SBUV/2	NOAA-17	NOAA	V8	Partial columns
SBUV/2	NOAA-18	NOAA	V8	Partial columns
SCIAMACHY	ENVISAT	KNMI	-	Total columns

5 Improvement of the SCIAMACHY Limb-Nadir Matching retrieval

5.1 Introduction

The Limb-Nadir Matching method is a residual method (Sect. 3.1) that is developed for tropospheric trace gas retrieval using the SCIAMACHY instrument. The advantage of the Limb-Nadir Matching residual retrieval is that the total columns of the trace gases derived from SCIAMACHY nadir measurements and the stratospheric columns calculated from SCIAMACHY limb profiles not only have spatial and temporal coherence but also are measured by the same instrument. Thus the inter-instrument calibration that is normally required for, e.g., OMI/MLS is avoided. Hence the instrumental systematic errors are reduced. Sierk et al. (2006) performed the SCIAMACHY Limb-Nadir Matching approach on ozone and NO_2. The plausible preliminarily results motivated the development of the SCIAMACHY Limb-Nadir Matching retrieval for tropospheric NO_2 and lead to the establishing of tropospheric NO_2 data sets (Sioris et al., 2004; Beirle et al., 2010; Hilboll et al., 2013).

The Limb-Nadir Matching retrieval of tropospheric ozone, however, is quite challenging compared to the one of tropospheric NO_2. On one hand, most of the ozone in the atmosphere is formed in the stratosphere by the photolysis of O_2 with the absorption of UV radiation, whereas the TOCs only constitute a minor amount (~10 %) of the total ozone columns. The separation of the tropospheric ozone thus requires extremely accurate information on both stratospheric and total ozone columns. On the other hand, stratospheric ozone has its concentration maxima at ~18-25 km (depending on latitude). The highly variable stratospheric ozone together with appropriate meteorological conditions induces frequent STE activities. Consequently, the tropospheric ozone amount can vary largely with the stratospheric intrusions. The Mediterranean summer ozone pool is an emblematic example to present the influences of ozone STEs. In the case of NO_2, the stratospheric NO_2 is mainly produced by the photolysis of N_2O. The column density of the stratospheric NO_2 ($< 5x10^{15}$ molec/cm^2) is quite small compared to the amount of the tropospheric NO_2 over the polluted areas which easily reach 10^{16} molec/cm^2 and more. Besides, stratospheric NO_2 is concentrated at around

30 km. As this is far away from the tropopause, STEs of NO_2 rarely occur. In the Limb-Nadir Matching retrieval, the stratospheric NO_2 columns can be easily extracted to retrieve accurate tropospheric NO_2 columns.

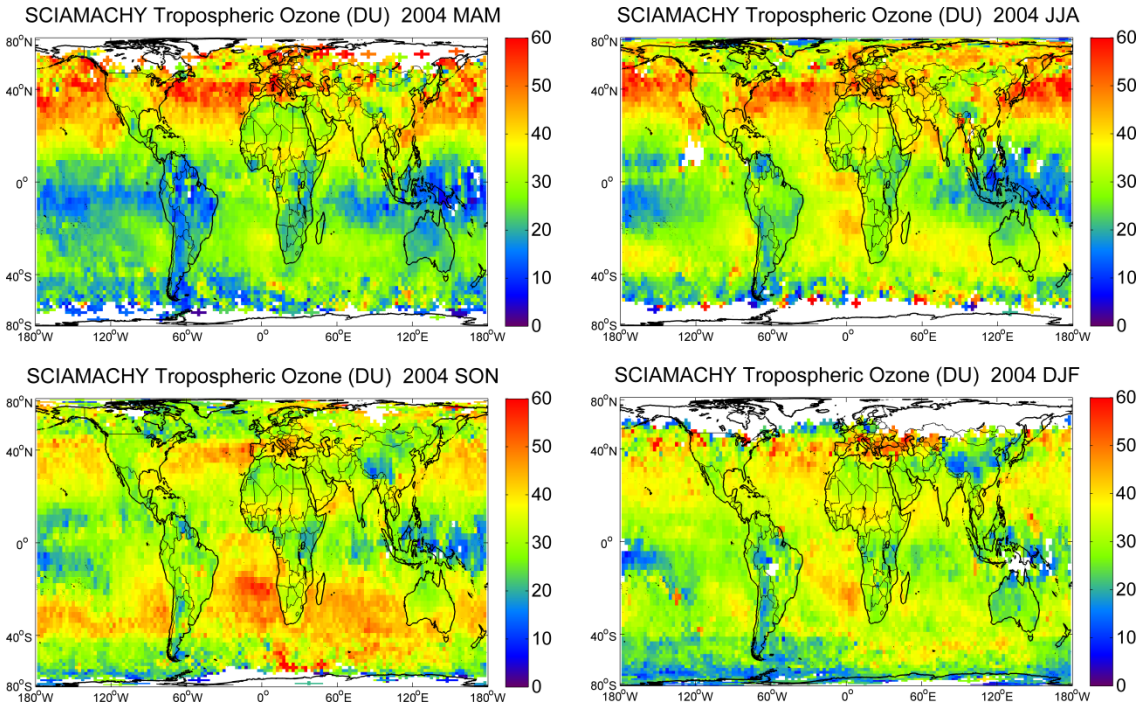

Figure 5.1. The seasonality of SCIAMACHY Limb-Nadir Matching TOCs V1.0 in 2003.

The first quantitative interpretation of tropospheric ozone retrieval results using the SCIAMACHY Limb-Nadir Matching method was described by Ebojie et al. (2014). The study reported that the tropospheric ozone results (hereafter V1.0) agreed with ozonesonde results to within 3 DU (by averaging all the available data between January 2003 and December 2011). The global distributions showed the expected seasonal and spatial patterns (Fig. 5.1) also seen by other instruments, e.g., OMI/MLS and TES. However, several issues are identified in the V1.0 data in the matter of both data amount and data quality (Fig. 5.2):

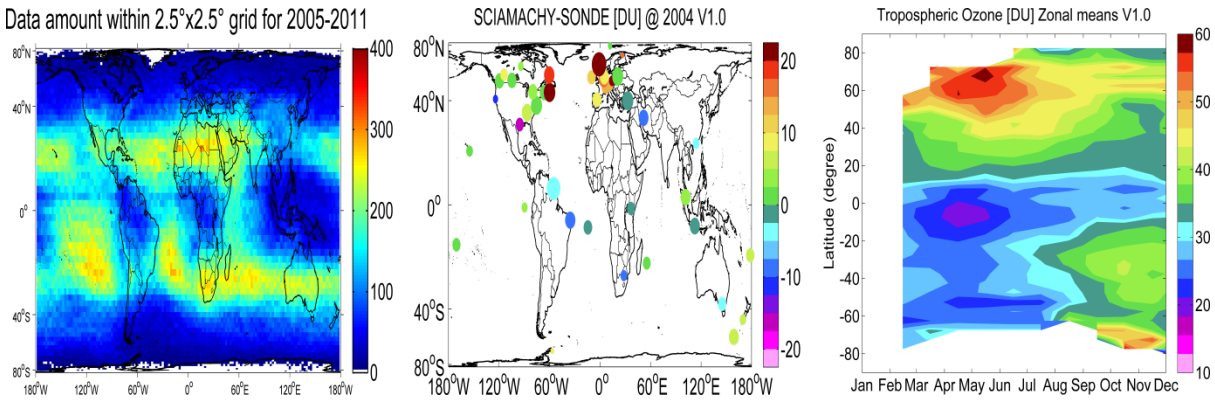

Figure 5.2. Issues in the V1.0 dataset. Left panel: the amount of quality-controlled measurement points per 2.5°× 2.5° grid box from the TOC calculation for 7 years (2005-2011). Middle panel: yearly averaged comparison results between V1.0 tropospheric ozone and ozonesonde measurements in 2004. The size of the dots represents 1σ standard deviation (0.2 - 24 DU). Right panel: V1.0 zonal mean (2.5° interval) climatology calculated from data in 2004.

1. A severe lack of data over the tropics and mid to high latitudes can be observed from the 7-year data amount analysis (left panel in Fig. 5.2).
2. Compared to the 3 DU difference with ozonesonde by averaging all the available data in 9 years, the yearly comparison results (not to mention the monthly results) showed more than 10 DU overestimations at the northern high latitudes, especially over Europe and the east coast of Northern America. Some underestimations are also observed in the tropics (middle panel in Fig. 5.2).
3. V1.0 failed to catch the well known biomass burning pattern properly (right panel in Fig. 5.2). The biomass burning induced autumn tropospheric ozone plume in the Southern Hemisphere extends too far in north-south direction in V1.0. Furthermore, unrealistically high values at southward of 60°S are observed in the zonal mean climatology.

In this chapter, various improvements of the Limb-Nadir Matching approach for tropospheric ozone retrieval are presented. To eliminate the existing issues in V1.0 and increase the data quality, the retrieval is modified in three steps. First, the CTH information is used in a more

sophisticated way in the data screening process to increase the data amount involved in the retrieval. Secondly, the TPH information is calculated more accurately by optimizing the TPH-Limb collocation scheme temporally and spatially. Error analysis showed that the stratospheric ozone columns induced most of the error in the tropospheric ozone retrieval (Ebojie et al., 2014). Thus, in the third step, the limb ozone retrieval algorithm is improved to minimize the error contribution. The TOC results obtained after the first and second optimizations are referred to as V1.1. The results after the third step are referred to as V1.2.

In Sect. 5.2, the retrieval algorithm used in V1.0 Limb-Nadir Matching retrieval is briefly described. The three optimization steps are described in detail in Sect. 5.3 - 5.5, respectively. The Limb-Nadir Matching TOCs V1.0, V1.1 and V1.2 results and the latest validation results are presented in Sect. 5.6. Finally, the conclusion of this chapter is given in Sect. 5.7.

5.2 Ozone Limb-Nadir Matching algorithm

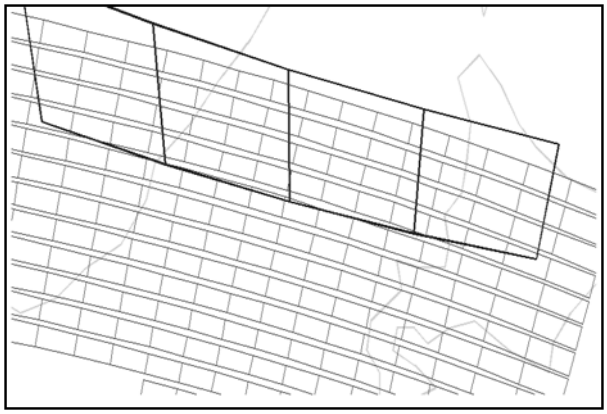

Figure 5.3. Example of SCIAMACHY swath for limb (large black rectangles) and nadir (small gray rectangles) observations in orbit 06541, UTC 01:13:14, on 01 June 2003.

This section describes the TOC retrieval algorithm by subtracting stratospheric ozone columns from the total ozone columns. First, the nadir and limb data sets are screened through data quality-controlling processes (Sect. 5.2.1). Second, SCIAMACHY nadir measurements

and ECMWF TPH are collocated to each limb measurement temporally and spatially (Sect. 5.2.2). For a typical SCIAMACHY Limb-Nadir matching, one limb pixel ideally (if no nadir data is screened) matches to ~12 nadir measurements (Fig. 5.3). We calculate one total column by averaging the selected geographic-fitted nadir measurements for every single SCIAMACHY limb measurement. In the next step, the screened limb profiles must be combined with (subtracted by) the collocated TPH data to calculate the stratospheric ozone columns (Sect. 5.2.3). The TOCs are then retrieved by subtracting the stratospheric columns from the total columns. The full procedure is depicted in Fig. 5.4.

5.2.1 Data quality control

Two parameters are used to screen both nadir and limb data in the Limb-Nadir Matching retrieval:

Clouds are a non-negligible factor for data quality. They affect the albedo, increase light paths (within clouds) absorption by the cloud, and cause a shielding effect. The cloud parameters contained in nadir and limb data sets are retrieved using different algorithms. The ones included in nadir data are default products determined by using SACURA, while the ones in limb data are retrieved by using SCODA algorithm (detailed in Chapter 4). To minimize the cloud influences, the 'cloud fraction' parameter is used to filter the nadir data with the aim of minimizing uncertainties induced by using the ghost vertical columns (Coldewey-Egbers et al., 2005). The 'cloud fraction' parameter is limited to CF<0.3, indicating that the nadir pixels with a cloud coverage larger than 30 percents will be identified as cloud contaminated pixels and will get rejected. One should keep in mind that the ozone values of nadir pixels with a cloud coverage <30 percents can still possibly be dominated by the cloudy part, and can cause underestimations of TOCs. This topic is not resolved in this thesis. Influences of using 'cloud fraction' <0.3 to screen data need to be further investigated. A limb measurement is defined to be 'clean' when the TPH is higher than the cloud top height (CTH) since the altitude layers below TPH are not used in the course of retrieval. However, the retrieval uncertainties in the higher layers caused by the effective albedo of clouds might still be non-negligible.

Solar zenith angle (SZA) affects the sensitivities of the satellite measurements. A threshold of

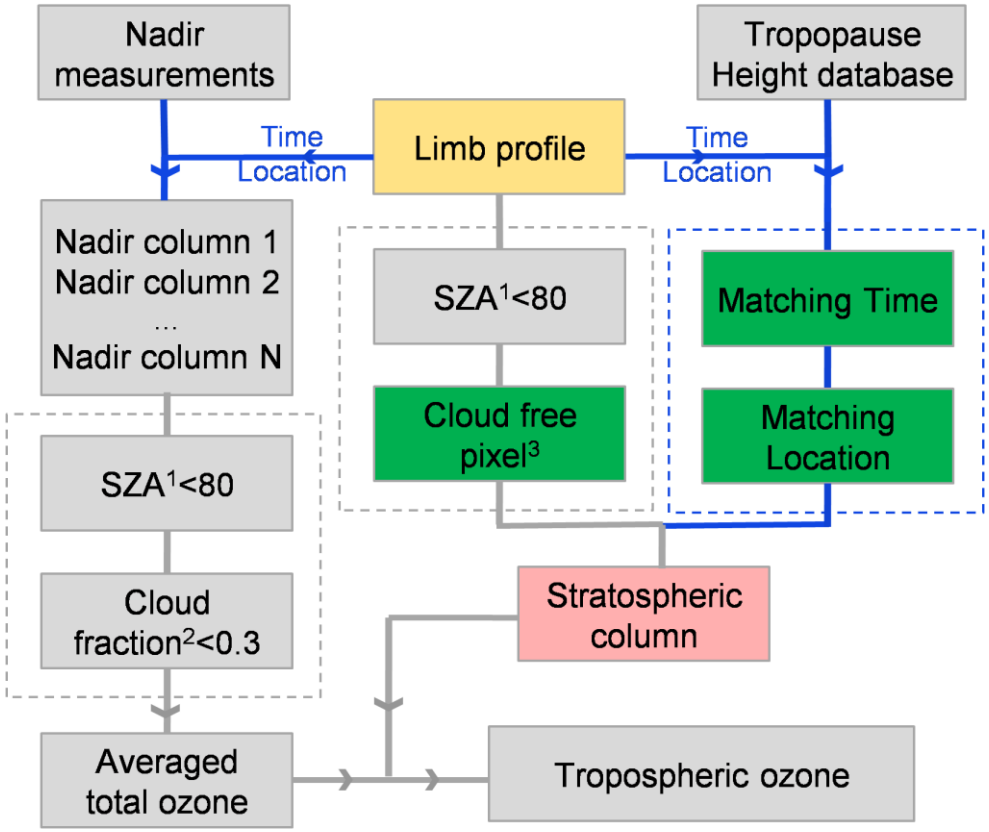

[1] SZA: solar zenith angle

[2] Cloud fraction: cloud coverage ratio in a pixel

[3] Cloud free: the relative CTH is lower than the tropopause height

Figure 5.4. Flow chart of calculating TOCs from SCIAMACHY measurements. Measurement quality control is shown in the dashed boxes. Collocation processes are marked in blue; changes from V1.0 to V1.1 are marked in green. Changes from V1.1 to V1.2 are marked in yellow.

80° is set in nadir data (Weber et al., 2005), and the limb data with SZA larger than 80° are eliminated according to the investigation.

5.2.2 Nadir-Limb, TPH-Limb collocation

The spatial collocation of the SCIAMACHY nadir and limb data is quite straight forward. For each limb measurement, the nadir pixels are matched by checking if the four corners of

the nadir scan are all inside the limb scan using the crossing number (CN) algorithm (Jordan, 1887). The CN method is further described in Ebojie (2014). The nadir measurements that are partially within the limb measurement are weighted based on the distance of its center to the nearest limb corner. After that, the nadir data that are confirmed to be totally or partially contained in the limb footprint are averaged to derive the corresponding total ozone column value. The temporal collocation between the nadir and limb data is achieved by selecting the measurements from the same orbit.

The method to determine the TPH from each Limb measurement used in V1.0 of the tropospheric ozone retrieval is illustrated in Fig. 5.5. The collocation is carried out at four corners C1, C2, C3 and C4 of the limb pixel. The global gridded TPH data retrieved from ECMWF P/T/wind information are provided at 00, 06, 12 and 18 UTC each day. At each corner of the limb pixel, the TPH grid that contains the geolocation of the corner is chosen at the four (00, 06, 12 and 18) UTC time (marked as black stars). Among the four chosen data, the one from the UTC time that is nearest to the SCIAMACHY local passing time (blue dot) is chosen as the corresponding TPH value for the corner (marked in red). The collocated TPH for the particular limb measurement is eventually defined as the minimum value of the four corners.

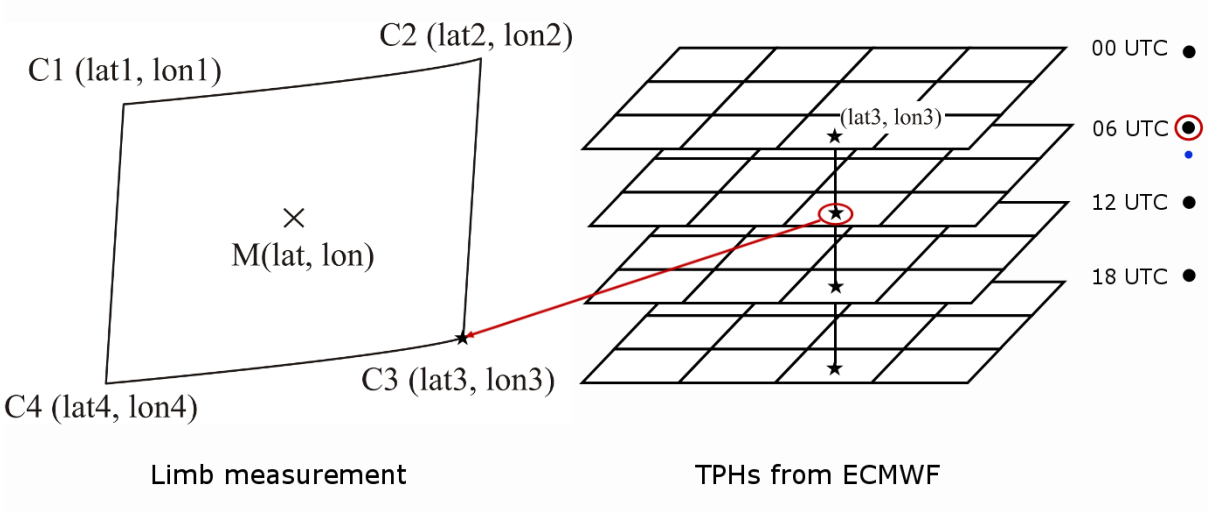

Figure 5.5. Sketch of the TPH-Limb collocation for V1.0. The blue dot in between 06 UTC and 12 UTC represents the overpass time of SCIAMACHY during the measurement.

5.2.3 Calculating stratospheric ozone columns

The SCIAMACHY limb ozone retrieval is sensitive down to approximately 12 km and provides profile data between 10 and 80 km (Sect. 4.2). When calculating the stratospheric ozone columns, the limb ozone profiles are first interpolated (TPH>10km) or linearly extrapolated (TPH<10 km) to the corresponding TPH. In the next step, the stratospheric ozone column is convolved as follows:

$$C_{strato} = \sum_{i_{tph}+1}^{i=80} \left(\frac{N(Z_{i-1}) + N(Z_i)}{2} \right) (Z_i - Z_{i-1}) . \qquad (5\text{-}1)$$

where N(z) is the stratospheric ozone profile in number density, z represents the altitude and i is the layer index. Eventually TOCs are retrieved by subtracting calculated stratospheric ozone columns from the averaged total columns.

5.3 Data amount improvement

As it is already mentioned in Sect. 5.1, the V1.0 database shows a severe lack of data over the tropics and high latitudes in the 7-year data set (left panel of Fig. 5.2). This shortage can also be clearly observed in the monthly tropospheric ozone results (Fig. 5.7). One could argue that this pattern is expected because these data-lack areas have high cloud-covering percentage thus more nadir data would be rejected. However, the screening analysis showed that the cloud screening in the limb data plays a key role in controlling the data amount compared to the cloud screening in the nadir data. To maximize the global coverage of the monthly data, it is quite important to avoid overly strict limb data screening criteria during the retrieval.

As is mentioned, a limb measurement is defined to be 'clean' when the TPH is higher than the CTH. The CTH used in V1.0 was derived from the cloud flag information contained in the limb data set. This information is retrieved by using the SCODA database (Sect. 4.2). However, the cloud flags in the limb data set mark the altitudes which are potentially affected by the clouds rather than cloud heights themselves. Because of a vertical interpolation used in the retrieval, a cloud might affect also vertical layers above its top height, resulting in a cloud flagging of some altitude layers above the CTH as well. Using cloud flag to determine the CTH in the previous study done by Ebojie et al. (2014) caused a positive bias of ~3.3 km

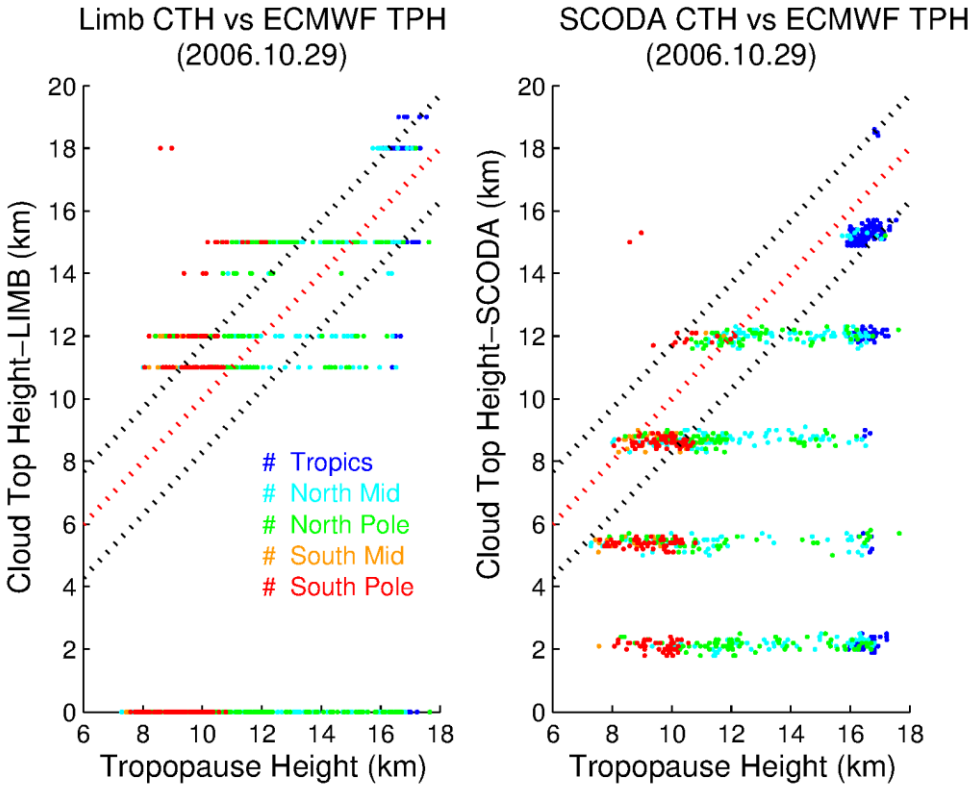

Figure 5.6. Comparison between ECMWF TPH and: (left) limb cloud flagging height, (right) SCODA CTH in 29 October 2006. All the data on the upper left side of the red dotted line were rejected according to the data screening criteria. The tropics is defined as 20°S-20°N, North/South Mid as 20-50°N/S, and North/South Pole as 50-90°N/S. *Figure provided by K. Eichmann from University of Bremen*.

compared to the real SCODA CTH. This difference can be observed in the comparison with TPH from ECMWF (Fig. 5.6) and causes over 50% of the limb data being eliminated by using the limb cloud flag information as a threshold.

In the new (V1.1 and V1.2) retrieval algorithms, the original SCODA CTH information is used to avoid the overly strict data screening. After this change, a double amount of the data is retrieved (right panels of Fig. 5.7). The data quality is quickly examined with the mean standard deviations before and after the change (lower panels of Fig. 5.7). The mean standard deviation is calculated as follows:

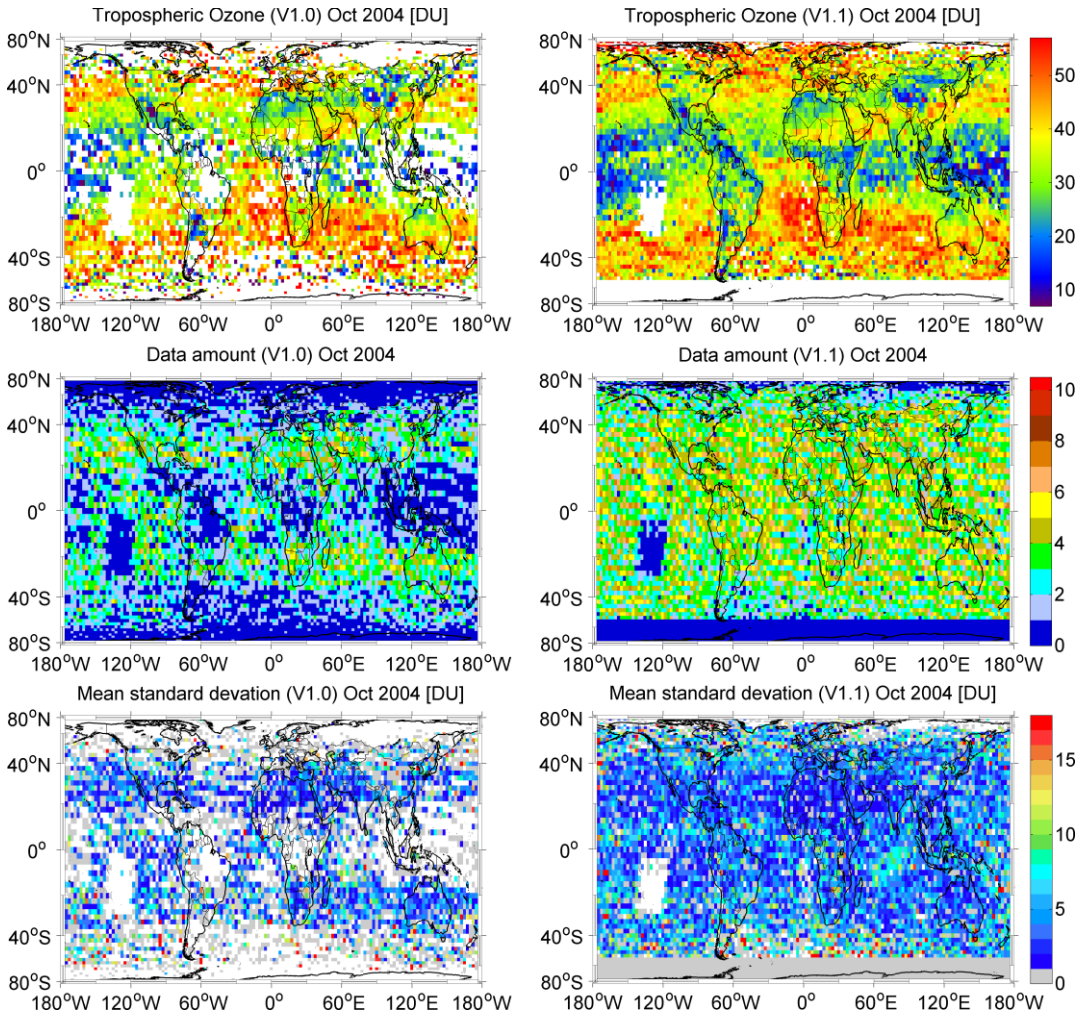

Figure 5.7. 2.5°× 2.5° gridded monthly results from V1.0 (left panels) and V1.1 (right panels) in October 2004. From top to bottom are: TOCs, the data amount included in averaging, and the mean standard deviations of the TOCs.

$$\sigma_m = \sigma / \sqrt{N} \,. \qquad (5\text{-}2)$$

where σ is the standard deviation of the sample measurements located in one grid cell and N is the sample size. In this term the variances are weighted by their respective sample sizes before taking the square root, so that the standard deviations with different sample sizes are comparable. The ±2 DU differences between the highest and lowest values in the mean stan-

dard deviations are determined in both V1.0 and V1.1 data. The quantitative validation results using ozonesonde TOCs are presented in Sect. 5.6.

5.4 TPH optimization

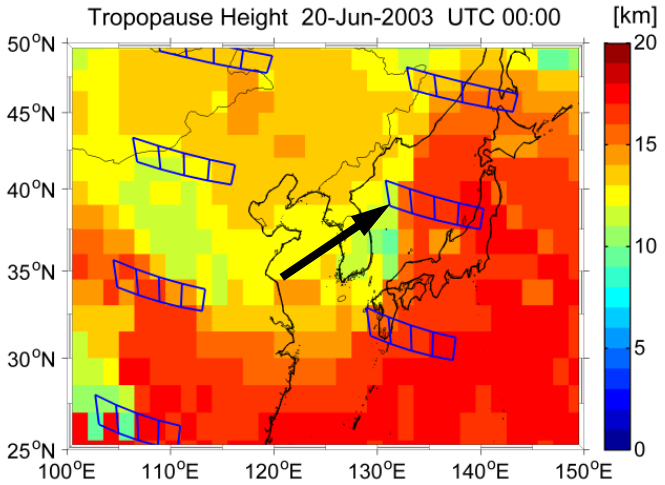

Figure 5.8. Regional tropopause height and SCIAMACHY limb swath geo-locations on 20 June 2003.

Stratospheric ozone is mostly located in the lower stratosphere. A small change in the TPH would cause a non-negligible change in the Limb-Nadir Matching retrieved TOCs. The TPH induced error was reported to be ~0.1 DU (Ebojie et al., 2014). Compared to this value, the TPH induced TOC variances reported in this study are ~3 DU (Fig. 5.10). This is possibly because the former error was calculated with the TPH increased or decreased by 500 meters (F. Ebojie, personal communication). In reality, the variation of the TPH is much higher than 500 meters both temporally and spatially, especially in the midlatitudes, where the variation is often more than 1 km within a short horizontal distance. Figure 5.8 shows an example. Within the footprint of a limb measurement (pointed with arrow), the ECMWF TPH changes from 11 km to 15 km. Therefore the TPH optimization is necessary.

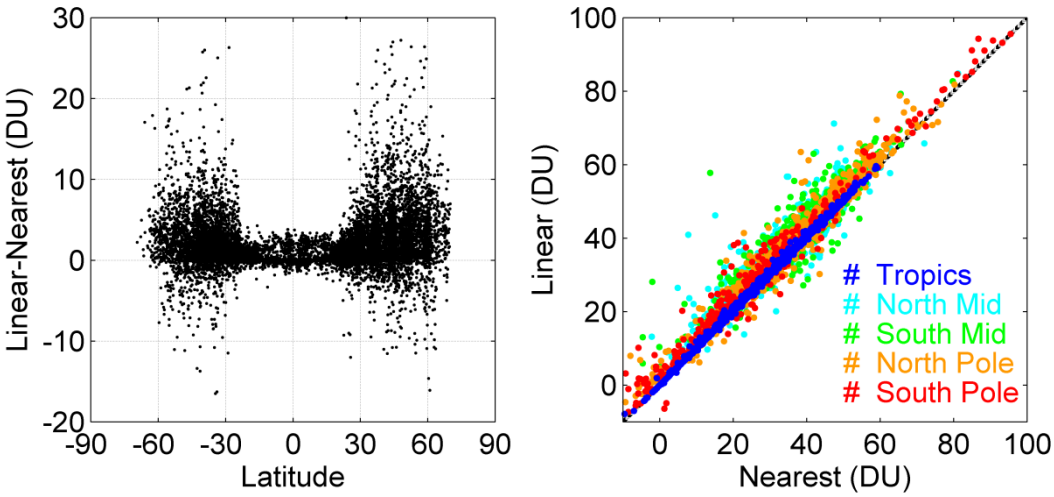

Figure 5.9. Tropospheric ozone column changes by using TPH from 'Nearest' scenario and from 'Linear' scenario for all the measurements in September 2002. Left panel showed the differences along with latitude for each measurement; right panel presented the scatter plot of the ozone values after 2.5° x 2.5° gridding.

The TPH-Limb collocation performed in V1.0 is described in Sect. 5.2.2. In V1.1 and V1.2, the TPH-Limb collocation methodology is optimized both temporally and spatially. At each corner of the limb swath, the TPH is derived by linearly interpolate the 4 UTC corresponded TPHs to the SCIMACHY overpass time, instead of by choosing the nearest neighbour. The SCIAMACHY overpass UTC time is obtained from the limb ozone profile.

Figure 5.9 shows the differences of the retrieved TOCs before/after the TPH temporal optimization. In general, the TPHs retrieved from the 'nearest' scenario are underestimated. The underestimation for single measurements (left panel) can easily reach 10 DU in the midlatitudes. The influence is smaller ($\pm$ 2 DU) in the tropics, but is still much higher than previously reported. The influences to the final monthly gridded TOC data set is shown as well (right panel). As is consistent with the single measurement results, the tropical value changed +1~2 DU. The differences in the mid-/high latitudes are more diverged. In most grid cells the differences are within 4 DU, while in 1/3 of the grid cells the changes are more than 7 DU.

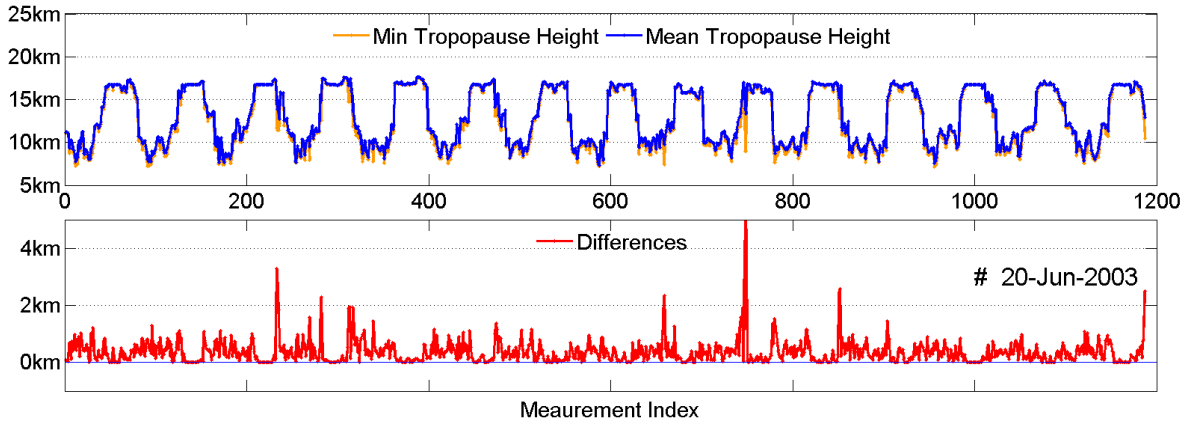

Figure 5.10. Differences between the minimum TPH and the averaged TPH at 14 orbits in 20 June 2003. In each orbit the measurement starts at northern high latitudes.

In V1.1 and V1.2 retrievals, the corresponding TPH for each limb measurement is defined as the mean value of the four corners instead of the minimum value as in V1.0, to avoid the influence of the sudden TPH change in a short distance. The TPH differences between the 'minimum' and 'mean' scenarios are on average less than 1 km with several over 2 km spikes (Fig. 5.10).

The total TPH differences before and after the temporal and spatial optimizations are shown in Fig. 5.11. The optimized TPHs are in general higher than the old ones by averaging the TPHs derived at 4 corners of the limb swath. The differences turn out to be larger with lower tropopause height (<10 km). The differences are also larger in midlatitudes than in other regions. The averaged changes of TPHs in the northern midlatitudes are ~1 km more than the ones in the southern midlatitudes.

5.5 Limb data improvement *

In this section the vertical ozone profiles retrieved from SCIAMACHY limb measurements at IUP Bremen are discussed. The error budget typical for the limb ozone V2.5 data set was reported by Rahpoe et al. (2013). Previous validation activities done by Mieruch et al. (2012)

* This subsection has been previously published as part of Jia et al. (2015).

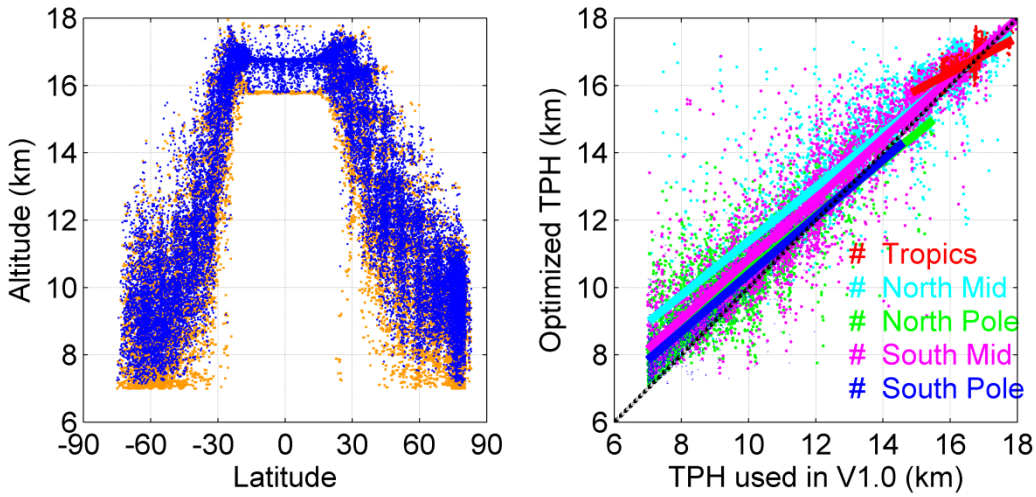

Figure 5.11. Differences between the TPHs used in the measurements of V1.0 and newer versions in September 2002. Left panel shows the TPHs used in V1.0 (orange dots) and the optimized TPHs (blue dots) along the latitude. Right panel is the scatter plot of the TPHs. The tropics is defined as 20°S-20°N, North/South Mid as 20-50°N/S, and North/South Pole as 50-90°N/S.

with respect to other satellite instruments showed an agreement of better than 10% and often within 5% between 20 km and 50 km, with a high bias below 20 km explained by the presence of high convective clouds. Tegtmeier et al. (2013) performed an intercomparison of vertically resolved monthly zonal mean ozone climatologies from 18 limb-viewing satellite instruments operated between 1978 and 2010, including SCIAMACHY observations. The agreement was within 5% in the middle stratosphere. The climatologies derived from SCIAMACHY were found to show a positive bias of up to +10% in the tropical and midlatitude upper stratosphere (5-1 hPa).

The current SCIAMACHY data set distributed by IUP Bremen is V2.9. The comparisons of this data set to ozonesondes showed a systematic negative bias of up to ~15% of the ozone concentrations between 15 km and 30 km in the northern high latitudes. The reason for that is believed to be the instrumental stray light occurring at small relative azimuth angles (sun is

close to the instrument field of view) typical for the measurements at high northern latitudes. To eliminate the observed negative bias, a new version of SCIAMACHY ozone limb data, V3.0, has been developed. As demonstrated by the validation with ozonesonde measurements, significant improvements have been achieved.

In this section, we present a systematic study of the limb data quality. The validation results comprising 10 years of SCIAMACHY limb data of versions V2.9 and V3.0 using globally distributed data from ozonesonde are presented. The limb partial-columns are used for tropospheric ozone Limb-Nadir Matching retrieval. Therefore, the results of partial-column comparisons are presented. Apart from partial column comparisons, the vertical accuracy of the limb ozone concentrations from both versions is investigated. The retrieval of V3.5 is still in process thus is only briefly introduced. In Sect. 5.5.1 and Sect. 5.5.2 the algorithms used and the limitations of both SCIAMACHY limb V2.9 and V3.0 retrievals are discussed. The methodologies of the limb-sonde comparisons are presented in Sect. 5.5.3. In Sect. 5.5.4 the statistical analysis of the pole-to-pole comparison results of V2.9 and V3.0 is shown, discussed and summarized. In Sect. 5.5.5, the up-coming V3.5 is briefly introduced. The conclusion and outlooks about the limb data are given in Sect. 5.5.5 and Sect. 5.5.6, respectively. The comparisons of SCIAMACHY V2.9 profiles with other satellite data sets have also been studied. The results are further described in Rahpoe et al. (2015) and will not be discussed here.

5.5.1 SCIAMACHY limb V2.9 retrieval algorithm

The current SCIAMACHY limb retrieval (V2.9) uses combined spectral information from the UV and visible spectral ranges to obtain vertical profiles of ozone (Flittner et al., 2000; Rohen et al. 2006). As the first step, the limb spectral radiances are integrated in ± 1 nm intervals around the central points. Then they are normalized with a limb measurement at an upper tangent height (often referred to as the reference tangent height): $I_n(\lambda, TH_i) = I(\lambda, TH_i)/I(\lambda, TH_{ref})$, with λ denoting wavelength and TH_i the tangent height at the elevation step i. The normalization removes the solar Fraunhofer structures and reduces the influence of the lower atmosphere, e.g. due to multiple scattering and reflection from the surface. Furthermore, it provides a kind of self-calibration of the instrument since the instrument calibration parameters do not differ much for different tangent heights. In the visible spectral range, the so-called triplet method (Flittner et al., 2000) is used subsequently to minimize the influence of

the broad-band spectral features, e.g., Rayleigh and aerosol scattering. In this way the measurement vector, y, is obtained from the normalized radiances at 525 nm, 589 nm and 675 nm as follows:

$$y(TH_i) = \ln\left(I_n(589nm, TH_i)\right) - \frac{1}{2}\left[\ln\left(I_n(525nm, TH_i)\right) + \ln\left(I_n(675nm, TH_i)\right)\right]. \quad (5\text{-}3)$$

Note that the central wavelength was at 600 nm (center of the Chappuis band) in the original triplet method. It is moved to 589 nm because of large calibration uncertainties near the boundary of SCIAMACHY channel 3 related to the dichroic mirror.

In the UV spectral range the method described by Rohen et al. (2006) is used. The measurement vector, y, is obtained from the normalized limb radiance profiles at eight single wavelengths (264, 267.5, 273, 283, 286, 288, 290.5, and 305 nm) with ± 1 nm spectral integration (Sonkaew et al., 2009). These wavelengths are chosen to avoid strong Fraunhofer lines and terrestrial airglow emissions. The SCIAMACHY limb ozone profiles are then retrieved by using a nonlinear inversion scheme with the first-order Tikhonov regularization (Rozanov et al., 2011). The relative change in the ozone concentrations with respect to a priori is retrieved. The forward modelling is done with the radiative transfer model SCIATRAN (Rozanov et al., 2014). In the V2.9 retrieval, the ECSTRA (Extinction Coefficient for STRatospheric Aerosol; Fussen et al., 1999) aerosol database was used in the model; the surface albedo was from Matthews (1983). The lowest and highest tangent heights used during the retrieval are around 12 km and 71 km, respectively.

5.5.2 SCIAMACHY limb V3.0 retrieval algorithm

In V3.0 retrieval approach, the extraterrestrial solar spectrum measured once per orbit by the SCIAMACHY instrument is used instead of the reference tangent height to normalize the measured limb radiances. The differential structure of the ozone absorption signature in the short-wavelength wing of the Chappuis absorption band is exploited, and the DOAS technique (differential optical absorption spectroscopy; Platt, 1994) is employed to retrieve the ozone vertical profiles instead of the computationally highly efficient triplet method. These two changes were carried out simultaneously because:

1. the short- and long-wavelength wings of the Chappuis absorption band are measured in different spectral channels of the SCIAMACHY instrument (see Sect. 2.4.2) and

usage of the whole Chappuis band in combination with the solar spectrum normalization requires a very high quality of the inter-channel calibration;

2. the signal-to-noise ratio (SNR) decreases with increasing tangent height. Normalization using reference tangent height at high altitude will reduce the SNR at the corresponding tangent height. Because of the large SNR caused by using the whole Chappuis band, the signal is sufficient when the reference tangent height is used. However, differential structure in channel 3 suffers from very low SNR, so this influence is much larger when used without the solar normalization.

Differential limb spectra are obtained as

$$y = \ln\left(I\left(\lambda_L, TH_i\right)\right) - P_n, \tag{5-4}$$

where I is the sun-normalized radiance and P_n is a polynomial of order n (cubic in our case) in λ, whose coefficients are obtained by fitting the logarithms of the normalized limb radiance in the wavelength domain for each tangent height independently. A shift-and-squeeze correction as well as scaling factors for Ring and water vapour absorption spectra are determined at each tangent height. The shift-and-squeeze correction is done with respect to the limb-measured spectrum for both the modelled spectra and the measurement at the reference tangent height (Rozanov et al., 2005).

Since the differential absorption structure of ozone in the short-wavelength wing of the Chappuis absorption band is significantly weaker than the differences of the absorption between the three wavelength used in the triplet Chappuis band, the influence of interfering weaker absorbers, namely – NO_2 and O_4, needs to be taken into account. The weighting function of the surface albedo is also included in the fit. The aerosol extinction coefficients retrieved from SCIAMACHY limb measurements (Ernst et al., 2012) are used in the forward model. The mathematical inversion then proceeds in a manner similar to that used in the V2.9 retrieval (Rozanov et al., 2007). In the V3.0 retrieval approach, the full spectrum of the UV band (229-306) with a zero-order polynomial is used instead of the selected wavelengths as in V2.9. This however does not play any role in the comparison with the vertical profile of ozone from ozonesondes discussed in this manuscript as the information from the UV range does not have any significant influence on the retrieved ozone values below 30 km (influence above ~35 km). The lowest and highest tangent heights used during this retrieval are around 8 km and 65 km, respectively.

5.5.3 Validation methodologies

To validate the scientific ozone profiles retrieved from SCIAMACHY limb measurements, ozonesonde data from WOUDC stations are used (Sect. 4.4). In order to select a reliable reference data set, only stations that have delivered more than 30 measurements between Jan 2003 and Dec 2012 are selected for the comparisons. Coincident SCIAMACHY limb profiles are selected for each ozonesonde profile. The geographic distance between the ozonesonde station and the footprint centre of the collocated SCIAMACHY measurement is required to be within 5° in latitude and 10° in longitude. The time difference between ozonesonde and collocated SCIAMACHY measurements should not exceed 24h. The coincident limb profiles having a solar zenith angle larger than 80° are rejected. In general, an altitude range between 15 km - 30 km is selected for the partial-column comparison. This choice is motivated by larger uncertainties of the current limb retrievals below 15 km and increasing uncertainty in the ozonesonde data above 30 km. The latter is mostly caused by the decaying pump efficiency at lower pressures (Johnson et al., 2002).

5.5.3.1 Vertical profile comparisons

Convolution of ozonesonde data

Satellite data have a much coarser vertical resolution compared to the ozonesondes. To make a quantitative comparison, the ozonesonde data are degraded to the vertical resolution of the satellite data. To this end the a priori profiles and the rows of the averaging kernels from the SCIAMACHY retrieval are resampled to the vertical grid of the sonde data. The elements of the resampled a priori profiles and averaging kernels are denoted as A_{ij} and X_{aj}, respectively. The low-resolution ozonesonde profiles are obtained then as follows:

$$X_{si} = X_{ai} \cdot \left(\sum_j \Delta Z_j \right)^{-1} \cdot \sum_j A_{ij} \cdot \frac{X_{sj} - X_{aj}}{X_{aj}} \cdot \Delta Z_j + X_{ai}, \qquad (5\text{-}5)$$

where i represents the satellite coarse grid, and j the fine grid of the ozonesonde; ΔZ_j is the altitude interval, i.e., a halfway distance between the layers above and below j. Note that the altitude information existed in ozonesondes is the geopotential height, while in SCIAMACHY measurements they are the geometric height. Therefore before any validation, the ozonesondes geopotential height needs to be converted to the geometric height.

Layer selection criteria

Two criteria were defined to screen proper vertical layers before the comparisons. Firstly, all averaging kernels used for the convolution (see Eq. 5-7) must not have significant nonzero elements above the maximum height of the corresponding ozonesonde measurement. Due to a coarser altitude grid in V3.0, a wider vertical range is rejected when excluding one altitude level, which results in a different upper altitude range in Fig. 5.12. Secondly, all layers below the CTH, as detected by the SCODA algorithm, are rejected; altitude grid points where the resulting vertical resolution is higher than 6 km are also not considered. Since the vertical resolution is different between the two versions, some differences in the altitude range are expected.

V3.0 profiles are retrieved at the measurement grid, which varies depending on the location and time. To obtain a common altitude grid for the mean profile, all altitude levels which belong to a certain elevation step are averaged over the whole measurement time (Jan 2003 to Dec 2011). Then each single profile is interpolated to the average altitude grid in each layer. At each layer the selected ozone profiles are averaged, denoted as $\overline{C_{SCIA}}$ and $\overline{C_{ref}}$. The relative mean difference at each layer is calculated as

$$D = \frac{\overline{C_{SCIA}} - \overline{C_{ref}}}{\overline{C_{ref}}} \times 100\% . \tag{5-6}$$

The corresponding standard deviation of the differences is given by

$$Dev = \sqrt{\frac{1}{k-1}\sum_{i=1}^{k}\left(AC(i) - \overline{AC}(i)\right)^2} \times 100\% . \tag{5-7}$$

where k is the number of profiles included in the comparison and

$$AC(i) = \left(C_{SCIA}(i) - C_{ref}(i)\right) / \overline{C_{ref}} . \tag{5-8}$$

$$\overline{AC}(i) = D = \frac{1}{k}\sum_{i=1}^{k} AC(i) . \tag{5-9}$$

5.5.3.2 Partial-column comparisons

In addition to the vertical profile comparison, both SCIAMACHY limb ozone data and original ozonesonde measurements are integrated and compared as the stratospheric partial ozone columns (hereafter SC). For each individual pair of SCIAMACHY-sonde profiles, the integration is started either from the first cloud-free level of SCIAMACHY limb data or from 15 km, whichever is higher, and ended at either the ozonesonde explosion position or at 30 km, whichever is lower:

$$C_{strato} = \sum_{i_{tph}}^{i=H_{\max}} \left(\frac{N(Z_{i-1}) + N(Z_i)}{2} \right) (Z_i - Z_{i-1}) \cdot \qquad (5\text{-}10)$$

where C_{strato} refers to an individual SC, $N(z)$ is the stratospheric ozone profile in number density units (mol/cm^3), z_i represents the altitude in kilometers and i is the layer index.

5.5.4 Results and discussion

5.5.4.1 Vertical profile comparison results for V2.9 and V3.0

Average vertical profiles from the coincident SCIAMACHY and ozonesonde measurements at the six selected stations for the period Jan 2003-Dec 2011 are compared in Fig. 5.12. The stations Nairobi, Ankara, Praha, Eureka, Lauder and Marambio are chosen as representatives of the latitude bins 20°S-20°N, 20-40°N, 40-60°N, 60-90°N, 20-60°S, 60-90°S, respectively. The panels represent the results of V2.9 on the left-hand side and of V3.0 on the right-hand side. For each station, the vertical comparisons are shown as vertical profiles (left panels) and relative mean differences (right panels). The number densities for both sonde and SCIAMACHY limb data at each layer are obtained by averaging the filtered data (see Sect. 5.5.3.1) over the entire time period. At Nairobi, V2.9 agrees with ozonesonde results to within 3% for most cases below 30 km. There are good agreements at Ankara, Lauder and Marambio with usually less than 5% relative differences. The differences become larger at Lauder below 18 km. A negative bias shows up at Praha and becomes stronger at Eureka, which has a higher latitude (Fig. 5.12). Furthermore, the relative differences at these latitudes exhibit vertical oscillations of about 3% amplitude. The maxima of the relative differences are seen at around 22 km and 28 km. The oscillations are most probably caused by the fact that the radiance profiles, sampled by the SCIAMACHY instrument at different tangent heights, are not exactly

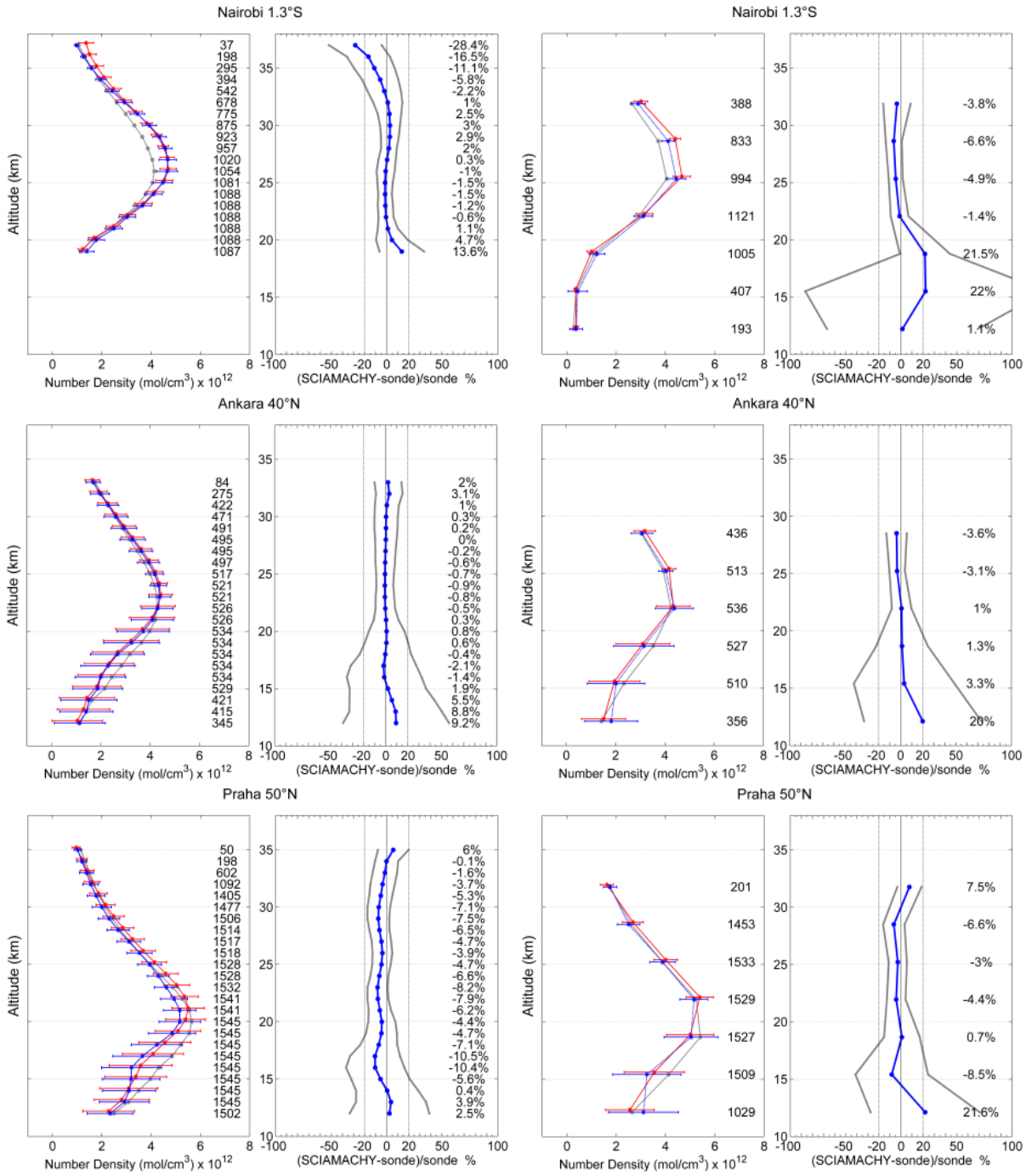
Nairobi 1.3°S
Nairobi 1.3°S
Ankara 40°N
Ankara 40°N
Praha 50°N
Praha 50°N
Altitude (km)
Number Density (mol/cm3) x 10^12
(SCIAMACHY-sonde)/sonde %

Figure 5.12.

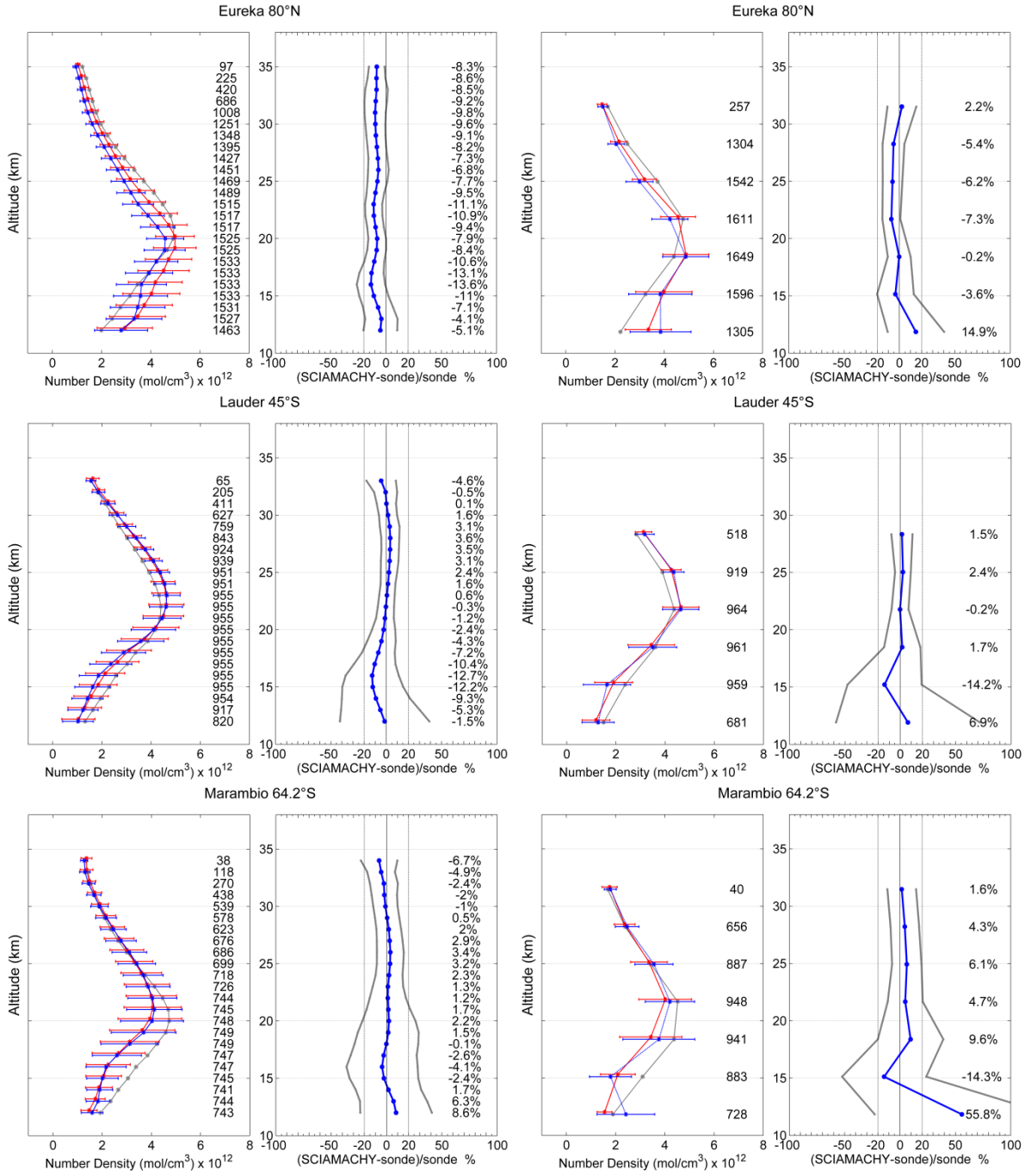

Figure 5.12. Vertical profile comparisons at Nairobi (1.2°N 36.8°E), Ankara (40.0°N 32.8°E), Praha (50.0°N 14.4°E), Eureka (80.0°N 85.9°W), Lauder (44.9°S 169.7°E) and Marambio (64.2°S 56.6°W) averaged from Jan 2003 to Dec 2012. The four panels show the results for the ozone profiles for V2.9 on the left-hand side and for V3.0 on the right-hand side. In the

left subpanels, the red and blue curves represent the ozone number densities with 1 sigma standard deviations for ozonesonde and SCIAMACHY limb data, respectively. The gray lines show a priori information used in the SCIAMACHY retrieval. In the right subpanels, the blue lines represent the relative mean differences of the ozone concentrations. The gray solid lines depict 1σ standard deviations. The numbers on the right denote the number of SCIAMACHY limb profiles used in the comparisons and the relative differences for each layer.

aligned vertically (Brinksma et al., 2006). At these latitudes, the horizontal variations of the stratospheric ozone are usually stronger as compared to other latitudes and thus the oscillations are more pronounced.

To give a global overview of the results, the altitude-versus-latitude cross sections of the relative differences for both versions are given in Fig. 5.13. They are calculated by contouring the relative mean differences between SCIAMACHY limb data and correlative sonde data at all considered sonde stations (61 stations in total). In general, the current V2.9 data well reproduce the ozone vertical distribution by following the shapes of ozonesonde data at each station (upper panel of Fig. 5.13). The relative differences between V2.9 and ozonesonde data are within 5% between 20 km - 30 km southward of 40° N. The good agreement seen at Nairobi holds for most of the cases in the tropical region. One exception is seen around the ozone peak altitude (~ 26 km) in the near-equatorial northern tropics. This overestimation can be clearly observed (see upper panel of Fig. 5.13) at Sepang Airport (Kuala Lumpur) and Hong Kong stations with more than 10% relative differences in the upper stratosphere (25 km to 30 km). In the middle and high southern latitudes, V2.9 still represents the ozone vertical distribution very well by agreeing with ozonesonde data to within 5%, which is consistent with the results of station Ankara, Lauder and Marambio in Fig. 5.12. In the Northern Hemisphere, this consistent agreement degrades northward of ~40° N, showing stronger underestimation with increasing latitude up to ~15%. The oscillations we see in Praha and Eureka in Fig. 5.12 can be observed, too.

The vertical profile comparison results from V3.0 data sets are presented in the lower panel of Fig. 5.13 in the same way as for V2.9. In comparison to the current V2.9 data sets, V3.0 shows similar retrieval quality in most of the cases, with the exception of a slightly worse

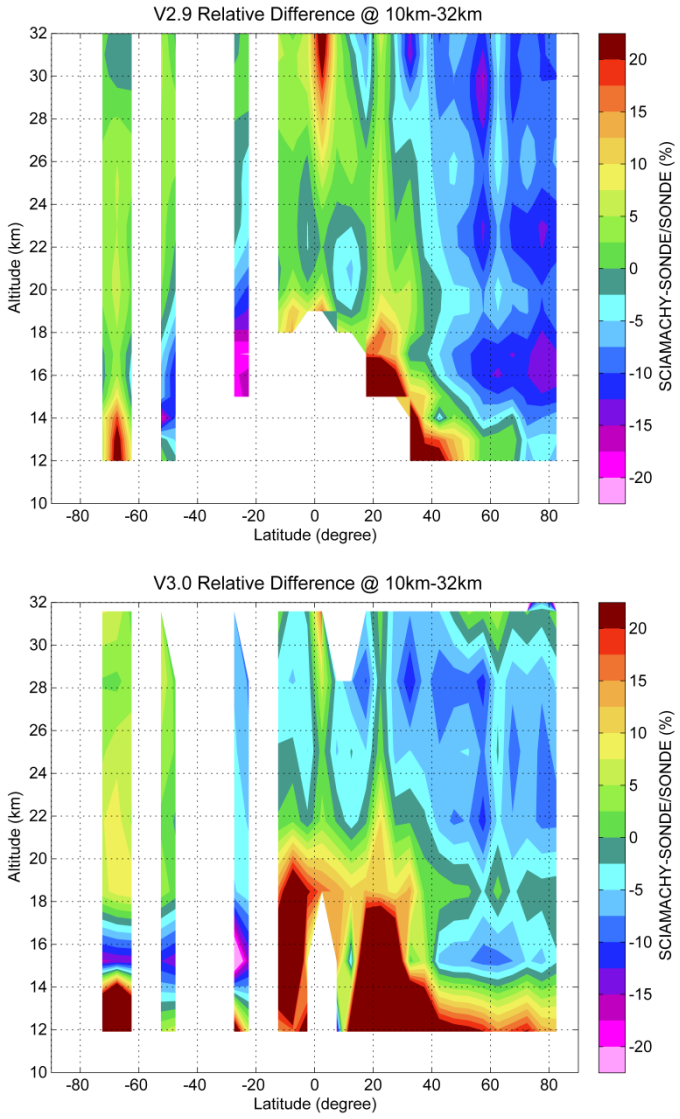

Figure 5.13. The altitude-versus-latitude cross section of the relative differences. V2.9 in the upper panel and V3.0 in the lower panel. The improvement is mainly in the Northern Hemispheric high latitudes.

agreement at Nairobi (shown in the panel of Fig. 5.12), while the overestimations over Southeast Asia (e.g., Kuala Lumpur, Hong Kong) in V2.9 are revised (Fig. 5.13). It is clearly seen that the ozone concentrations at middle and high northern latitudes, e.g., Praha and

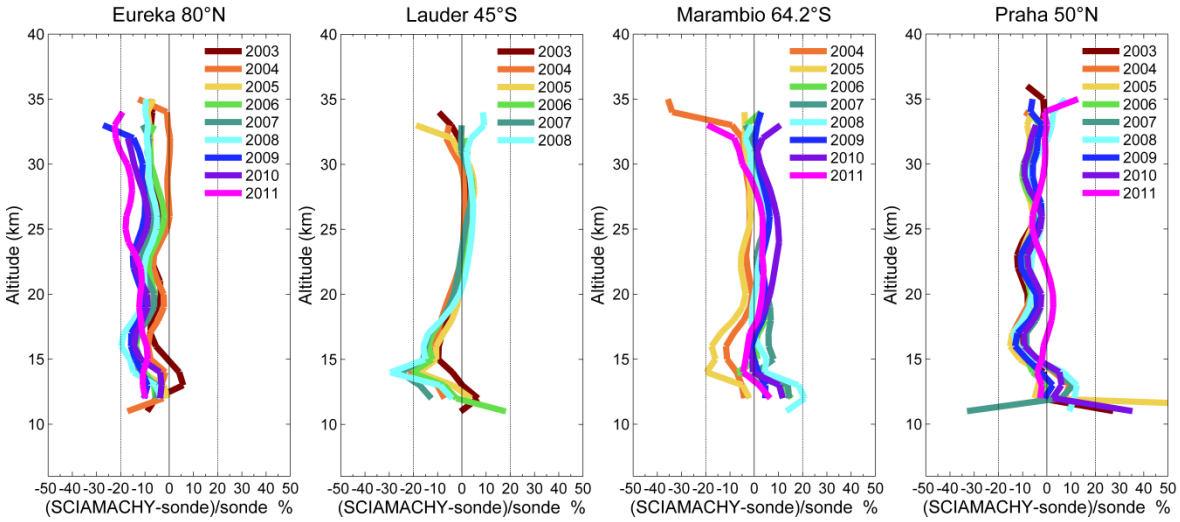

Figure 5.14. V2.9 yearly vertical profile comparisons of the relative differences between SCIAMACHY and ozonesondes at Eureka, Lauder, Marambio and Praha.

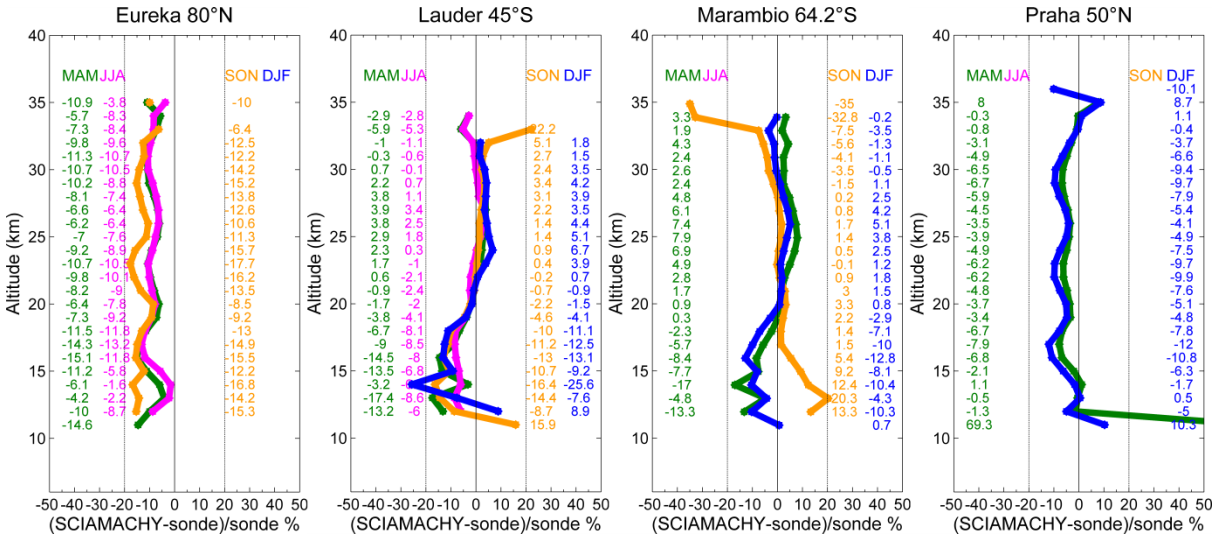

Figure 5.15. V2.9 seasonal vertical profile comparisons of the relative differences between SCIAMACHY and ozonesondes from 2003 to 2011 at Eureka, Lauder, Marambio and Praha. No/not enough corresponding measurements in DJF (December-January-February) for Eureka, in JJA (June-July-August) for Marambio and in JJA and SON (September-October-November) for Praha.

Eureka, are captured more accurately in V3.0 than in V2.9. For example, at Eureka the relative differences are reduced from ~13 to within 7.5%. The vertical oscillations can still be observed but are much weaker. V3.0 agrees with ozonesonde within 10% globally, with a significant improvement northwards of 40° N (Fig. 5.13). One exception remains below 18 km at southern high latitudes, where the relative differences vary strongly. The reasons for this strong uncertainty can be the dynamically instable troposphere.

Fig. 5.14 and 5.15 show annual and seasonal relative differences for V2.9, respectively. The relative mean differences at all tropical (not shown in the paper) and midlatitude stations don't have much dependence on the year of measurements. However, the relative differences drift from year to year at high latitudes of both hemispheres (see Fig. 5.14). The statistics of the seasonal behaviour is presented in Fig. 5.15. No obvious seasonal influence can be identified in this comparison. Since V3.0 has similar seasonal and yearly behaviour (apart from the reduced bias at Eureka and Praha) of the vertical profiles to that of V2.9, the results are not shown.

5.5.4.2 Partial-column comparison results for V2.9 and V3.0

In addition to the vertical profile comparison, the results of partial-column comparisons are presented in Figs. 5.16-5.18. Figure 5.16 depicts the time series of ozonesonde data sets (red dots), SCIAMACHY data sets (green dots) and their differences (blue dots) at Nairobi and Eureka. The ozone amounts are represented as daily averaged SCs in DU. The left panels represent the current V2.9, while the right ones represent the V3.0. Figs. 5.17-5.18 show the statistical results for the differences of SCs in DU between the ozonesonde and the SCIAMACHY data on a global scale. Fig. 5.17 shows a global overview of both absolute and relative averaged daily differences, while Fig. 5.18 presents scatterplots of the absolute differences for latitude bins. Note that the absolute differences in Fig. 5.17 are calculated as the averages of the daily mean SCs differences while in Fig. 5.18 each dot represents the absolute difference for a single collocation.

Similar conclusions to those for the vertical profile comparisons can be drawn from the partial-column comparisons. For the V2.9 data set, the seasonal variations in the time series agree well with those from sonde data (left panels of Fig. 5.16). The drift of relative differences with time that is mentioned in Sec. 5.5.4.1 can be observed also in Fig. 5.16 at Eureka.

So far there is no explanation about this drift. The agreement of daily mean differences is mostly within 5 DU southwards from 40° N. The overestimation in Southeast Asia observed in Fig. 5.13 corresponds to ~10 DU absolute differences as shown in Fig. 5.17. A general overestimation in the Pacific Ocean can also be observed. In the northern middle and high latitudes, a rapid decrease in the quality of the V2.9 ozone data results in, e.g., a median difference of 22 DU (over 10%) at Eureka. The underestimations are depicted by the purple and pink dots in Fig. 5.17 and amount to about ~13 DU in Europe and Canada and more than 20 DU in the high northern latitudes.

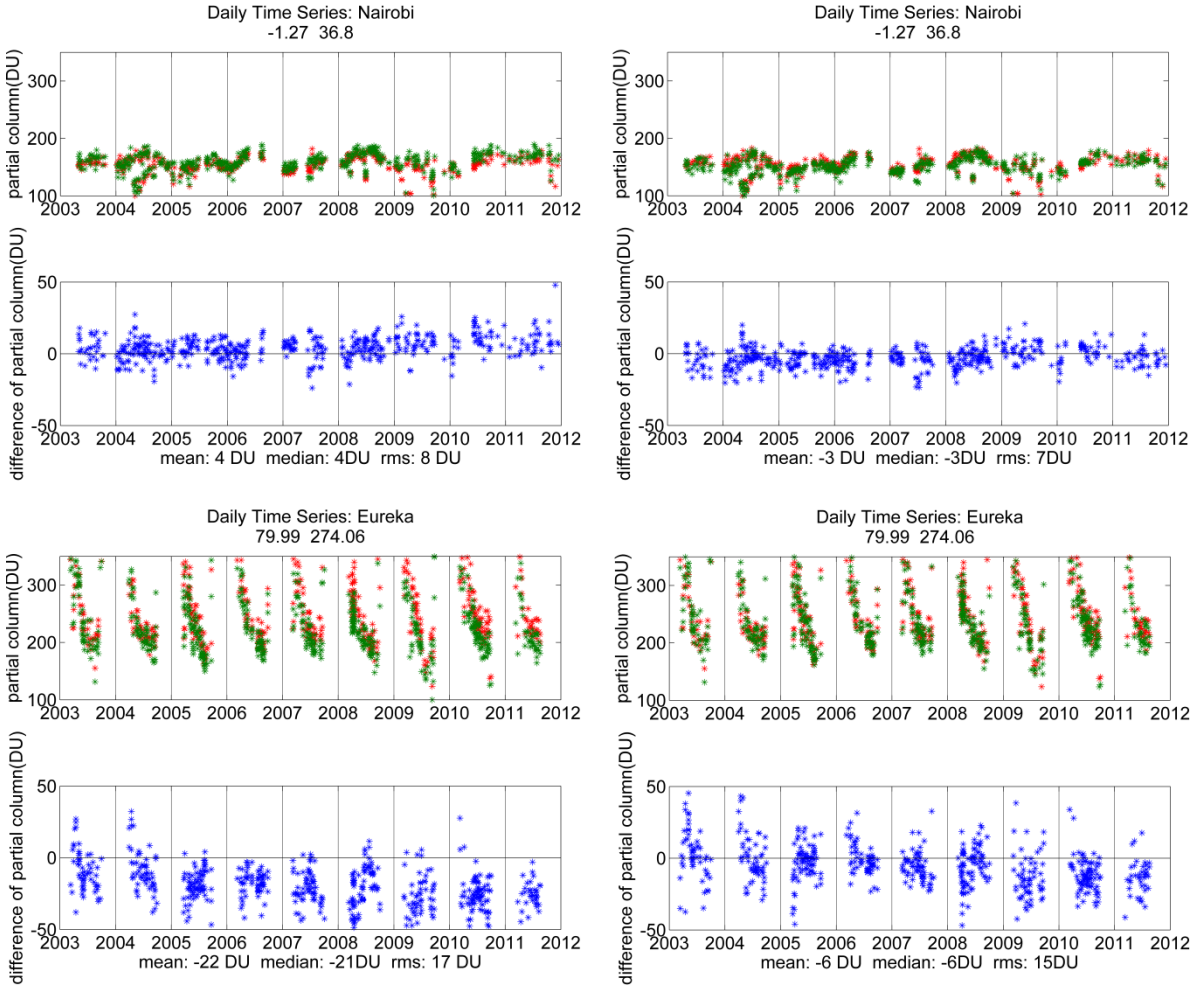

Figure 5.16. Time series of stratospheric ozone partial-columns from SCIAMACHY V2.9 and V3.0 (left and right panels, respectively) limb data (green), ozonesonde data (red) (upper panel) and their absolute difference in SCs (blue) in DU. The results are presented unsmoothed.

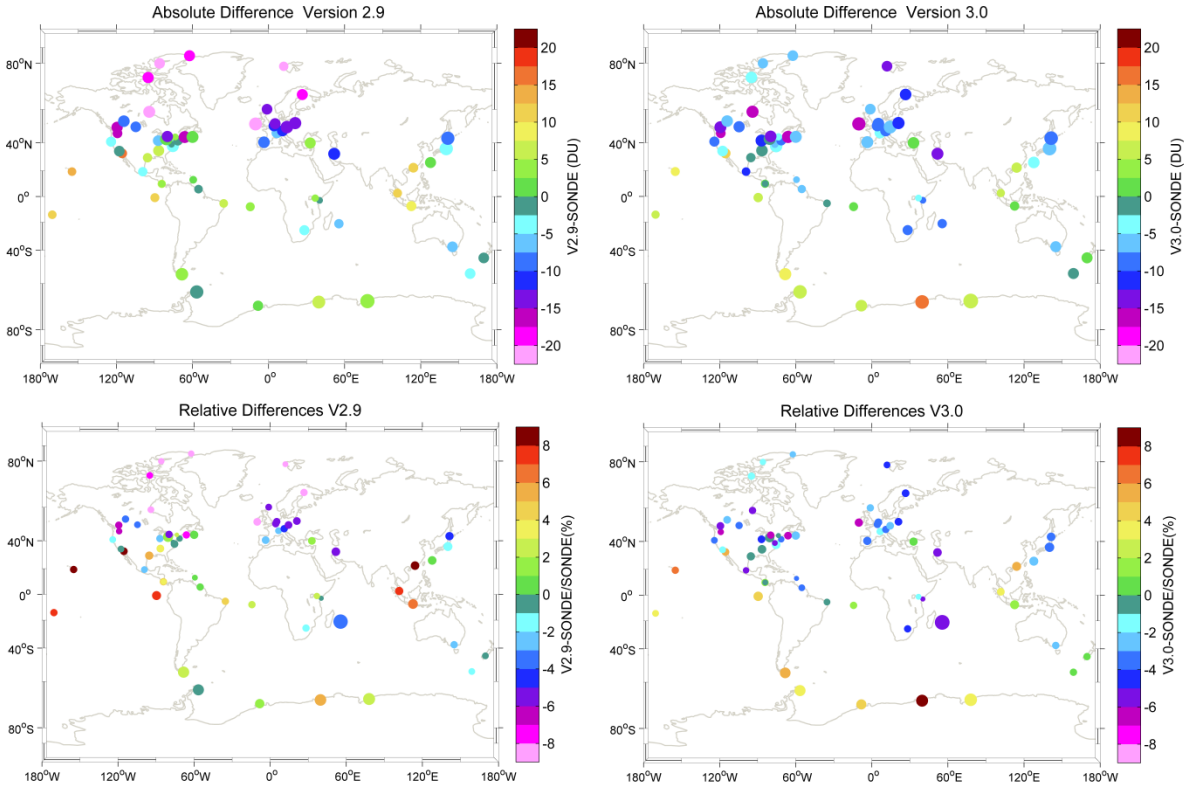

Figure 5.17. Comparison with all considered ozonesonde station data for the averaged daily differences in partial-columns over the entire time period. The upper panels are the absolute differences; The lower panels are the relative differences. In each panel, the color of the dots depicts the mean difference/relative mean difference, while the size of the dots represents 1σ standard deviation.

For V3.0, the seasonal variations in the time series are in good agreement with those from sonde data; at Eureka a median difference in partial-columns decreases by 16 DU to only 6 DU (right panel of Fig. 5.16). The improvement northwards of 40° N changes the color in Fig. 5.17 from purple-pink to blue. V3.0 also improved the partial-column accuracy at most tropical stations (10 out of 12 stations with abundant measurements) with a remarkable ~5% improvement from more than 8 to within 4% over the tropical Pacific region.

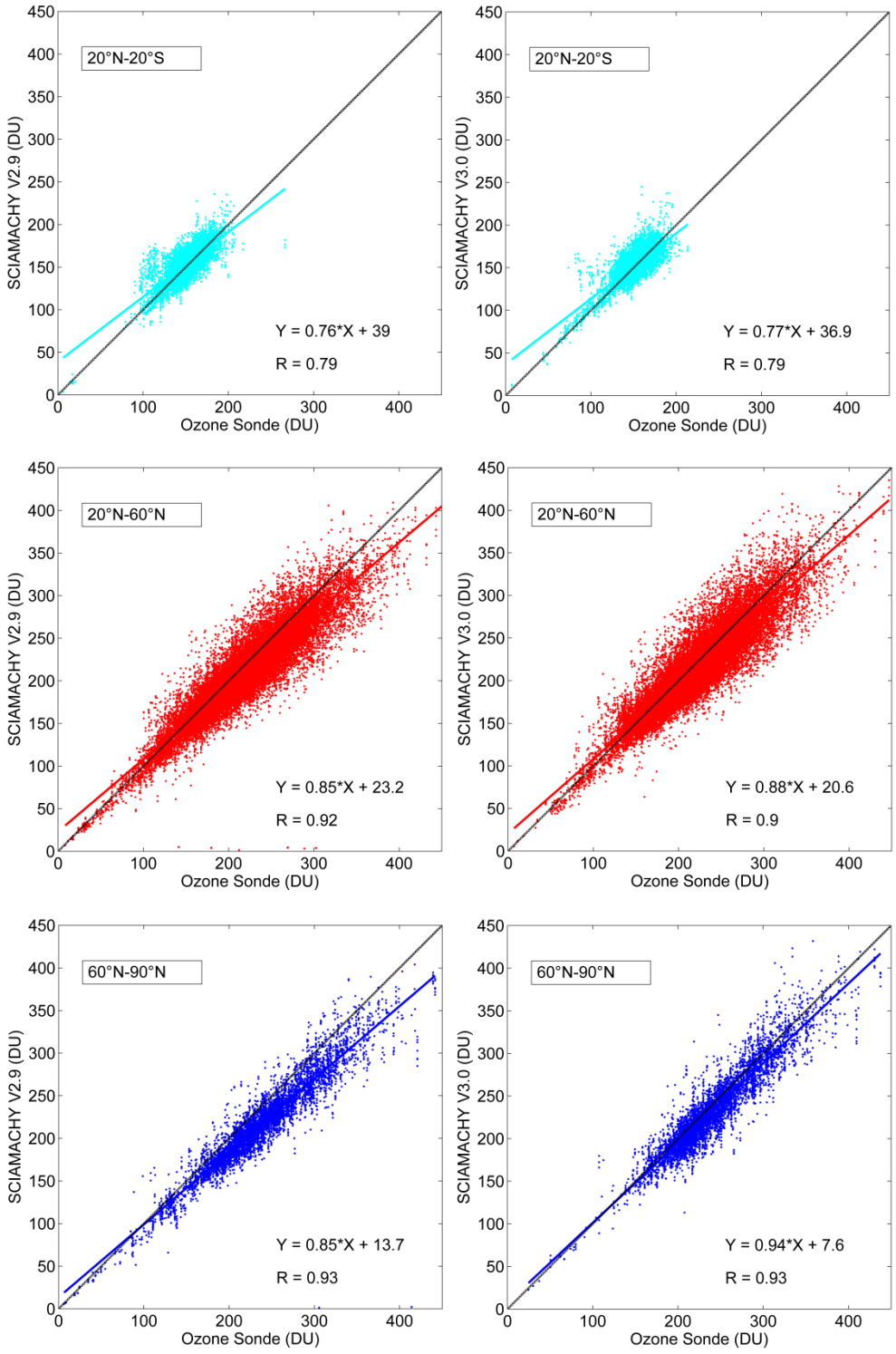
20°N-20°S
Y = 0.76*X + 39
R = 0.79
SCIAMACHY V2.9 (DU)
Ozone Sonde (DU)
20°N-20°S
Y = 0.77*X + 36.9
R = 0.79
SCIAMACHY V3.0 (DU)
Ozone Sonde (DU)
20°N-60°N
Y = 0.85*X + 23.2
R = 0.92
SCIAMACHY V2.9 (DU)
Ozone Sonde (DU)
20°N-60°N
Y = 0.88*X + 20.6
R = 0.9
SCIAMACHY V3.0 (DU)
Ozone Sonde (DU)
60°N-90°N
Y = 0.85*X + 13.7
R = 0.93
SCIAMACHY V2.9 (DU)
Ozone Sonde (DU)
60°N-90°N
Y = 0.94*X + 7.6
R = 0.93
SCIAMACHY V3.0 (DU)
Ozone Sonde (DU)

Figure 5.18.

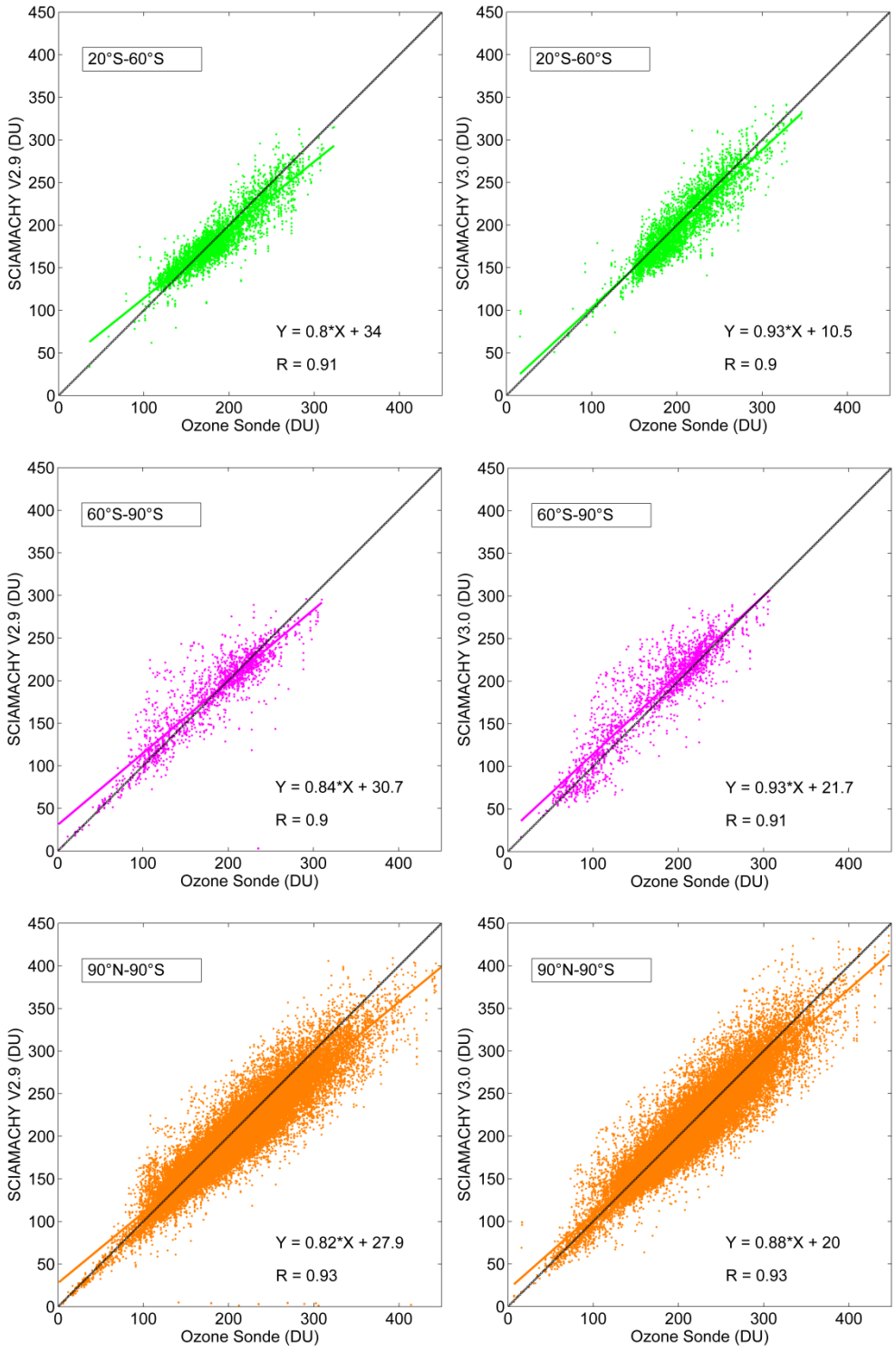

Figure 5.18. Scatter plots for the partial-columns from SCIAMACHY and ozonesonde data within 20°S-20°N, 20-60°N, 60-90°N, 20-60°S, 60-90°S and 90°S-90°N latitude bins. Left panels from V2.9; right panels from V3.0.

A global improvement can be observed in the statistical results for different latitude bins (Fig. 5.18), illustrating better retrieval results for each single measurement. A striking improvement is seen in the high-latitude bin (60-90°N). With an improved linear slope of 0.94 vs. 0.85 and smaller standard deviation of σ = 7.4 DU vs. 13.7 DU, the V3.0 data set exhibits a much better agreement with ozonesonde data at northern high latitudes. At the same time, the correlations at other latitude bins also become higher in varying degrees. A very strong improvement can be observed also in southern midlatitudes (Fig. 5.18). Due to the relatively low and centred ozone partial-column, a smaller correlation is obtained in the tropics for both versions.

5.5.4.3 Discussions

The reasons for the underestimation found in V2.9 limb ozone data at higher latitudes can be identified by analyzing the left panel of Fig. 5.19. The figure shows a comparison of ozone vertical profiles from SCIAMACHY V2.9 data (blue solid line) and from ozonesonde (black solid line) at Eureka for 22 March, 2006. A clear underestimation of the peak value near 17 km is observed in V2.9 data. This is a typical behaviour that explains the underestimation described above. As this artifact could not be reproduced in the synthetic retrievals, which include a full range of forward model parameters, it is most probably caused by instrumental issues. One possible explanation is a presence of an increased external stray light when performing limb measurements at large solar zenith angles and small azimuth angles. In this geometry, which is typical for SCIAMACHY observations at high northern latitudes, the extra-terrestrial solar radiance is believed to be reflected by some part of Envisat into the field of view of the SCIAMACHY instrument.

The retrieval methodology used in V3.0 aims to reduce the underestimations in the northern high latitudes shown by V2.9. In the V3.0 retrieval processor, signals from different wavelengths are exploited (Sect. 5.5.2). The spectral window used in the Vis wavelength region is narrower compared to V2.9. On the one hand it uses weaker absorption features of ozone, thus gaining less information from the spectra. On the other hand, by using the narrow spectral window and higher order of the closure polynomial the influence of the systematic errors is reduced. The right panel of Fig. 5.19 shows the comparison of ozone vertical profiles from SCIAMACHY V3.0 limb data with ozonesonde data presented in the same way as V2.9 re-

sults in the left panel. It is seen clearly that the ozone maximum at 17 km observed by the sonde is now captured properly by SCIAMACHY. Furthermore, the V3.0 data set also better reproduces the ozone maximum around 25 km in the tropics (Fig. 5.20), which corrects the overestimation in Southeast Asia as seen from both vertical and partial-column comparisons. General improvement in the Pacific and the South Atlantic Ocean regions can be observed in the partial-column comparisons (Fig. 5.17). This may be partly due to the opposite sign of differences at different altitudes. As shown in the sections above, the V3.0 is a success in solving the underestimation at northern high latitudes.

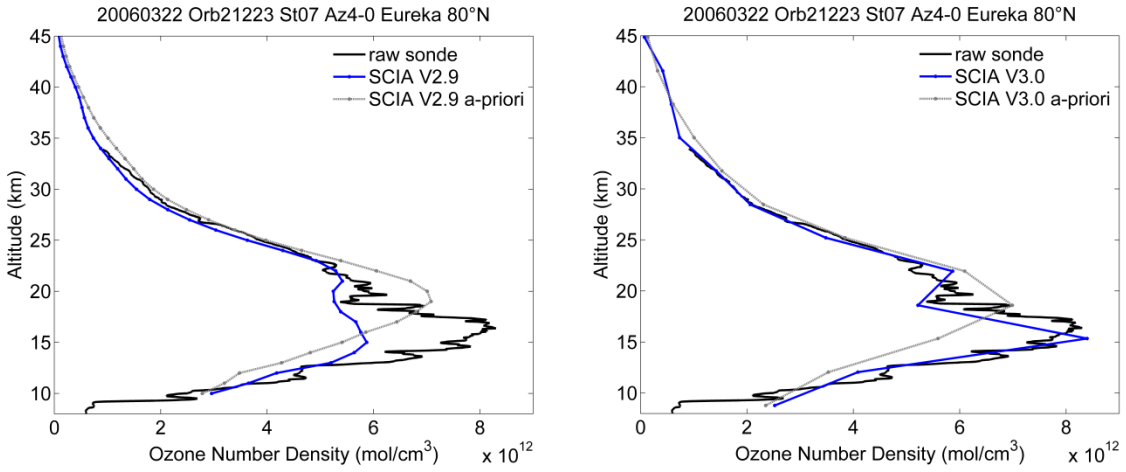

Figure 5.19. Comparison of ozone vertical profiles from SCIAMACHY and from ozonesonde at the Eureka station.

5.5.5 Progress of limb ozone V3.5 data set

After validating the limb ozone profiles, the limb data used in the tropospheric ozone retrieval was updated from the V2.9 to the V3.0 database in order to improve the retrieval accuracy. However, the newly retrieved TOCs showed unexpectedly high values. A striking result is the over 30 DU TOCs in the tropical Pacific, where ozone columns are expected to be ~25 DU (e.g., Thompson et al., 2003). The V3.0 limb data was very soon found to have an under-

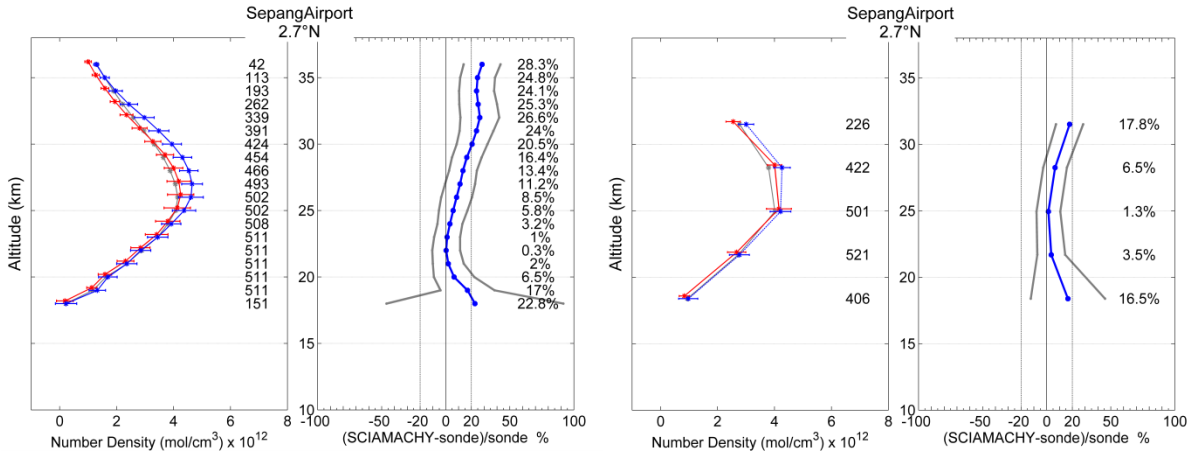

Figure 5.20. Same as Fig. 5.12 but for the station SepangAirport (2.7°N 101.7°E).

estimation at around 35 km (left panel of Fig. 5.21), which was not present in V2.9 data. Statistical analysis shows that the ozone partial-column (30-40 km) differences to MLS at 69 ozonesonde station locations have a strong variation along with latitude. The underestimations are smaller over high latitudes whereas they reach maxima in the tropics (right panel of Fig. 5.21). There is no obvious seasonal pattern of the differences.

This underestimation of V3.0 is believed to be caused by the lack of retrieval information at ~35 km. While the information from the UV range only influences the retrieved ozone values above ~35 km, the Vis range is mostly responsible for the ozone information below 30 km. Thus 35 km becomes the least sensitive retrieval altitude. For V2.9, this shortage can be compensated by the broader visible spectral range. This is to say that the signal is stronger when the whole Chappuis band is used, which results in a higher sensitivity around 35 km. The usage of Huggins band is believed to improve ozone retrieval accuracy between 30 km and 35 km. Therefore, it is included in the further developed limb ozone retrieval (e.g., for V3.1-V3.5).

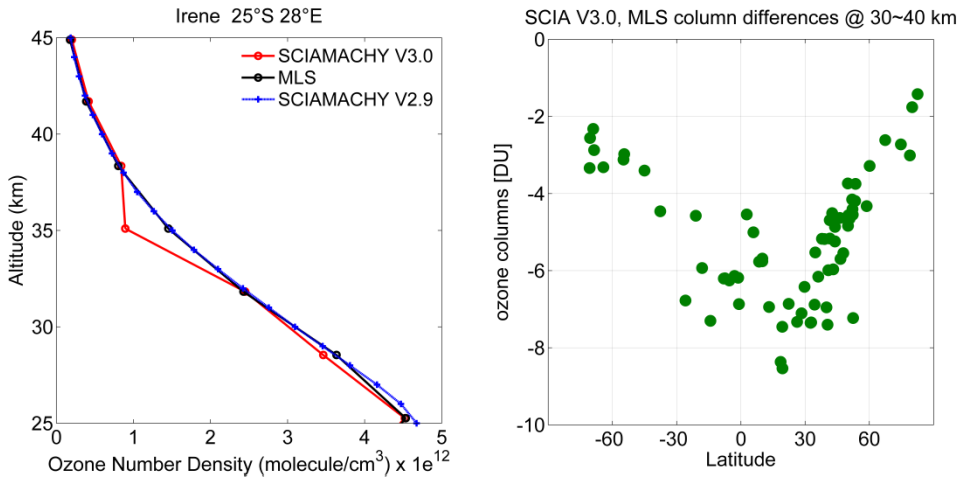

Figure 5.21. Underestimations around ~35 km altitude in the SCIAMACHY limb V3.0 data set. Left panel shows the vertical profile comparisons at the station Irene averaged from Jan 2003 to Dec 2011. Right panel shows the ozone partial-column differences between MLS and SCIAMACHY V3.0 data from 69 locations of ozone sonde stations over the same time period as the left panel.

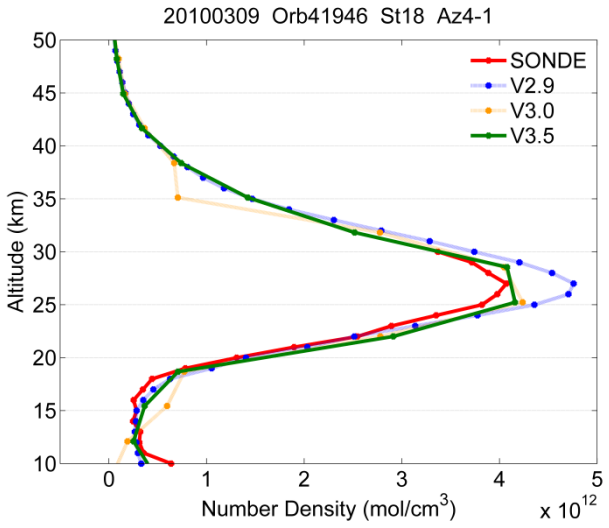

Figure 5.22. Vertical profile comparisons at the station Ascension Island (8.0°S 14.4°W). The measurements are taken on March 9th, 2010.

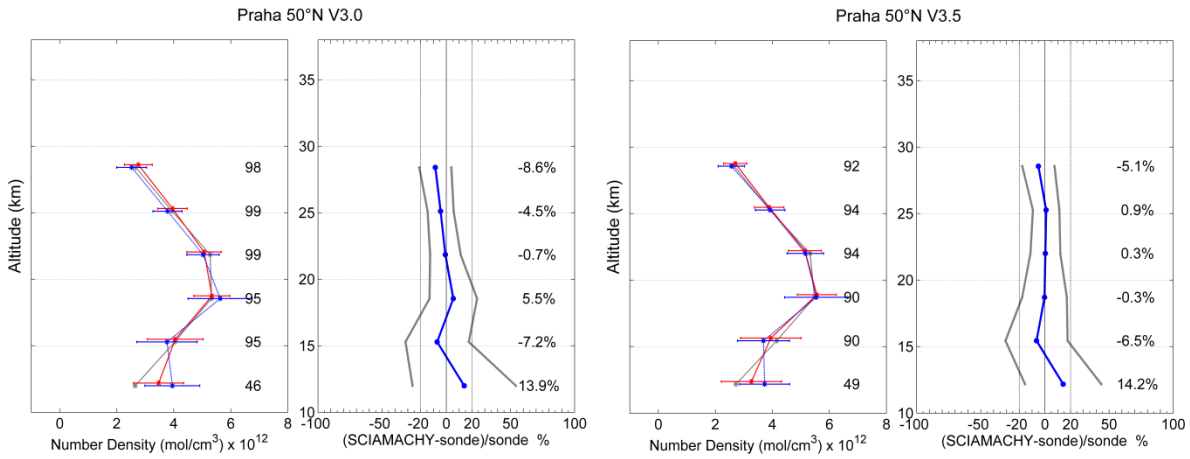

Figure 5.23. Same as Fig. 5.12 but for the comparison between ozonesonde and V3.0 (left-hand side) / V3.5 (right-hand side), averaged from Jan 2010 to Dec 2010.

Figures 5.22 and 5.23 illustrate the preliminary results of the newly developed V3.5 limb database in 2010 by comparing to ozonesonde and previous versions of SCIAMACHY limb data. In Fig. 5.22, a profile example in the tropics is showed for different SCIAMACHY limb data versions. A clear underestimation of the value near 35 km is observed in V3.0 data. This feature is corrected in the V3.5 data. Once 35 km underestimation is fixed, it is crucial to know if the profile accuracy of V3.5 stays at the similar level as V3.0. I have compared the ozonesonde-collocated SCIAMACHY limb ozone measurements from both versions. Fig. 5.23 shows the comparison results at Praha as an example. The figure presents the profile accuracy at 12-28 km. All the limb layers have been improved in V3.5 compared with V3.0.

5.5.6 Conclusions of the limb ozone improvement

The improvements of the limb ozone vertical profiles are presented and discussed in Sect. 5.5. As an important step of the improvement of the TOC retrieval, this section is concluded separately.

The two versions of SCIAMACHY limb ozone scientific data sets, namely the V2.9 and the

V3.0, were extensively compared to ozonesonde measurements for the time period of 2003-2011, from 61 sonde stations. The two versions of SCIAMACHY limb data use different retrieval processors. The main differences are the retrieval of surface albedo, and that in the visible spectral region, V2.9 uses a reference tangent height and the triplet method, while V3.0 employs a solar spectrum as the reference and performs a DOAS-type fit. There are also some changes in the UV band (Sect. 5.5.1 and Sect. 5.5.2); these however do not provide information at altitudes lower than 30 km. The retrieval differences are listed in Tab. 5.1.

V2.9 agrees well with the ground-based data within a latitude range of 90°S-40°N. The relative differences between the two databases are within 5% (SCIAMACHY is mostly overestimating) at 20 km - 30 km. It shows very good retrieval results in the tropics with a difference of less than 3% for each layer. The partial-column comparisons show less than 5 DU absolute differences with rather small standard deviation, with the exception of the tropical Pacific region, where overestimations of more than 10% are observed. These overestimations result from a significant positive bias above 25 km (so far there is no explanation for the reason behind this bias). In the northern high latitudes, V2.9 shows an up to ~15% negative bias with observable vertical oscillations, which is believed to be the consequences of the increased external stray light. The ozone partial-columns are underestimated by 12 - 20 DU.

The V3.0 has been developed to reduce the underestimation in the northern high latitudes identified in V2.9. As a result, the differences are reduced to within 10% for vertical profiles and 5 DU to 10 DU for partial-columns northward of 40°N. At the same time, the overestimations of the ozone profile concentrations around the tropical Pacific are eliminated. V3.0 maintains the good retrieval results also southwards of 40°N, with deviations slightly larger than 5% in the tropics and within 10% in the southern high latitudes.

The tropospheric ozone retrieved using V3.0 limb ozone data directly does not yield good results. The reason is found to be an underestimation at ~ 35 km altitude, perhaps due to a lack of spectral information. The Huggins band is believed to improve ozone retrieval accuracy between 30 km-45 km and is included in the further developed limb ozone retrieval. The up-coming V3.5 fixes the underestimation while maintaining the good vertical accuracy in V3.0.

Table 5.1. Summary of the parameter differences between limb ozone data versions V2.9, V3.0 and V3.5.

Parameters	V2.9	V3.0	V3.1-3.5 *
Spectral windows (nm)	264 – 265, 266.5 – 268.5, 272 – 274, 282 – 284, 285 – 287, 287 – 289, 289.5 - 291.5, 304 – 306, 306 – 308, 523.66 – 524.34, 587.74 – 590.34, 673.79 – 676.21 (averaging within the sub-windows)	289 – 306, 495 - 587	(a) 264 – 274.9, (b) 276.5 –287, (c) 289 – 309.5, (d) 325.5 – 331, (e) 495 – 576
Method	Radiance profiles in UV, triplet in Vis	DOAS, 0-th order polynomial in UV, 3-rd order polynomial in Vis	DOAS, none polynomial in wavelength range (a), 0-th order polynomial in range (b) and (c), 1-st order polynomial in range (d), 2-nd order polynomial in range (e)
Reference	Upper tangent height	Extraterrestrial solar spectrum	(a-c) Upper tangent height (d-e) Solar spectrum
SNR	15 – 140 pre-estimated constant value	Estimated from the residual spectra	(a) 20, (b) 40, (c-e) Estimated from the residual spectra
Clouds	Ignored	THs with clouds in FOV are rejected	THs with clouds in FOV are rejected
Aerosols	LOWTRAN background aerosols (global mean)	Retrieved from SCIAMACHY measurements (Ernst et al., 2012)	ESCTRA (based on SAGE II climatology)

* Recent test versions V3.1 to V3.5 are retrieved in a similar way as V3.5 with continuous minor improvements in the retrieval.

5.6 Results from the improved tropospheric ozone column retrieval

After the data amount improvement, TPH optimization and the limb data improvement, the results of different tropospheric ozone versions are reported in this section. The three versions of the tropospheric ozone results are validated with ozonesonde measurements. In Sect. 5.6.1, the tropospheric ozone validation methodology is described. The validation results with ozonesondes and the comparisons among the versions are given in Sect. 5.6.2.

Table 5.2. Summary of the retrieval differences among TOC data versions V1.0, V1.1, and V1.2

Retrieval differences	**V1.0**	**V1.1**	**V1.2**
CTH used in limb data screening process	Cloud flag	SCODA	SCODA
TPH at each corner of the limb pixel	Nearest UTC	Linear interpolated to SCIAMACHY over pass time	Linear interpolated to SCIAMACHY over pass time
TPH for each limb pixel	Minimum of the corners	Mean of the corners	Mean of the corners
Limb data	V2.9	V2.9	'modified' V3.0

One should be informed that here the V1.2 TOCs are retrieved by replacing limb ozone data from V2.9 to 'modified' V3.0. As mentioned above, V3.0 limb data underestimated ozone at ~ 35 km, which will cause the retrieved TOCs being overestimated globally, especially in the tropics (Sect. 5.5.5). However, the V3.5 limb ozone retrieval is still under development. Thus in the V1.2 tropospheric ozone retrieval, before being imported to the retrieval process, V3.0 limb data is modified at the layer near 35 km by linearly interpolating the values at the layers above and below. The differences of the retrieval of V1.0, V1.1 and V1.2 TOC data are summarised in Tab. 5.2.

5.6.1 Validation methodology of the tropospheric ozone vertical column

The SCIAMACHY Limb-Nadir Matching TOC data has been validated with different methods in previous studies. The SCIAMACHY monthly mean results have been directly compared to the ozonesonde monthly mean results (Ebojie et al., 2014). In this method, the ozonesonde tropospheric ozone is integrated using the WMO (thermal defined) TPH. Another way of comparison is to check single TOC result versus one ozonesonde profile (Bötel et al., 2008). None of these methods considered the possibility of big differences between the TPHs used in the satellite and ozonesonde measurements, in which case the two data sets are not comparable. In this study, the geo-collocated SCIAMACHY and ozonesonde measurements are compared only when their TPH differences are not larger than $\pm$1 km. My preliminary results showed that the launch time is not a main influence for the validation results. Thus, the satellite and ozonesonde data measured within one month are temporally collocated.

The details of the validation process are as follows: For each ozonesonde profile, the corresponding TPH is interpolated in the same way as for the optimized TPH_Limb collocation (Sect. 5.5). The ozonesonde TOC is then calculated as the integration of the measurement from the ground to the TPH. Please be reminded that the geopotential height included in the ozonesonde data needs to be converted to the geometric height. Coincident SCIAMACHY TOCs are selected for each ozonesonde profile. The geographic distance between the ozonesonde station and the footprint centre of the collocated SCIAMACHY TOC is required to be within 5° in latitude and 10° in longitude. The TPH difference between ozonesonde and collocated SCIAMACHY measurements should not exceed $\pm$1 km. The coincident SCIAMACHY TOCs are averaged to be the daily result for each ozonesonde measurement. These daily results are then averaged into monthly results for validation.

5.6.2 Comparisons of the tropospheric ozone column results

Quantified improvements in V1.1 and V1.2 can be concluded from the SCIAMACHY - ozonesonde comparisons and zonal mean climatology.

Average column values from the coincident SCIAMACHY and ozonesonde measurements at 61 stations for the period Feb - Dec 2004 are compared in Figs. 5.24 -5.26. Figure 5.24 shows

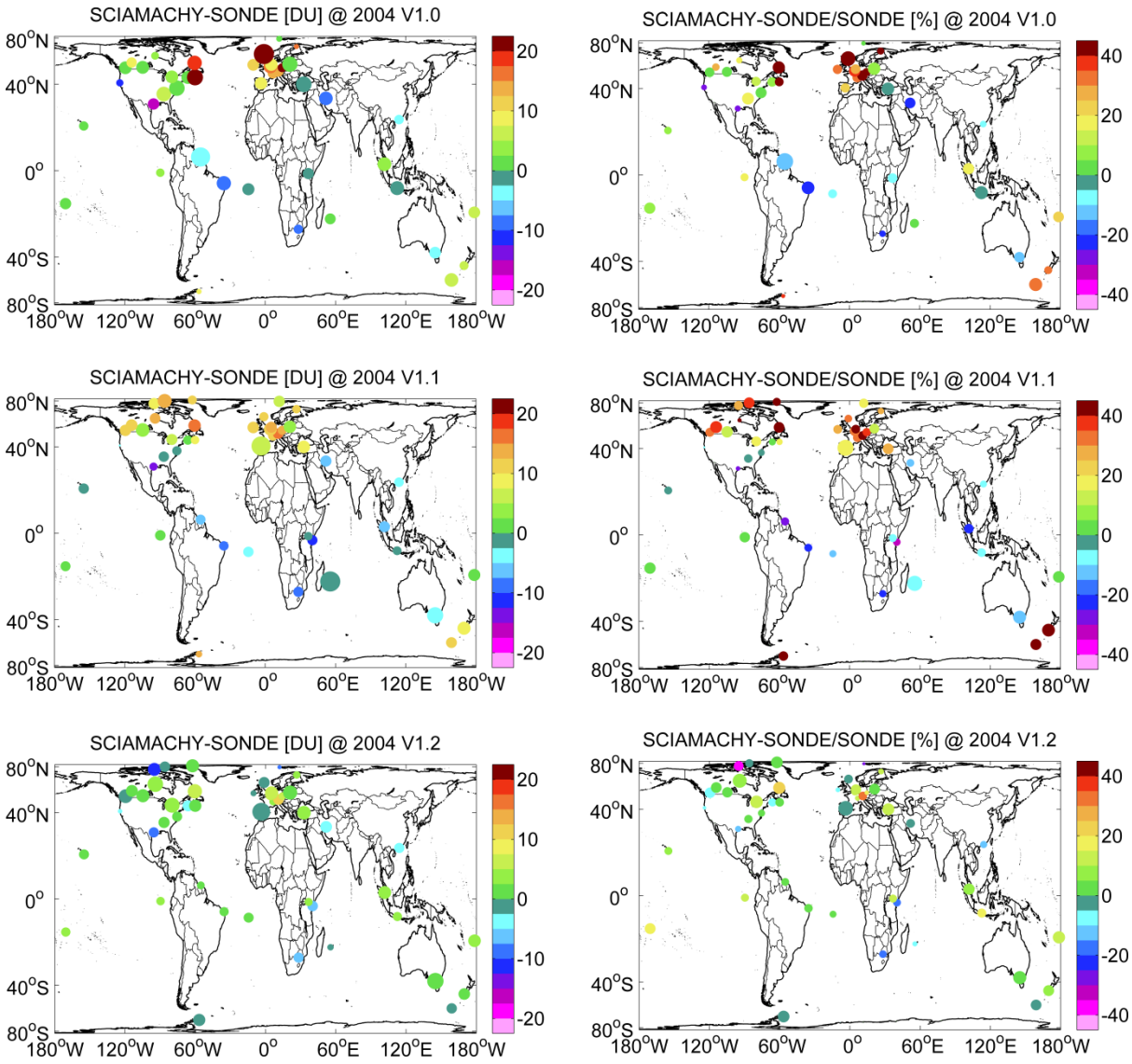

Figure 5.24. SCIAMACHY TOC comparison with ozonesonde in 2004. Left panels illustrate the absolute monthly differences, while the relative differences are presented on the right-hand side. In each panel, the color of the dots depicts the mean differences, while the size of the dots represents 1σ standard deviation. The standard deviation is between 0.2 - 24 DU for the absolute differences and between 1-90 % for the relative differences.

the global overview of the daily mean absolute (left panels) and relative (right panels) averaged daily differences between the ozonesonde TOCs and the SCIAMACHY TOC versions 1.0, 1.1, and 1.2. The V1.0 tropospheric ozone overestimations over the northern mid- and

high latitudes are observed in both the absolute and relative comparisons. The bluish color over the tropical Atlantic and South America indicates the negative biases of the SCIAMACHY TOCs. Due to the increased data amount and more accurate TPH information, in V1.1, 4 more stations can be included for the comparison at northern high latitudes. The extremely high differences (over 20 DU, which equals to more than 40%) in V1.0 decreased to within 15 DU. On the other hand, the negative biases in the tropics are enhanced, while the positive biases around New Zealand (the southern high latitudes) also increases. These changes are provoked by the increased data amount (see stations Maxaranguape and Lauder in Figs 5. 32 and 5. 33). Thus the V1.1 results are more authentic to represent the TOCs retrieved using V2.9 limb data. In general, the absolute differences between the V1.0 and V1.1 SCIAMACHY TOCs and the ozonesonde TOCs mostly lies below 10 DU southward of 40°N. Northward of 40°N, overestimated high ozone columns can be observed, which is consistent with the underestimations of the V2.9 limb ozone data at the same latitudes (Sect. 5.5).

In comparison to the V1.0 and V1.1, V1.2 shows improved results globally. With the benefit of the V3.0 limb ozone profile information, the overestimations of the TOCs at northern high latitudes, and the underestimations in the tropics are reduced in V1.2. The TOC values around New Zealand also agree well with ozonesondes as well (Fig. 5.24). The comparison of V1.2 TOCs with ozonesonde measurements showed yearly mean absolute differences of less than 5 DU globally. The relative differences are reduced from larger than 40% to below 10%.

The comparison results between the SCIAMACHY and ozonesonde TOCs are depicted as time series at each ozonesonde station. Figures 5.25 and 5.26 show the results at the stations Maxaranguape (also known as Natal), Ankara, Payerne, Eureka, Lauder, and Marambio in 2004 and 2008. These stations are chosen to represent the latitude bands 20°S-20°N, 20-40°N, 40-60°N, 60-90°N, 20-60°S, 60-90°S, respectively. The results at all other stations are listed in the Appendix. Maxaranguape is located in northern Brazil, the very east of the south American continent. In this region, tropospheric ozone is highly influenced by biomass burning. Every year from April to June fewer burning events happen compared to other months (Crutzen and Andreae, 1990). Thus the TOCs have a minimum during these months while they are above 40 DU in the other time period. Both V1.0 and V1.1 reproduced the seasonality at Maxaranguape. Nevertheless, TOCs are underestimated by ~10 DU in V1.0 and V1.1,

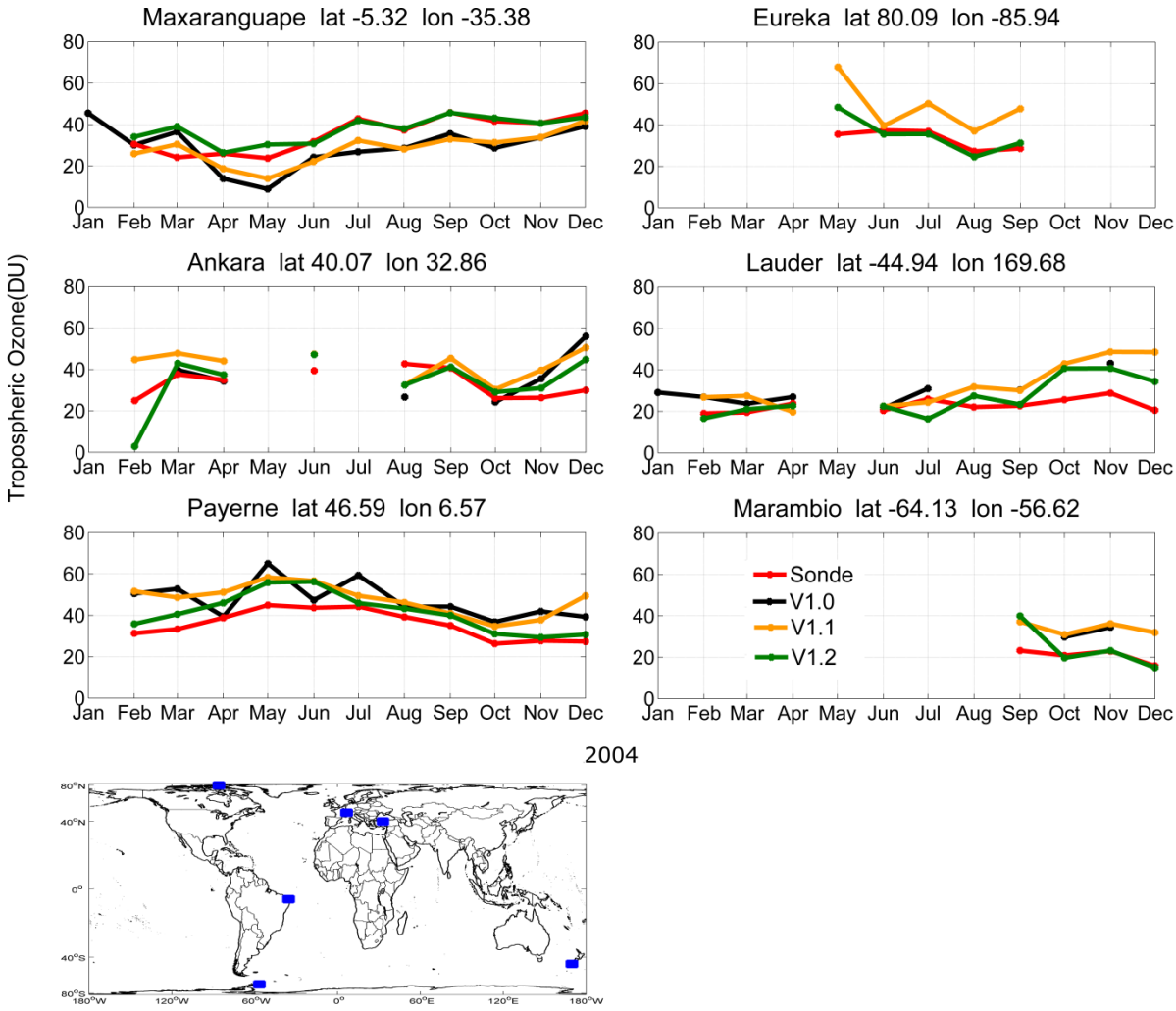

Figure 5.25. Time series of monthly averaged TOCs from SCIAMACHY V1.0, V1.1, V1.2 data and ozonesonde data in Maxaranguape/Natal, Ankara, Pyerne, Eureka, Lauder, and Marambio in 2004. The location of the stations are marked in blue in the global map. The results are presented unsmoothed.

while V1.1 better follows the sonde structure than V1.0 (e.g., in July). V1.2 agrees with ozonesonde results within ~3DU while the seasonality is the same as in V1.1. Ankara and Payerne are located in the Middle East and central Europe, where the tropospheric ozone is mostly influenced by anthropogenic emissions of ozone precursors. The highest TOCs show

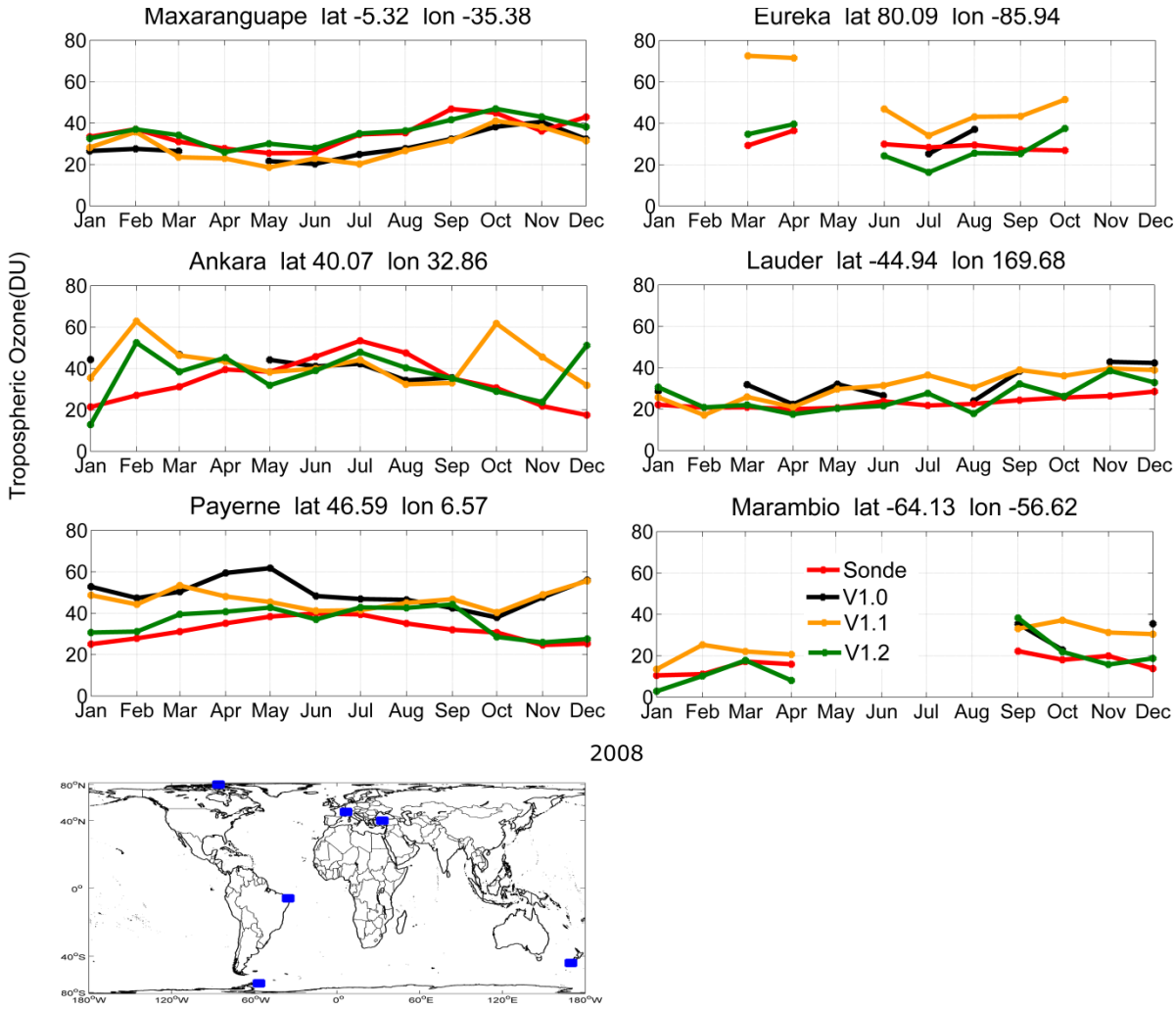

Figure 5.28. Same as Fg. 5.25 but for the year 2008.

up in late spring/early summer, when the photochemical reactions are most efficient. Correspondingly, ozone reaches its minima during winter. At Ankara, older versions V1.0 and V1.1 underestimated ozone columns in summer while overestimated them in winter. Although V1.2 catches most of the seasonal patterns, all three versions show extreme overestimations during winter time. At Payerne, the TOCs retrieved from the older versions V1.0 and V1.1 are 10-20 DU higher than those measured from ozonesondes. In the year 2004, oscillations of values in-between months are observed in March - July in V1.0. These oscillations can be signs of insufficient data used in the analysis as they no longer exist in V1.1. V1.2,

compared to the older versions (V1.0 and V1.1), significantly improves the agreement with ozonesonde measurements to within 5 DU in yearly average. Nevertheless, the positive biases can still reach ~10 DU in the ozone maxima months. Lauder is located in the southern rural area of New Zealand. The region is not much influenced by industry. Hence, the ozone columns in boreal summer at this station can be considered as the background ozone level (~20 DU). The TOCs show sharp peaks (~35 DU) during boreal winter time of each year when wide-spread biomass burning occurs in the Southern Hemisphere tropics near the end of the dry season and generate CO and NMVOCs (Rinsland et al., 2002). Similar to the northern midlatitudes, the ozone results from V1.0 and V1.1 exhibit ~ 5-10 DU higher biases compared to ozonesonde measurements in the southern midlatitudes. V1.2 shows better agreements in general, yet an overestimation of up to 10-15 DU can be observed during the ozone maxima time period. At Eureka, because of the missing measurements from SCIAMACHY during the polar night, only the summer month results can be retrieved. All the V1.0 data are eliminated by the limb cloud-free criterion. Compared to ozonesonde results, V1.1 results show an overestimation of ~15 DU on average. There is very good agreement (~3 DU) between V1.2 and the ozonesonde monthly results in both stations. Similar conclusions can be drawn for Marambio at southern high latitudes.

To conclude, V1.0 TOCs exhibit ~10 DU underestimation in the tropical Atlantic, > 10 DU overestimation at high latitudes, and variable overestimations at midlatitudes. V1.1 corrects most of the unrealistic seasonal oscillations and provides much dense sampling. With the improvement of limb ozone data, the V1.2 TOCs (retrieved using V3.0 limb ozone data sets) reaches very good agreement with ozonesonde measurements over the tropics and high latitudes. The column values are improved over the midlatitudes as well. But a positive bias is still present in the local summer period when TOCs reach its peaks.

The zonal mean climatologies of the three tropospheric ozone versions are shown in Fig. 5.27. In general, the SCIAMACHY Limb-Nadir Matching data well reproduces the TOC distribution, with spring-summer maxima in the northern hemisphere and the boreal autumn - winter ozone peaks over the Southern Hemisphere. As is shown in the SCIAMACHY/ ozonesonde comparisons, the zonal mean TOCs in V1.0 and V1.1 maintain larger than 40 DU northward of 40°N through the whole year. This value is more than 10 DU (>25%) higher compared to the ozonesonde measurements (upper and middle panels of Fig. 5.24). The biomass burning provoked ozone plume in the Southern Hemisphere is observed to be extended in north-south

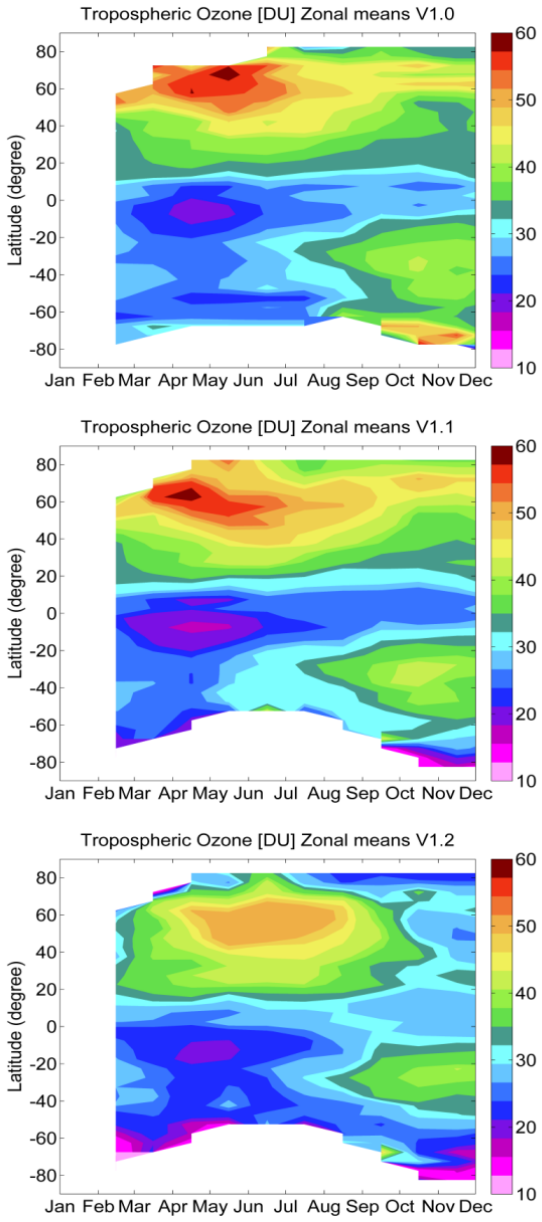

Figure 5.27. SCIAMACHY Limb-Nadir Matching tropospheric ozone zonal mean climatology derived from February 2004 to December 2004 from 2.5° latitude bin. From top to bottom are V1.0, V1.1 and V1.2.

direction in V1.0. In V1.1, the shape of the plume is similar to the result in V1.0, while underestimation of the tropical tropospheric ozone appears. This underestimation is because of the overestimation of the V2.9 limb ozone data that is used in the retrieval. It exists in V1.0 as well, yet due to insufficient data this underestimation was not illustrated in the zonal mean climatology. The decreased ozone peaks at northern midlatitudes, and properly displayed biomass burning plumes at southern midlatitudes are observed in V1.2.

To give an intuitive global view of the results from different versions, the global distribution of the yearly averaged SCIAMACHY TOCs are shown in Fig. 5.28. In spite of all three versions showing the well-known Southern Hemisphere burning provoked plume, the wave-one tropical ozone structure and the relatively high northern mid-latitude ozone belt due to the anthropogenic pollution, the yearly averaged global TOCs show different patterns among the three versions (see Sect. 3.2). V1.0 has the most sparse sampling. The results become noisy at higher latitudes (>45°). With improved spatial sampling, V1.1 highlights the over 55 DU high ozone values northwards of 30°N. In V1.2, the biomass burning plume is quite properly displayed. The high TOC values in the Northern Hemisphere and low TOC values in the tropics are reduced compared to V1.0 and V1.1. The orbit gap in V1.2 is caused by the lack of V3.0 limb data (initial product).

The monthly averaged SCIAMACHY TOC results observed for October 2004 are presented in Fig. 5.29. A typical global tropospheric ozone distribution in boreal autumn should exhibit at least three patterns: a clear ozone plume in the Southern Hemisphere due to biomass burning activities in Australia, Southern Africa, and South America; relatively low ozone values in the Northern Hemisphere due to the weaker solar radiation and lower concentration of precursors; and the wave-one pattern in the tropics. In V1.0, none of the three patterns can be observed clearly. Few tropical data can be used to identify the wave-one pattern. There are insufficient data in the northern high latitudes (northward of 50°N) as well. The biomass burning provoked high ozone values can be observed, but with no clear shape in spatial coverage. The massively increased data amount in V1.1 helps to get a global impression of the SCIAMACHY Limb-Nadir Matching tropospheric ozone using V2.9 limb data. In V1.1, the tropical wave-one pattern and the southern biomass burning pattern – although still broad – are clearly presented. It provides a chance to observe the overestimated high ozone columns in the northern high latitudes, which is consistent with the underestimations of the V2.9 limb ozone data at these latitudes. With the benefit of the V3.0 limb ozone data, these overestima-

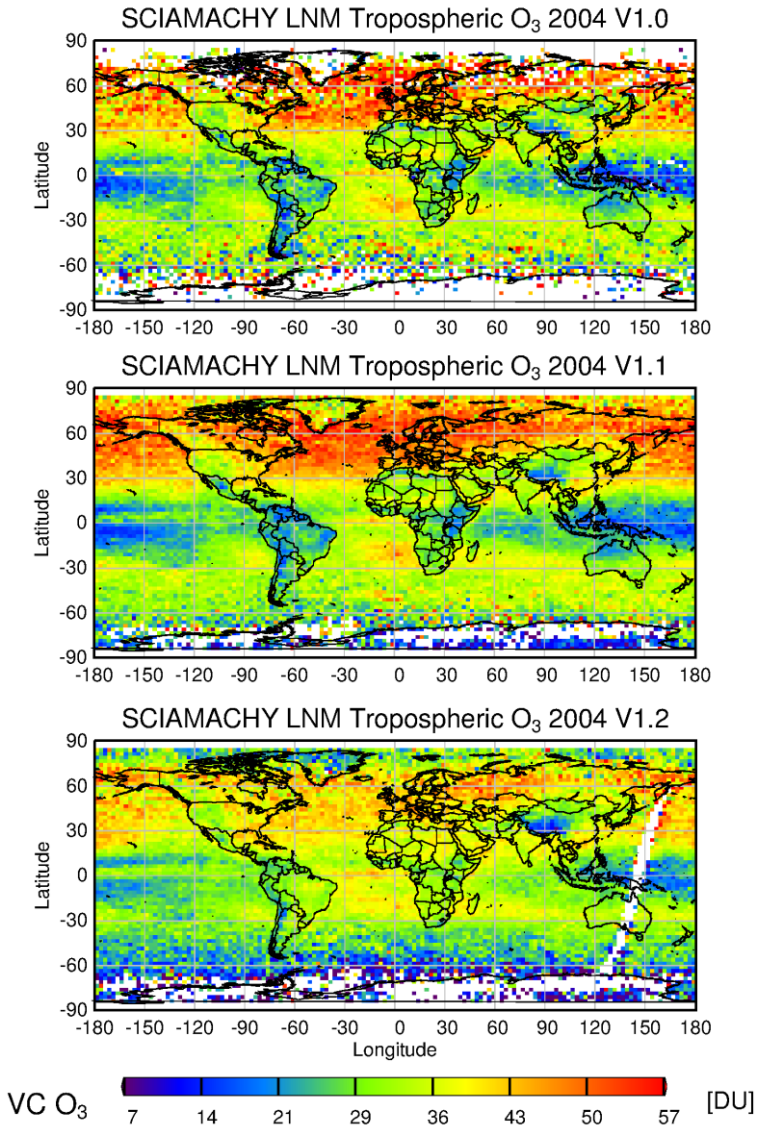

Figure 5.28. Yearly TOC results in 2004. From top to bottom are V1.0, V1.1 and V1.2.

tions are significantly reduced in V1.2. The biomass burning plume is now very properly observed as an advantage of using the new limb ozone data as well, since the new (V3.0) limb partial columns were not only improved for the Northern Hemisphere but also for the southern midlatitudes (see Sect. 5.5.4.2).

Similar conclusions can be drawn from the seasonal comparison results of V1.0 and V1.2 in NH autumn (third row in Fig. 5.30). In the other seasons, while keeping the main features

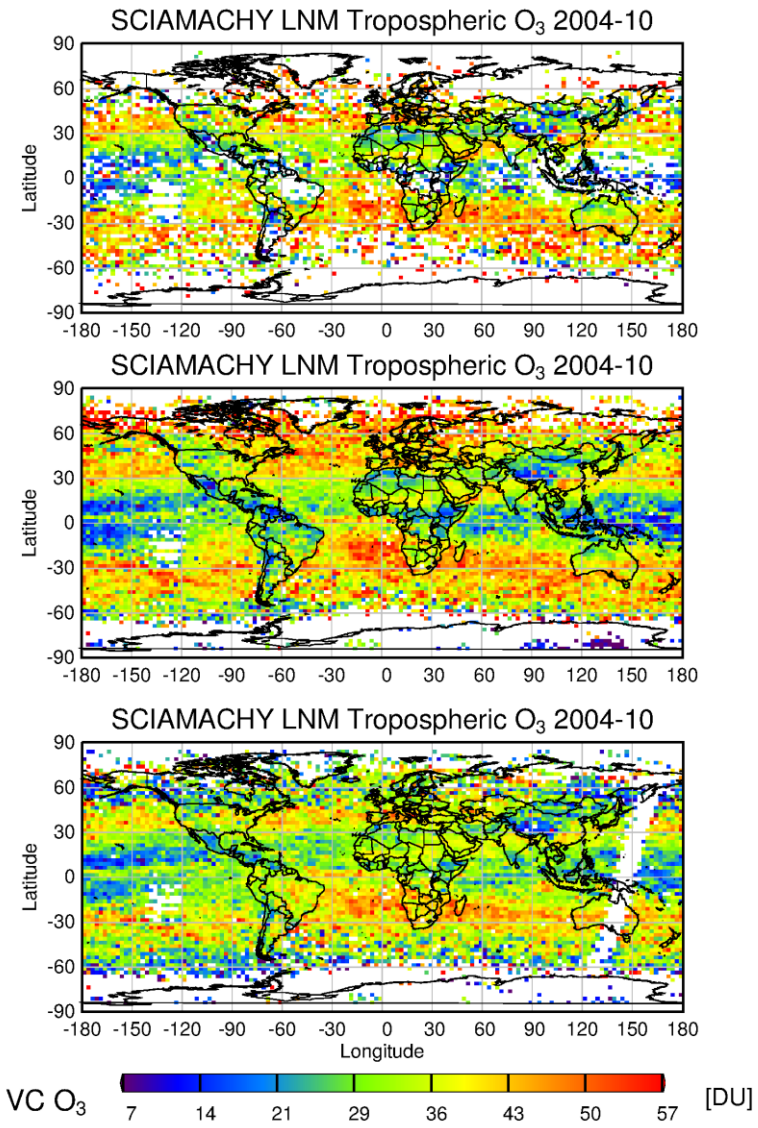

Figure 5.29. Monthly TOC results in October 2004. From top to bottom are V1.0, V1.1 and V1.2.

(details are given in Sect. 3.3) and reducing the northern mid-/high latitude values, more structure details are exhibited in V1.2.

In spring, a stronger and larger ozone plume can be observed over the Southeast Asia region centred over the Arabian Sea (AS). This feature is depicted in Fig. 5.31 in details. Over this region, big differences can be observed in each season. Compared to V1.0, the low ozone

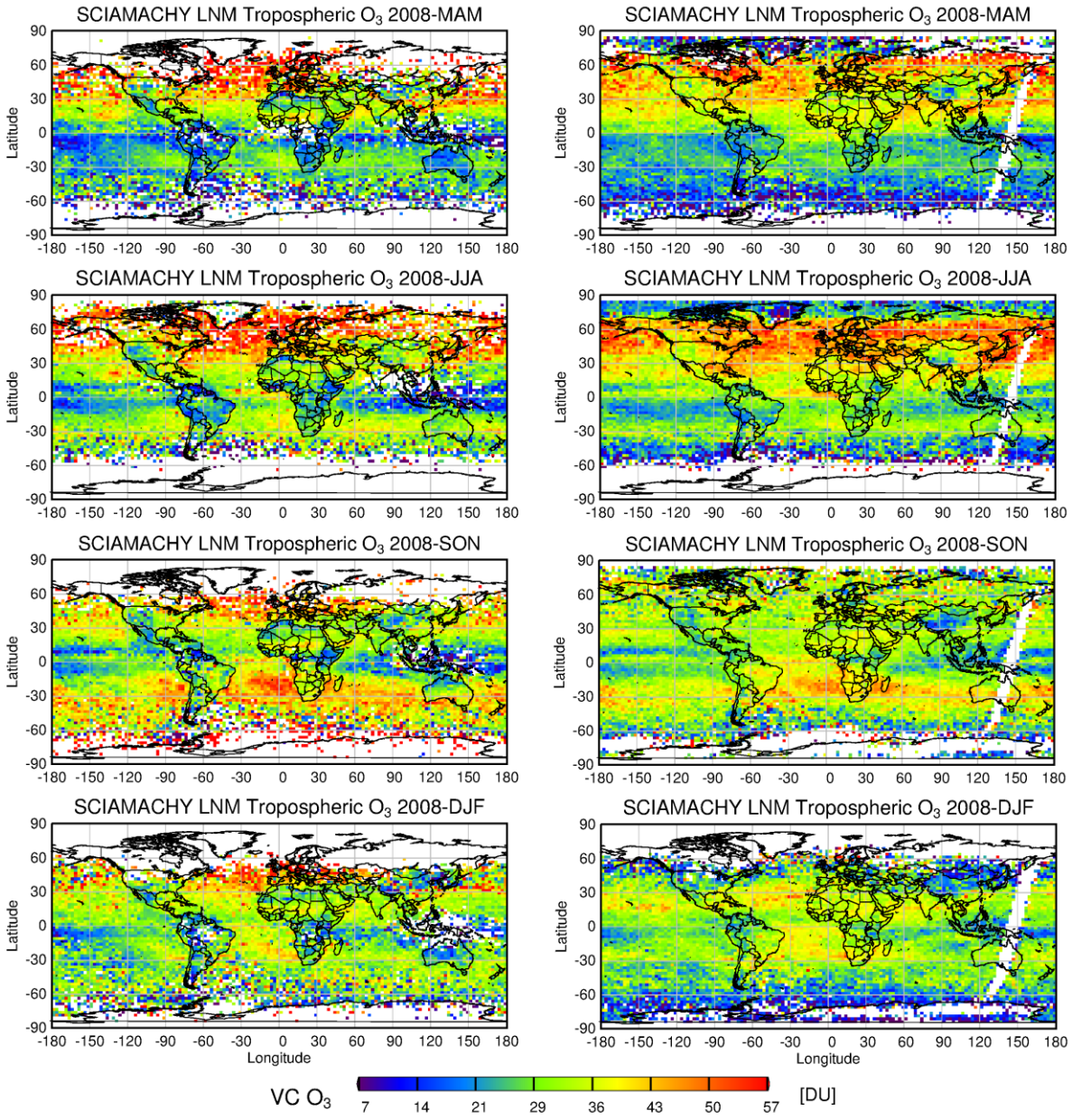

Figure 5.30. Seasonal TOC results of V1.0 (left panels) and V1.2 (right panels) in 2004. From top to bottom are spring (MAM), summer (JJA), autumn (SON) and winter (DJF).

values over the Tibetan Plateau in SON and DJF can be better observed in V1.2. The high photochemically produced ozone from anthropogenic activities in the Middle East and the Indo-Gangetic Plain in MAM and JJA are more properly revealed as well. The Arabian Sea spring maximum can be very well shown in V1.2. The clear pattern inspired the investigation of the spring maximum phenomenon. The related results are further presented in Chapter 6. In general, the seasonality in Southeast Asia is much better structured in SCIAMACHY V1.2.

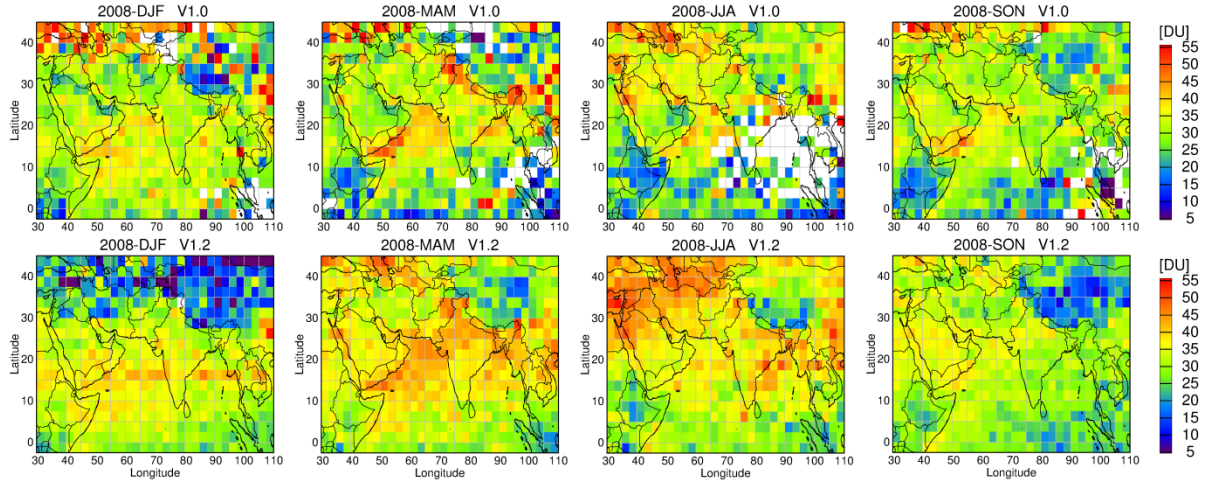

Figure 5.31. The seasonal averaged regional TOC results from V1.0 (upper panels) and V1.2 (lower panels) in 2008.

In summer, the Mediterranean ozone pool is well captured in V1.2. This ozone pool is caused by STE and reported by Zanis et al. in 2014. The ozone outflow at the Central Atlantic Ocean from Central Africa, which is believed to be mainly triggered by the biomass burning and the lightning during the summer monsoon (Bouarar et al., 2011), is also properly revealed.

In winter, the ozone maximum is observed in the southern Atlantic region. It can be explained by the fire induced ozone being transported downwind from Western Africa, together with upper tropospheric ozone produced from lightning NO_x and subsidences from the Walker circulation (e.g. Thompson et al., 2000; Fishman et al., 2003). V1.2 shows smoother ozone distribution with lower values in the northern midlatitudes compared to V1.0.

5.7 Conclusions

The Limb-Nadir Matching method is a residual method that is developed for TOC retrieval using the SCIAMACHY instrument. In this method the stratospheric ozone columns retrieved from the limb measurements are subtracted from the collocated total ozone columns acquired from nadir measurements by using the tropopause height data. Along with the fact that the TOCs are only ~10% of the total ozone columns, the accuracy of the retrieved TOCs is quite challenging. The original TOCs exhibit an underestimation of ~10 DU in the tropical Atlantic, more than 10 DU overestimation in the high latitudes, and variable overestimation in the mid-latitudes. The biomass burning provoked ozone plume during the burning season in the Southern Hemisphere is displayed with unrealistic propagation. A three-step optimization is applied to the original retrieval approach.

Firstly, CTH data needed in the retrieval is switched to using the SCODA database to screen cloud-free limb data instead of using the cloud flag information available in the limb ozone data sets. This yields a significant data amount increase of ~100% for the finally retrieved TOC data sets.

Secondly, the ECMWF TPH implemented in the retrieval is optimized temporally and spatially for each collocated SCIAMACHY limb ozone data. On average, the original strategy to derive the limb-collocated TPH (nearest UTC time and lowest values) induces an underestimation of ~3 DU of the gridded (2.5° x 2.5°) TOCs. The underestimation can exceed 7 DU for individual grid boxes and can easily be larger than 10 DU for individual TOCs. An improvement is achieved by the chosen interpolation scheme for matching TPH data and limb measurements. The new TPH for the matching limb measurement is calculated as the mean value of the TPH values at the four corners of the measurement footprint. At each corner the corresponding TPH is calculated by linearly interpolating ECMWF data from the UTC time to the SCIAMACHY overpass time.

Thirdly, SCIAMACHY V3.0 limb ozone scientific data set is implemented instead of the previous V2.9 data set after extensive comparisons with ozonesonde measurements for the time period of 2003-2011. The new V3.0 has been developed to reduce the underestimation (up to ~15% negative bias with observable vertical oscillations in the vertical structure, corresponding to 12 - 20 DU bias in stratospheric ozone partial-columns in the 20-30 km range) in

the northern high latitudes that was identified in V2.9. The retrievals between limb ozone V2.9 and V3.0 are substantially different. In the visible spectral region V2.9 uses a reference tangent height and the triplet method, while V3.0 employs a solar spectrum as reference and performs a DOAS-type fit. As a result, the differences between the satellite retrieved tropospheric ozone and the ozonesondes are reduced to within 10% for vertical profiles and 5 DU to 10 DU for stratospheric partial-columns (in the 20-30 km range) northward of 40°N. The V3.0 limb ozone data cannot be used for Limb-Nadir Matching directly due to a negative bias existing at an altitude of ~ 35 km caused by a lack of spectral information from the Huggins band. The up-coming V3.5 fixed the underestimation while maintaining the good vertical accuracy of V3.0. However, V3.5 is still under investigation, thus the V3.0 limb ozone data set is implemented in the present study with a linear interpolation correction at 35 km.

After the optimization in CTH and the TPH, the resulting data amount of the retrieved TOCs is increased by a factor of two as compared to the original retrieval. This version (V1.1) of TOCs correct most of the artificial oscillations encountered before and shows a more clearly overview of the achievements and disadvantages in using V2.9 limb ozone data.

The TOCs retrieved using V3.0 reduced the negative and the positive biases over tropics and high latitudes, respectively. The column values are also optimized over the midlatitudes by decreasing the positive biases. However, a positive bias still occurs in the local summer period when ozone reaches its peaks. The V1.2 results agree with ozonesonde measurements within 5 DU in the annual global mean. The biomass burning pattern is properly observed. More details are successfully captured, including the Mediterranean ozone pool, the ozone outflow from Central Africa, as well as the spring ozone maxima over the Arabian Sea (AS) during the pre-monsoon period.

In the following chapter, the V1.2 TOC captured regional pattern, the spring ozone maxima over the AS during the pre-monsoon period, is interpreted.

6 Tropospheric ozone observed over the Arabian Sea

6.1 Introduction

Inspired by the clear seasonal variation of TOCs over the AS observed in the V1.2 SCIAMACHY TOC product, in this chapter, I assessed the tropospheric ozone maximum observed over the AS. 7 years (2005-2011) of Tropospheric Ozone Column (TOC) data products from different satellite instrumentations: SCIAMACHY limb-nadir matching TOC (Ebojie et al., 2014) and the OMI/MLS TOC (Ziemke et al., 2006) showed an enhancement of TOC similar in magnitude as TOC's enhancements observed during the follow events: 1) the well-known biomass burning plume in the Southern Hemisphere that was transported over the South Atlantic, the coast of South Africa, along the Indian Ocean and towards Australia, 2) TOC attributed to anthropogenic sources in the Northern Hemisphere, and 3) the Mediterranean summer ozone pool (Fig. 6.1). A spring (or so called pre-monsoon, see Sect. 6.3) TOC maximum of ~42 DU on monthly average was identified from the study of the seasonality of the TOC.

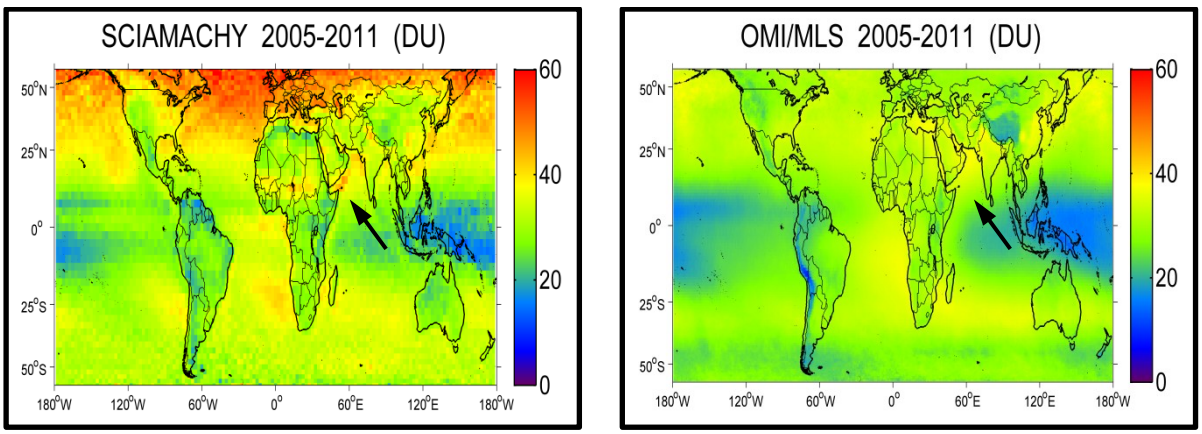

Figure 6.1. 7 years composite average for TOC retrieved from (left) SCIAMACHY Limb-Nadir Matching V1.0 and (right) OMI/MLS.

Spring maxima in TOC is not unique over AS but rather a well-known large scale phenomenon in the Northern Hemisphere. Nevertheless, the origin and mechanisms explaining this phenomenon are still a matter for debate (e.g. Monks, 2000, 2015 and references therein). The increase of tropospheric pollutants, presumably increase of longer lived VOCs which are ozone precursors, during winter, may play an important role by influencing the two major contributors to tropospheric ozone concentrations: the STE intrusions and the photochemical production process (Holton et al.,1995; Penkett et al., 1998; Monks, 2000). In a remote region like AS, an intuitive hypothesis is that long range transport (LRT) of ozone from more polluted regions or from STE may be the drivers. This is because of the longer ozone lifetime in spring and the weak local production over remote areas (Wang et al., 1998b).

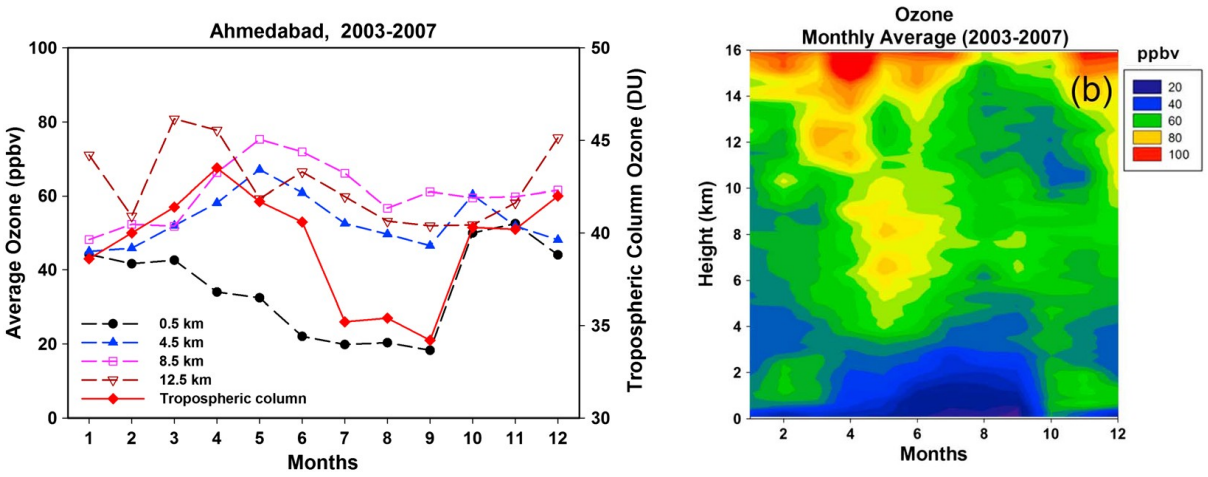

Figure 6.2. Average ozone (left) columns (ppbv and DU) and (right) vertical profiles of monthly averaged ozone mixing ratios (ppbv) during different months observed from the balloon ascents above the station Ahmedabad (23.03°N, 72.54°E) during 2003-2007 (Figs. 4(b) and 6 in Lal et al., 2014).

In previous studies using ozonesonde measurements above the west coast of India and the data from two campaigns (the 1998 and 1999 INDOEX – INDian Ocean EXperiment campaigns and the ICARB – Integrated Campaign for Aerosols, Gases and Radiation Budget campaign which was conducted during March-May 2006), the AS lower tropospheric ozone during pre-monsoon season was confirmed to be significantly influenced by LRT of the con-

tinental anthropogenically influenced outflows from the Middle East, Western India, Africa, North America and Europe (Lal and Lawrence, 2001; Chand et al, 2003; Srivastava et al., 2011, 2012; Lal et al., 2013, 2014). In addition, by comparing the INDOEX ozone measurements from both sides (northern and southern) of the ITCZ (InterTropical Convergence Zone), the influence of the ITCZ functioning as a sink for ozone was determined by the observed 4 times higher TOC values on the northern side of AS compared to the southern side (Chand et al., 2003). The seasonal variation of tropospheric ozone at Ahmadabad (23.03°N, 72.54°E) was reported to have an averaged maximum of ~44 DU in April during the years 2003–2007 (Fig. 6.2) (Lal et al., 2014). The possibility of the STE influencing the ozone mixing ratio up to ~10 km altitude was also discussed (right panel of Fig. 6.2). However, the mechanisms explaining this phenomenon need to be better understood.

Here, the TOC enhancement over the AS is investigated and interpreted by using TOC data products from several satellite remote sensors (i.e. SCIAMACHY Limb-Nadir Matching, OMI/MLS and TES), MACC (Monitoring Atmospheric Composition and Climate) reanalysis data (Inness et al., 2013) and simulations from the global tropospheric CTM MOZART-4 model (Model for Ozone and Related Tracers) (Emmons et al., 2010). This study focuses on the analysis of the regional contribution to LRT, the influence of the meteorological conditions, the local chemistry and STE, and the inter-annual variability of the spring ozone maxima. In Sect. 6.2, the regional distribution and the time series of tropospheric ozone and its precursors are investigated. Meteorological and photochemical sources of ozone plumes due to LRT, local chemistry and STE are discussed in Sect. 6.3. The role of accumulation of pollutants is also highlighted in this section. In Sect. 6.4 the impact of El Niño on the inter-annual variability is identified. Finally, conclusions are given in Sect. 6.5.

6.2 Observation of a pre-monsoon enhancement in TOC data products

Satellite retrieved TOCs have a better spatial and temporal coverage compared to ozonesonde measurements. However in situ measurements of ozone from ozonesondes are considered more accurate. Combining the two types of measurements provides an opportunity to investigate data-sparse regions such as the AS. Figure 6.3 shows the regional distribution of the TOC and two of its photochemical precursors: NO_2 and CO. Seasonal cycles of TOC, CO and NO_2 over the AS are shown in Fig. 6.4.

A seasonal pattern of TOC is observed in both OMI/MLS and TES. An offset of ~5 DU exists between the two investigated TOC data products. Regarding the SCIAMACHY Limb-Nadir Matching TOC, as referred in Sect. 5.6, only V1.2 can reproduce the ozone seasonality over AS. Since the V1.2 data set currently covers only 2 years, it is not suitable to be presented in the time series in the present manuscript. A maximum of TOC over AS is observed

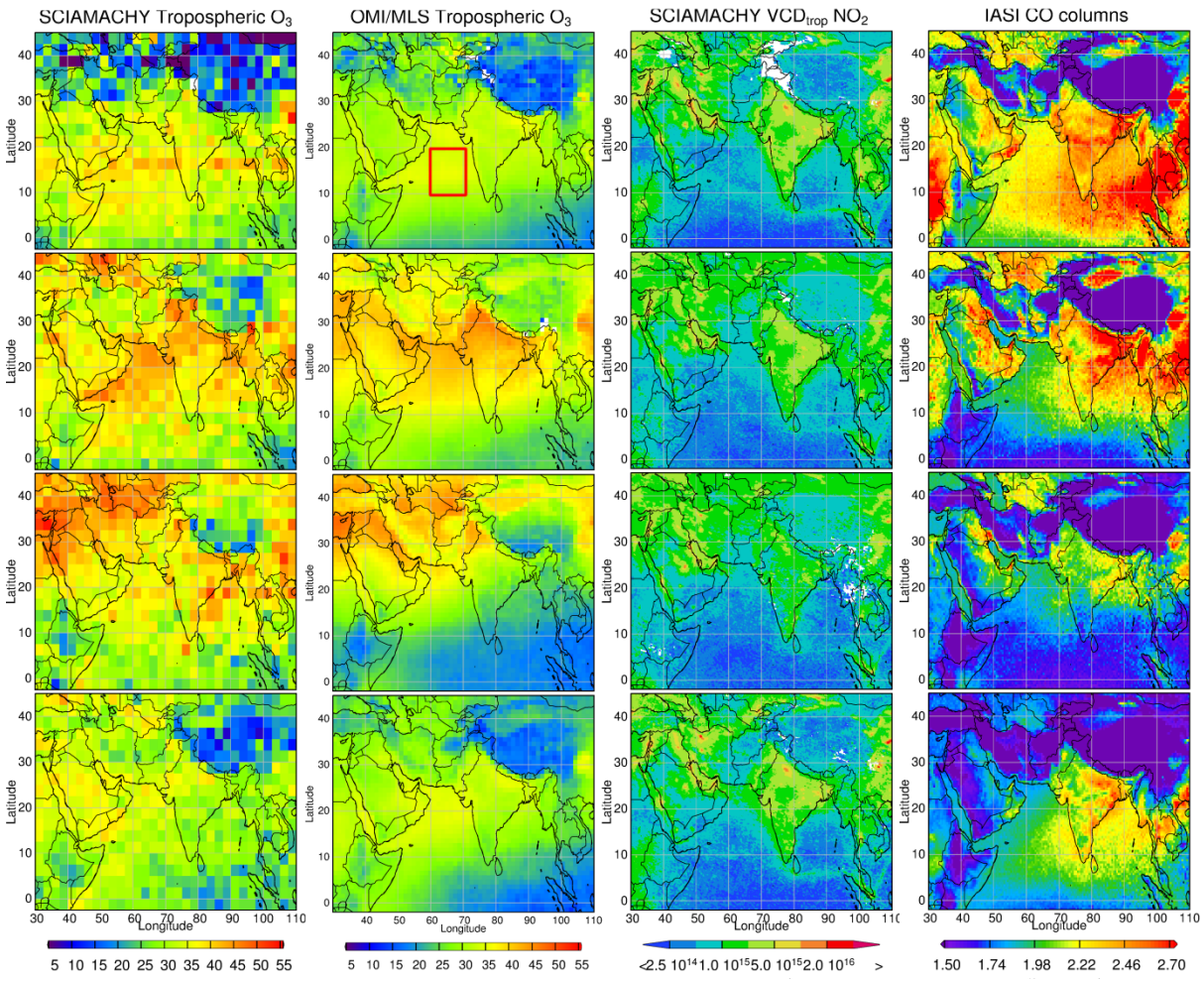

Figure 6.3. Plots of the TOCs (DU), NO_2 (molec/cm^2) and CO (x10^{18} molec/cm^2) as a function of season in 2008. Shown are from top to bottom DJF, MAM, JJA and SON.

(~42/47 DU) in every April during the years 2005–2012, followed by monsoon/summer minima of ~20 DU. TOC recovers to ~35 DU in the post monsoon autumn but drops down slightly during the winter monsoon. This seasonal pattern is consistent with the results from

the sonde station Ahmedabad (Fig. 6.2) and depends on the meteorological conditions (Sect. 6.3.1). The ozone precursors, CO and NO_2, show a different behaviour than ozone. As NO_2 has a short lifetime (2-8 hours, Beirle et al., 2011), the tropospheric NO_2 data products retrieved from observations of SCIAMACHY or other related instrumentation in space show high values over anthropogenic sources and relatively low values, often below the detection

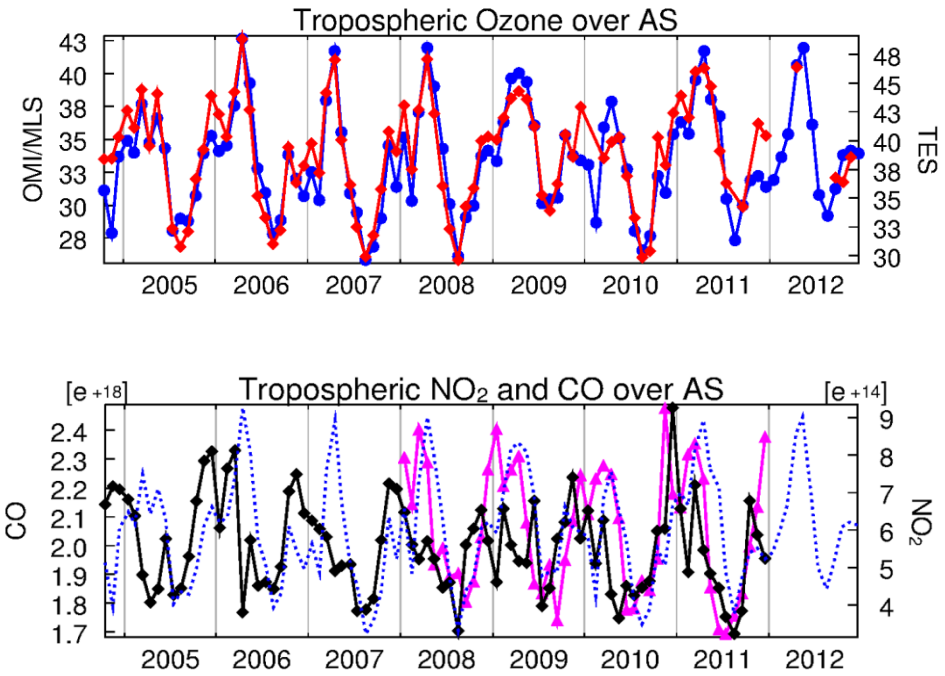

Figure 6.4. Trace gas time series over the AS (10-20°N, 60-70°E) from 2004 to 2012. The blue (solid and dashed) curves represent OMI/MLS ozone, red is TES ozone, magenta is IASI CO, and black stands for SCIAMACHY NO_2. The vertical columns are given in DU for ozone and molec/cm^2 for NO_2 and CO. The region used for this time series calculation is marked with a red rectangle in Fig. 6.3.

limit, over the remote regions. Over the AS, tropospheric NO_2 columns are small being around 10^{14} molec/cm^2. This small concentration originates from ship emissions and continental outflow (Richter et al., 2004). Higher values can be observed during the winter monsoon from transport off the Asian coast. CO has a longer life time than ozone (~2 months in average for CO and ~23 days for tropospheric ozone, Novelli et al., 1998b; Young et al.,

2013). Due to the relatively long lifetime of CO and ozone, both trace gases show a similar transport pattern. For instance, the biomass burning plume originating from Southern Africa in boreal autumn in the Southern Hemisphere can be observed as well for CO as for ozone. However, in comparison to ozone, the spatial pattern of CO is known to be more driven by emission than dynamical processes (Logan et al., 2008), which is not directly emitted itself, but produced due to the photochemical production. Thus, the time series of the data products for tropospheric CO reveal a similar winter maximum as NO_2, and it also shows a smaller peak in spring time as TOC. The spring peaks of CO are observed one month earlier than that those of TOC. This shift can be caused by the combustion emission of CO in Southern Asia (Fig. 6 in Duncan et al., 2003).

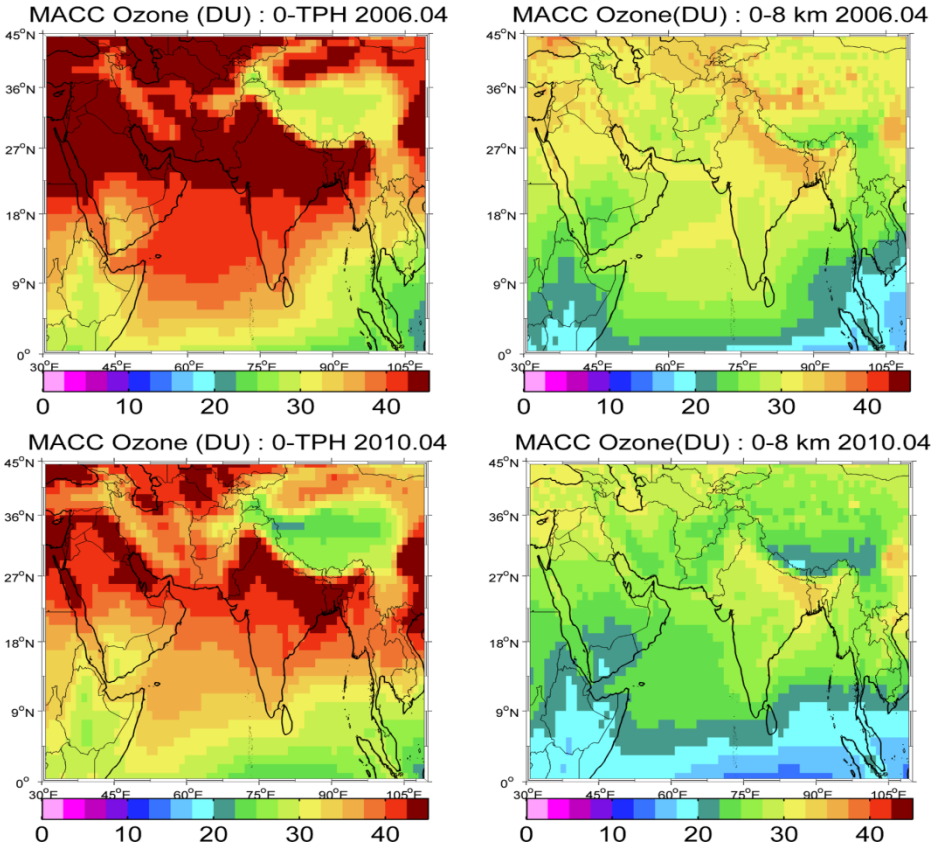

Figure 6.5. Ozone partial columns (TOC in the left panels and 0-8 km column of tropospheric ozone in the right panels) from MACC reanalysis data in April 2006 (upper panels) and 2010 (lower panels).

In this thesis, MACC reanalysis data is used to provide vertical information of ozone. This choice is motivated by the fact that OMI and MLS satellite ozone data were actively assimilated in the MACC reanalysis and constrain tropospheric ozone (Tab. 4.2). Figure 6.5 shows MACC results of ozone partial columns between 0 km and the TPH, determined from ECMWF retrieval as introduced in Sect. 4.3, and between 0-8 km, respectively. In a normal year (for instance in 2006, upper panels), the enhanced ozone during pre-monsoon is ~30 DU out of ~40 DU (~3/4) originating from the lower troposphere (0-8 km). Because of this result, possible origins will be discussed in the following section (Sect. 6.3) by analysing 4 various altitude ranges: 0-4 km, 4-8 km, 8-12 km and 12-18 km.

6.3 Potential origins of the AS pre-monsoon ozone pool

6.3.1 Influence of meteorology

The AS region is defined in this study as 10-20°N, 60-70°E on the west side of the subcontinental India. This location is influenced by the tropical/subtropical air mass exchanges and the sea breeze circulation (e.g., Lawrence and Lelieveld, 2010). The climate of AS can be devided into 4 different seasons, due to the seasonal variation of the ITCZ: winter-spring monsoon (Dec-Feb), pre-monsoon transition (Mar-May), summer monsoon (Jun-Aug), and post-monsoon transition (Sep-Nov). The strong westerly wind related to the summer Somali jet can be observed in the NCEP 10 meter sea surface wind data (Fig. 6.6) when the ITCZ is at its northernmost position. This condition causes strong precipitation, higher cloud cover frequency and increased air humidity over AS (David and Nair, 2013). The wind and strong precipitation 'wash' the air masses and remove soluble pollutants. A summer monsoon minimum for the trace gases such as shown in Fig. 6.4 may be expected. The destruction of ozone by reactive halogens is another potential sink for the ozone in the marine boundary layer (Dickerson et al., 1999; Ali et al., 2009). During the pre-monsoon transition, surface winds are westerly at the northern AS with an anticyclonic pattern centred over the middle AS. At this time, the AS is most of the time cloud-free and dynamically steady. This cloud-free anticyclonic condition possibly causes subsidence of air masses and results in accumulation of pollutants (Sect. 6.3.2). The ITCZ located at the southern part of the AS can become the

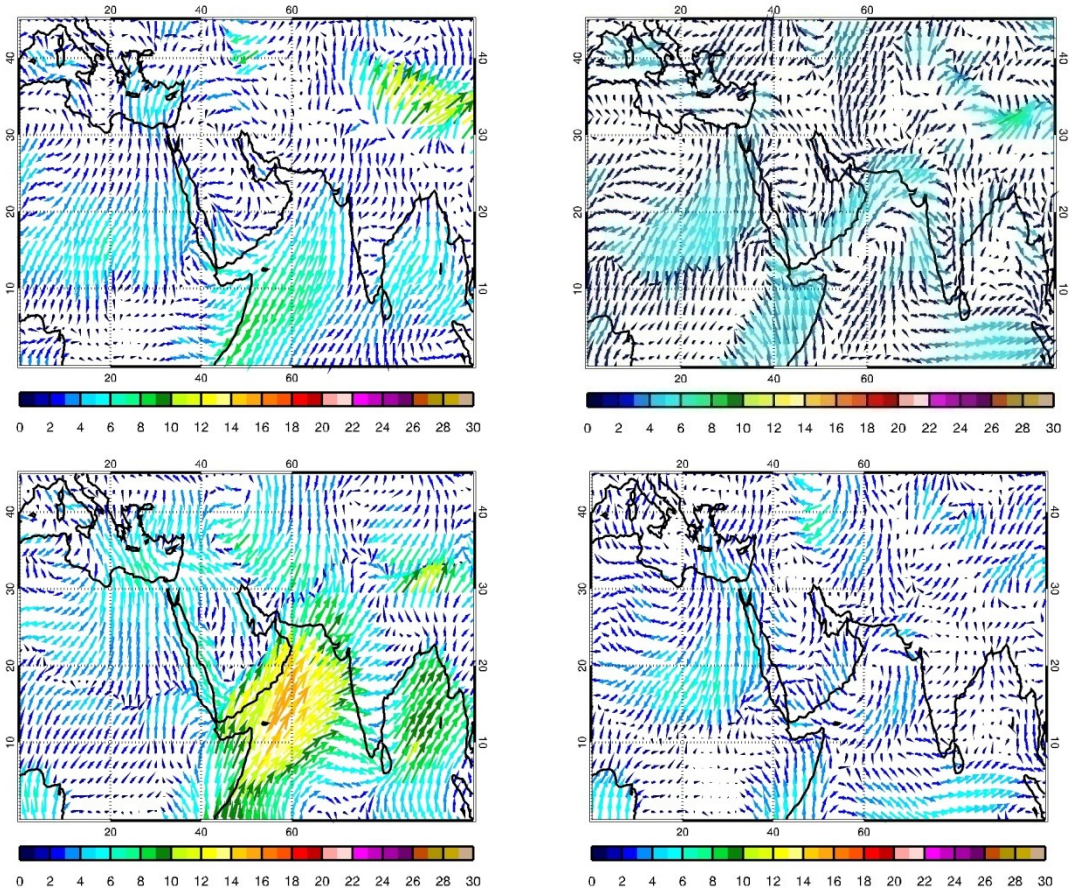

Figure 6.6. 10 meter sea surface wind on January (upper left), April (upper right), July (lower left) and October (lower right) over AS at 2008. Figure provided by Anne Blechschmidt from the University of Bremen.

'border' that stops the pollutants (in this case, tropospheric ozone) diffusing to the Indian ocean with ozone depletion on the surface of cloud droplets in the convective region (Lelieveld and Crutzen, 1990).

It is worth mentioning that the solar radiation over the AS, unlike in the middle/high latitudes where it is strongest in summer, reaches its maximum during pre-monsoon (Weller et al., 1998; David and Nair, 2013). One could argue that a maximum solar radiation can cause stronger photochemical reactions and thus an increased ozone concentrations. The contribution of the photochemical production will be investigated in Sect. 6.3.3.

6.3.2 Long range transport mechanism and air mass accumulation

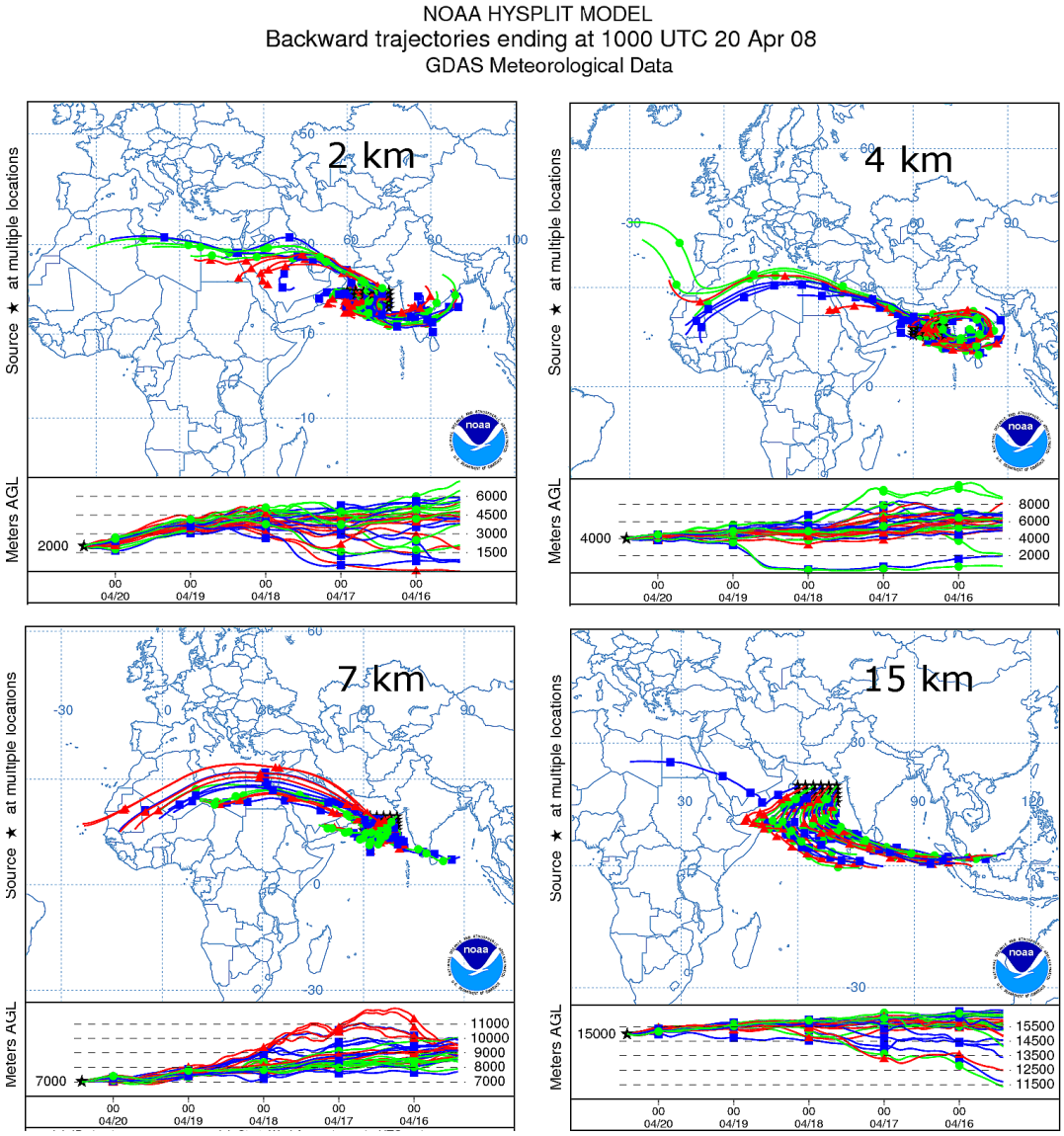

Figure 6.7. HYSPLIT trajectory model results for air masses at AS with source location at 2, 4, 7 and 15 km. The results are from the 120 hr backward trajectories.

It is established in the previous studies that LRT plays an important role in the AS pre-monsoon ozone pool (Lal and Lawrence, 2001; Chand et al, 2003; Srivastava et al., 2011, 2012; Lal et al., 2013, 2014). For example, the satellite data products for CO and TOC are highly correlated (Fig. 6.4). Trajectory models are used to investigate the LRT pathways of

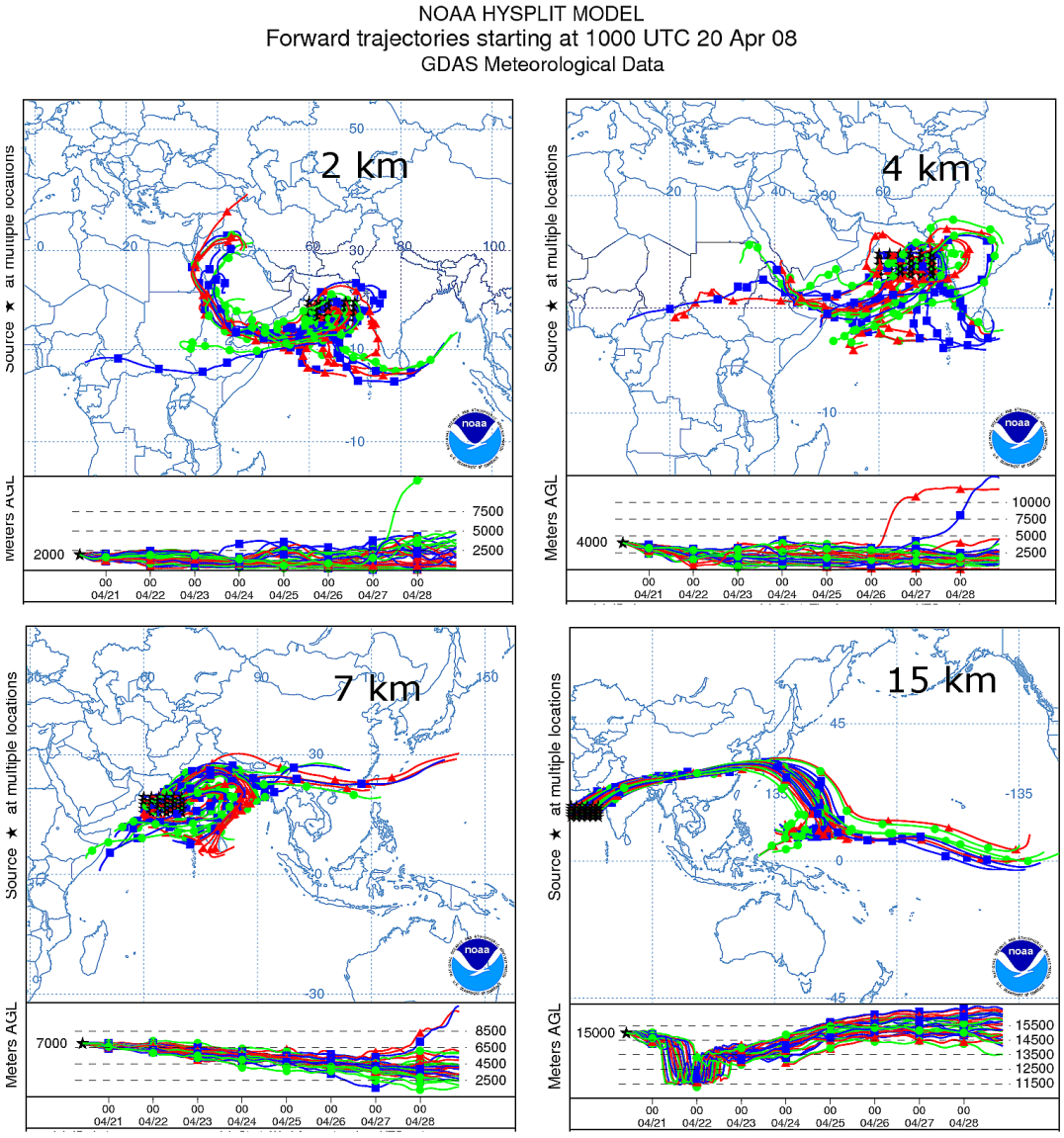

Figure 6.8. HYSPLIT trajectory model results for air masses at AS with source location at 2, 4, 7and 15 km. The results from the 240 hr forward trajectories.

the air parcels. Figures 6.7 and 6.8 show an example of the HYSPLIT backward and forward trajectory results for air masses over AS at 2, 4, 7 and 15 km in April 2008. In the lower troposphere (0-8 km), the sources are identified as the Middle East, India and North Africa, which are consistent with the previous studies. The higher tropospheric ozone (12-18 km) is

found in air which was uplifted and transported from the North Indian Ocean and Southeast Asia. The air masses in the lower troposphere subsides 4-5 km locally within a high pressure system within 10 days. This confirms the conclusion on accumulation of pollutant which was derived from the wind field information in Sect. 6.3.1 (see Fig. 6.6). This theory was also proved by Srivastava et al. (2011) from the TPSCF (Total Potential Source Contribution Function) results. One explanation for the larger TOC over the AS in comparison to surrounded regions is the lower humidity which provide less favorable condition for ozone depletion by OH radicals (Fig. 6.13). This is further discussed in Sect. 6.3.3. In addition to the sources, here I also investigate the areas that are influenced by the AS ozone pool (Fig. 6.8). The ozone-rich air over the AS is transported back to India (lower left panel). HYSPLIT also simulates transportation to the Red Sea through the Gulf of Aden in the lower troposphere (upper panels), which is expected because of the mountains aside acting as a barrier for pollution transport. The elevated tropospheric air masses are also transported towards the Pacific Ocean via China (lower right panel).

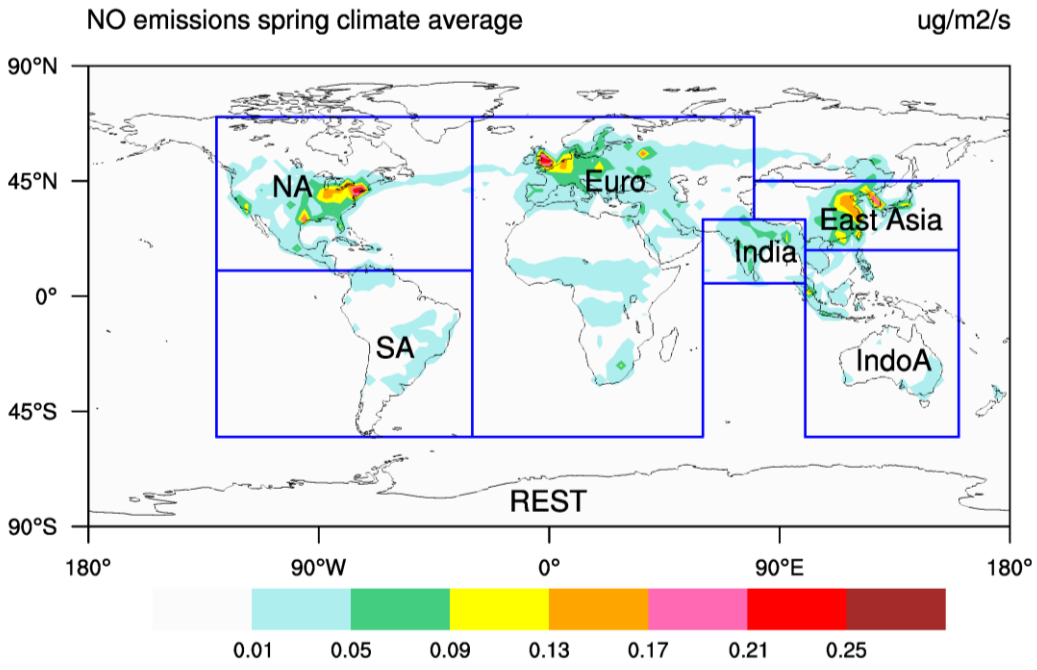

Figure 6.9. Regional separation for tracer tagging with distributions of the spring mean emission rate (µg/m^2/s) of NO (including anthropogenic, biomass burning, and soil emissions) at the surface used in the model simulations during 1997–2007. Figure provided by Xuewei Hou from Nanjing University of Information Science and Technology.

To quantify contributions to LRT from different source locations, the tagged tracer simulation with MOZART-4 CTM (Sudo and Akimoto, 2007; Hou et al., 2014) during 1997-2007 was used. Figure 6.9 shows the seven tagged regions. Europe, Africa and the Middle East are combined into one hot spot as the closer western region (named 'Euro'). India, Bay of Bengal and AS are presented together as the closer eastern region (named 'India'). Note that when evaluating the contribution from this region, the influence from pollutant accumulation over the AS should always be considered. The Indian ocean is included in the 'Rest' region. 'NA' and 'SA' represent North America and South America respectively. The regions are divided due to the time consumption of the model calculation. For further studies, another arrangement can be considered.

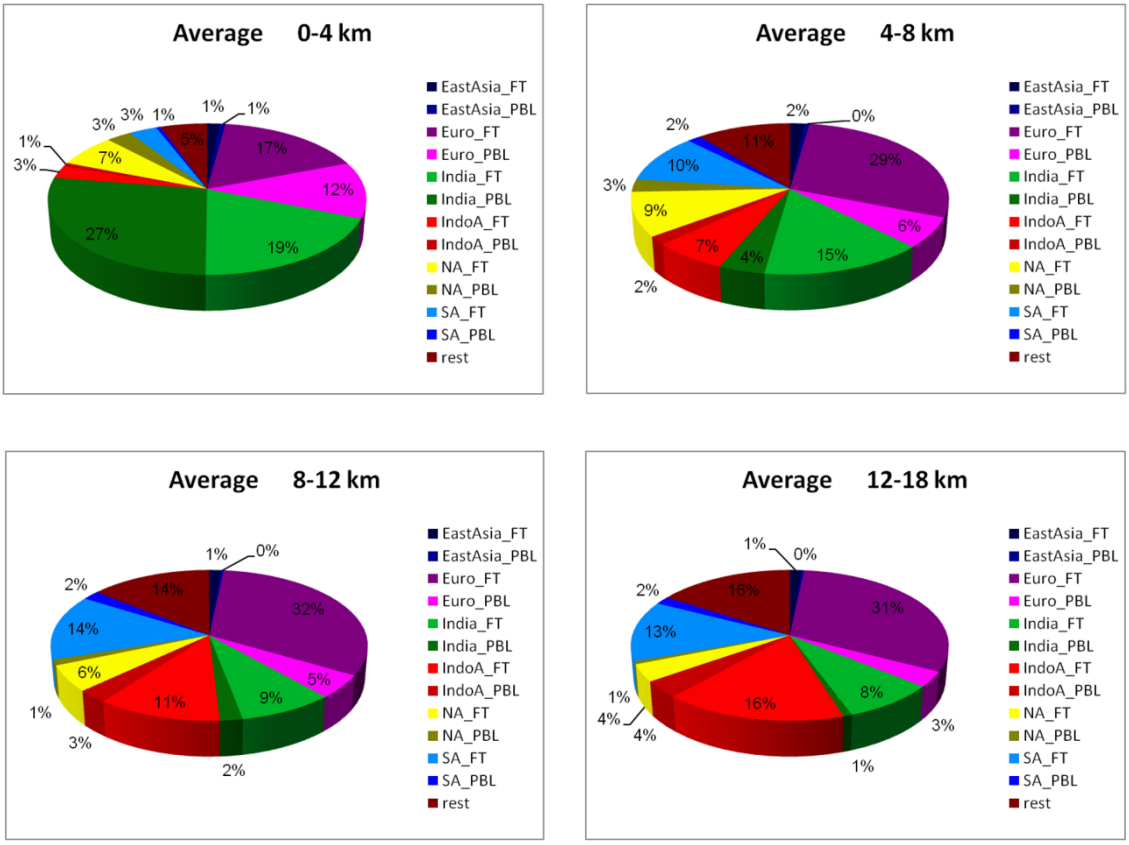

Figure 6.10. Averaged LRT contributions to the AS tropospheric ozone concentration from different source regions to 4 atmospheric layers over the AS in April 1997-2007. PBL (planetary boundary layer) is defined as the region from surface to the top of the boundary layer. FT (free troposphere) is defined as extending to the tropopause above the BL.

The source region distribution varies for different altitude ranges (Fig. 6.10). In the 0-4 km layer, ~30% of the transported ozone comes from the 'Euro' region. The 'India' region is the biggest source region that contributes 50%, of which 60% comes from the boundary layer. In the 4-8 km layer, the influences of the boundary layers are much smaller, while 'Euro_FT' contributes ~10% more than to the 0-4 km layer. The far-away source regions ('NA', 'SA' and 'IndoA') become non-negligible (~10% each). The contribution from 'IndoA' increases with height. Since the Indian ocean is included, an increased contribution from 'Rest' with altitude is expected. In conclusion, the main contributor to LRT is 'Euro_FT' with 30% contribution in average, followed by the 'India' region with over 20% contribution. The inputs from far-away source regions are similar, with ~10% each. The influence from East Asia is negligible. Note that the air masses in the higher altitudes are normally quickly removed by the strong advection (Fig. 6.11). The contributors in the lower altitudes (<12 km) have more influences on the ozone accumulation.

6.3.3 Local chemistry

This section addresses two questions: (1), What is the role of the photochemistry for TOC above AS? (2), Has more ozone been photochemically produced during the long accumulation time in the middle (4-8 km) or lower (0-4 km) troposphere?

The ozone budget is calculated in the MOZART-4 model (Fig. 6.11) within the 1997-2007 time period. Photochemistry plays a very different role in the four altitude ranges. In the 0-4 km layer, water vapour acts as a source of OH radicals and depletes ozone. Compared to the photochemical production, this depletion process dominates (Nair et al., 2011). Thus a net reduction of ozone in chemistry was observed. In the higher layers (8-12 km, 12-18 km), photochemical production becomes a major source of ozone, while advection being the major sink. Zahn et al. (2002) estimated that the annual net ozone production rates over AS are 17.6 $x10^{10}$ molecules cm^{-2} s^{-1}, by using the CARIBIC (Civil Aircraft for the Regular Investigation of the atmosphere Based on an Instrumented Container) aircraft data from 10-11 km altitude. However, Livesey et al. (2013) showed in MLS data that such maximum of ozone amount around 215 hPa (~ 11 km) in pre-monsoon season is most likely a zonal pattern. In the 4-8 km layer, the budget is rather small with a net inflow by advection. The net chemistry is less than -0.1 ppbv per day, indicating a negligible sink.

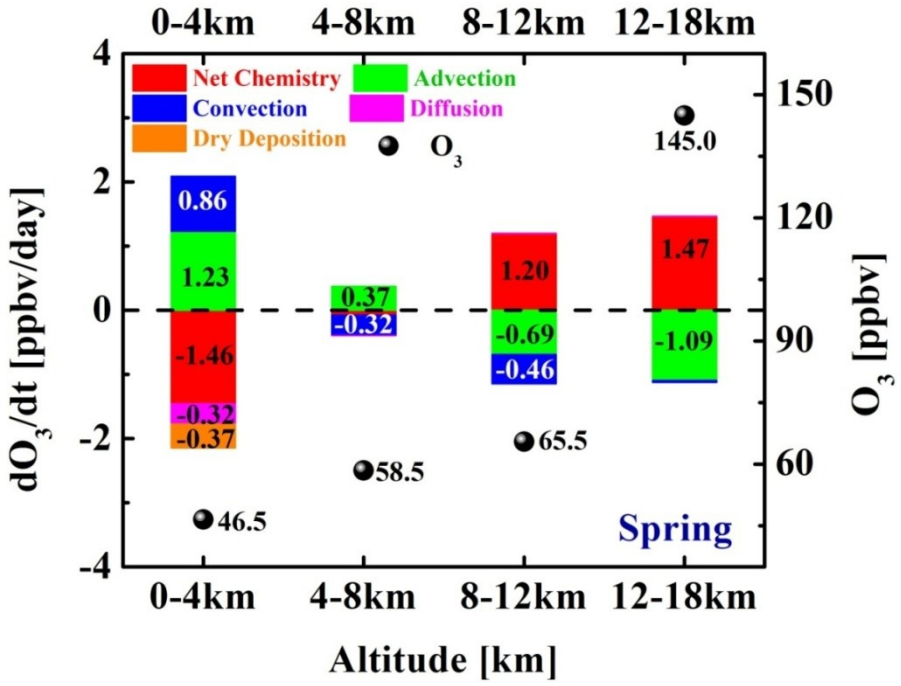

Figure 6.11. Averaged ozone budget in pre-monsoon from MOZART-4 at four layers over AS region. The ozone partial columns (ppbv) calculated from MOZART-4 is presented as black dots. Figure provided by Xuewei Hou from Nanjing University of Information Science and Technology.

The O_3-CO correlation has been broadly used to indicate tropospheric O_3 sources (Fishman and Seiler, 1983; Kim et al., 2013). A positive O_3-CO correlation denotes considerable chemical production of O_3. A negative correlation, on the other hand, can originate from chemical O_3 loss or deposition, or can suggest that the air mass is either transported from the stratosphere, or moved by advection from the free troposphere. Figure 6.12 shows the O_3-CO correlation at 4-8 km in April using MACC data. The left panel is a typical correlation result with strong negative correlations over AS (See also appendix Fig. A1). This correlation suggests that a chemical production of ozone is most likely not the cause for the observed ozone enhancement. Some ozone production is expected (e.g., year 2006 in the right panel), but this kind of situation is rare.

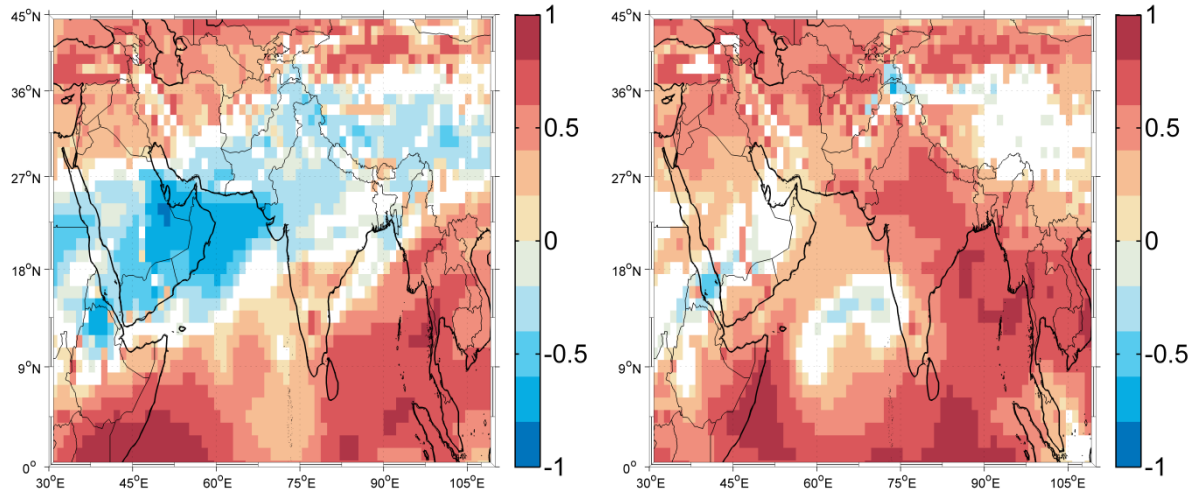

Figure 6.12. O_3-CO correlations calculated for 4-8 km column abundances with 3 hr temporal interval in April 2008 (left panel) and 2006 (right panel) from MACC reanalysis data.

The averaged specific humidity in-between 4-8 km was used to investigate evidence for the impact of HO_x removal on ozone in clean air conditions (Fig. 6.13):

$OH + CO + O_2 \rightarrow HO_2 + CO_2$ (R 24)

$HO_2 + O_3 \rightarrow OH + 2\ O_2$ (R 25)

Net $CO + O_3 \rightarrow CO_2 + O_2$

Unlike the humid lowest troposphere, the air masses over the AS at 4-8 km are rather dry compared to the surroundings. This can be explained by adiabatic lifting and expansion of marine boundary air followed by condensation and removal for H_2O. The lifting is stronger over land than over ocean due to the temperature differences. This is also one of the reasons that Southeast Asia has strongest convection. The dry air at 4-8 km can cause the depletion contribution from OH radicals to be smaller, thus it is more suitable for ozone accumulation. Hence the AS ozone columns in the 4-8 km altitude region are expected to be higher than its surroundings.

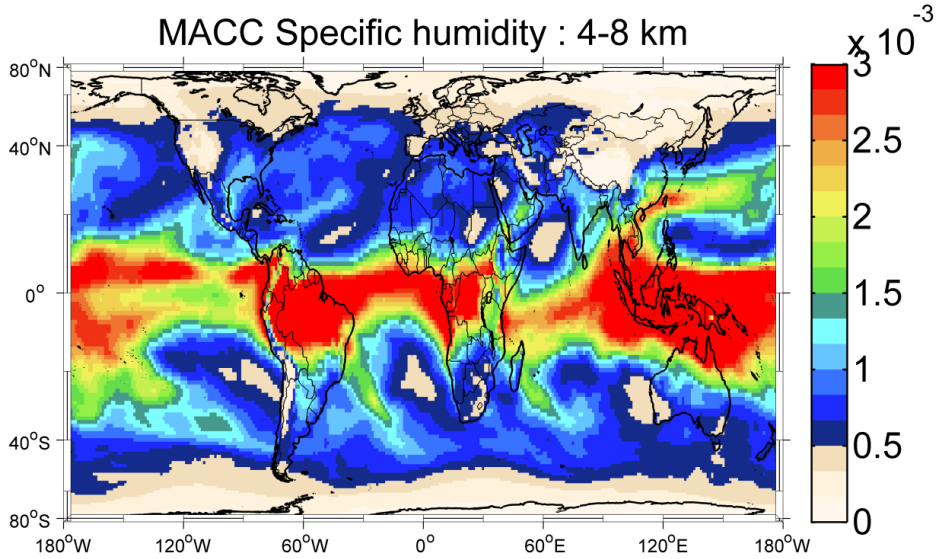

Figure 6.13. Specific humidity (kg/kg) at 4-8 km in April 2006 from MACC reanalysis dataset.

6.3.4 Stratosphere-troposphere exchange

The ozone concentrations in the extra-tropical lower stratosphere show a maximum in late winter/early spring as driven by the Brewer-Dobson circulation (e.g., Fortuin and Kelder, 1998; IPCC/TEAP, 2005). Fadnavis et al. (2010) indicated ozone stratospheric intrusion during winter and pre-monsoon season over the Indian region (5-40°N, 65-100°E) by using both satellite and model data. One stratospheric intrusion was observed over AS during the ICARB campaign (Lal et al., 2013) in 5 May 2006 (Fig. 6.14). However, it is not clear yet how much and how deep the influence can be. In our study, the STE contribution simulated by MOZART-4 tagged tracer method is comparable with the ones transported from 'Euro_FT' in each altitude range. The STE origin might be a reason for the strong negative O_3-CO correlation since the chemical loss and deposition are excluded (Sect. 6.3.3).

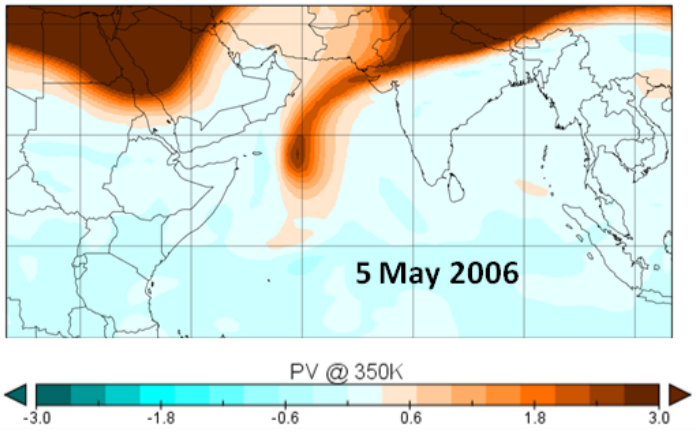

Figure 6.14. Potential Vorticity from ECMWF data.

6.4 ENSO and Interannual variation

Two spring anomalies are depicted in 2005 and 2010 where ozone is ~5 DU lower compared to other years (upper panel of Fig. 6.4). The decrease in 2010 is most likely to be the anomaly of the lower troposphere ozone as observed in Fig. 6.5. The two following facts suggest the anomaly to be dynamical: (1), the ozone reduced in a similar amount at continental surroundings; (2), similar to ozone, a lower CO maximum appeared in 2010 (lower panel of Fig. 6.4).

The El Niño events, as driven by the persistent Walker Circulation, affect the temperature, humidity and biomass burning emissions, thus influence the trace gases including ozone. Particularly, the tropospheric ozone anomaly related to El Niño events during the year 1997-1998 was intensively studied (e.g. Chandra et al., 1998; Sudo and Takahashi, 2001). The tropospheric ozone increased (up to 25 DU in the burning season) over the equatorial western Pacific due to a reduced convection and growing burning emissions, whereas decreased (4-8 DU) over the eastern Pacific because of the change in meteorological conditions. By using a model simulation, Zeng and Pyle (2005) reported that the tropospheric ozone concentration at specifically the equatorial region 40-70°E decreases with similar amount as over the eastern Pacific during El Niño events. Ziemke et al. (2010) showed that the ENSO related response of tropospheric ozone over the western and eastern Pacific dominated interannual variability. An Ozone ENSO Index (OEI) was formed to represent the ENSO impact. The OEI was calculated by subtracting the eastern and central tropical Pacific region tropospheric ozone

(15°S-15°N, 110-180°W) from the western tropical Pacific-Indian Ocean region (15°S-15°N, 70-140°E) with the fact that the zonal variability of tropic stratospheric ozone is only ~1 DU.

Figure 6.15 shows the OEI index that is produced from OMI/MLS data for the related time period (dark red curve). I performed a 'correction' of OMI/MLS TOCs over the AS by adding the OEI index. The ozone spring maxima anomalies at pre-monsoon season in 2005 and 2010 (blue curve) can no more be seen after the 'correction'. This indicates that the El Niño induced dynamics might contribute to the interannual variability over pre-monsoon AS ozone. Since OEI contains both chemical (fire) and dynamical influences in the burning season, ozone peaks (in the red curve) can be observed in the winter of 2006 and 2009 when strong fires happened in Indonesia.

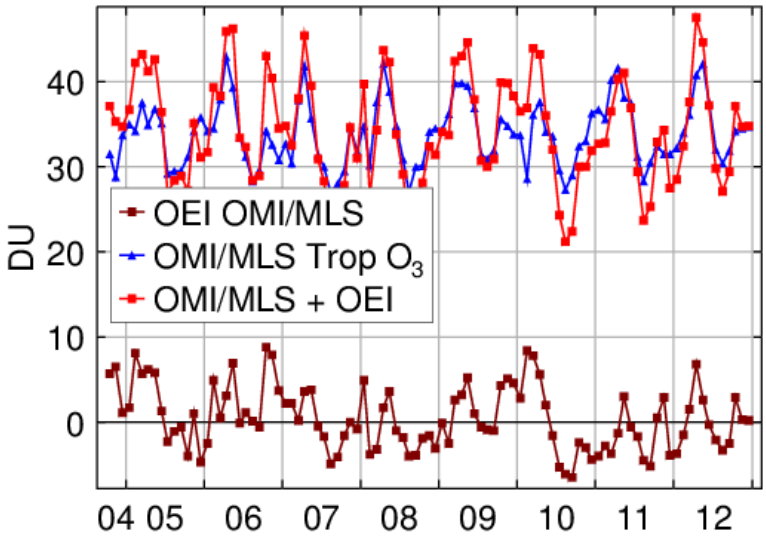

Figure 6.15. Tropospheric ozone time series 'corrected' with OEI over AS (10-20°N, 60-70°E) from 2004 to 2012. The blue curve represents OMI/MLS ozone, dark red is OEI calculated from OMI/MLS and red stands for OMI/MLS ozone with OEI 'correction'.

The dynamical influence of El Niño can be found in two aspects. El Niño can induce an increase of Sea Surface Temperature (SST) thus strengthen the water vapor upwelling to the middle troposphere, and then reduce the life time of ozone. It also possibly triggers changes in STE flux as mentioned by e.g. Neu et al. (2014). Moister air masses are observed from MACC reanalysis data in April 2010 (appendix Fig. A2). This confirms the assumption of the

SST influence over AS. A STE flux variation can be caused by both El Niño and La Niña events. In this case La Niña events (in 2011) didn't contribute as much as El Niño events (in 2005 and 2010). The impact of El Niño is mainly expressed by the SST anomaly instead of the STE anomaly.

6.5 Conclusions

The 7 years composite averaged values for TOC presented here exhibit a seasonal pattern and have values similar to those in the Southern hemispheric biomass burning plume. A disciplined tropospheric ozone seasonality with a ~42 DU maximum at the pre-monsoon season was shown in the satellite based OMI/MLS and TES observations as well as in the MACC reanalysis model. The seasonal feature is found to be strongly related to the meteorological conditions.

Previous studies illustrated the importance of LRT to the pre-monsoon ozone enhancement and confirmed the source locations to be the Middle East, West India, Africa, North America and Europe. Here various regional contributions to the AS pre-monsoon ozone through LRT were analysed by dividing the global range into 7 regions using the MOZART-4 tagging tracer simulation method. In the lowest 4 km, the sources from India contributed ~50% of the transported AS ozone amount. The free troposphere of the Middle East, Africa and Europe (so called 'Euro_FT') started to play a major role from 4 km altitude and higher. The contribution is on average 30%. The Indian region is still the second important source region at 4-8 km with ~20%. Its contribution is slowly replaced by the further-away source regions at higher altitude range. It is worth mentioning that South America plays a more important role compared to North America, yet there is no explanation for this result so far.

In addition, the vertical pollutant accumulation in the lower troposphere, especially at 4-8 km, is important to the AS spring ozone pool. The suitable meteorological conditions were discovered from wind field data from NECP and specific humidity data from MACC. First, the cloud-free anticyclonic condition that is observed from the wind field data can cause air to be transported upside down. This point is supported by the forward model results of HYSPLIT showing that from ~7/8 km on the air circles down over the AS region for around 10 days without diffusion. Second, at 4-8 km the air over AS is much dryer than the surroundings.

This is most probably due to relatively lower temperature over the sea which caused that the moisture cannot be lifted up as high as over land. The dry air conditions induce the accumulation of ozone with a longer life time thus cause the AS ozone to be outstanding from the sub continental regions.

The averaged spring ozone budget was calculated using MOZART-4 to improve our understanding of the additional local chemical activity. Ozone is photochemically produced at high altitudes (8-18 km) and is removed by advection. In the lowest 4 km ozone is depleted by OH radicals. Positive ozone budgets from advection and convection can be observed, which supported the LRT and accumulation mechanisms. At 4-8 km, despite the weak ozone destruction from OH radicals, the net chemical budget is negligible. This suggests a low photochemical production, which is also supported by the negative O_3-CO correlation. According to the simulation results and the O_3-CO correlation, a net contribution from STE can also influence the local ozone amount.

The two spring ozone interannual anomalies are believed to be influenced by the dynamical variations (SST anomaly) during the El Niño events.

7 Conclusions and outlook

Tropospheric ozone is one of the most important green-house gases and one of the most important components of photochemical smog. Monitoring satellite-based tropospheric ozone columns (TOCs) is of critical importance in order to gain knowledge on phenomena affecting air quality and the greenhouse effect. This thesis is focused on the improvement and interpretation of satellite-based TOCs retrieved from SCIAMACHY measurements using Limb-Nadir-Matching method.

Improvement of the Limb-Nadir-Matching retrieval

The Limb-Nadir Matching method is a residual method that is developed for TOC retrieval using the SCIAMACHY instrument. In this method the stratospheric ozone columns retrieved from the limb measurements are subtracted from the collocated total ozone columns acquired from nadir measurements by using the tropopause height data. Along with the fact that the TOCs are only ~10% of the total ozone columns, the accuracy of the retrieved TOCs is quite challenging. A three-step optimization is applied to the original retrieval approach.

1) Cloud top height (CTH) data needed in the retrieval is switched to using the SCODA database to screen cloud-free limb data. Previously, the cloud flag information available in the limb ozone data sets was applied. The CTH data plays a crucial role in selecting the uncontaminated limb ozone profiles. This selection directly influences the accuracy of the stratospheric ozone columns as well as the total data amount of retrieved TOCs. The cloud flag information that was originally used corresponds to a CTH ~3.3 km larger than the SCODA CTH values. For a cloud flag equal to 0, the limb data is guaranteed to be cloud-free in the respective vertical field of view of ~2.7-3.3 km. Using the SCODA CTH instead of the cloud flag yields a significant data amount increase of ~100% for the finally retrieved TOC data sets while the low standard deviation of the measurements remains preserved.
2) The ECMWF tropopause height (TPH) implemented in the retrieval is optimized temporally and spatially for each collocated SCIAMACHY limb ozone data. TPH is an imperative information which is required to gain the exact stratospheric ozone column by interpolating existing limb profiles down to the altitude of the tropopause. A

variation of 500 m in the TPH induces an error of the stratospheric ozone of only ~0.1 DU. However, this range of variation is only suitable in the tropics. In the mid- and high latitudes, the TPH variation is often more than 1 km within a short horizontal distance. On average, the original strategy to retrieve the limb-collocated TPH (nearest UTC time and lowest values, details presented in Sect. 3.2.2) induces an underestimation of ~3 DU of the gridded (2.5° x 2.5°) TOCs. The underestimation can exceed 7 DU for individual grid boxes and can easily be larger than 10 DU for individual TOCs. An improvement is achieved by the chosen interpolation scheme for matching TPH data and limb measurements. The new TPH for the matching limb measurement is calculated as the mean value of the TPH values at the four corners of the measurement footprint. At each corner the corresponding TPH is calculated by linearly interpolating ECMWF data from the UTC time to the SCIAMACHY overpass time.

3) A new version of the SCIAMACHY limb ozone scientific data set (V3.0) is implemented instead of the previous V2.9 data set after extensive comparisons with ozonesonde measurements for the time period of 2003-2011. The V2.9 limb ozone data underestimate ozone by up to ~15% vertically in the northern high latitudes, which equals to 12 - 20 DU for stratospheric ozone partial-columns in the 20-30 km altitude range. The new V3.0 has been developed to reduce the underestimation. The retrieval between limb ozone V2.9 and V3.0 are substantially different. In the visible spectral region V2.9 uses a reference tangent height and the triplet method, while V3.0 employs a solar spectrum as reference and performs a DOAS-type fit. As a result, the differences between the satellite retrieved tropospheric ozone and the ozonesondes are reduced to within 10% for vertical profiles and 5 DU to 10 DU for stratospheric partial-columns (in the 20-30 km range) northward of 40°N. The V3.0 limb ozone data cannot be used for Limb-Nadir Matching directly due to a negative bias existing at an altitude of ~ 35 km caused by a lack of spectral information from the Huggins band. The up-coming V3.5 fixed the underestimation while maintaining the good vertical accuracy of V3.0. However, V3.5 is still under investigation, thus the V3.0 limb ozone data set is implemented in the present study with a linear interpolation correction at 35 km.

The original TOCs exhibit an underestimation of ~10 DU in the tropical Atlantic, more than 10 DU overestimation in the high latitudes, and variable overestimation in the midlatitudes. The boreal autumn biomass burning provoked ozone propagation pattern in the Southern

Hemisphere of this version displays an unrealistic distribution pattern due to the incorrect determination of diffusion.

After the optimization in CTH and the TPH, the resulting data amount of the retrieved TOCs is increased by a factor of two as compared to the original retrieval. This version (V1.1) of TOCs correct most of the artificial oscillations encountered before and shows a more clear overview of the achievements and disadvantages in using V2.9 limb ozone data.

The TOCs retrieved using V3.0 reduced the negative and the positive biases over tropics and high latitudes, respectively. The column values are also optimized over the midlatitudes by decreasing the positive biases. However, a positive bias still occurs in the local summer period when ozone reaches its peaks. The V1.2 results agree with ozonesonde measurements within 5 DU in the annual global mean. The biomass burning pattern is properly observed. More details are successfully captured, including the Mediterranean ozone pool, the ozone outflow from Central Africa, as well as the spring ozone maxima over the Arabian Sea (AS) during the pre-monsoon period.

In summary, the Limb-Nadir Matching retrieval improvement scheme developed in this thesis leads to a much more accurate TOC product measured by SCIAMACHY.

Tropospheric ozone maxima over the AS

The 7-year averaged values for TOC presented over the AS exhibit a seasonal pattern and have values similar to those in the Southern hemispheric biomass burning plume. A distinct tropospheric ozone seasonality with ~42 DU maximum in the pre-monsoon season was shown in the satellite based SCIAMACHY Limb-Nadir Matching, OMI/MLS and TES observations as well as with the MACC reanalysis model. The seasonal feature is strongly related to the meteorological conditions. The potential sources are investigated and reported:

- LRT is of importance for the pre-monsoon ozone enhancement. Various regional contributions to the AS pre-monsoon ozone through LRT are analysed using the MOZART-4 tagging tracer simulation method. For this purpose, the global map is divided into seven regions. The source from India contributed ~50% of the transported AS ozone amount in the lowest 4 km, and ~20% in the 4-8 km altitude range. The free troposphere of Middle East, Africa and Europe play the main role in altitudes above 4 km with an averaged contribution of ~30%.

- In addition, the vertical pollution accumulation in the lower troposphere, especially at 4-8 km, is important for the AS spring ozone pool. NCEP wind field data were used to analyse suitable meteorological conditions for the generation of the ozone pool. It was discovered that during anticyclonic conditions tropospheric ozone levels increase due to air being transported from higher altitudes downwards. Furthermore, as observed from MACC specific humidity data, the air over AS is much dryer than in the surroundings at altitudes of 4-8 km. This dry condition induces a longer lifetime of the accumulated ozone thus causing the AS ozone to exceed the ozone amount above the sub continentals.
- The additional local chemical activity was investigated by calculating the averaged spring ozone budget using MOZART-4. At 8-18 km altitude, ozone is mainly photochemically produced and removed by advection. In the lowest 4 km, ozone is depleted by OH radicals. At 4-8 km, despite the weak ozone destruction from OH radicals, the net chemical budget is negligible, suggesting a low photochemical production of ozone.
- Due to the simulation result and the correlation between ozone and CO, it can be concluded that a net contribution from STE may also influence the local ozone amount.

Two identified spring ozone interannual anomalies are believed to be influenced by the dynamical variations during the El Niño events.

Outlook for future studies

Based on the work presented in this thesis, the following prospects for future research are identified.

Regarding the TOC retrieval using the SCIAMACHY Limb-Nadir-Matching method:

- The retrieval method of the limb ozone may be further improved based on the results of V3.0 and V3.1. An optimized version needs to be chosen from the developed versions with the help of validation. Validation has been applied to the recent versions V3.2 to V3.5 showing continuous minor improvements in the retrieval. These efforts will continue.
- The chosen limb ozone data shall be implemented into a further improved Limb-Nadir Matching method to retrieve the TOCs. Because the limb data is still under optimiza-

tion and a final version is not available yet, in this thesis no report on the final retrieval error of the new V1.2 TOC data set could be included. With a fixed new limb data set, it will become possible to quantify the biases and retrieval errors of the correspondingly generated TOCs. With a longer data set time span (August 2002-April 2012), the global tropospheric ozone variations can be updated from the ones reported by Ebojie et al. (2016) as well.

Regarding the application of the TOC data set:

- Ziemke et al. (2010) used the correlation between TOC and the ENSO index (upper panel in the left side of Fig. 7.1) to investigate the Ozone ENSO Index that shows the ENSO related response of tropospheric ozone over the western and eastern Pacific. I have investigated the correlation relationship between tropospheric ozone and tropospheric NO_2. Both data sets are retrieved by the SCIAMACHY Limb-Nadir Matching method (lower panel in the left side of Fig. 7.1). The global correlation distribution map of tropospheric ozone and NO_2 shows the potential to distinguish sources, e.g., urban pollution (red boxes), biomass burning (green boxes), or lightning (blue box). In addition, the correlation results can help to understand the behaviour of other trace gases (purple boxes), e.g., long range transport of tropospheric NO_2 over the Indian Ocean (Kunhikrishnan et al., 2004), by using TOC data from SCIAMACHY. Following this framework, it is possible to further exploit the potential of combining tropospheric ozone with its precursors.
- The negative correlation of tropospheric ozone with CO over AS in April hints at the possible influence by STE, chemical deposition, or lightning. The positive correlation with NO_2 over the Tibetan Plateau may indicate a possible influence of lightning in producing ozone besides the influence of STE. The influence of lightning on tropospheric ozone values over AS and over Tibetan Plateau needs to be better understood. Further investigation is possible by performing simulations with/without the impact of lightning using models such as MACC.

Regarding a continuous limb data record, thus a continuous Limb-Nadir Matching TOC data record:

- While most of the limb/occultation instruments mentioned in the present thesis have unfortunately stopped working due to their limited lifetime, there are currently still three limb instruments in orbit – the limb-scattering Odin-OSIRIS, the limb-emission

Aura-MLS, and the latest launched limb-scattering OMPS. The OMPS (Ozone Mapping and Profiler Suite) is the next generation of back-scattered Ultraviolet radiation sensors as a part of the NASA project JPSS (Joint Polar Satellite System). OMPS is proposed by Ball Aerospace and Technology Corporation as the ozone measurement component of the National Polar-Orbiting Environmental Satellite System (NPOESS) in 1998 (Jaross et al., 2014). It is desired to measure global ozone, aerosols and reflectivity. The first OMPS instrument is currently onboard the Suomi NPP (Suomi National Polar-orbiting Partnership, launched on 28 October 2011) spacecraft with a 13:30 local equator crossing ascending node. The following OMPS instruments will be included on the future JPSS-1 and JPSS-2 satellites which are planned to be launched in 2017 and 2021, respectively. OMPS contains three spectrometers: a downward-looking nadir mapper (OMPS-NM), a nadir profiler (OMPS-NP) and a limb profiler (OMPS-LP) (Wu et al., 2014; Seftor et al., 2014; Jaross et al., 2014). The OMPS-LP views the Earth's limb through three vertical slits and with three telescopes. Unlike most limb scatter sensors that scan vertically through the atmosphere at different tangent heights, OMPS-LP collects the limb radiance simultaneously from all altitudes. Nevertheless, the experience gained from the SCIAMACHY limb retrieval will certainly benefit the OMPS-LP data processing to achieve better data quality in the next decades. This will lead to a better understanding of stratospheric ozone. The simultaneous monitoring in nadir and limb mode with OMPS-NM and OMPS-LP may yield the next generation of Limb-Nadir Matching retrieved TOC product with better sampling compared to SCIAMACHY Limb-Nadir Matching.

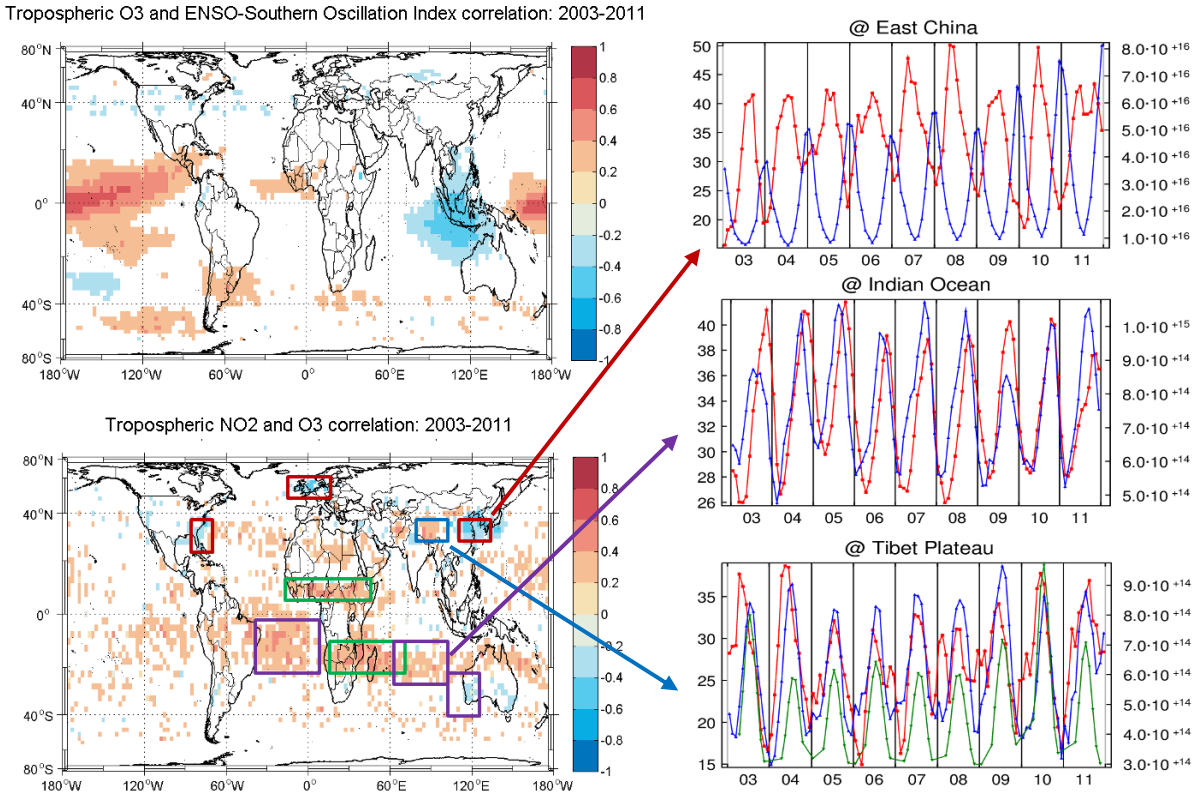

Figure 7.1. Satellite based TOCs collocated with other parameters for the years 2003-2011. Upper panel in the left side: OMI/MLS TOCs collocated with ENSO index; Lower panel in the left side: SCIAMACHY TOCs (V1.0) collocated with SCIAMACHY tropospheric NO_2 columns. Right panels are the time series of TOC (red curve) in DU and tropospheric NO_2 column (blue curve) in molec/ cm^2 at different locations. The green curve in the right lowest panel represents the lightning flash rate from LIS/OTD database.

Appendix

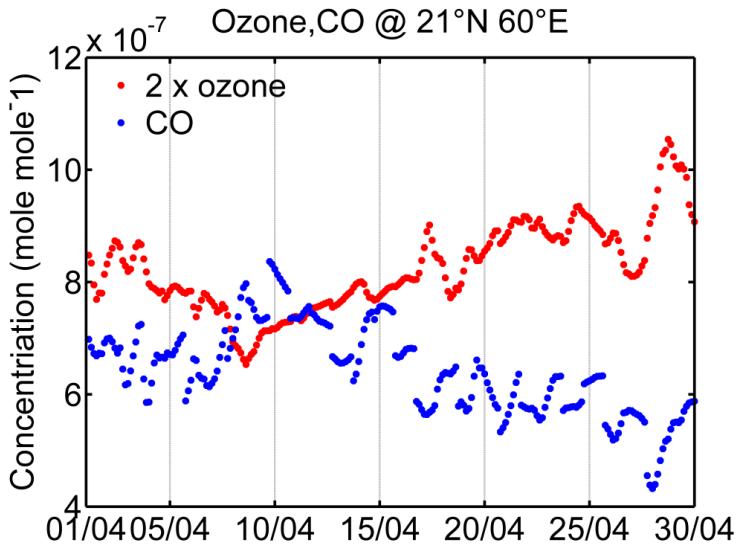

Figure A1. O_3 and CO partial column (4-8 km) time series at 21°N, 60°E over AS at April 2008 from MACC reanalysis data. The plot is a 'point' example of Fig. 6.11.

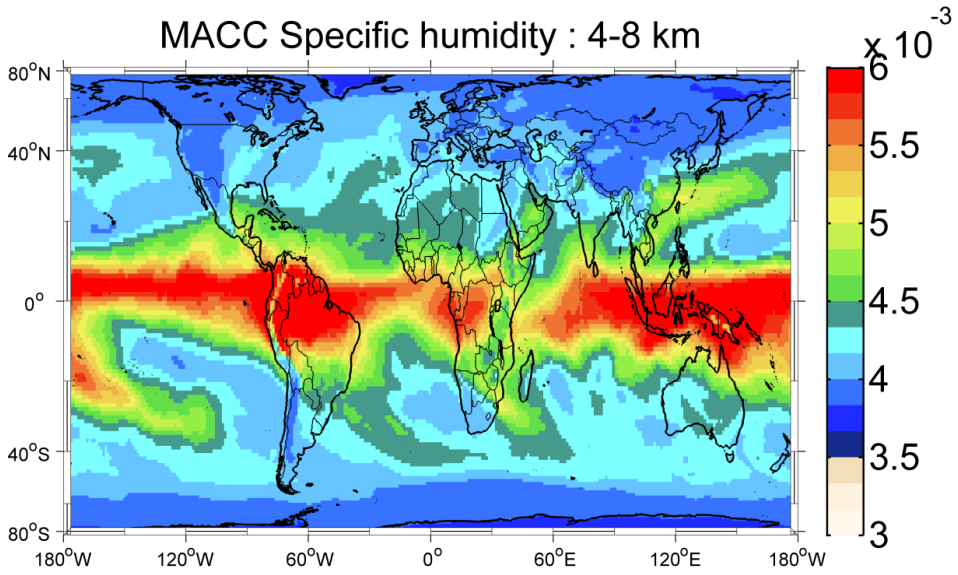

Figure A2. same as Fig. 6.13 but for the year 2010.

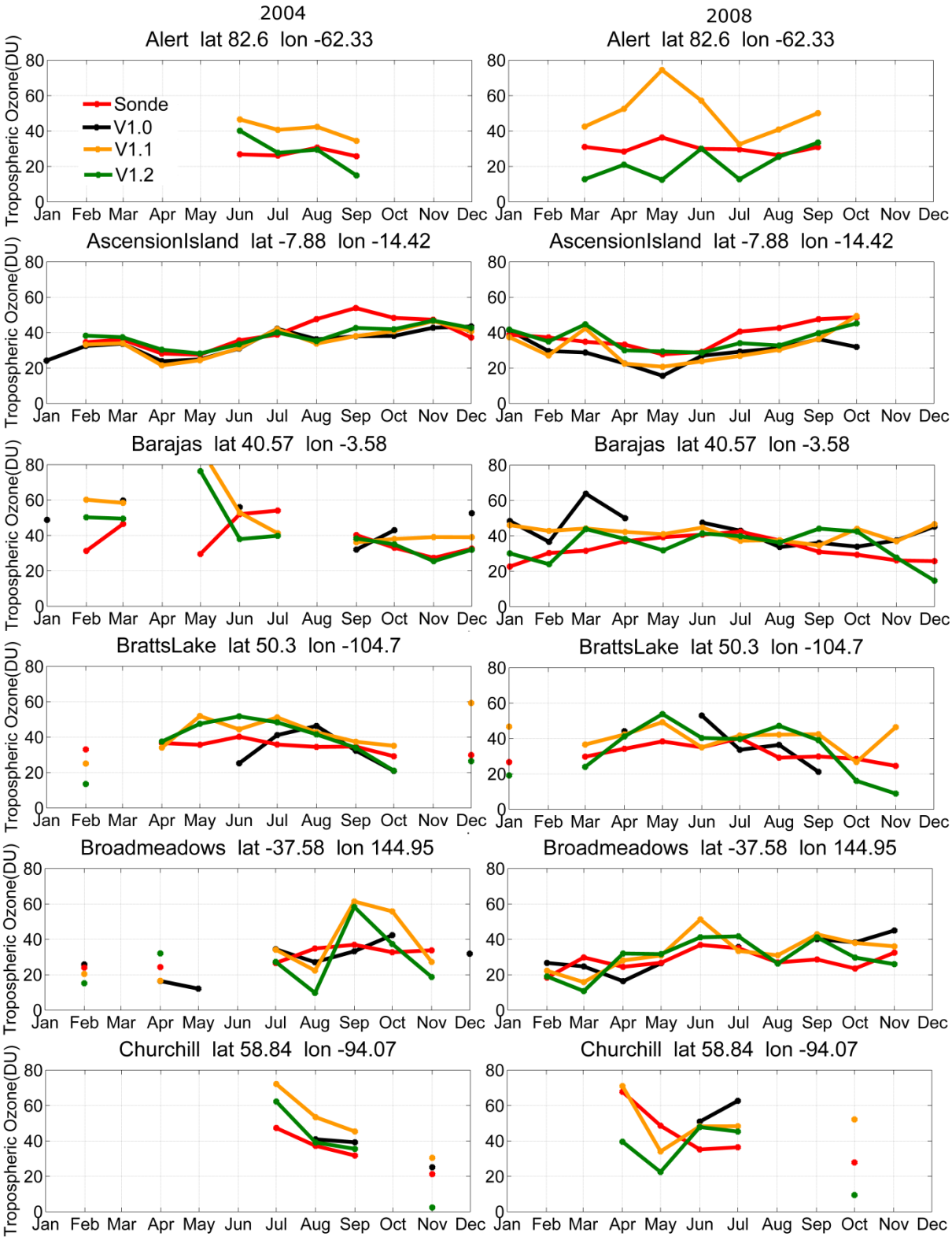

Figure A3. Time series of monthly averaged tropospheric ozone columns from SCIAMACHY V1.0, V1.1 V1.2 data and ozonesonde data in the year 2004 (left panels) and 2008 (right panels) at all available stations (in alphabetic order).

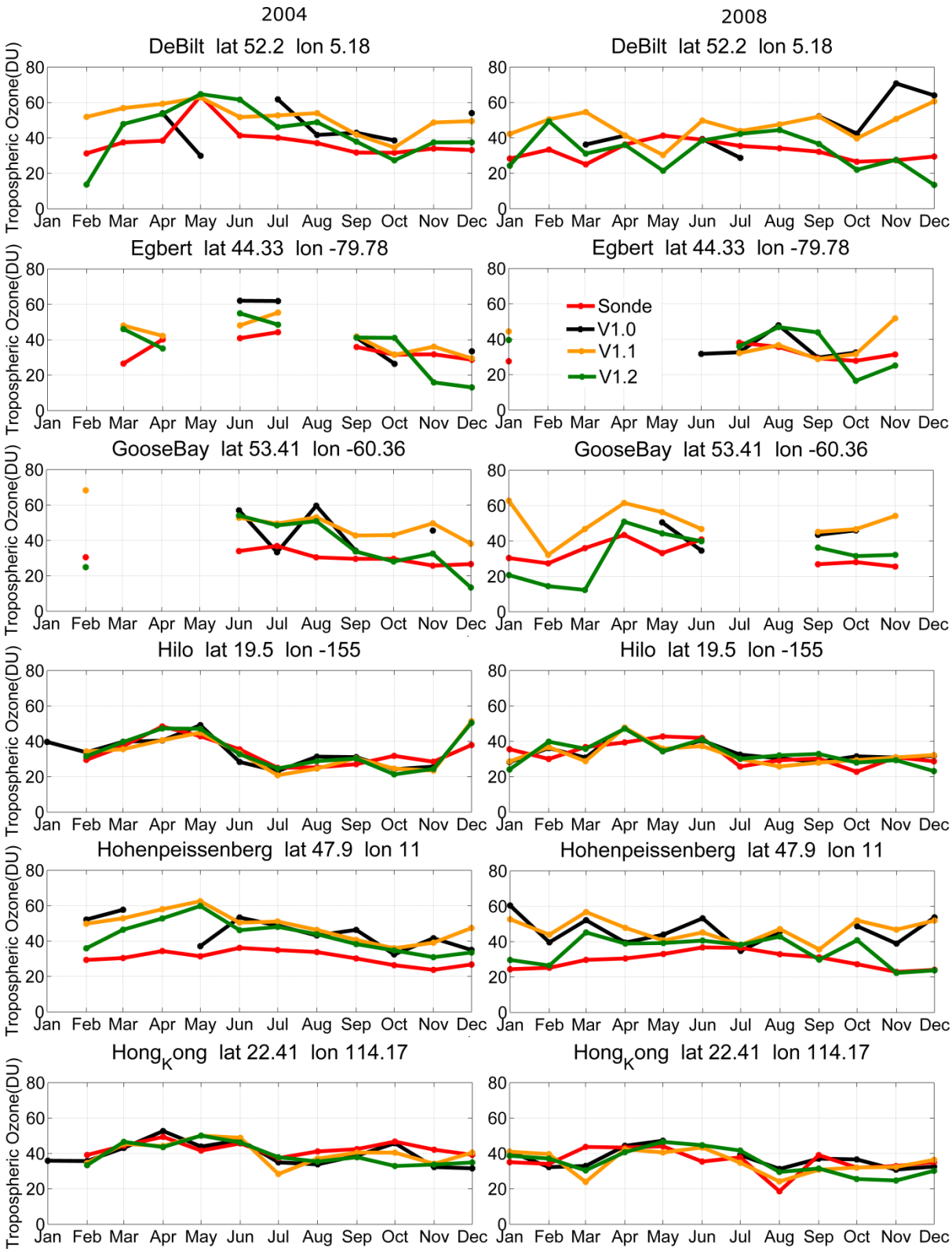

Figure A3. Continue

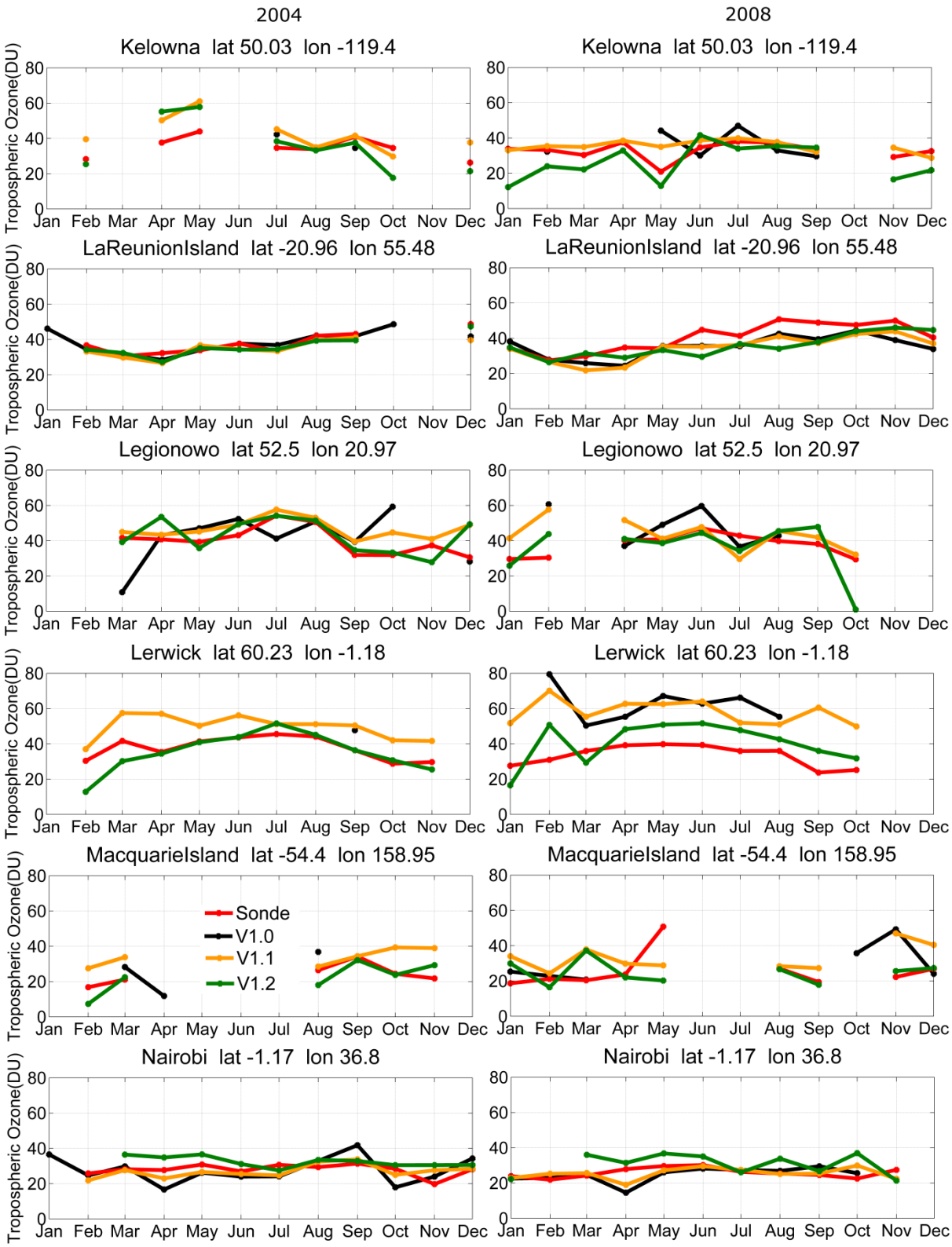

Figure A3. Continue

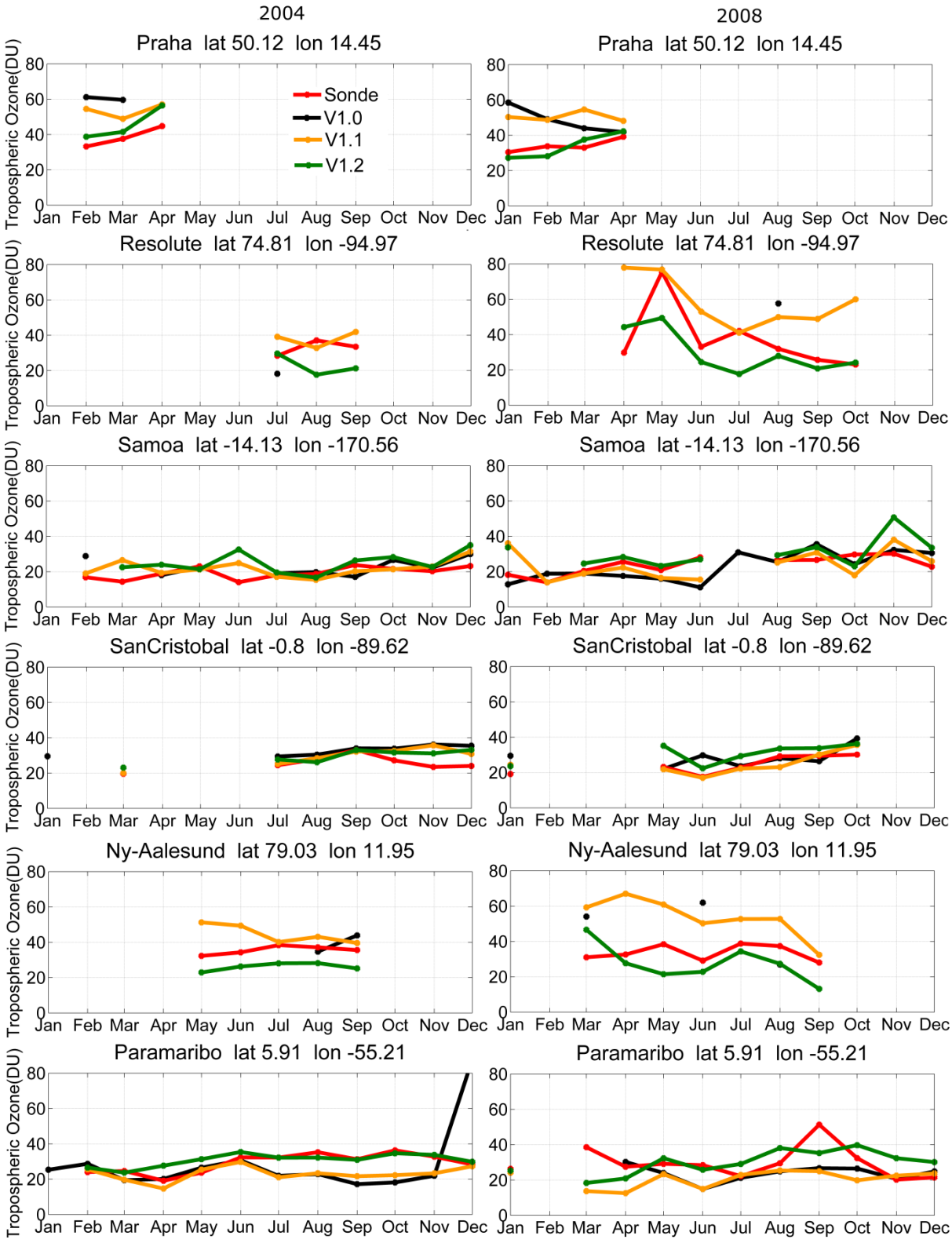

Figure A3. Continue

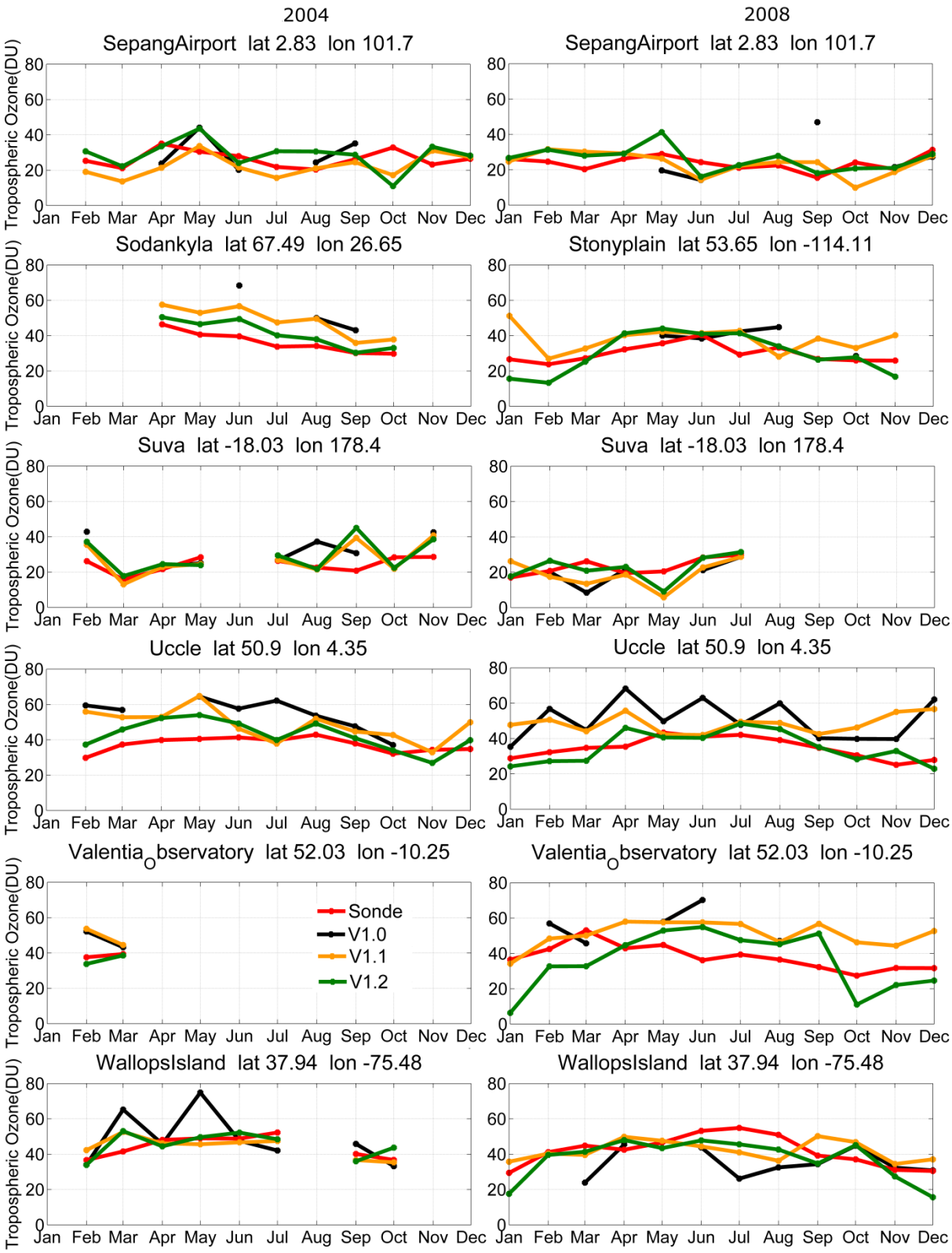

Figure A3. Continue

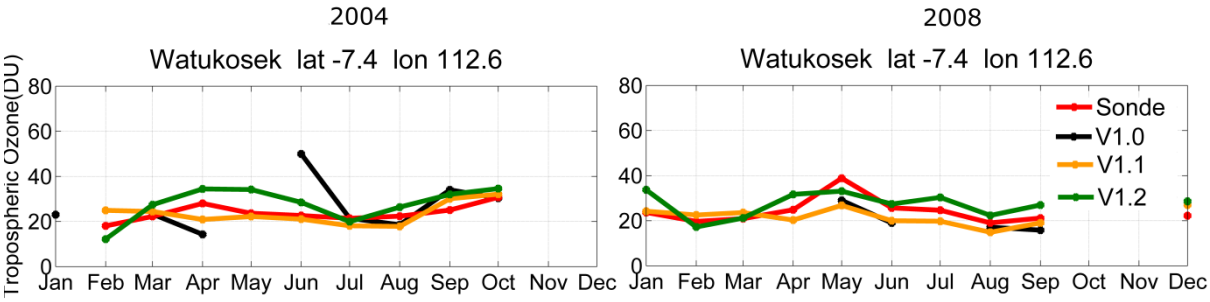

Figure A3. Continue

List of abbreviations

ACCO - Above cloud column of ozone

ACE - Atmospheric chemistry experiment

Ar - Argon

AS - Arabian Sea

CARIBIC - Civil Aircraft for the Regular Investigation of the atmosphere Based on an Instrumented Container

CCD - Charge coupled device

CCD method - Convective cloud differential method

CF - Cloud fraction

CFC - Chlorofluorocarbon

CH_4 - Methane

CN - Crossing Number

CO - Carbon monoxide

CO_2 - Carbon dioxide

COPD - Chronic obstructive pulmonary disease

CS - Cloud slicing

CTH - Cloud top height

DCC - Deep convective cloud

DJF - December-January- February

DOAS - Differential optical absorption spectroscopy

DOF - Degree of freedom

DU - Dobson unit

ECC - Electrochemical concentration cell

ECSTRA - Extinction Coefficient for STRatospheric Aerosol

ECMWF - European Centre for Medium-Range Weather Forecasts

ENSO - El Nino-Southern Oscillation

Envisat - Environmental satellite

EOS - Earth Observing System

ERS - European Remote Sensing satellite

ESA - European Space Agency

FORLI-O_3 - Fast Optimal Retrievals on Layers for IASI ozone product

FURM - Full Retrieval Method

GDAS - Global Data Assimilation System

GMES - Global Monitoring for Environment and Security

GOME - Global Ozone Monitoring Experiment

GOMOS - Global Ozone Monitoring by Occultation of Stars

GVC - Ghost vertical column

HALOE - Halogen Occultation Experiment

H_2O - Water vapor

HYSPLIT - HYbrid Single-Particle Lagrangian Integrated Trajectory

IARC - International Agency for Research on Cancer

IASI - Infrared Atmospheric Sounding Interferometer

ICARB - Integrated Campaign for Aerosols, Gases and Radiation Budget campaign

INDOEX -INDian Ocean EXperiment campaign

IR - Infrared

ITCZ - InterTropical Convergence Zone

IUP - Institute for Environmental Physics in University of Bremen

JJA - June-July-August

JPSS - Joint Polar Satellite System

LIS/OTD - Lightning Imaging Sensor/ spaceborne Optical Transient Detector

LNM - Limb-Nadir Matching

LOS - Line of Sight

LRT - Long Range Transport

MACC - Monitoring Atmospheric Composition and Climate

MAM - March-April-May

MetOp - Meteorological operational satellite

MIPAS - Michelson Interferometer for Passive Atmospheric Sounding

MLS - Microwave Limb Sounder

MOZART - Model for OZone and Related chemical Tracers

MR - Modified Residual

MW - Microwaves

N_2 - Nitrogen

N_2O - Nitrous oxide

NCEP - National Center Environmental Prediction

NMHC - Non-Methane Hydro Carbon

NN - Neutral Network

NNORSY - Neutral Network Ozone Retrieval System

NOAA - National Oceanic and Atmospheric Administration

NO_x - Nitrogen oxides

NPOESS - National Polar-Orbiting Environmental Satellite System

O_2 - Oxygen

O_3 - Ozone

OE - Optimal Estimation

OEI - Ozone ENSO Index

OH - Hydroxyl radical

OMI - Ozone Monitoring Instrument

OMPS - Ozone Mapping and Profiler Suite

OMPS-NM - Ozone Mapping and Profiler Suite nadir mapper

OMPS-NP - Ozone Mapping and Profiler Suite limb profiler

OPERA - Ozone ProfilE Retrieval Algorithm

OSIRIS - Optical Spectrograph and InfraRed Imager System

PMD - Polarization Measurement Devices

PSC - Polar Stratospheric Cloud

RF - radiate forcing

ro-vibrational - rotational-vibrational

RRS - Rotational Raman Scattering

RSM - Reference Sector Method

RTM - Radiative transfer model

SACURA - SemiAnalytical CLoUd Retrieval Algorithm

SAGE - Stratospheric Aerosol and Gas Experiment

SBUV - Solar Backscatter Ultraviolet

SCs - Stratospheric partial ozone columns at 20-30 km altitude range

SCIAMACHY - SCanning Imaging Absorption spectroMeter for Atmospheric CHartography

SCODA - SCIAMACHY Cloud Detection Algorithm

SHADOZ - Southern Hemisphere ADditional OZonesondes

SNR - Signal-to-noise ratio

SO_2 - Sulfur dioxide

SON - September-October-November

SST - Sea Surface Temperature

STE - Stratosphere troposphere exchange

Suomi NPP - Suomi Polar-obriting Partnership

SZA - Solar zenith angle

TCO - Total column of ozone

TEM - Tropospheric Excess Method

TES - Tropospheric Emission Spectrometer

TOC - Tropospheric Ozone Column

TOMS - Total Ozone Mapping Spectrometer

TOR - Tropospheric ozone residual

TPH - Tropopause height

TTO - Tropical Tropospheric Ozone Columns

UV - UltraViolet

Vis - Visible

VMR - Volume mixing ratio

VOCs - Volatile organic compunds

WFDOAS - Weighting Function Differential Optical Absorption Spectroscopy

WHO - World Health Organization

WOUDC - World Ozone and Ultraviolet Radiation Data Centre

Bibliography

Akagi, S.K., Yokelson, R.J., Wiedinmyer, C., Alvarado, M.J., Reid, J.S., Karl, T., Crounse, J.D., Wennberg, P.O.: Emission factors for open and domestic biomass burning for use in atmospheric models, Atmos. Chem. Phys., 11, 4039-4072, 2011.

Ali, K., Beig, G., Chate, D. M., Momin, G. A., Sahu, S. K., and Safai, P. D.: Sink mechanism for significantly low level of ozone over the Arabian Sea during monsoon, J. Geophys. Res., 114, D17306, doi:10.1029/2008JD011256, 2009.

Archibald, A. T., Levine, J. G., Abraham, N. L., Cooke, M. C., Edwards, P. M., Heard, D. E., Jenkin, M. E., Karunaharan, A., Pike, R. C., Monks, P. S., Shallcross, D. E., Telford, P. J., Whalley, L. K., and Pyle, J. A.: Impacts of HO(x) regeneration and recycling in the oxidation of isoprene: Consequences for the composition of past, present and future atmospheres, Geophys. Res. Lett., 38, L05804 doi:10.1029/2010gl046520, 2011.

Backus, G. E., and Gilbert, F. E.: Uniqueness in the Inversion of Inaccurate Gross Earth Data, Phil. Trans. Roy. Soc. London, A266, 1173, 123-192, 1970.

Beer, R.: TES on the Aura mission: Scientific objectives, measurements, and analysis overview. IEEE T. Geosci. Remote, 44, 1102 – 1105. 20, 60, 2006.

Beer, R., T. A. Glavich, T. A., and Rider, D. M.,: Tropospheric Emission Spectrometer for the Earth Observing System's Aura satellite, Appl. Opt., vol. 40, pp. 2356–2367, May 20, 2001.

Beirle, S., Platt, U., Wenig, M. O., and Wagner, T.: Highly resolved global distribution of tropospheric NO_2 using GOME narrow swath mode data, Atmos. Chem. Phys., 4, 1913–1924, 2004.

Beirle, S., Kühl, S., Puķīte, J., and Wagner, T.: Retrieval of tropospheric column densities of NO_2 from combined SCIAMACHY nadir/limb measurements, Atmos. Meas. Tech., 3, 283-299, doi:10.5194/amt-3-283-2010, 2010.

Beirle, S., Boersma, K. F., Platt, U., Lawrence, M. G., and Wagner, T.: Megacity emissions and lifetimes of nitrogen oxides probed from space, Science, 333, 1737–1739, doi:10.1126/science.1207824, 2011.

Bertaux, J. L., Kyrölä, E., Fussen, D., Hauchecorne, A., Dalaudier, F., Sofieva, V., Tamminen, J., Vanhellemont, F., Fanton d'Andon, O., Barrot, G., Mangin, A., Blanot, L., Lebrun, J. C., Pérot, K., Fehr, T., Saavedra, L., Leppelmeier, G. W., and Fraisse, R.: Global ozone monitoring by occultation of stars: an overview of GOMOS measurements on ENVISAT, Atmos. Chem. Phys., 10, 12091–12148, doi:10.5194/acp-10-12091-2010, 2010.

Bey, I., Jacob, D. J., Yantosca, R. M., Logan, J. A., Field, B. D., Fiore, A. M., Li, Q., Liu, H. Y., Mickley, L. J., and Schultz, M. G.: Global modeling of tropospheric chemistry with assimilated meteorology: model description and evaluation, J. Geophys. Res., 106(D19), 23073–23096, 2001.

Bishop, C. M.: Neural networks for pattern recognition, Oxford University Press, New York, USA, 1995.

Bohren, C. F. and Clothiaux, E. E.: Fundamentals of Atmospheric Radiation, Wiley-VCH, Weinheim, 2006.

Bouarar, I., Law, K. S., Pham, M., Liousse, C., Schlager, H., Hamburger, T., Reeves, C. E., Cammas, J.-P., Nédélec, P., Szopa, S., Ravegnani, F., Viciani, S., D'Amato, F., Ulanovsky, A., and Richter, A.: Emission sources contributing to tropospheric ozone over Equatorial Africa during the summer monsoon, Atmos. Chem. Phys., 11, 13395-13419, doi:10.5194/acp-11-13395-2011, 2011.

Bowman, K. W., Rodgers, C. D., Kulawik, S. S., Worden, J., Sarkissian, E., Osterman, G., Steck, T., Lou, M., Eldering, A. and Shephard, M.: Tropospheric emission spectrometer: Retrieval method and error analysis, IEEE T. Geosci. Remote Sens., 44, 1297–1307, 2006.

Bovensmann, H., Burrows, J. P., Buchwitz, M., Frerick, J., Noël, S., Rozanov, V. V., Chance, K. V., and Goede, A. P. H.: SCIAMACHY: mission objectives and measurement modes. J. Atmos. Sci., 56, 127–150, 1999.

Boynard, A., Clerbaux, C., Coheur, P.-F., Hurtmans, D., Turquety, S., George, M., Hadji-Lazaro, J., Keim, C., and Meyer-Arnek, J.: Measurements of total and tropospheric ozone from IASI: comparison with correlative satellite, ground-based and ozonesonde observations, Atmos. Chem. Phys., 9, 6255-6271, doi:10.5194/acp-9-6255-2009, 2009.

Brinksma, E. J., Bracher, A., Lolkema, D. E., Segers, A. J., Boyd, I. S., Bramstedt, K., Claude, H., Godin-Beekmann, S., Hansen, G., Kopp, G., Leblanc, T., McDermid, I. S., Meijer, Y. J., Nakane, H., Parrish, A., von Savigny, C., Stebel, K., Swart, D. P., Taha, G., and

Piters, A. J.: Geophysical validation of SCIAMACHY limb ozone profiles, Atmos. Chem. Phys., 6, 197–209, 2006.

Burrows, J. P., Hölzle, E., Goede, A., Visser, H., and Fricke, W.:SCIAMACHY – scanning imaging absorption spectrometer for atmospheric chartography, Acta Astronaut., 35, 445–451, 1995.

Burrows, J. P., Platt, U., and Borrell, P.: The Remote Sensing of Tropospheric Composition from Space, 1st Edn., Springer, Heidelberg, Germany, 2011.

Burrows, J. P., Weber, M., Buchwitz, M., Rozanov, V. V., Ladstätter-Weißenmayer, A., Richter, A., de Beek, R., Hoogen, R., Bramstedt, K., Eichmann, K.-U., Eisinger M., and Perner, D.: The Global Ozone Monitoring Experiment (GOME): Mission Concept and First Scientific Results, J. Atmos. Sci., 56, 151–175, 1999.

Callies, J., Corpaccioli, E., Eisinger, M., Hahne, A., and Lefebvre, A.: GOME-2 – Metop's Second-Generation Sensor for Operational Ozone Monitoring, ESA Bulletin, 102, 28–36, 2000.

Carmona-Moreno, C., Belward, A., Malingreau, J., Hartley, A., Garcia-Algere, M., Antonovskiy, M., Buchshtaber, V., and Pivovarov, V.: Characterizing interannual variations in global fire calendar using data from Earth observing satellites, Glob. Change Biol., 11, 1537–1555, 2005.

Clerbaux, C., Boynard, A., Clarisse, L., George, M., Hadji-Lazaro, J., Herbin, H., Hurtmans, D., Pommier, M., Razavi, A., Turquety, S., Wespes, C., and Coheur, P.-F.: Monitoring of atmospheric composition using the thermal infrared IASI/MetOp sounder, Atmos. Chem. Phys., 9, 6041-6054, doi:10.5194/acp-9-6041-2009, 2009.

Chance, K. and Spurr R. J. D.: Ring effect studies: Rayleigh scattering, including molecular parameters for rotational Raman scattering, and the Fraunhofer spectrum, Appl. Optics, 36, 5224–5230, 1997.

Chandra, S., Ziemke, J. R., Min, W., and Read, W. G.: Effects of 1997–1998 El Niño on tropospheric ozone. Geophys. Res. Lett., 25, 3867–3870, 1998.

Chandra, S., Ziemke, J. R., and Martin, R. V.: Tropospheric ozone at tropical and middle latitudes derived from TOMS/MLS residual: comparison with a global model, J. Geophys. Res., 108, 4291, doi:10.1029/2002JD002912, 2003.

Chand, D., Lal, S., and Naja, M.: Variations of ozone in the marine boundary layer over the Arabian Sea and the Indian Ocean during the 1998 and 1999 INDOEX campaigns, J. Geophys. Res., 108, 4190, doi:10.1029/2001JD001589, 2003.

Chapman, S.: On ozone and atomic oxygen in the upper atmosphere, Phil. Mag. S7, 369–383, 1930.

Coldewey-Egbers, M., Weber, M., Lamsal, L. N., de Beek, R., Buchwitz, M., and Burrows, J. P.: Total ozone retrieval from GOME UV spectral data using the weighting function DOAS approach, Atmos. Chem. Phys., 5, 1015-1025, doi:10.5194/acp-5-1015-2005, 2005.

Cooper, O. R., Parrish, D. D., Ziemke, J., Balashov, N. V., Cupeiro, M., Galbally, I. E., Gilge, S., Horowitz, L., Jensen, N.R., Lamarque, J. -F., Naik, V., Oltmans, S. J., Schwab, J., Shindell, D. T., Thompson, A. M., Thouret, V., Wang, Y., and Zbinden, R. M.: Global distribution and trends of tropospheric ozone: An observation-based review. Elem. Sci. Anth. 2: 000029. doi: 10.12952/journal.elementa.000029, 2014.

Crutzen, P.J., Heidt, L.E., Krasnec, J.P., Pollock,W.H., Seiler,W.: Biomass burning as a source of atmospheric gases CO, H_2, N_2O, NO, CH_3Cl and COS. Nature 282, 253-256, 1979.

Crutzen, P. J. and Andreae, M. O.: Biomass burning in the tropics: Impact on atmospheric chemistry and biogeochemical cycles, Science, 250(4988):1669-1678, doi: 10.1126/science.250.4988.1669, 1990.

Crutzen, P. J. and Stoermer, E. F.: The ”Anthropocene”, Global Change Newsletter, 41, 17–18, 2000.

Cuesta, J., Eremenko, M., Liu, X., Dufour, G., Cai, Z., Höpfner, M., von Clarmann, T., Sellitto, P., Foret, G., Gaubert, B., Beekmann, M., Orphal, J., Chance, K., Spurr, R., and Flaud, J.-M.: Satellite observation of lowermost tropospheric ozone by multispectral synergism of IASI thermal infrared and GOME-2 ultraviolet measurements over Europe, Atmos. Chem. Phys., 13, 9675-9693, doi:10.5194/acp-13-9675-2013, 2013.

David, L. M. and Nair, P. R.: Tropospheric column O_3 and NO_2 over the Indian region observed by Ozone Monitoring Instrument (OMI): seasonal changes and long-term trends, Atmos. Environ., 65, 25–39, doi:10.1016/j.atmosenv.2012.09.033, 2013.

Dee, D. P., Uppala, S. M., Simmons, A. J., Berrisford, P., Poli, P., Kobayashi, S., Andrae, U., Balmaseda, M. A., Balsamo, G., Baffer, P., Bechtold, P., Beljaars, A. C. M., fian de Berg, L.,

Bidlot, J., Bormann, N., Delsol, C., Dragani, R., Fffentes, M., Geer, A. J., Haimberger, L., Healy, S. B., Hersbach, H., Hólm, E. V., Isaksen, L., Kållberg, P., Köhler, M., Matricardi, M., McNally, A. P., Monge-Sanz, B. M., Morcrette, J.-J., Park, B.-K., Peffbey, C., de Rosnay, P., Tafiolato, C., Thépafft, J.-N., and Vitart, F.: The ERA Interim reanalysis: configuration and performance of the data assimilation system, Quarterly Journal of the Royal Meteorological Society, 137, 553–597, 2011.

Dessler, A. E.: The Chemistry and Physics of Stratospheric Ozone, vol. 74 of International Geophysics Series, Academic Press, 1st ed., 2000.

Dickerson, R. R., Rhoads, K. P., Carsey, T. P., Oltmans, S. J., Burrows, J. P., and Crutzen, P. J.: Ozone in the remote marine boundary layer: a possible role for halogens, J. Geophys. Res., 104, 21385–21395, 1999.

Duncan, B. N., Martin, R. V., Staudt, A. C., Yevich, R., and Logan, J. A.: Interannual and seasonal variability of biomass burning emissions constrained by satellite observations, J. Geophys. Res., 108(D2), 4100, doi:10.1029/2002JD002378, 2003.

Ebojie, F., von Savigny, C., Ladstätter-Weißenmayer, A., Rozanov, A., Weber, M., Eichmann, K.-U., Bötel, S., Rahpoe, N., Bovensmann, H., and Burrows, J. P.: Tropospheric column amount of ozone retrieved from SCIAMACHY limb–nadir-matching observations, Atmos. Meas. Tech., 7, 2073-2096, doi:10.5194/amt-7-2073-2014, 2014.

Ebojie, F.: Tropospheric ozone columns retrieval from SCIAMACHY limb-nadir-matching observations, Ph.D. thesis, University of Bremen, 2014.

Eichmann, K.-U., von Savigny, C., Weigel, K., Reichl, P., Robert, C., Steinwagner, J., Bovensmann, H. & Burrows, J.P.: SCODA V1.9: SCIAMACHY Cloud Detection Algorithm from Limb Radiance Measurements, Algorithm Theoretical Baseline Document (ATBD), University of Bremen, Bremen, Germany, 2011.

Emmons, L. K., Walters, S., Hess, P. G., Lamarque, J.-F., Pfister, G. G., Fillmore, D., Granier, C., Guenther, A., Kinnison, D., Laepple, T., Orlando, J., Tie, X., Tyndall, G., Wiedinmyer, C., Baughcum, S. L., and Kloster, S.: Description and evaluation of the Model for Ozone and Related chemical Tracers, version 4 (MOZART-4), Geosci. Model Dev., 3, 43-67, doi:10.5194/gmd-3-43-2010, 2010.

EPA Assessment of the impacts of global change on regional U.S.air quality a synthesis of climate change impacts on ground-levelozone, National Center for Environmental Assess-mentWashingtonDC, 2009.

Ernst, F.: Stratospheric aerosol extinction profile retrievals from SCIAMACHY limb-scatter observations, Ph.D. thesis, University of Bremen, 2013.

Ernst, F., von Savigny, C., Rozanov, A., Rozanov, V., Eichmann, K.-U., Brinkhoff, L. A., Bovensmann, H., and Burrows, J. P.: Global stratospheric aerosol extinction profile retrievals from SCIAMACHY limb-scatter observations, Atmos. Meas. Tech. Discuss., 5, 5993-6035, doi:10.5194/amtd-5-5993-2012, 2012.

Fadnavis, S., Chakraborty, T., and Beig, G.: Seasonal stratospheric intrusion of ozone in the upper troposphere over India, Ann. Geophys., 28, 2149-2159, doi:10.5194/angeo-28-2149-2010, 2010.

Finlayson-Pitts, B. J., and Pitts, J. N.: The chemical basis of air quality: Kinetics and mecha-nism of photochemical air pollution and application to control strategies. Adv. Environ. Sci. Technol., 7, 75-162, 1977.

Fishman, J., Ramanathan, V., Crutzen, P. J., and Liu, S. C.: Tropospheric ozone and climate, Nature, 282, pp. 818–820, doi:10.1038/282818a0, 1979.

Fishman, J. and Seiler, W.: Correlative nature of ozone and carbon monoxide in the tropo-sphere: Implications for the tropospheric ozone budget, J. Geophys. Res., 88, 3662–3670, doi:10.1029/JC088iC06p03662, 1983.

Fishman, J., P. Minnis, and H. G. Reichle, Jr., The use of satellite data to study tropospheric ozone in the tropics, J. Geophys. Res., 91, 14,451-14,465, 1986.

Fishman, J., Watson, C., Larsen, J., and Logan, J.: Distribution of tropospheric ozone deter-mined from satellite data. J. Geophys. Res., 95, 3599–3617. 3, 59, 60, 1990.

Fishman, J., Fakhruzzaman, K., Cros, B., and Nganga, D.: Identification of widespread pollution in the Southern Hemisphere deduced from satellite analyses, Science, 252, 1693–1696, 1991.

Fishman, J., Brackett, V. G., Browell, E. V., and Grant, W. B.: Tropospheric ozone derived from TOMS/SBUV measurements during TRACE A, J. Geophys. Res., 101,24069-24082, 1996.

Fischer, H., Birk, M., Blom, C., Carli, B., Carlotti, M., von Clarmann, T., Delbouille, L., Dudhia, A., Ehhalt, D., Endemann, M., Flaud, J. M., Gessner, R., Kleinert, A., Koopman, R., Langen, J., López-Puertas, M., Mosner, P., Nett, H., Oelhaf, H., Perron, G., Remedios, J., Ridolfi, M., Stiller, G., and Zander, R.: MIPAS: an instrument for atmospheric and climate research, Atmos. Chem. Phys., 8, 2151-2188, doi:10.5194/acp-8-2151-2008, 2008.

Flittner, D. E., Bhartia, P. K., and Herman, B. M.: O3 profiles retrieved from limb scatter measurements: Theory, Geophys. Res. Lett., 27, 2601–2604, 2000.

Fortuin, J. P. F., and Kelder, H.: An ozone climatology based on ozonesonde and satellite measurements, J. Geophys. Res., 103(D24), 31,709 – 31,734, 1998.

Fu, D., Worden, J. R., Liu, X., Kulawik, S. S., Bowman, K. W., and Natraj, V.: Characterization of ozone profiles derived from Aura TES and OMI radiances, Atmos. Chem. Phys., 13, 3445-3462, doi:10.5194/acp-13-3445-2013, 2013.

Fuhrer, J., Skärby, L. and Ashmore, M. R.: Critical levels for ozone effects on vegetation in Europe, Environmental Pollution, Vol. 97, No. 1-~2, pp. 91 106, 1997.

Fussen, D. and Bingen, C.: A volcanism dependent model for the extinction profile of stratospheric aerosols in the UV-visible range, Geophys. Res. Lett., 26, 703–706, 1999.

Gillett, N. P., Weaver, A. J., Zwiers, F. W., Flannigan, M. D.: Detecting the effect of climate change on Canadian forest fires. Geophysical Research Letters 31, L18211, 2004.

Gorshelev, V., Serdyuchenko, A., Weber, M., Chehade, W., and Burrows, J. P.: High spectral resolution ozone absorption cross-sections – Part 1: Measurements, data analysis and comparison with previous measurements around 293 K, Atmos. Meas. Tech., 7, 609-624, doi:10.5194/amt-7-609-2014, 2014.

Gould, N. I. M., Orban, D., and Toint, Ph. L.: GALAHAD, a library of thread-safe Fortran 90

packages for large-scale nonlinear optimization, ACM Trans. actions on Mathematical Software 29(4) 353--372, 2003.

Gottwald, M. and Bovensmann, H., eds.: SCIAMACHY - Exploring the Changing Earth's Atmosphere, Springer Netherlands, Dordrecht, 2011.

Guenther, A., Hewitt, C. N., Erickson, D., Fall, R., Geron, C., Graedel, T., Harley, P., Klinger, L., Lerdau, M., McKay, W. A., Pierce, T., Scholes, B., Steinbrecher, R., Tallamraju, R., Tay-

lor, J., and Zimmerman, P.: A global model of natural volatile organic compound emissions, J. Geophys. Res., 100, 8873–8892, doi:10.1029/94jd02950, 1995.

Hassler, B., Petropavlovskikh, I., Staehelin, J., August, T., Bhartia, P. K., Clerbaux, C., Degenstein, D., Mazière, M. De, Dinelli, B. M., Dudhia, A., Dufour, G., Frith, S. M., Froidevaux, L., Godin-Beekmann, S., Granville, J., Harris, N. R. P., Hoppel, K., Hubert, D., Kasai, Y., Kurylo, M. J., Kyrölä, E., Lambert, J.-C., Levelt, P. F., McElroy, C. T., McPeters, R. D., Munro, R., Nakajima, H., Parrish, A., Raspollini, P., Remsberg, E. E., Rosenlof, K. H., Rozanov, A., Sano, T., Sasano, Y., Shiotani, M., Smit, H. G. J., Stiller, G., Tamminen, J., Tarasick, D. W., Urban, J., van der A, R. J., Veefkind, J. P., Vigouroux, C., von Clarmann, T., von Savigny, C., Walker, K. A., Weber, M., Wild, J., and Zawodny, J. M.: Past changes in the vertical distribution of ozone – Part 1: Measurement techniques, uncertainties and availability, Atmos. Meas. Tech., 7, 1395-1427, doi:10.5194/amt-7-1395-2014, 2014.

Hilboll A.: Tropospheric nitrogen dioxide from satellite measurements: SCIAMACHY Limb/Nadir matching and multi-instrument trend analysis, PhD thesis, University of Bremen, Bremen, Germany, 2013.

Hilboll, A., Richter, A., and Burrows, J. P.: Long-term changes of tropospheric NO_2 over megacities derived from multiple satellite instruments, Atmos. Chem. Phys., 13, 4145-4169, doi:10.5194/acp-13-4145-2013, 2013.

Hoinka, K. P.: Statistics of the Global Tropopause Pressure, Monthly Weather Review, 126, 3303–3325, 1998.

Holloway, A. M. and Wayne, R. P.: Atmospheric Chemistry, RSC Publishing, 2010.

Holton, J.R., Haynes, P.H., McIntyre, M.E., Douglass, A.R., Rood, R.B., Pfister, L.: Stratosphere-troposphere exchange, Reviews of Geophysics 33, 403-439, 1995.

Hoogen, R., Rozanov, V. V., and Burrows, J. P.: Ozone profiles from GOME satellite data: Algorithm description and first validation, J. Geophys. Res., 104, 8263–8280, 1999.

Horowitz, L. W., Walters, S. M., Mauzerall, D. L., Emmons, L. K., Rasch, P. J., Granier, C., Tie, X., Lamarque, J.-F., Schultz, M. G., and Brasseur, G. P.: A global simulation of tropospheric ozone and related tracers: Description and evaluation of MOZART, version 2, J. Geophys. Res., 108, 4784, doi:10.1029/2002JD002853, 2003.

Hou, X., Zhu, B., Kang, H., and Gao, J.: Analysis of seasonal ozone budget and spring ozone latitudinal gradient variation in the boundary layer of the Asia-Pacific region, Atmos. Environ., 94, 734–741, doi:10.1016/j.atmosenv.2014.06.006, 2014.

HTAP: Hemispheric Transport of Air Pollution 2010, Part A: Ozone and Particulate Matter; Air Pollution Studies No. 17, edited by F. Dentener, T. Keating, and H. Akimoto. United Nations, New York and Geneva. 82, 2010.

Hubert, D., Lambert, J.-C., Verhoelst, T., Granville, J., Keppens, A., Baray, J.-L., Cortesi, U., Degenstein, D. A., Froidevaux, L., Godin-Beekmann, S., Hoppel, K. W., Kyrölä, E., Leblanc, T., Lichtenberg, G., McElroy, C. T., Murtagh, D., Nakane, H., Russell III, J. M., Salvador, J., Smit, H. G. J., Stebel, K., Steinbrecht, W., Strawbridge, K. B., Stübi, R., Swart, D. P. J., Taha, G., Thompson, A. M., Urban, J., van Gijsel, J. A. E., von der Gathen, P., Walker, K. A., Wolfram, E., and Zawodny, J. M.: Ground-based assessment of the bias and long-term stability of fourteen limb and occultation ozone profile data records, Atmos. Meas. Tech. Discuss., 8, 6661-6757, doi:10.5194/amtd-8-6661-2015, 2015.

Hudson, R. D., and Thompson, A.M.: Tropical tropospheric ozone (TTO) from TOMS by a modified-residual method, J. Geophys. Res., 103, 22,129-22,145, 1998.

Hurtmans, D., Coheur, P. F., Wespes, C., Clarisse, L., Scharf, O., Clerbaux, C., Hadji-Lazaro, J., George, M., and Turquety, S.: FORLI radiative transfer and retrieval code for IASI, J. Quant. Spectrosc. Ra., 113, 1391–1408, doi:10.1016/j.jqsrt.2012.02.036, 2012.

Inness, A., Baier, F., Benedetti, A., Bouarar, I., Chabrillat, S., Clark, H., Clerbaux, C., Coheur, P., Engelen, R. J., Errera, Q., Flemming, J., George, M., Granier, C., Hadji-Lazaro, J., Huijnen, V., Hurtmans, D., Jones, L., Kaiser, J. W., Kapsomenakis, J., Lefever, K., Leitão, J., Razinger, M., Richter, A., Schultz, M. G., Simmons, A. J., Suttie, M., Stein, O., Thépaut, J.-N., Thouret, V., Vrekoussis, M., Zerefos, C., and the MACC team: The MACC reanalysis: an 8 yr data set of atmospheric composition, Atmos. Chem. Phys., 13, 4073-4109, doi:10.5194/acp-13-4073-2013, 2013.

Inness, A., Benedetti, A., Flemming, J., Huijnen, V., Kaiser, J. W., Parrington, M., and Remy, S.: The ENSO signal in atmospheric composition fields: emission-driven versus dynamically induced changes, Atmos. Chem. Phys., 15, 9083-9097, doi:10.5194/acp-15-9083-2015, 2015.

IPCC Climate Change 2001: The Scientific Basis Contribution of Working Group I to the Third Assessment Report of the Intergovernmental Panel on Climate Change, edited by: J. T.

Houghton, Y. Ding, D.J. Griggs, M. Noguer, P. J. van der Linden and D. Xiaosu, Cambridge Univ. Press, Cambridge, UK. pp. 944, 2001.

IPCC (Intergovernmental Panel on Climate Change). 2013. Working Group I contribution to the IPCC Fifth Assessment Report "Climate Change 2013: The Physical Science Basis", Final Draft Underlying Scientific-Technical Assessment. Available at http://www.ipcc.ch.

IPCC/TEAP, Bert Metz, Lambert Kuijpers, Susan Solomon, Stephen O. Andersen, Ogunlade Davidson, José Pons, David de Jager, Tahl Kestin, Martin Manning, and Leo Meyer (Eds), Cambridge University Press, UK. pp 478, 2005.

Jacob, D. J.: Introduction to Atmospheric Chemistry, Princeton University Press, 1999.

Jacobson, M., Charlson, R. J., Rodhe, H., and Orians, G. H.: Earth System Science: From Biogeochemical Cycles to Global Changes, vol. 72 of International Geophysics Series, Academic Press, 1st ed., 2000.

Jaeglé, L., Steinberger, L., Martin, R. V., and Chance, K.: Global partitioning of NOx sources using satellite observations: Relative roles of fossil fuel combustion, biomass burning and soil emissions, Faraday Discuss., 130, 407–423, 2005.

Jaffe, D., Anderson, T., Covert, D., Kotchenruther, R., Trost, B., Danielson, J., Simpson, W., Berntsen, T., Karlsdottir, S., Blake, D., Harris, J., Carmichael, G., and Itsushi, U.: Transport of Asian air pollution to North America, Geophys. Res. Lett., 26, 711– 714, 1999.

Jaffe, D. A. and Wigder, N. L.: Ozone production from wildfires: A critical review, Atmos. Environ., 51, 1–10, doi:10.1016/j.atmosenv.2011.11.063, 2012.

Jaross, G., Bhartia, P. K., Chen, G., Kowitt, M., Haken, M., Chen, Z., Xu, P., Warner, J. and Kelly, T.: OMPS Limb Profiler instrument performance assessment, J. Geophys. Res., 119, doi:10.1002/2013JD020482, 2014.

Johnson, B. J., Oltmans, S. J., Vömel, H., Smit, H. G. J., Deshler, T., and Kroger, C.: Electrochemical concentration cell (ECC) ozonesonde pump efficiency measurements and tests on the sensitivity to ozone of buffered and unbuffered ECC sensor cathode solutions, J. Geophys. Res., 107(D19), 4393, doi:10.1029/2001JD000557, 2002.

Jones, H. G. and Vaughan, R. A.: Remote sensing of vegetation: principles, techniques and applications, Oxford University Press, Oxford, NY, ISBN978-0-19-920779-4, 2010.

Jordan, C.: Cours DAnalyse de l Ecole Polytechnique. Paris, Gauthier-Villars et fils. 62, 1887.

Rinsland, C. P., Jones, N. B., Connor, B. J., Wood, S. W., Goldman, A., Stephen, T. M., Murcray, F. J., Chiou, L. S., Zander, R., and Mahieu, E.: Multiyear infrared solar spectroscopic measurements of HCN, CO, C_2H_6, and C_2H_2 tropospheric columns above Lauder, New Zealand (45°S latitude), J. Geophys. Res., 107, ACH 1-1–ACH 1-12, doi:10.1029/2001JD001150, 2002.

Kaifel, A. K., Felder, M., Kaptur, J., Lambert, J., and de Clercq, C.: Neural Network Ozone Retrieval System for GOME (NNORSY-GOME), Atmospheric Science Conference, Frascati, Italy, 8–12 May 2006, Pres 876, 2006. Accessible under: http://earth.esa.int/workshops/atmos2006/participants/876/pres_876_kaifel.pdf.

Kim, J. -H., Hudson, R. D., and Thompson, A.M.: A new method of deriving time-averaged tropospheric column ozone over the tropics using total ozone mapping spectrometer (TOMS) radiances: Inter-comparison and analysis using TRACE-A data, J. Geophys. Res., 101, 24,317-24,330, 1996.

Kim, P. S., Jacob, D. J., Liu, X., Warner, J. X., Yang, K., Chance, K., Thouret, V., and Nedelec, P.: Global ozone–CO correlations from OMI and AIRS: constraints on tropospheric ozone sources, Atmos. Chem. Phys., 13, 9321–9335, doi:10.5194/acp-13-9321-2013, 2013.

Komhyr, W. D.: Electrochemical concentration cells for gas analysis. Ann.Geoph., 25, 203–210, 1969.

Kunhikrishnan, T., Lawrence, M. G., von Kuhlmann, R., Richter, A., Ladstätter-Weißenmayer, A., and Burrows, J. P.: Semiannual NO2 plumes during the monsoon transition periods over the central Indian Ocean, GRL, 31, L08110, doi:10.1029/2003GL019269, 2004.

Lal, S. and Lawrence, M. G.: Elevated mixing ratios of surface ozone over the Arabian Sea, Geophys. Res. Lett., 28(8), 1487–1490, doi:10.1029/2000GL011828, 2001.

Lal, S., Venkataramani, S., Srivastava, S., Gupta, S., Mallik, C., Naja, M., Sarangi, T., Acharya, Y. B., and Liu, X.: Transport effects on the vertical distribution of tropospheric ozone over the tropical marine regions surrounding India, J. Geophys. Res. Atmos., 118, 1513–1524, doi:10.1002/jgrd.50180, 2013.

Lal, S., Venkataramani, S., Chandra, N., Cooper, O. R., Brioude, J., and Naja, M.: Transport effects on the vertical distribution of tropospheric ozone over western India, J. Geophys. Res. Atmos., 119, 10012–10026, doi:10.1002/2014JD021854, 2014.

Lawrence, M. G. and Lelieveld, J.: Atmospheric pollutant outflow from southern Asia: a review, Atmos. Chem. Phys., 10, 11017-11096, doi:10.5194/acp-10-11017-2010, 2010.

Lelieveld, J. and Crutzen, P. J.: Influences of cloud photochemical processes on tropospheric ozone, Nature, 343, 227–233, 1990.

Lelieveld, J. and Dentener, F. J.: What controls tropospheric ozone?, J. Geophys. Res.-Atmos., 105, 3531–3551, doi:10.1029/1999jd901011, 2000.

Lelieveld, J., Evans, J. S., Fnais, M., Giannadaki, D. and Pozzer, A.: The contribution of outdoor air pollution sources to premature mortality on a global scale, Nature, 525, pp. 367–371, 2015.

Levelt, P. F., Hilsenrath, E., Leppelmeier, G. W., van den Oord, G. B. J., Bhartia, P. K., Tamminen, J., de Haan, J. F., and Veefkind, J. P.: Science objectives of the Ozone Monitoring Instrument, IEEE Trans. Geosci. Remote Sens., vol. 44, no. 5, pp. 1199–1208, 2006.

Levelt, P. F., van den Oord, G. H. J., Dobber, M. R., Mälkki, A., Visser, H., de Vries, J., Stammes, P., Lundell, J., and Saari, H.: The Ozone Monitoring Instrument (OMI). IEEE T. Geoscu. Remote, 44(5), 1093–1101. 16, 20, 2006.

Leventidou, E., Eichmann, K.-U., Weber, M., and Burrows, J. P.: Tropical tropospheric ozone columns from nadir retrievals of GOME-1/ERS-2, SCIAMACHY/Envisat, and GOME-2/MetOp-A (1996-2012), Atmos. Meas. Tech. Discuss., doi:10.5194/amt-2015-401, in review, 2016.

Liou, K.N.: An introduction to atmosphere radiation, Academic Press, International Geophysical Series, Vol. 84, 2002.

Liu, X., Bhartia, P. K., Chance, K., Spurr, R. J. D., and Kurosu, T. P.: Ozone profile retrievals from the Ozone Monitoring Instrument, Atmos. Chem. Phys., 10, 2521-2537, doi:10.5194/acp-10-2521-2010, 2010.

Livesey, N. J., Logan, J. A., Santee, M. L., Waters, J. W., Doherty, R. M., Read, W. G., Froidevaux, L., and Jiang, J. H.: Interrelated variations of O3, CO and deep convection in the tropical/subtropical upper troposphere observed by the Aura Microwave Limb Sounder (MLS) during 2004–2011, Atmos. Chem. Phys., 13, 579-598, doi:10.5194/acp-13-579-2013, 2013.

Llewellyn, E. J., Lloyd, N. D., Degenstein, D. A., Gattinger, R. L., Petelina, S. V., Bourassa, A. E., Wiensz, J. T., Ivanov, E. V., McDade, I. C., Solheim, B. H., McConnell, J. C., Haley,

C. S., von Savigny, C., Sioris, C. E., McLinden, C. A., Griffioen, E., Kaminski, J., Evans, W. F. J., Puckrin, E., Strong, K., Wehrle, V., Hum, R. H., Kendall, D. J. W., Matsushita, J., Murtagh, D. P., Brohede, S., Stegman, J., Witt, G., Barnes, G., Payne, W. F., Piché, L., Smith, K., Warshaw, G., Deslauniers, D.-L., Marchand, P., Richardson, E. H., King, R. A., Wevers, I., McCreath, W., Kyrölä, E., Oikarinen, L., Leppelmeier, G. W., Auvinen, H., Mégie, G., Hauchecorne, A., Lefèvre, F., de La Nöe, J., Ricaud, P., Frisk, U., Sjoberg, F., von Schéele, F., and Nordh, L.: The OSIRIS instrument on the Odin spacecraft, Can. J. Phys., 82, 411–422, doi:10.1139/P04-005, 2004.

Logan, J. Megretskaia, A., Nassar, I., R., Murray, L. T., Zhang, L., Bowman, K. W., Worden, H. M., and Luo, M.: Effects of the 2006 El Niño on tropospheric composition as revealed by data from the Tropospheric Emission Spectrometer (TES), Geophys. Res. Lett., 35, L03816, doi:10.1029/2007GL031698, 2008.

Lutgens, F. K. and Tarbuck, E. J.: The Atmosphere, Prentice Hall, 6th ed., pp14-17, 1995.

Matthews, E.: Global vegetation and land use: new high resolution data bases for climate studies, J. Appl. Meteorol., 22, 474–487, 1983.

Mauzerall, D.L., Logan, J.A., Jacob, D.J., Anderson, B.E., Blake, D.R., Bradshaw, J.D., Heikes, B., Sachse, G.W., Singh, H., Talbot, B.: Photochemistry in biomass burning plumes and implications for tropospheric ozone over the tropical South Atlantic. Journal of Geophysical Research-Atmospheres 103,8401-8423, 1998.

McCormick, M. P., Zawodny, J. M., Viega, R. E., Larson, J. C., and Wang, P. H.: An overview of SAGE I and II ozone measurements, Planet. Space Sci., 37, 1567–1586, doi:10.1016/0032-0633(89)90146-3, 1989.

McElroy, C. T., Nowlan, C. R., Drummond, J. R., Bernath, P. F., Barton, D. V., Dufour, D. G., Midwinter, C., Hall, R. B., Ogyu, A., Ullberg, A., Wardle, D. I., Kar, J., Zou, J., Nichitiu, F., Boone, C. D., Walker, K. A., and Rowlands, N.: The ACE-MAESTRO instrument on SCISAT: Description, performance, and preliminary results, Appl. Optics, 46(20), 4341–4356, 2007.

McPeters, R. D., Labow, G. J., and Logan, J. A.: Ozone climatological profiles for satellite retrieval algorithms, J. Geophys. Res., 112, D05308, doi:10.1029/2005JD006823, 2007.

Mieruch, S., Weber, M., von Savigny, C., Rozanov, A., Bovensmann, H., Burrows, J. P., Bernath, P. F., Boone, C. D., Froidevaux, L., Gordley, L. L., Mlynczak, M. G., Russell III, J.

M., Thomason, L. W., Walker, K. A., and Zawodny, J. M.: Global and long-term comparison of SCIAMACHY limb ozone profiles with correlative satellite data (2002–2008), Atmos. Meas. Tech., 5, 771-788, 2012.

Mills, G., Harmens, H., Wagg, S., Sharps, K., Hayes, F., Fowler, D., Sutton, M., and Davies, B.: Ozone impacts on vegetation in a nitrogen enriched and changing climate, Environmental Pollution, 208, 898-908, doi: 10.1016/j.envpol.2015.09.038, 2016.

Monks, P. S.: A review of the observations and origins of the spring ozone maximum, Atmos. Environ., 34, 3545–3561, 2000.

Monks, P. S., Archibald, A. T., Colette, A., Cooper, O., Coyle, M., Derwent, R., Fowler, D., Granier, C., Law, K. S., Mills, G. E., Stevenson, D. S., Tarasova, O., Thouret, V., von Schneidemesser, E., Sommariva, R., Wild, O., and Williams, M. L.: Tropospheric ozone and its precursors from the urban to the global scale from air quality to short-lived climate forcer, Atmos. Chem. Phys., 15, 8889–8973, doi:10.5194/acp-15-8889-2015, 2015.

Müller, M. D., Kaifel, A. K., Weber, M., Tellmann, S., Burrows, J. P., and Loyola, D.: Ozone profile retrieval from Global Ozone Monitoring Experiment (GOME) data using a neural network approach (Neural Network Ozone Retrieval SYstem (NNORSY)), J. Geophys. Res., 108, 4497–4515, 2003.

Nair, P. R., David, L. M., Girach, I. A., and George, S. K.: Ozone in the marine boundary layer of Bay of Bengal during post-winter period: spatial pattern and role of meteorology, Atmos. Environ., 45, 4671e4681, 2011.

Nassar, R., Logan, J. A., Worden, H. M., Megretskaia, I. A., Bowman, K. W., Osterman, G. B., Thompson, A. M., Tarasick, D. W., Austin, S., Claude, H., Dubey, M. K., Hocking, W. K., Johnson, B. J., Joseph, E., Merrill, J., Morris, G. A., Newchurch, M., Oltmans, S. J., Posny, F., Schmidlin, F. J., Vömel, H., Whiteman, D. N., and Witte, J. C.: Validation of Tropospheric Emission Spectrometer (TES) nadir ozone profiles using ozonesonde measurements, J. Geophys. Res., 113, D15S17, doi:10.1029/2007JD008819, 2008.

Neu, J. L., Flury, T., Manney, G. L., Santee, M. L., Livesey, N. J., and Worden, J.: Tropospheric ozone variations governed by changes in stratospheric circulation, Nat. Geosci., 7, 340–344, doi:10.1038/ngeo2138, 2014.

Novelli, P. C., Masarie, K. A., and Lang, P. M.: Distributions and recent changes of carbon monoxide in the lower troposphere, J. Geophys. Res.-Atmos., 103, 19015–19033, 1998.

Parrington, M., Palmer, P. I., Lewis, A. C., Lee, J. D., Rickard, A. R., Di Carlo, P., Taylor, J. W., Hopkins, J. R., Punjabi, S., Oram, D. E., Forster, G., Aruffo, E., Moller, S. J., Bauguitte, S. J.-B., Allan, J. D., Coe, H., and Leigh, R. J.: Ozone photochemistry in boreal biomass burning plumes, Atmos. Chem. Phys., 13, 7321-7341, doi:10.5194/acp-13-7321-2013, 2013.

Parrish, D. D., Law, K. S., Staehelin, J., Derwent, R., Cooper, O. R., Tanimoto, H., Volz-Thomas, A., Gilge, S., Scheel, H.-E., Steinbacher, M., and Chan, E.: Long-term changes in lower tropospheric baseline ozone concentrations at northern mid-latitudes, Atmos. Chem. Phys., 12, 11485-11504, doi:10.5194/acp-12-11485-2012, 2012.

Penkett, S. A., Reeves, C. E., Bandy, B. J., Kent, J. M., Richer, H. R.: Comparison of calculated and measured peroxide data collected in marine air to investigate prominent features of the annual cycle of ozone in the troposphere, J. Geophys. Res., 103, 13377-13388, 1998.

Pfister, G. G., Emmons, L. K., Hess, P. G., Honrath, R., Lamarque, J. F., Martin, M. V., Owen, R. C., Avery, M. A., Browell, E. V., Holloway, J. S., Nedelec, P., Purvis, R., Ryerson, T. B., Sachse, G. W., and Schlager, H.: Ozone production from the 2004 North American boreal fires. Journal of Geophysical Research-Atmospheres 111, D24S07, 2006.

Pickering, K. E., Thompson, A. M., Wang, Y., Tao, W., McNamara, D. P., Kirchhoff, V. W. J. H., Heikes, B. G., Sachse, G. W., Bradshaw, J. D., Gregory, G. L., and Blake, D. R.: Convective transport of biomass burning emissions over Brazil during TRACE A. Journal of Geophysical Research 101, 23993-24012, 1996.

Platt, U.: Differential optical absorption spectroscopy (DOAS). Chem. Anal. Series, 127, 27-83, 1994.

Platt, U. and Stutz, J.: Differential Optical Absorption Spectroscopy, Physics of Earth and Space Environments, Springer, Berlin, 2008.

Rahpoe, N., von Savigny, C., Weber, M., Rozanov, A.V., Bovensmann, H., and Burrows, J. P.: Error budget analysis of SCIAMACHY limb ozone profile retrievals using the SCIATRAN model, Atmos. Meas. Tech., 6, 2825-2837, 2013.

Rahpoe, N., Weber, M., Rozanov, A. V., Weigel, K., Bovensmann, H., Burrows, J. P., Laeng, A., Stiller, G., von Clarmann, T., Kyröla, E., Sofieva, V. F., Tamminen, J., Walker, K., Degenstein, D., Bourassa, A. E., Hargreaves, R., Bernath, P., Urban, J., and Murtagh, D. P.: Relative drifts and biases between six ozone limb satellite measurements from the last decade, Atmos. Meas. Tech. Discuss., 8, 3697-3728, 2015.

Ramanathan, V. and Dickinson, R. E.: The Role of Stratospheric Ozone in the Zonal and Seasonal Radiative Energy Balance of the Earth-Troposphere System, J. Atmos. Sci., 36, 1084–1104, 1979.

Read, P. L.: Theory of planetary atmospheres: An introduction to their physics and chemistry. (2nd edition). By J. W. Chamberlain and D. M. Hunten. International Geophysics Series, 36. Academic Press Inc. Florida. 1987. Pp. 481. £41.50. Q.J.R. Meteorol. Soc., 114: 551–552. doi: 10.1002/qj.49711448014, 1988.

Richter, A., Eyring, V., Burrows, J. P., Bovensmann, H., Lauer, A., Sierk, B., and Crutzen, P. J.: Satellite measurements of NO_2 from international shipping emissions, Geophys. Res. Lett., 31, L23110, doi:10.1029/2004GL020822, 2004.

Rodgers, C. D.: Inverse Methods for Atmospheric Sounding: Theory and Practice, World Scientific, Series on Atmospheric, Oceanic and Planetary Physics, 2, Hackensack, N. J., 2000.

Rohen, G. J., von Savigny, C., Llewellyn, E. J., Kaiser, J. W., Eichmann, K.-U., Bracher, A., Bovensmann, H., Burrows, J. P.: First results of ozone profiles between 35 and 65 km retrieved from SCIAMACHY limb spectra and observations of ozone depletion during the solar proton events in Oct./Nov. 2003. Adv. Space Res., 37, 2263-2268, 2006.

Rozanov, A., Bovensmann, H., Bracher, A., Hrechanyy, S., Rozanov, V., Sinnhuber, M., Stroh, F. and Burrows, J. P.: NO2 and BrO vertical profile retrieval from SCIAMACHY limb measurements: sensitivity studies. Adv. Space Res., 36 (5), 846-854, 2005.

Rozanov, A., Eichmann, K.-U., von Savigny, C., Bovensmann, H., Burrows, J. P., von Bargen, A., Doicu, A., Hilgers, S., Godin-Beekmann, S., Leblanc, T., and McDermid, I. S.: Comparison of the inversion algorithms applied to the ozone vertical profile retrieval from SCIAMACHY limb measurements, Atmos. Chem. Phys., 7, 4763-4779, 2007.

Rozanov, A., Kühl, S., Doicu, A., McLinden, C., Puķīte, J., Bovensmann, H., Burrows, J. P., Deutschmann, T., Dorf, M., Goutail, F., Grunow, K., Hendrick, F., von Hobe, M., Hrechanyy, S., Lichtenberg, G., Pfeilsticker, K., Pommereau, J. P., Van Roozendael, M., Stroh, F., and Wagner, T.: BrO vertical distributions from SCIAMACHY limb measurements: comparison of algorithms and retrieval results, Atmos. Meas. Tech., 4, 1319-1359, 2011.

Rozanov, V., Rozanov, A., Kokhanovsky, A., and Burrows, J.: Radiative transfer through terrestrial atmosphere and ocean: software package SCIATRAN, J. Quant. Spectrosc. Ra., 133, 13–71, 2014.

Rozanov, V. V. and Kokhanovsky, A. A.: Semianalytical cloud retrieval algorithm as applied to the cloud top altitude and the cloud geometrical thickness determination from top-of-atmosphere reflectance measurements in the oxygen A band, J. Geophys. Res., 109, D05202, doi:10.1029/2003JD004104, 2004.

Russell, J. M. III, Gordley, L. L., Deaver, L. E., Thompson, R. E., and Park, J. H.: An Overview of the Halogen Occultation Experiment (HALOE) and Preliminary Results, Adv. in Space Res., Vol. 14, No. 9, pp. (9) 13, (9) 20, 1994.

Safieddine, S., Boynard, A., Hao, N., Huang, F., Wang, L., Ji, D., Barret, B., Ghude, S. D., Coheur, P.-F., Hurtmans, D., and Clerbaux, C.: Tropospheric Ozone Variability during the East Asian Summer Monsoon as Observed by Satellite (IASI), Aircraft (MOZAIC) and Ground Stations, Atmos. Chem. Phys. Discuss., 15, 31925-31950, doi:10.5194/acpd-15-31925-2015, 2015.

Sellitto, P., Del Frate, F., Solimini, D., Retscher, C., Bojkov, B., and Bhartia, P. K.: Neural networks algorithms for ozone profile retrieval from ESA-Envisat SCIAMACHY and NASA-Aura OMI satellite data, in: Proceedings of International Geosciences and Remote Sensing Symposium, 2008.

Sellitto, P., Bojkov, B. R., Liu, X., Chance, K., and Del Frate, F.: Tropospheric ozone column retrieval at northern mid-latitudes from the Ozone Monitoring Instrument by means of a neural network algorithm, Atmos. Meas. Tech., 4, 2375-2388, doi:10.5194/amt-4-2375-2011, 2011.

Sellitto, P., Solimini, D., Del Frate, F., and Casadio, S.: Tropospheric ozone column retrieval from ESA-Envisat SCIAMACHY nadir UV/VIS radiance measurements by means of a neural network algorithm, IEEE T. Geosci. Remote, doi:10.1109/TGRS.2011.2163198, in press, 2012.

Seftor, C. J., Jaross, G., Kowitt, M., Haken, M., Li, J., and Flynn, L. E.: Postlaunch performance of the Suomi National Polar-orbiting Partnership Ozone Mapping and Profiler Suite (OMPS) nadir sensors, J. Geophys. Res. Atmos., 119, doi:10.1002/2013JD020472, 2014.

Shiotani, M., Annual, quasi-biennial, and El Nino-Southern Oscillation (ENSO) timescale variations in equatorial total ozone, J . Geophys. Res., 97, 7625-7634, 1992.

Shiotani, M., and Hasebe, F.: Stratospheric ozone variations in the equatorial region as seen in Stratospheric Aerosol and Gas Experiment data, J . Geophys. Res., 99, 14,575-14,584, 1994.

Sierk, B., Richter, A., Rozanov, A., von Savigny, C., Schmoltner, A. M., Buchwitz, M., Bovensmann, H., and Burrows, J. P.: Retrieval and Monitoring of Atmospheric Trace Gas Concentrations in Nadir and Limb Geometry using the Space-Borne SCIAMACHY Instrument, Environ. Monitor. Assess., 120, 65–77, doi:10.1007/s10661-005-9049-9, 2006.

Sinha, P., Jaegle, L., Hobbs, P., Liang, Q.: Transport of biomass burning emissions from southern Africa. Journal of Geophysical Research-Atmospheres 109, D20204, 2004.

Sioris, C. E., Kurosu, T. P., Martin, R. V., and Chance, K.: Stratospheric and tropospheric NO_2 observed by SCIAMACHY: first results, Adv. Space Res., 34, 780–785, 2004.

Sofieva, V. F., Rahpoe, N., Tamminen, J., Kyr l , E., Kalakoski, N., Weber, M., Rozanov, A., von Savigny, C., Laeng, A., von Clarmann, T., Stiller, G., Lossow, S., Degenstein, D., Bourassa, A., Adams, C., Roth, C., Lloyd, N., Bernath, P., Hargreaves, R. J., Urban, J., Murtagh, D., Hauchecorne, A., Dalaudier, F., van Roozendael, M., Kalb, N., and Zehner, C.: Harmonized dataset of ozone profiles from satellite limb and occultation measurements, Earth Syst. Sci. Data, 5, 349-363, doi:10.5194/essd-5-349-2013, 2013.

Sonkaew, T., Rozanov, V. V., von Savigny, C., Rozanov, A., Bovensmann,H., and Burrows, J. P.: Cloud sensitivity studies for stratospheric and lower mesospheric ozone profile retrievals from measurements of limb-scattered solar radiation, Atmos. Meas. Tech., 2, 653–678, 2009.

Srivastava, S., Lal, S., Venkataramani, S., Gupta, S., and Acharya, Y. B.: Vertical distribution of ozone in the lower troposphere over the Bay of Bengal and the Arabian Sea during ICARB-2006: Effects of continental outflow, J. Geophys. Res., 116, D13301, doi:10.1029/2010JD015298, 2011.

Srivastava, S., Lal, S., Naja, M., Venkataramani, S., and Gupta, S.: Influence of regional pollution and long range transport over Western India: analysis of ozonesonde data, Atmos. Environ., 47 (2012), pp. 174–182, 2012.

Staudt, A.C., Jacob, D.J., Logan, J.A., Bachiochi, D., Krishnamurti, T.N., Poisson, N.: Global chemical model analysis of biomass burning and lightning influences over the South Pacific in austral spring, J. Geophys. Res., 107, 4200, 2002.

Stevenson, D. S., Doherty, R. M., Sanderson, M. G., Collins, W. J., Johnson, C. E., and Derwent, R. G.: Radiative forcing from aircraft NO_x emissions: Mechanisms and seasonal dependence, J. Geophys. Res., 109, D17307, doi:10.1029/2004JD004759, 2004.

Stevenson, D. S., Dentener, F. J., Schultz, M. G., et al.: Multimodel ensemble simulations of present-day and near-future tropospheric ozone, J. Geophys. Res., 111, D08301, doi:10.1029/2005JD006338, 2006.

Stohl, A. and Eckhardt, S.: Intercontinental Transport of Air Pollution: An Introduction, Intercontinental Tranport of Air Pollution, The Handbook of Environmental Chemistry, Part G, Springer, Berlin Heidelberg New York, 2004.

Sudo, K. and Akimoto, H.: Global source attribution of tropospheric ozone: Long-range transport from various source regions, J. Geophys. Res., 112, D12302, doi:10.1029/2006JD007992, 2007.

Sudo, K., and Takahashi, M.: Simulation of tropospheric ozone changes during 1997–1998 El Niño: Meteorological impact on tropospheric photochemistry, Geophys. Res. Lett., 28, 4091–4094, 2001.

Tegtmeier, S., Hegglin, M. I., Anderson, J., Bourassa, A., Brohede, S., Degenstein, D., Froidevaux, L., Fuller, R., Funke, B., J. Gille, J., Jones, A., Kasai, Y., Krüger, K., Kyrölä, E., Lingenfelser, G., Lumpe, J., Nardi, B., Neu, J., Pendlebury, D., Remsberg, E., Rozanov, A., Smith, L., Toohey, M., Urban, J., von Clarmann, T., Walker, K. A. and Wang, R. H. J.: SPARC Data Initiative: A comparison of ozone climatologies from international satellite limb sounders, J. Geophys. Res. Atmos., 118(21), 12,229–12, 247, 2013.

Thompson, A. M., and Hudson, R. D.: Tropical tropospheric ozone (TTO) Maps from Nimbus 7 and Earth-Probe TOMS by the modified-residual method: Evaluation with sondes, ENSO signals and trends from Atlantic regional time series, J. Geophys. Res.,104, 26,961–26,975, 1999.

Thompson, A. M., Pickering, K. E., McNamara, D. P., Schoeberl, M. R., Hudson, R. D., Kim, J. H., Browell, E. V., Kirchhoff, V. W. J. H., Nganga, D.: Where did tropospheric ozone over southern Africa and the tropical Atlantic come from in October 1992? Insights from TOMS, GTE TRACE A, and SAFARI 1992 J. Geophys. Res., (D19), 24,251-24,278 , 1996.

Thompson, A.M., Witte, J.C., Hudson, R.D., Guo, H., Herman, J.R., Fujiwara, M.: Tropical tropospheric ozone and biomass burning, Science 291, 2128-2132, 2001.

Uysal, N., and Schapira, R. M.: Effects of ozone on lung function and lung diseases. Curr. Opin. Pulm. Med. 9, 144–150. doi: 10.1097/00063198-200303000-00009, 2003.

Valks, P. J. M.: Variability in tropical tropospheric ozone: Analysis with Global Ozone Monitoring Experiment observations and a global model, J. Geophys. Res., 108(D11), 4328, doi:10.1029/2002JD002894, 2003.

Valks, P., Hao, N., Gimeno Garcia, S., Loyola, D., Dameris, M., Jöckel, P. and Delcloo, A.: Tropical tropospheric ozone column retrieval for GOME-2, Atmos. Meas. Tech. Discuss., 7(1), 727-768, doi:10.5194/amtd-7-727-2014, 2014.

Van Dingenen, R., Dentener, F. J., Raes, F., Krol, M. C., Emberson, L., and Cofala, J.: The global impact of ozone on agricultural crop yields under current and future air quality legislation, Atmos. Environ., 43, 604–618, doi:10.1016/j.atmosenv.2008.10.033, 2009.

Wallace, J. M.: Atmospheric Science: an introductory survey, vol. 92 of International Geophysics Series, Academic Press, 2nd ed., 2006.

Waters, J. W., Froidevaux, L., Harwood, R. S., Jarnot, R. F., Pickett, H. M., Read, W. G., Siegel, P. H., Cofield, R. E., Filipiak, M. J., Flower, D. A., Holden, J. R., Lau, G. K. K., Livesey, N. J., Manney, G. L., Pumphrey, H. C., Santee, M. L., Wu, D. L., Cuddy, D. T., Lay, R. R., Loo, M. S., Perun, V. S., Schwartz, M. J., Stek, P. C., Thurstans, R. P., Boyles, M. A., Chandra, K. M., Chavez, M. C., Chen, G. S., Chudasama, B. V., Dodge, R., Fuller, R. A., Girard, M. A., Jiang, J. H., Jiang, Y. B., Knosp, B. W., LaBelle, R. C., Lam, J. C., Lee, K. A., Miller, D., Oswald, J. E., Patel, N. C., Pukala, D. M., Quintero, O., Scaff, D. M., Van Snyder, W., Tope, M. C., Wagner, P. A., and Walch, M. J.: The Earth Observing System Microwave Limb Sounder (EOS MLS) on the Aura satellite, IEEE Trans. Geosci. Remote Sens., 44 (5), 1075–1092, doi:10.1109/TGRS.2006.873771, 2006.

Wang, Y., Jacob, D.J., Logan, J.A.: Global simulation of tropospheric O_3-NOx-hydrocarbon chemistry: 3. Origin of tropospheric ozone and effects of nonmethane hydrocarbons, Journal of Geophysical Research 103, 10757-10767, 1998b.

Weber, M., Lamsal, L. N., Coldewey-Egbers, M., Bramstedt, K., and Burrows, J. P.: Pole-to-pole validation of GOME WFDOAS total ozone with ground based data, Atmos. Chem. Phys., 5, 1341-1355, doi:10.5194/acp-5-1341-2005, 2005.

Weller, R. A., Baumgartner, M. F., Josey, S. A., Fischer, A. S., and Kindle, J. C.: Atmospheric Forcing in the Arabian Sea during 1994–1995: Observations and Comparisons with Climatology and Models, Deep Sea Research Part II: Topical Studies in Oceanography 45: 1961–1999. doi:10.1016/S0967-0645(98)00060-5, 1998.

Wu, X., Liu, Q., Zeng, J., Grotenhuis, M., Qian, H., Caponi, M., Flynn, L., Jaross, G., Sen, B., Buss, R., Johnson, W., Janz, S., Pan, C., Niu, J., Beck, T., Beach, E., Yu, W., Rama V., Raja, M. K., Stuhmer, D., Cumpton, D., Owen, C., and Li, W.: Evaluation of the Sensor Data Record from the nadir instruments of the Ozone Mapping Profiler Suite (OMPS), J. Geophys. Res. Atmos., 119, 6170–6180, doi:10.1002/2013JD020484, 2014.

Young, P. J., Archibald, A. T., Bowman, K. W., Lamarque, J.-F., Naik, V., Stevenson, D. S., Tilmes, S., Voulgarakis, A., Wild, O., Bergmann, D., Cameron-Smith, P., Cionni, I., Collins, W. J., Dalsøren, S. B., Doherty, R. M., Eyring, V., Faluvegi, G., Horowitz, L. W., Josse, B., Lee, Y. H., MacKenzie, I. A., Nagashima, T., Plummer, D. A., Righi, M., Rumbold, S. T., Skeie, R. B., Shindell, D. T., Strode, S. A., Sudo, K., Szopa, S., and Zeng, G.: Pre-industrial to end 21st century projections of tropospheric ozone from the Atmospheric Chemistry and Climate Model Intercomparison Project (ACCMIP), Atmos. Chem. Phys., 13, 2063–2090, doi:10.5194/acp-13-2063-2013, 2013.

Zahn, A., Brenninkmeijer, C. A. M., Asman, W. A. H., Crutzen, P. J., Heinrich, G., Fischer, H., Cuijpers, J. W. M., and van Velthoven, P. F. J.: Budgets of O_3 and CO in the upper troposphere: CARIBIC passenger aircraft results 1997–2001, J. Geophys. Res., 107(D17), 4337, doi:10.1029/2001JD001529, 2002.

Zanis, P., Hadjinicolaou, P., Pozzer, A., Tyrlis, E., Dafka, S., Mihalopoulos, N., and Lelieveld, J.: Summertime free-tropospheric ozone pool over the eastern Mediterranean/Middle East, Atmos. Chem. Phys., 14, 115-132, doi:10.5194/acp-14-115-2014, 2014.

Zeng, G. and Pyle, J. A.: Influence of El Niño Southern Oscillation on stratosphere/troposphere exchange and the global tropospheric ozone budget, Geophys. Res. Lett., 32, L01814, doi:10.1029/2004GL021353, 2005.

Ziemke, J. R. and Chandra, S.: Development of a climate record of tropospheric and stratospheric column ozone from satellite remote sensing: evidence of an early recovery of global stratospheric ozone, Atmos. Chem. Phys., 12, 5737-5753, doi:10.5194/acp-12-5737-2012, 2012.

Ziemke, J. R., Chandra, S., and Bhartia, P. K.: Two new methods for deriving tropospheric column ozone from TOMS measurements: Assimilated UARS MLS/HALOE and convective-cloud differential techniques, J. Geophys. Res., 103(D17), 22115–22128, 1998.

Ziemke, J. R., Chandra, S., Duncan, B. N., Froidevaux, L., Bhartia, P. K., Levelt, P. F., and Waters, J. W.: Tropospheric ozone determined from Aura OMI and MLS: Evaluation of measurements and comparison with the Global Modeling Initiative's Chemical Transport Model, J. Geophys. Res., 111, D19303, doi:10.1029/2006JD007089, 2006.

Ziemke, J. R., Chandra, S., Labow, G. J., Bhartia, P. K., Froidevaux, L., and Witte, J. C.: A global climatology of tropospheric and stratospheric ozone derived from Aura OMI and MLS measurements, Atmos. Chem. Phys., 11, 9237–9251, doi:10.5194/acp-11-9237-2011, 2011.

Ziemke, J. R., Chandra, S., Oman, L. D., and Bhartia, P. K.: A new ENSO index derived from satellite measurements of column ozone, Atmos. Chem. Phys., 10, 3711-3721, doi:10.5194/acp-10-3711-2010, 2010.

Ziemke, J. R., Chandra, S., Thompson, A.M., and McNamara, D. P.: Zonal asymmetries in southern hemisphere column ozone: Implications of biomass burning, J . Geophys. Res., 101, 14,421-14,427, 1996.